EFFECT OF MULTIAXIAL STATE OF STRESS ON CREEP BEHAVIOUR OF FERRITIC STEELS

By

SUNIL GOYAL

(Enroll. No. ENGG02200704010)

INDIRA GANDHI CENTRE FOR ATOMIC RESEARCH,

KALPAKKAM- 603 102, INDIA

A thesis submitted to the
Board of Studies in Engineering Science Discipline

In partial fulfillment of requirements
For the Degree of

DOCTOR OF PHILOSOPHY

of

HOMI BHABHA NATIONAL INSTITUTE

August, 2013

Homi Bhabha National Institute

Recommendations of the Viva Voce Board

As members of the Viva Voce Board, we certify that we have read the dissertation prepared by **Sunil Goyal** entitled **"Effect of Multiaxial State of Stress on Creep Behaviour of Ferritic Steels"** and recommend that it may be accepted as fulfilling the dissertation requirement for the award of Degree of Doctor of Philosophy.

Chairman – **Dr. B.P.C. Rao** Date: 25/5/15

Guide/Convener- **Dr. K. Laha** Date: 25.5.2015.

Member 1- **Dr. A.K. Bhaduri** Date: 25/5/2015

Member 2- **Dr. K. Velusamy** Date: 25/5/2015

External Examiner B. P. KASHYAP Date: 25/5/2015

Final approval and acceptance of this dissertation is contingent upon the candidate's submission of the final copies of the dissertation to HBNI.

I hereby certify that I have read this dissertation prepared under my direction and recommend that it may be accepted as fulfilling the dissertation requirement.

Date: 25.5.2015.

Place: Kalpakkam.

25.5.2015

Guide- Dr. K. Laha

STATEMENT BY AUTHOR

This dissertation has been submitted in partial fulfillment of requirements for an advanced degree at Homi Bhabha National Institute (HBNI) and is deposited in the Library to be made available to borrowers under rules of the HBNI.

Brief quotations from this dissertation are allowable without special permission, provided that accurate acknowledgement of source is made. Requests for permission for extended quotation from or reproduction of this manuscript in whole or in part may be granted by the Competent Authority of HBNI when in his or her judgment the proposed use of the material is in the interests of scholarship. In all other instances, however, permission must be obtained from the author.

Sunil Goyal

(Sunil Goyal)

DECLARATION

I, hereby declare that the investigation presented in the thesis has been carried out by me. The work is original and has not been submitted earlier as a whole or in part for a degree / diploma at this or any other Institution / University.

Sunil Goyal

(Sunil Goyal)

LIST OF PUBLICATIONS ARISING FROM THE THESIS

Journal Papers

1. Analysis of creep rupture behaviour of Cr-Mo ferritic steels in the presence of notch, **Sunil Goyal**, K. Laha and M.D. Mathew, *Metallurgical and Materials Transactions A*, 46 (**2015**) 205- 217.

2. Creep life prediction of 9Cr-1Mo steel under multiaxial state of stress, **Sunil Goyal** and K. Laha, *Materials Science and Engineering A* 615 (**2014**) 348-360.

3. Mechanistic approach for prediction of creep deformation, damage and rupture life of different Cr-Mo ferritic steels, **Sunil Goyal**, K. Laha, S. Panneer Selvi and M.D. Mathew, *Materials at High Temperatures*, 31 (**2014**) 211- 220.

4. Effect of constraint on creep behaviour of 9Cr-1Mo steel, **Sunil Goyal**, K. Laha, C.R. Das, S. Panneer Selvi and M.D. Mathew, *Metallurgical and Materials Transactions A*, 45 (**2014**) 619- 632.

5. Creep life prediction of modified 9Cr-1Mo steel under multiaxial state of stress, **Sunil Goyal**, K. Laha and M. D. Mathew, *Procedia Engineering*, 86 (**2014**) 150- 157.

6. Effect of multiaxial state of stress on creep rupture behaviour of 2.25Cr-1Mo steel, **Sunil Goyal**, K. Laha, V.D. Vijayanand, S. Panneerselvi and M.D. Mathew, *Procedia Engineering*, 55 (**2013**) 510- 516.

7. Finite element analysis of uniaxial and multiaxial state of stress on creep rupture behaviour of 2.25Cr- 1Mo steel, **Sunil Goyal**, K. Laha, C.R. Das, S. Panneer Selvi, M.D. Mathew, *Materials Science and Engineering A*, 563 (**2013**) 68- 77.

8. Finite element analysis of state of triaxial state of stress on creep cavitation and rupture behaviour of 2.25Cr-1Mo steel, **Sunil Goyal**, K. Laha, C.R. Das, S. Panneer Selvi and M.D. Mathew, *International Journal of Mechanical Sciences*, 75 (**2013**) 233- 243.

Conference Proceedings

1. Creep rupture behaviour of Cr-Mo ferritic steels under multiaxial state of stress, K. Laha, **Sunil Goyal**, M.D. Mathew and T. Jayakumar, International Congress on Advances in Nuclear Power Plants (ICAPP-2014), North Carolina, USA, April 6- 9, **2014**.

2. Creep life prediction of modified 9Cr-1Mo steel under multiaxial state of stress, **Sunil Goyal**, K. Laha and M.D. Mathew, 1st Int. Conference on Structural Integrity (ICONS-2014), Kalpakkam, India, Feb. 4- 7, **2014**, pp. 456- 462.

3. Effect of Multiaxial State of Stress on Creep Rupture Behaviour of 2.25Cr-1Mo Steel, **Sunil Goyal**, K. Laha, V.D. Vijayanand, S. Panneer Selvi and M.D. Mathew, 6th Int. Conf. on Creep, Fatigue and Creep-Fatigue Interaction (CF-6), Mamallapuram, India, Jan 22- 25, **2012**, pp. 410.

Dedicated to…

My beloved parents

ACKNOWLEDGEMENTS

I wish to express my deep sense of gratitude and sincere thanks to my research guide **Dr. K. Laha**, Head, Creep Studies Section (CSS) for his generous inspiration, guidance, encouragement, useful suggestions and good wishes throughout the research tenure. I also thank him for guidance and for critically reviewing my manuscripts and thesis.

I am grateful to **Dr. B.P.C. Rao** (Chairman, Doctoral committee) and **Dr. K. Velusamy** (Member, Doctoral committee) for their encouragement and insightful comments. I would like to specially thank **Dr. A.K. Bhaduri** (Associate Director, MDTG and Member of Doctoral committee) for guidance in carrying out the analysis, valuable discussions and constant encouragement. I thank **Dr. T. Jayakumar** (Director, Metallurgy and Materials Group, IGCAR and Dean, HBNI (Engineering Sciences, IGCAR)) and **Dr. M. Sai Baba** (Associate Director, Resources Management Group) for granting me permission to pursue the Ph.D. degree at the Homi Bhabha National Institute.

It is my great privilege to acknowledge **Dr. M.D. Mathew**, Head MMD for valuable scientific suggestions during the course of this research work. I would like to thank **Dr. R. Sandhya**, Head, FSS and **Dr. B.K. Chaudhary**, Head, DDMS for their cooperation and constant support. I wish to acknowledge the painstaking efforts put in by **Dr. C.R. Das** for SEM investigations. I thank **Dr. C. Ravishankar** and Shri **Utpal Borah** for fruitful discussions while carrying out finite element analysis. I sincerely appreciate the help rendered by Ms. **Panneerselvi** and Shri **M. Srinivasa Rao** for help in preparing samples for SEM. I would like to thank Shri **J. Christopher**, Shri

G. Sainath and **Dr. V. S. Srinivasan** for helpful discussions on continuum damage mechanics.

I record my thanks to my colleagues Smt. **K.S. Chandravathi**, **Dr. Isaac Samuel**, Shri **S. Ravi**, Shri **G.V.P. Reddy**, Shri **V. D. Vijayanand**, Shri **T. Sakthivel**, **J. Ganesh Kumar**, Smt. **J. Vanaja**, Shri **R. Kannan**, Shri **M. Nandagopal**, Shri **J. Veerababu**, Shri **V. Ganesan**, Shri **K. Mariappan,** Shri **S. Sakthy**, Shri **N.S. Thampi** and Shri **M. Gandhi** for valuable help on varied occasions.

Friendly advice and encouragement received from **Dr. A. Nagesha**, **Dr. C. Phaniraj, Dr. Vani Shankar** and **Dr. A. Moitra** are acknowledged.

I wish to extend my sincere esteem and appreciation to my friends S/Shri **Kumar Krovvidi**, **G.K. Sharma**, **N.K. Rathore**, **Alok Chaurey**, **S.K. Khandelawal**, **S.K. Das**, **V.K. Mittal** and **Ashish Jain**.

While I'm writing this dissertation, I can never forget the sacrifices and blessings of my father Shri **Brijendra Goyal** and my mother Smt. **Shushila Goyal** without whom I could ever be what I am now. My brothers Shri **Sudheer**, Shri **Pramod** and Shri **Mahendra** and sister Smt. **Seema** have always been my inspiration and have provided me with all care and moral support during the difficult times. A special word of thanks is due for my wife, Smt. **Smita** for her constant support, love and encouragement, without which, this thesis would not have been possible. I express my heartfelt appreciation for my son **Utkarsh** and daughter **Deeksha** for keeping me in good cheer with their revitalizing company.

CONTENTS

SYNOPSIS

Structural components operating in the creep regime are subjected to multiaxial state of stress which arises due to change in geometry, microstructural inhomogeneity as in weld joint and also due to the mode of loading during service. The components are generally designed based on uniaxial creep data. For realistically assessment of life of such components, it is important to evaluate and predict the creep rupture life under multiaxial state of stress which influences the creep deformation and rupture behaviour appreciably. The effect of multiaxial state of stress on creep deformation and rupture behaviour of materials is generally studied by the introduction of notch in cylindrical specimens.

Creep rupture behaviour of 2.25Cr-1Mo, 9Cr-1Mo and modified 9Cr-1Mo ferritic steels under multiaxial state of stress have been assessed and compared in this investigation. Multiaxial state of stress was incorporated in cylindrical specimen of the steels by introducing circumferentially U-notch with various notch root radius keeping the minimum diameter of the specimen constant (5 mm) similar to plain specimen and shoulder diameter of 8.35 mm. Notches of different root radii of 5 mm, 2.5 mm, 1.25 mm, 0.83 mm, 0.5 mm and 0.25 mm were used to vary the multiaxial state of stress. These notch configurations led to the variation in notch acuity ratio (ratio of notch plane diameter to notch root radius) from 1 to 20 and stress concentration factor of 1 to 3.4. Creep tests have been carried out at net applied stresses ranging from 90 - 230 MPa and at 873 K on the plain and circumferentially U-notched specimens of the steels. Scanning electron microscopy investigation was carried out to assess the effect of notch sharpness on creep fracture appearance and damage accumulation in the steels.

The creep deformation of the ferritic steels under uniaxial stress was characterized by a small instantaneous strain on loading, a transient primary stage, a secondary stage followed by relatively prolonged tertiary creep regime. The variation of steady state creep rate ($\dot{\varepsilon}_s$) with applied stress (σ) for all the three ferritic steels followed Norton's law, a power law relation of the form, $\dot{\varepsilon}_s = A\sigma^n$. The 2.25Cr-1Mo steel was found to have lowest creep deformation resistance and modified 9Cr-1Mo steel exhibited highest creep deformation resistance among the steels. The stress exponent '*n*' value was 6.02 for 2.25Cr-1Mo steel, 8.24 for 9Cr-1Mo steel and 12.92 for modified 9Cr-1Mo steel. The modified 9Cr-1Mo steel possessed higher creep rupture life than both the 2.25Cr-1Mo and 9Cr-1Mo steels. The 9Cr-1Mo and 2.25Cr-1Mo steels exhibited comparable creep rupture life over the investigated stress range. All the steels failed in the ductile dimple appearance. The estimated damage tolerance factor of more than 4 revealed that in all the steels microstructural degradation was the main creep damage mechanism in the steels. The 2.25Cr-1Mo was found to be more prone to creep damage than the 9Cr-steels.

The rupture life of all the steels increased in presence of notch. The creep strengthening of the steels in presence of notch was found to be in the increasing order of 2.25Cr-1Mo steel, 9Cr-1Mo steel and modified 9Cr-1Mo steel. Ductility of the steels decreased in presence of notch. Fractographic studies carried out on 2.25Cr-1Mo steel exhibited typical cup and cone transgranular ductile fracture at relatively higher stresses. Width of the shear lip zone was found to decrease with decrease in applied stress. The evidence of creep cavitation induced brittle fracture at relatively lower applied stresses was observed. In 9Cr-1Mo steel, the fracture appearance in presence of notch as in plain specimen was predominantly transgranular ductile at all the stresses investigated.

Effect of degree of multiaxial state of stress on creep behaviour has been assessed by carrying out creep tests on specimens having different notch radius. The rupture life increased with notch sharpness (notch acuity ratio) for all the steels. The notch strengthening was found to saturate at relatively higher notch acuity ratio. The extent of strengthening with notch acuity ratio was found to depend on the material's deformation characteristics. It was in the increasing order of 2.25Cr-1Mo, 9C-1Mo and modified 9Cr-1Mo steel. With increase in notch acuity ratio, the strengthening increased more rapidly in modified 9Cr-1Mo steel than that in 2.25Cr-1Mo and 9Cr-1Mo steels. The increase in strengthening with notch acuity ratio was comparable for 2.25Cr-1Mo and 9Cr-1Mo steels. Creep rupture ductility of the steels decreased significantly with increase in notch acuity ratio and tends to saturate at higher notch acuity ratio. The 9Cr-1Mo steel exhibited relatively higher ductility than the 2.25Cr-1Mo steel whereas the modified 9Cr-1Mo the least. The increase in notch sharpness decreased the creep rupture ductility to a greater extent in modified 9Cr-1Mo steel and least in 9Cr-1Mo steel.

Creep fracture appearance was found to vary significantly with the notch sharpness (notch acuity ratio). Shear-lip type of failure of the notched specimen was observed for notches of relatively lower notch acuity ratio < 4, as in plain specimen. Shear-lip, characteristic of cup and cone type of failure was caused by final mechanical instability around the notch root region. This suggests that the failure initiated at the central region of the notch throat plane by plasticity-induced intragranular ductile dimple failure mode and propagated towards the notch root. For relatively sharper notches of notch acuity ratio ≥ 4, quite appreciable change in fracture appearance was observed. Intergranular creep cavitation close to notch root and the ductile dimple fracture around the central region of notch throat plane were observed for relatively sharper notches at relatively lower net applied stresses. These evidences clearly indicate that creep cavitation would have started from the notch root region and propagated towards the central region leading to ductile dimple failure by plastic instability at the central region. The fracture appearance changed from predominantly dimple ductile appearance to predominantly intergranular creep cavitation appearance with increase in notch acuity ratio and decrease in net applied stress. The fracture appearance in 9Cr-1Mo showed relatively more ductile dimple appearance for a given net applied stress and notch acuity ratio than that in 2.25Cr-1Mo steel and this has been reflected in higher creep rupture ductility of the 9Cr-1Mo steel than in the 2.25Cr-1Mo steel. Fracture appearance in modified 9Cr-1Mo steel was similar to those in 2.25Cr-1Mo and 9Cr-1Mo steels but the prevalence of intergranular creep cavitation was more for a given applied stress and notch acuity ratio. Metallographic evidences have substantiated the changes in failure mode with notch acuity ratio.

The experimentally observed notch strengthening and its extent, and the difference in fracture appearance of the steels have been explained on the basis of the finite element (FE) analysis of stress distribution across the notch. Due to geometrical and loading symmetry, 2D axisymmetric analysis was carried out using quadrilateral elements. FE analysis was performed incorporating elasto-plastic-creep behaviour of the steels. The plastic deformation of the steels was considered to be governed by Hollomon equation ($\sigma_t = K(\varepsilon_p)^{n'}$) whereas creep deformation by Norton's law ($\dot{\varepsilon}_s = A\sigma^n$). The FE analysis revealed that the multiaxial state of stress was generated in presence of notch in cylindrical specimen of the steels subjected to uniaxial stress due to the imposed constraint. Stresses were found to vary significantly across the notch. As creep deformation progresses, the regions of high stress shed its load to the regions of lower stresses. Stresses distribution across the notch was found to change with creep exposure and approached to a stationary state.

Creep rupture life of the material under multiaxial state of stress depends on the components of stresses viz., maximum principal stress, hydrostatic stress and von-Mises stress in governing the creep deformation and cavitation. The von-Mises stress governs the creep deformation and cavity nucleation processes whereas the maximum principal and hydrostatic stresses control the cavity growth. The von-Mises stress was found to remain below the net applied stress and increased towards notch root. The maximum principal stress was found to be lower than the net applied stress at the central and notch root regions and showed a maximum value which was more than the net applied stress. The behaviour of hydrostatic stress under stationary state condition across the notch throat plane was similar to that of principal stress but the maximum value of the hydrostatic stress remained below the net stress. The decrease in von-Mises stress below the net applied stress after stress redistribution led to the notch strengthening in the steels.

Notch strengthening was found to be comparable for 2.25Cr-1Mo and 9Cr-1Mo steel. However, modified 9Cr-1Mo steel exhibited greater extent of notch strengthening. The von-Mises stress relaxed with creep exposure at different rates and to a different extent depending upon the steels. The relaxation was relatively faster for modified 9Cr-1Mo steel and slowest for 2.25Cr-1Mo steel, because of higher stress sensitivity of creep deformation in modified 9Cr-1Mo steel than that in 2.25Cr-1Mo and 9Cr-1Mo steels. The normalized (with respect to the respective yield stress) von-Mises stress was found to be in the increasing order of modified 9Cr-1Mo, 9Cr-1Mo and 2.25Cr-1Mo steel. Higher von-Mises stress across the notch throat plane in 2.25Cr-1Mo steel was resulted due to the relatively less extent of stress relaxation than in the other two steels. This implies that at a given net applied stress, 2.25Cr-1Mo steel would spend most of its life time at higher von-Mises stress than in modified 9Cr-1Mo steel, resulting in lower notch strengthening, as observed experimentally.

FE analysis was extended to study the effect of notch sharpness on the stress distribution across the notch throat plane to assess its influence on creep rupture life of the steels. The von-Mises across the notch throat plane was found to decrease with increase in notch acuity ratio. The variation in von-Mises stress across the notch throat plane was not found to change appreciably for relatively shallow notches (notch acuity ratio < 4). However, in relatively sharp notches (notch acuity ratios ≥ 4), the von-Mises stress increased gradually at the notch root region, however remained below the net stress for all the notch acuity ratios investigated. The variation in maximum principal stress across the notch throat plane showed a maxima and it had value more than the net applied stress for all notch acuity ratios. The maxima in principal stress increased with notch acuity ratio and its position progressively shifted towards the notch root region. Similar variation in hydrostatic stress across the notch throat plane for different notch acuity ratios was observed; however, the maximum value of hydrostatic stress remained below the net stress for all the notch acuity ratios investigated. The decrease in von-Mises stress with increase in notch acuity ratio led to higher notch strengthening. The saturating tendency of von-Mises stress with increase in notch acuity ratio would have been the cause for saturation of notch strengthening at higher notch acuity ratio. The von-Mises stress decreases significantly with increase in notch acuity ratio for all the steels. Larger extent of decrease in von-Mises stress with notch acuity ratio in all the steels increased the notch strengthening to greater extent. The stress was found to relax with creep exposure at different rate and to a different extent depending upon the material and notch sharpness (notch acuity ratio). The stress relaxation was relatively faster for modified 9Cr-1Mo steel especially for sharper notches and slowest for 2.25Cr-1Mo steel. This resulted in higher extent of notch strengthening in modified 9Cr-1Mo steel than those in 2.25Cr-1Mo and 9Cr-1Mo steels.

The observed variations in fracture appearance in the steels with notch sharpness have been explained based on the FE analysis of stress distribution across the notch throat plane. For the relatively shallow notches (notch acuity ratio < 4), the presence of relatively high and uniform von-Mises stress across notch throat plane has been expected to produce more or less uniform cavity nucleation across the notch throat plane. Growth of the nucleated cavity is influenced by the multiaxial state of stress. The hydrostatic stress plays a significant role in cavity growth under constrained conditions. Presence of high hydrostatic stress at the central region of notch throat plane would have caused preferential growth of the nucleated cavities. Thus, even though nucleation of cavities occurred through out the notch throat plane of shallow notch, the cavities at the central region of notch throat plane would have grown faster. At some critical strain, plastic deformation becomes localized at the ligament between the cavities causing them to rupture by mechanical instability. This result in cavities coalescence and fracture follows. This mechanism becomes important under high strain-rate conditions as in the shallow notch, where significant strain is realized.

For relatively sharper notches (notch acuity ratio ≥ 4), von-Mises stress at the notch root region was found to be maximum. As the nucleation of creep cavities is controlled by von-Mises stress through plastic deformation, nucleation of creep cavities is expected to be more in the notch root region. High principal stress along with high hydrostatic stress would have led to the growth of the nucleated cavities at the near notch root region. The cavity growth by principal stress occurs by diffusive transfer of material from cavity surface to the grain boundary. The fracture surface appearance is expected to be intergranular as observed experimentally. Coalescence of the creep cavities would have led to the propagation of crack from the notch root region towards the central region of the notch throat plane. Final failure of the ligament at the central region of notch throat plane would have occurred due to mechanical instability, resulting in ductile dimple fracture appearance, as observed experimentally.

For component operating under multiaxial state of stress in creep condition, it is important to predict its creep rupture life. FE analysis was used to predict the rupture life of steels subjected to multiaxial state of stress by estimating the representative stress. The representative stress has been defined as the stress applied to the uniaxial plain specimen, which would result in the same creep rupture life as that of notched specimen. The relative contribution of maximum principal stress, hydrostatic stress and von-Mises stress to the representative stress in governing the creep rupture life under multiaxial state of stress has been assessed considering the available models in open literature. Since the stresses vary significantly across the notch during creep exposure, it is difficult to identify the location in notch throat plane at which the stresses should be considered in defining the representative stress for creep rupture life prediction. FE analysis revealed that there exist a point in the notch throat plane, called as skeletal point, at which the variation of stress across the notch throat plane for different stress exponent '*n*' in Norton's law, intersects. The stresses estimated at this point were implemented to estimate the representative stress for predicting the creep rupture life of the steels under multiaxial state of stress. The model proposed by Cane, which has considered the inter-relationship between creep deformation and cavitation, represented the experimental multiaxial creep data well for the steels. The von-Mises stress was found to predominantly govern the creep rupture life of the steels under multiaxial state of stress.

Detailed FE analysis has also been carried out incorporating continuum damage mechanics (CDM) to predict the damage evolution and creep rupture life of the steels under multiaxial state of stress and to validate the experimentally observed variations in fractography. The creep damage law was incorporated in FE analysis using VUMAT subroutine. The user subroutine was written in FORTRAN and implemented in the ABAQUS FE solver for calculating the stresses, creep strains and damage in the plain and notched specimens. VSPRINC utility subroutine was used for calculating the maximum principal stress at each integration point which was used for estimating representative stress along with von-Mises stress. The creep strain and damage rate equations were solved and increment of these variables was calculated. The variables were updated at the end of increment and passed on to main program. The program was terminated on the attainment of damage to the limit of 0.5. As the damage parameter increased beyond this value, the accelerated creep rate led to severe distortion of the elements. The VUMAT subroutine was first implemented for prediction of creep strains and rupture lives of the steels under uniaxial state of stress before applying it to multiaxial state of stress. The predicted creep strains and rupture life was found to be in good agreement with the experimental data, which validated the procedure adopted in the subroutine for FE analysis considering CDM.

The damage evolution in the notched specimens with creep exposure was assessed based on FE analysis coupled with CDM. The damage was found to initiate at the notch root region due to the higher stresses developed as a result of stress concentration for shallow notches. However, the stress relaxation resulted in shifting of damage towards the centre of notch. Finally, the critical damage ($\omega = 0.5$) reaches at the centre of notch resulting cup and cone type fracture as observed experimentally for shallow notches. Quite different accumulation of creep damage behaviour in relatively sharper notches was observed. The stress redistribution across the notch throat plane led to the higher stresses at the notch root region for relatively sharper notches. Unlike in shallow notches, in sharper notches the damage continues to accumulate at the notch root region and attained the critical value. The crack propagated from the notch root region towards centre resulting in fracture appearance as observed experimentally for sharper notches.

The creep damage accumulation was significantly high for 2.25Cr-1Mo than those in 9Cr-steels. The extent was in the decreasing order of 2.25Cr-1Mo, 9Cr-1Mo and modified 9Cr-1Mo steel. This could be attributed to the higher creep deformation resistance observed in modified 9Cr-1Mo steel than that in 2.25Cr-1Mo and 9Cr-1Mo steels. Experimentally observed higher propensity to creep cavitation in 2.25Cr-1Mo steel than in 9Cr-1Mo steel clearly substantiated the FE-CDM analysis of creep damage evolution in the steels. Observed higher tendency to creep cavitation in modified 9Cr-1Mo steel than that in 9Cr-1Mo steel might be due to its enhanced rupture life, which would have facilitated the nucleated creep cavities to grow leading to intergranular creep cavitation.

The rupture life of the steels under multiaxial state of stress predicted based on the continuum damage mechanics coupled with FE analysis was found to be in good agreement with the experiments within a factor of 3.

LIST OF FIGURES

CHAPTER 2

CHAPTER 3

CHAPTER 4

CHAPTER 5

CHAPTER 6

LIST OF TABLES

NOMENCLATURE

σ	Applied stress
σ_{net}	Net applied stress on notched specimen (in the minimum area)
σ_{rep}	Representative stress
σ_t	True stress
σ'_{ij}	Deviatoric stress component
σ_{vm}	Von-Mises stress
σ_m	Mean (hydrostatic) stress
σ_1, σ_2 and σ_3	Maximum, intermediate and minimum principal stresses
σ_{11}, σ_{22} and σ_{33}	Stresses in radial, axial and hoop (tangential) directions
ε_c	Creep strain
$\dot{\varepsilon}_c$	Creep strain rate
$\dot{\varepsilon}_s$	Steady state creep rate
$\dot{\varepsilon}_{c\,ij}$	Component of creep strain rate
ε_p	True plastic strain
ε_f	Creep fracture strain
ω	Creep damage
ω_{cr}	Critical creep damage
$\dot{\omega}$	Creep damage rate
λ	Damage tolerance factor
A and n	Coefficients of Norton's creep law (relating stress with steady state creep rate)
α and C	Monkman-Grant relation coefficients

M and m (or χ)	Coefficients of relation between stress and rupture life
ϕ and B	Coefficients of damage rate equation
K and n'	Coefficients of power law relation for tensile deformation
t_r	Rupture life
t_{rp}	Rupture life of plain specimen
t_{rn}	Rupture life of notched specimen
t_{ot}	Time to reach tertiary creep
T_m	Absolute melting temperature
G	Shear modulus
D	Shoulder diameter in notched specimen
d	Notch throat plane diameter
r	Notch root radius

Abbreviations

2D	two dimensional
CDM	Continuum damage mechanics
FE	Finite element
FE-CDM	Finite element - Continuum damage mechanics
GB	Grain boundary
GBS	Grain boundary sliding
HT	High temperature creep
HD	Harper-Dorn creep
LT	Low temperature creep

MSRC	Multiaxial stress rupture criteria
NH	Nabarrow-Herring creep
PL	Power law creep
PLB	Power law breakdown
RA	Reduction in area
SEM	Scanning Electron Microscopy
ST	Stress triaxiality
VUMAT	User defined material subroutine in ABAQUS

INTRODUCTION

Structural components operating at relatively high temperatures are subjected to creep deformation and damage. Multiaxial state of stress arises in such components as a result of change in geometry, inhomogeneous microstructure as in weld joint and also due to the mode of loading during service. The design of components is generally based on uniaxial creep data; however, it is more appropriate to use creep data under multiaxial state of stress. Notched specimens are widely used to study the effect of multiaxial state of stress on creep deformation and rupture behaviour of materials. The presence of notches may exhibit notch strengthening or weakening depending on the notch geometry, testing conditions and deformation characteristics of the material. Notch strengthening is expected when the high axial stresses across the notch throat plane redistributes quickly during creep exposure and decreases below the applied stress. This kind of behaviour is typically observed in relatively ductile materials. However, the notch weakening is expected in situations where the very high axial stress due to the presence of notch redistributes very slowly. This leads to longer exposure of the material at relatively higher stresses than applied stress which results in creep cavity nucleation at the notch root region. This behaviour is typically observed in relatively brittle materials. Different creep rates across the notch root because of continuous change in cross-sectional area impose constraint to creep deformation to maintain the strain continuity, which facilitates creep cavitation.

The stresses around the notch redistribute during creep deformation and approach to a stationary state condition. Finite element (FE) analysis coupled with continuum damage mechanics (CDM) has been extensively used to understand the stress redistribution and damage accumulation across the notch under creep conditions. It has been observed that for every notch geometry, there is a skeletal point where the stresses are almost constant irrespective of the value of stress exponent ‘*n*’ in Norton’s creep law relating steady state creep rate ($\dot{\varepsilon}_s$) with applies stress (σ) as $\dot{\varepsilon}_s = A\sigma^n$, with *A* and *n* are material constants. The stresses at skeletal point obtained from FE analysis have been used to characterize the deformation and failure behaviour of material under multiaxial state of stress. The creep rupture life under multiaxial state of stress can be expressed similar to uniaxial condition by replacing the applied stress with representative stress. Number of models has been proposed to account for the roles of different components of multiaxial stresses in governing the creep deformation, nucleation and growth of creep cavity and rupture life prediction of material under multiaxial state of stress. These models relate the different contributions of von-Mises and principal stresses in representative stress for prediction of creep rupture life under multiaxial state of stress.

Renewed interest are shown on ferritic steels due to their good thermo-physical properties, adequate high temperature oxidation resistance and mechanical properties and cost effectiveness compared to austenitic stainless steels. Ferritic steels are used in steam generator of Prototype Fast Breeder Reactor (PFBR) at Kalpakkam, fossil power plants, petrochemical industries and heat transport systems. Continuous demand for energy resulted in evolution of 2.25Cr-1Mo steel designated as ASTM Grade 22. Subsequently, 9Cr-1Mo (ASTM Grade 9) steel has been developed to improve high temperature oxidation resistance. Creep properties of the 9Cr-1Mo steel have been improved by alloying with niobium, vanadium and nitrogen (ASTM Grade 91). The Grade 91 steel derives its creep strength from intragranular (V,Nb)(C,N) and intergranular $M_{23}C_6$ on sub-boundaries and from the tempered martensitic lath structure with high dislocation density.

Literature on experiments and modeling of creep behaviour of materials in presence of relatively shallow notches are extensively available. However, little exist on the experiments and validation of such models for relatively sharper notches emphasizing the effect of systematic variation in notch sharpness and deformation characteristics of the materials. In the present investigation, effect of multiaxial state of stress on creep rupture behaviour of three different ferritic steels having different mechanical properties have been studied.

Responses to multiaxial state of stress on creep rupture behaviour of 2.25Cr-1Mo, 9Cr-1Mo and modified 9Cr-1Mo steels have been studied in this investigation. Multiaxial state of stress was incorporated in plain specimens of the steels by introducing circumferentially U-notch with various notch root radius keeping the minimum diameter of the specimen constant (5 mm) similar to plain specimen. Notches of different root radii of 5 mm, 2.5 mm, 1.25 mm, 0.83 mm, 0.5 mm and 0.25 mm were used to create different multiaxial state of stresses in the notched specimens. These notch configurations led to the variation in notch acuity ratio (ratio of notch plane diameter to notch root radius) from 1 to 20 and stress concentration factor of 1 to 3.4. Creep tests have been carried out at net applied stresses ranging from 110 - 230 MPa and at 873 K on the plain and circumferentially U-notched specimens of the steels. Two notches, 20 mm apart, were introduced in the specimens for post-test metallographic investigation on un-failed notch for creep damage evaluation.

Finite element analysis of stress distribution across the notch throat plane during creep exposure has been carried out to understand creep rupture behaviour of the notched specimens. FE analysis was performed incorporating elasto-plastic-creep behaviour of the steels considering plastic deformation of the material represented by Holloman equation ($\sigma_t = K(\varepsilon_p)^{n'}$) along with Norton's creep ($\dot{\varepsilon}_s = A\sigma^n$)

deformation law. Creep and tensile properties required for FE analysis were obtained from the tests carried out on the plain specimens of the steels at 873 K. To assess the different extent of notch strengthening observed in different steels, FE analysis of stress distribution across the notch throat plane has been carried out on incorporating the tensile and creep deformation properties of the individual steels. Detailed FE analysis has also been carried out using continuum damage mechanics to predict the damage evolution and creep rupture life of the steels under uniaxial and multiaxial state of stress. The creep damage law was incorporated in FE analysis using VUMAT subroutine. The user subroutine was written in FORTRAN and implemented in the ABAQUS FE solver for calculating the stresses, creep strains and damage in the plain and notched specimens. The creep strain and damage rate equations were solved and increment of these variables was calculated. The variables were updated at the end of increment and passed on to main program. The program was terminated on the attainment of damage to the limit of 0.5. The rupture life under multiaxial state of stress has been predicted based on representative stress considering the available models. Skeletal point concept was adopted for estimating the representative stress in notched specimens. The analysis of damage evolution across the notch was carried out based on FE-CDM to validate the experimentally observed variations in fractography under multiaxial state of stress in the different ferritic steels.

In this thesis, the experiments, results and the interpretations are consolidated in seven chapters. The chapter 1 gives a general introduction and detailed literature review pertaining to the present investigation. The chapter 2 deals with the materials, notch geometries, experimental procedures and steps involved in FE analysis and CDM. Results on the uniaxial tensile and creep behaviour of the materials are presented and discussed in Chapter 3. In Chapter 4, the effects of notch on creep behaviour of the steels are presented and have been corroborated based on the finite element analysis of stress distribution across the notch on incorporating tensile and creep deformation behaviour of the materials. Chapter 5 deals with the effect of notch sharpness on creep behaviour of the steels and the results have been substantiated with the finite element analysis and fractographic investigation. Predictions of creep rupture life of the materials under multiaxial state of stress has been discussed in Chapter 6 on incorporating damage evolution based on finite element analysis coupled with continuum damage mechanics (FE-CDM). The overall conclusions highlighting the salient finding of the investigation along with the scope for future work are summarized in Chapter 7.

CHAPTER 1

LITERATURE REVIEW

Literature review

1.1 Introduction

Ferritic steels are extensively used as structural materials in steam generating systems of nuclear power plants, fossil fired power plants and petrochemical industries. Structural components operating at high temperatures are subjected to creep damage, which results from the formation, growth and coalescence of cavities and also from the enhanced microstructural degradation in the form of coarsening of precipitates and dislocation substructure under stress. The components are generally designed based on uniaxial creep data. However, the components experience multiaxial state of stress as a result of change in geometry, inhomogeneous microstructure as in weld joint and also due to the mode of loading during service. Prediction of creep rupture life and damage is an important factor for the design of such components.

The chapter describes in brief about the mechanisms of creep deformation and fracture, operating in different stress and temperature regimes. Creep damage mechanisms put forward by different investigators has been reviewed. Different models of creep continuum damage mechanics proposed by different researchers have also been discussed. Means of incorporating multiaxial state of stress in specimens undergoing creep deformation have been introduced emphasizing the importance of circumferential notches to generate different state of stresses in laboratory scale. Effect of notch sharpness on creep rupture behaviour of different materials has been discussed. Finite element analysis of stress distribution across the notch has been critically assessed. Applicability of continuum damage mechanics coupled with FE analysis to estimate the creep rupture life of the materials under multiaxial state of stress has been discussed. Introduction of the materials studied in this investigation has also been made.

1.2 Creep

Creep of materials is classically associated with time-dependent plasticity under a constant stress/load at an elevated temperature, often greater than roughly 0.3 T_m, where T_m is the absolute melting temperature. A typical creep curve under uniaxial loading is shown in Fig. 1.1. The creep curve consists of three regimes viz. primary, secondary and tertiary creep. During the primary stage of creep deformation, the strain rate decreases with increase in strain and time. Primary creep is the period of predominantly transient creep in which the creep resistance of the material increases by virtue of its own deformation. During the secondary creep, the strain rate remains constant which results from the balance between the competing processes of strain hardening and recovery. During tertiary creep, the strain rate increases drastically due to creep cavitation, mechanical instability and metallurgical changes in the material and eventually leads to fracture. The shape of the creep curve is determined by several competing reactions [1], including (i) strain hardening (ii) softening processes such as recovery, recrystallization, strain softening and precipitate overaging; and (iii) damage processes such as cavitation, cracking and specimen necking. Of these factors, strain hardening tends to decrease the creep rate whereas the other factors tend to increase the creep rate. The balance among these factors determines the shape of the creep curve. During primary creep, the decreasing slope of primary curve is attributed to the strain hardening. Secondary stage creep is explained in terms of a balance between strain hardening and the softening and damage processes, resulting in a nearly constant creep rate. The tertiary stage marks the onset of internal or external damage processes, which results in a decrease in the resistance to load or a significant increase in the net section stress. Neubauer et al. [2] attempted to correlate the creep cavitation to the creep life of the power plant components. They characterized the creep cavitation into four stages viz, isolated cavities, oriented cavities, linked cavities (microcracks) and macrocracks, Fig. 1.2.

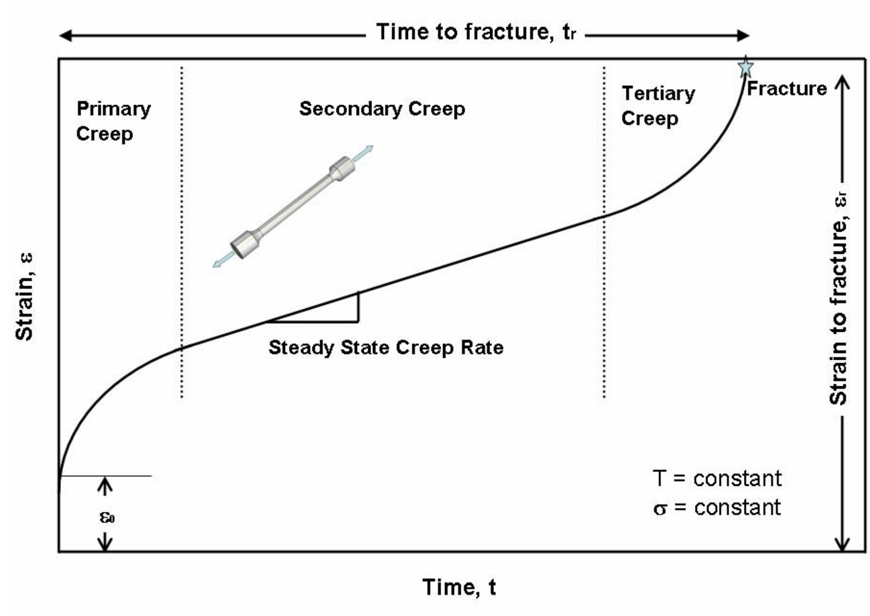

Fig. 1.1 Typical creep curve of materials.

1.3 Deformation mechanisms

Crystalline solids deform plastically by a number of alternative and often competitive mechanisms depending on the macroscopic variables of deformation namely stress (σ), temperature (T) and strain rate ($\dot{\varepsilon}$). These deformation mechanisms are introduced through a deformation mechanisms map, which summarizes the range of dominance of each of the mechanisms of deformation in a compact and cohesive manner. A typical example of an Ashby type deformation mechanism map [3] of normalized stress σ/G (where G is the shear modulus) plotted against homologous temperature T/T_m (where T_m is the melting point in Kelvin) is shown in Fig. 1.3.

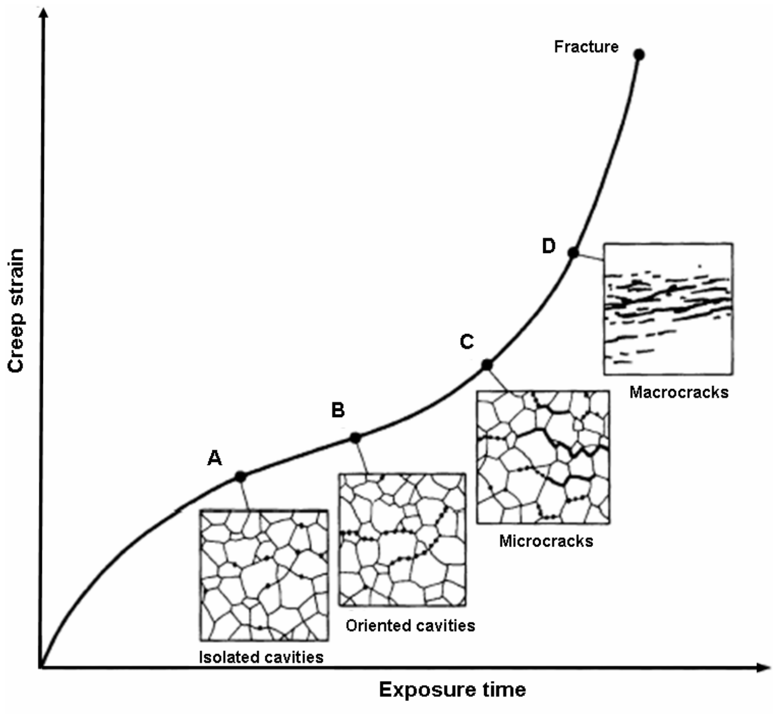

Fig. 1.2 Different stages of creep cavity nucleation and growth as a function of creep exposure [2].

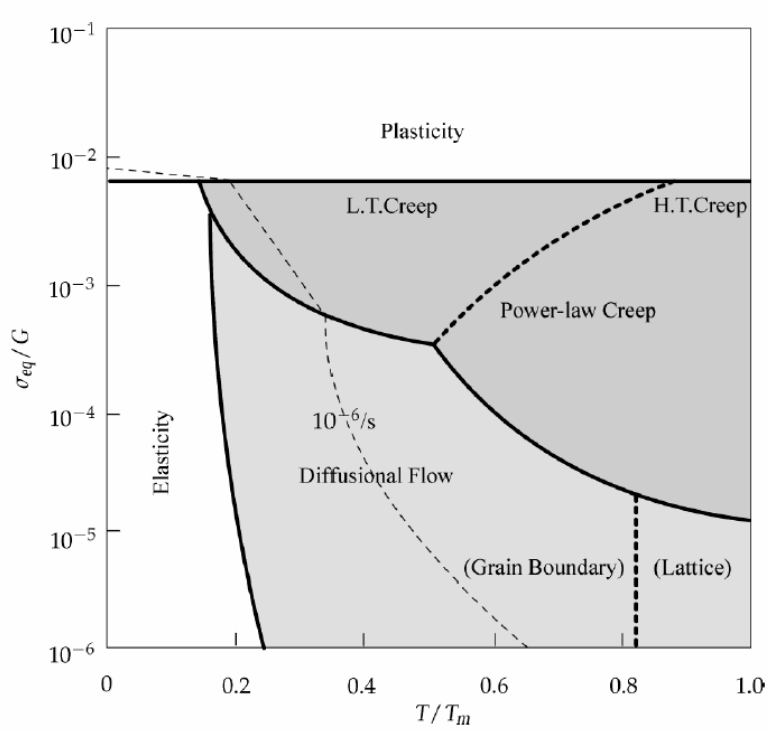

Fig. 1.3 Typical deformation mechanism map (where H.T. means high temperature and L.T. means low temperature) [3].

The deformation mechanism map is divided into various fields in which specific deformation mechanism are rate controlling. The upper limit of the diagram is defined by the ideal shear strength above which deformation ceases to be elastic and becomes catastrophic. Below the ideal shear strength, flow occurs by dislocation glide in the regime of plasticity. The time dependent deformation, i.e., creep regime is divided broadly into dislocation creep and diffusion creep regimes [3]. Dislocation creep regime is further divided into high temperature creep (H-T creep) and low temperature creep (L-T creep) regions. The diffusion creep is divided into Nabarrow-Herring creep (N-H creep) and Coble creep regions [3].

At intermediate temperatures and stresses, creep rate becomes sensitive to stress and exhibits a power law of the form $\dot{\varepsilon}_s = A\sigma^n$, where $\dot{\varepsilon}_s$ is the steady state creep rate and n is the stress exponent. In this power law (PL) creep regime, dislocations acquire a new degree of freedom at high temperature, where thermal activation assists climb and glide process of dislocation (Fig. 1.4).

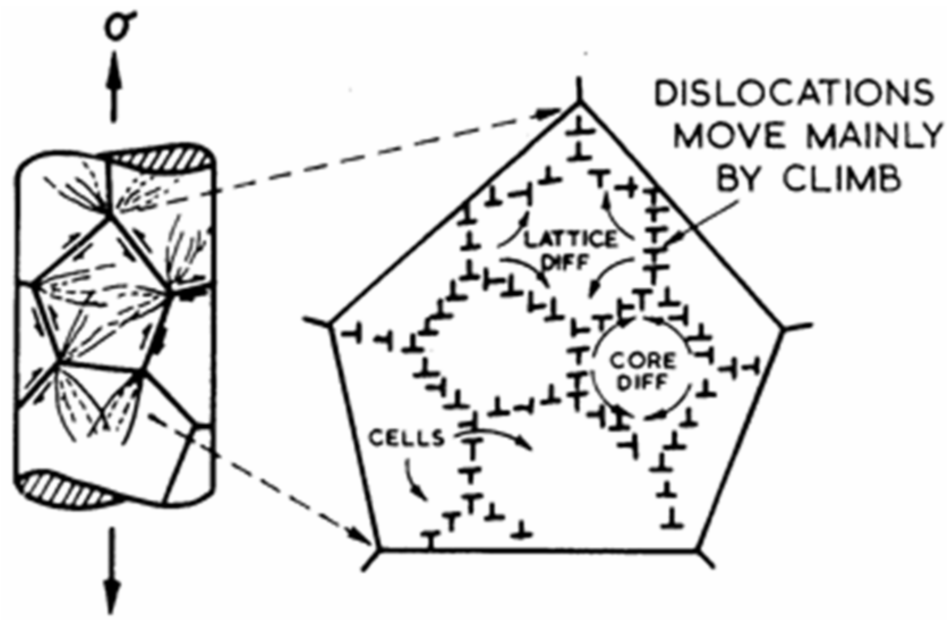

Fig. 1.4 Schematic representation of power law creep involving cell formation by climb [3].

The glide step is responsible for almost all the creep strain but the rate controlling process is the diffusive motion of the single ion or vacancy to or from the climbing dislocation rather than thermally activated glide. In the H-T creep regime, creep is controlled by lattice diffusion and the activation energy for creep deformation is close to that of self diffusion. On the other hand, at low temperatures and high stresses, the transport of matter via dislocation core contributes significantly to the overall diffusive transport of the matter and the field appears as low temperature creep (L-T creep) (Fig. 1.4).

The activation energy for L-T creep is approximately two third of that of lattice diffusion and the strain rate varies as sigma-power σ^{n+2}. At high stresses ($\sigma > 10^{-3}$ G), the simple power law breaks down and dependence of strain rate on stress varies exponentially. This region is known as power law breakdown (PLB) and the flow is glide controlled.

At high temperatures and low stresses, creep occurs by diffusion processes and does not involve dislocation movement to generate strain. In the regime, the stress field with normal stress component changes the chemical potential of atoms on some grain surfaces more than others, thereby introducing a chemical potential gradient. Consequently, creep results from stress directed diffusional transport of matter (Fig. 1.5). At high temperatures, lattice diffusion (N-H creep) controls the rate, while at relatively lower temperatures grain boundary diffusion (Coble creep) takes over. In both the diffusional creep regimes, creep rate exhibits a linear stress dependency but varies as D_l/d^2 for N-H creep and D_{gb}/d^3 for Coble creep. At sufficient low stresses, another creep mechanism known as Harper-Dorn (H-D) creep was observed for larger grain size. In H-D creep, the creep rate exhibits a linear stress dependence but is independent of grain size, and the creep rate is much higher than those possible by diffusional flow. The mechanism underlying H-D creep is complex and the most plausible explanation is that of climb controlled dislocation process under conditions such that the dislocation density does not change with stress. Also at high temperatures, grain boundary sliding takes place, giving a contribution to plastic strain. This sliding, if not accommodated by intragranular deformation either by dislocation glide or by diffusion creep, can lead to grain boundary cavitation.

Thus, the deformation mechanism map summarizes the deformation behaviour and is useful in the following ways: (1) to identify the mechanism by which a component or structure deforms in service, (2) to identify the constitutive law that should be used in design, (3) to estimate the total strain or strain rate of a component in service and (4) to give guidance in alloy design and selection.

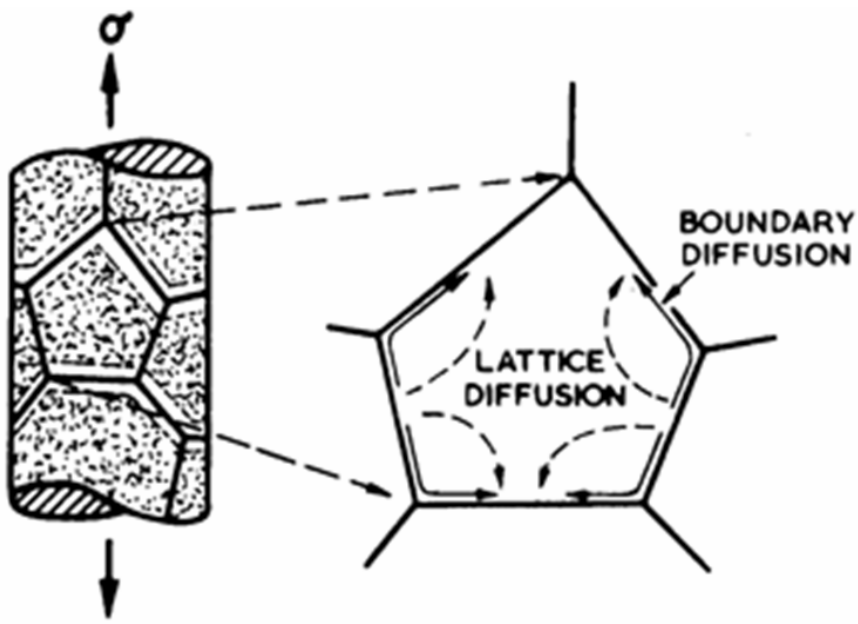

Fig. 1.5 Schematic representation of diffusion flow by diffusional transport through and around the grains [3].

1.4 Fracture mechanisms

If a cylindrical bar of polycrystalline solid is pulled in tension, it may fail in one of the several ways given in Fig. 1.6 [4]. At low temperatures, it may fail by cleavage, by a brittle intergranular fracture, or in a ductile manner. At high temperatures, it may fail by various types of creep fracture which could be transgranular or intergranular depending on the mechanism operating. Fracture mechanism maps are the diagrams with tensile stress as one axis and temperature as the other, showing the fields of dominance of a given mechanism, Fig. 1.7 [4].

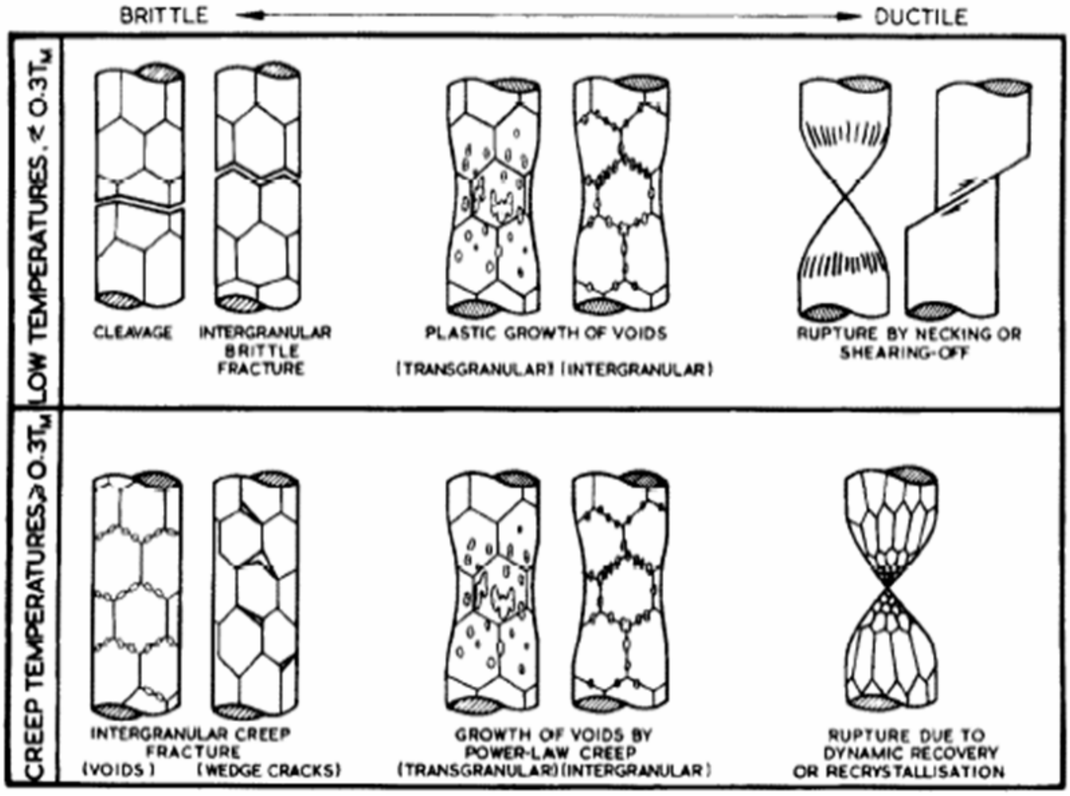

Fig. 1.6 A schematic diagram showing classification of fracture mechanisms [4].

If the stress applied in the specimen overcomes the inter-atomic forces in a perfect crystal, it causes the specimen to separate on a plane normal to the stress axis, and defines its upper limiting strength, Fig. 1.7. Almost all crystalline solids fail by cleavage or intergranular brittle fracture if the temperature is sufficiently low [4];

certain FCC metals and alloys appear to be the only exceptions. Cracks, either pre-existing or nucleated by slip, twinning or grain boundary sliding, can propagate catastrophically to give this type of failure.

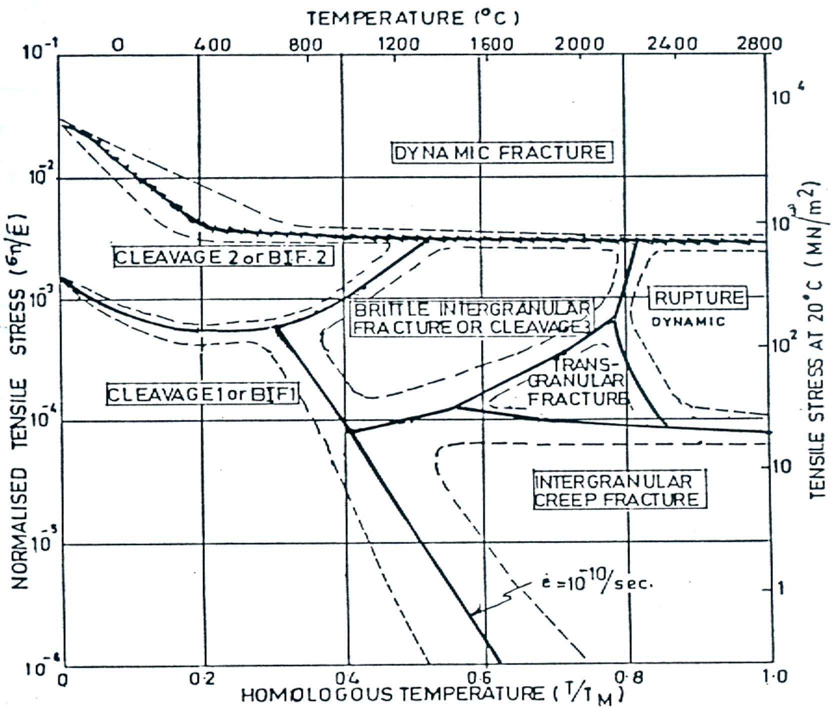

Fig. 1.7 A schematic fracture mechanism map illustrating the dominance of different fracture mechanism in the stress- temperature domain.

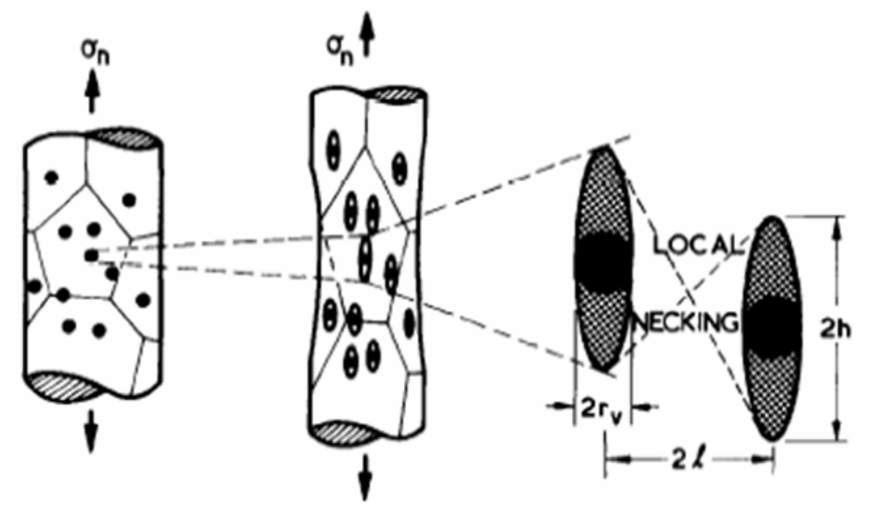

(a) (b) (c)

Fig. 1.8 Schematic representation of ductile and transgranular creep fracture (a) pre-existing holes or they nucleate at stress concentration sites (b) the holes elongate as the specimen deforms (c) they link causing fracture [4].

The stress required for crack propagation would be lower than required for slip or twin to occur. This kind of fracture occurs without gross plastic deformation and is called as *cleavage 1*.

If pre-existing cracks are small or absent, then the stress can reach the level required to initiate slip or twinning. Slip on a limited number of systems (< 5) or twinning generates internal stresses which can nucleate cracks. This regime is called as slip or twin-nucleated cracking *cleavage 2*. This brittle fracture involves crack nucleation and propagation stages and found to have limited ductility (<1%). The increase in temperature decreases the flow stress of the material and this kind of fracture is called as *cleavage 3*. In this regime sufficient plastic deformation (1-10 %) occurs which is sufficient to blunt the pre-existing cracks. General plasticity or grain boundary sliding either nucleates a larger grain boundary crack or causes a pre-existing crack to grow in a stable manner, until its increased length, coupled with the higher stress due to work-hardening, leading to propagate unstably as cleavage crack.

Ductile transgranular fracture involves nucleation and growth of voids. The hard inclusion disturbs both the elastic and plastic displacement field in the deforming body. The local stress built up at the inclusion-matrix interface, if reaches a critical value, fractures the inclusions or tears open its interface with the matrix, thereby nucleating a void [5]. A spherical void concentrates stress and because of this it elongates and becomes ellipsoidal in shape. At some critical strain, plasticity becomes localized, the voids coalesce and fracture follows (Fig. 1.8) [4].

1.4.1 Creep fracture mechanisms

At temperatures above 0.3 T_m where the flow stress depends on strain rate through power law, several fracture mechanisms operate. For ductile transgranular creep fracture, voids nucleate in the same way as low temperature ductile fracture. Since the material is creeping, the stress within it tends to be lower than before and the nucleation may be postponed to longer strains [4]. Also the strain rate dependence of creep can stabilize flow and thereby postpone the coalescence of voids.

Creep cavitation proceeds with the nucleation of creep cavities at a grain boundary and their growth and linkage into discrete cracks leading to final fracture. Creep cavity nucleation is generally associated with stress and strain concentrations at the discontinuities on the grain boundary, such as precipitates, ledges, grain boundary triple points, etc.

1.4.1.1 Cavity nucleation

The mechanism of creep cavity nucleation is not yet well established. It has generally been observed that cavities frequently nucleate on grain boundaries (GB), particularly on those transverse to a tensile stress [6]. In commercial alloys, the cavities appear to be associated with second-phase particles. The nucleation theories fall into several categories [7] that are illustrated in Fig. 1.9: (a) grain-boundary sliding leading to voids at the head (e.g., triple point) of a boundary or formation of voids by ‘‘tensile’’ GB ledges, (b) vacancy condensation, usually at grain boundaries at areas of high stress concentration, (c) the cavity formation at the head of a dislocation pile-up. These mechanisms can involve particles as well (d).

1.4.1.1.1 Vacancy accumulation

Raj and Ashby [8] indicated that vacancies can agglomerate and form stable voids (nuclei). Basically, the cavity nucleation by vacancy accumulation thus appears to require significant stress concentration. However, in elevated temperature plasticity, relaxation by creep plasticity and/or diffusional flow will accompany the elastic loading and relax the stress concentration. The other mechanisms illustrated in Fig. 1.9 can involve Cavity nucleation by direct ‘‘decohesion’’ which, of course, also requires a stress concentration.

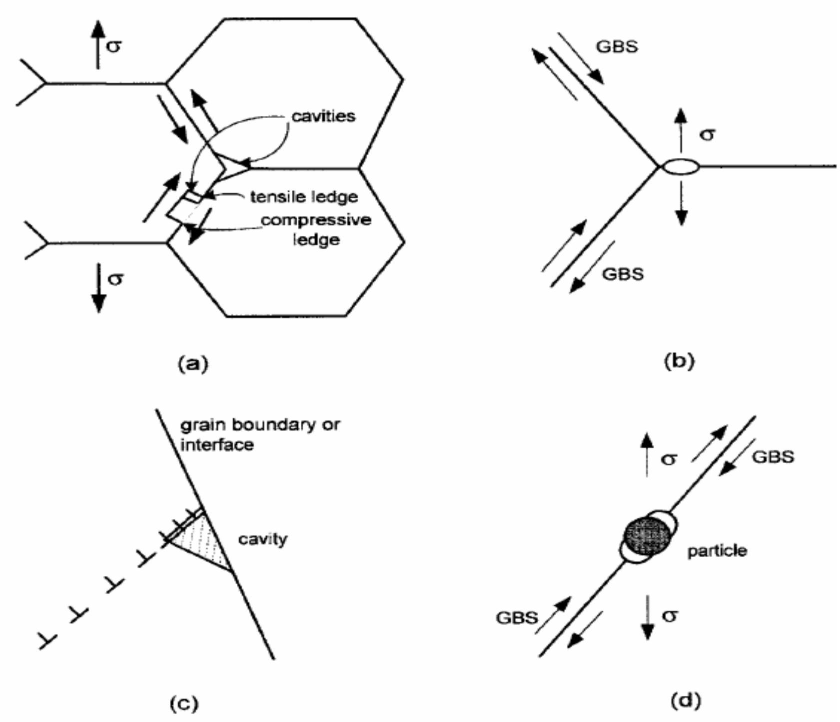

Fig. 1.9 Cavity nucleation mechanisms (a) sliding leading to cavitation from ledges (b) vacancy condensation (c) Zener- Stroh mechanism (d) formation of cavity at matrix particle interface [7].

1.4.1.1.2 Grain boundary sliding

Grain boundary sliding (GBS) can lead to stress concentrations at triple points and hard particles on the grain boundaries. The mechanisms are illustrated in Fig. 1.9(a), (b) and (d). The sliding mechanism includes (tensile) ledges (Fig. 1.9(a)) where tensile stresses generated by GBS may be sufficient to cause cavity nucleation. The formation of ledges may occur as a result of slip along planes intersecting the grain boundaries. The transverse boundaries (perpendicular to the principal tensile stress) generally have propensity to cavitate more [6]. Cavitation observed in bicrystals [9], in which the boundary is perpendicular to the applied stress and no shear stress exists, indicates that the GBS may not be a necessary condition for cavity nucleation.

1.4.1.1.3 Decohesion at inhomogeneity on grain boundary

If the stress concentrations, produced when grain boundary sliding is held up by a finite amount of material around discontinuity like precipitate on grain boundary, are not relaxed, then cavities nucleate at the precipitate/matrix interface by athermal decohesion of atomic bonds between the precipitate and matrix [10]. Nucleation of creep cavity by this mechanism is expected in materials having low particle/matrix interfacial energy and with high stress concentration developed at the interface.

1.4.1.1.4 Plastic deformation

This mechanism of creep cavity nucleation is based on the criteria of critical strain accumulation at or close to particle/matrix interface. At lower stresses and longer times to fracture, a transition from transgranular to intergranular fracture is observed. In this range, cavities nucleate at grain boundaries lying normal to the tensile axis and occur due to grain boundary sliding [11]. The local strain at grain boundary perturbations (precipitates, inclusions, ledges etc.) due to grain boundary sliding reaches a value required to nucleate cavities at grain boundaries before they do so within the grain. If the strain produce by local stress concentration exceeds the critical strain to rupture, then the local rupture can lead to the nucleation of creep cavity. Goods and Brown [5] reviewed the models of creep cavity nucleation in particle-strengthened material based on critical strain approach. With the assumption that under stress, the matrix undergoes plastic deformation while the particle deforms only elastically, cavitation by interface separation between particle and matrix will not occur unless the elastic energy released by removing the stress from the particle is at least as large as the surface energy created, that is: $\Delta E_{el}+\Delta E_s \leq 0$, where ΔE_{el} is the internal elastic energy of the particle and ΔE_s is the energy increase in forming the new internal surfaces. The elastic energy of the particle, estimated based on the combined continuum and micro-mechanical approaches, was approximated as $4/3\,\pi\mu^* r^3 \varepsilon_p^{*2}$, where ε_p^* is the measure of incompatibility between the matrix and particle deformation, μ^* is the shear modulus of the particle and r is the particle radius. If the stress relaxation by plastic deformation occurs due to secondary slip of dislocation around the particle then ε_p^* varies with ε_p as $(b\varepsilon_p/r)^{1/2}$, where ε_p is the shear strain producing the shape change of the material. The total cohesive energy of the interface was estimated as $4\pi r^2 \gamma$ and so the critical strain required for cavity nucleation by this mechanism was expressed by Brown and Stobbs [11] as: $\varepsilon_c = 3\gamma/\mu b$, where ε_c is the critical strain to nucleate cavity, b is the Burgers vector, γ is the particle/matrix interface energy.

1.4.1.2 Creep cavity growth

Though nucleation of creep cavities are expected to depend on principal stress (stress criterion) or von-Mises stress (strain criterion), their subsequent stability is determined by the following expression:

$$r_c = 2\gamma_c/\sigma_1 \,,$$

where, r_c is the critical size of cavity, γ_c is the surface energy and σ_1 is the maximum principal stress. For the growth of existing cavity, it has to attain the critical size otherwise the cavity will sinter.

1.4.1.2.1 Plasticity controlled growth

Cavity growth by plasticity occurs as a result of creep deformation of matrix surrounding the grain boundary cavities in the absence of vacancy flux [12,13]. This mechanism of cavity growth during creep is closely related to the cavity growth during low temperature ductile failure [4]. The strain concentration at cavity surface causes it to grow along the direction of maximum principal stress. The cavity growth rate according to this model is given as: $da/dt = a\dot{\varepsilon} - \gamma_c /2G$, where a is the cavity radius, γ_c is the surface energy of the cavity and G is the shear modulus. At some critical strain, plastic deformation becomes localized and cavities coalescence and fracture follows. This mechanism becomes important under high strain-rate conditions, where significant strain is realized.

Thomason [14,15] and Brown and Embury [16] both used a critical distance of approach of the growing cavities as a criterion for coalescence. Although their models differ in detail, both require a local slip-line field to be developed between adjacent cavities- a condition that is met when the cavity height, $2h$ is about equal to its separation from its neighbors: $2h=\alpha(2l-2a)$, where α is a constant, and $2l$ is the distance between cavities, Fig. 1.8.

1.4.1.2.2 Diffusion controlled growth

The growth of intergranular cavities occurs by absorption of vacancies by cavity surfaces controlled either by diffusion [17] (Fig. 1.10), by coupled diffusion and plastic flow [18] (Fig. 1.11) or by plastic flow alone [12].

In the diffusive growth mechanism, vacancies generated at grain boundaries diffuse to the cavity surfaces through the boundaries, while atoms from cavity surfaces are deposited on the boundaries (Fig. 1.10).

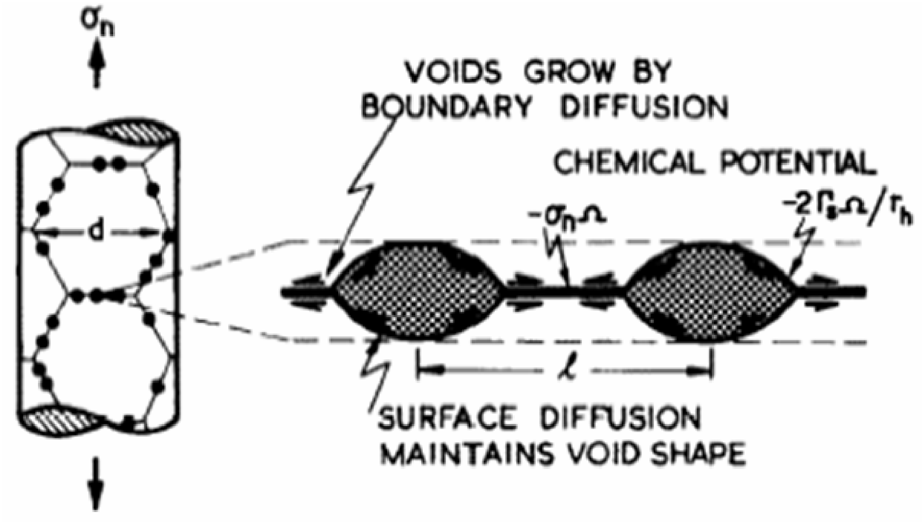

(a) (b)

Fig. 1.10 Schematic representation of void growth (a) and (b) voids lie on boundaries which carry a tensile stress and can grow by diffusional transport of matter from the periphery of the voids to the boundary plane by grain boundary diffusion [4].

Vacancy diffusion occurs because of difference in the chemical potential of vacancy in boundary acted on by tensile stress and the potential of vacancy at the cavity surface. The first detailed analysis of diffusive cavity growth was performed by Hull and Rimmer [17]. Among the different assumptions they made, most important are:

(a) the grains behave as rigid blocks,
(b) the movement of grains in a direction normal to the boundary is not constrained by external factors,
(c) grain boundary is a perfect source of vacancies and maintain an equilibrium between vacancy concentration and normal stress.

For non-rigid grains (i.e., when assumption (a) is not valid), the normal stress profile implicit in the classical diffusional growth model may be relaxed by dislocation creep. Beere and Speight [18] have shown that under this coupled diffusion and plastic flow (Fig. 1.11) circumstances, the resulting growth rate may be obtained by summing the normal stress controlled (diffusive) and the shear deformation controlled components. At high strain rates the deformation controlled component may dominate and the growth behaviour becomes analogous to plastic or continuum cavity growth [12].

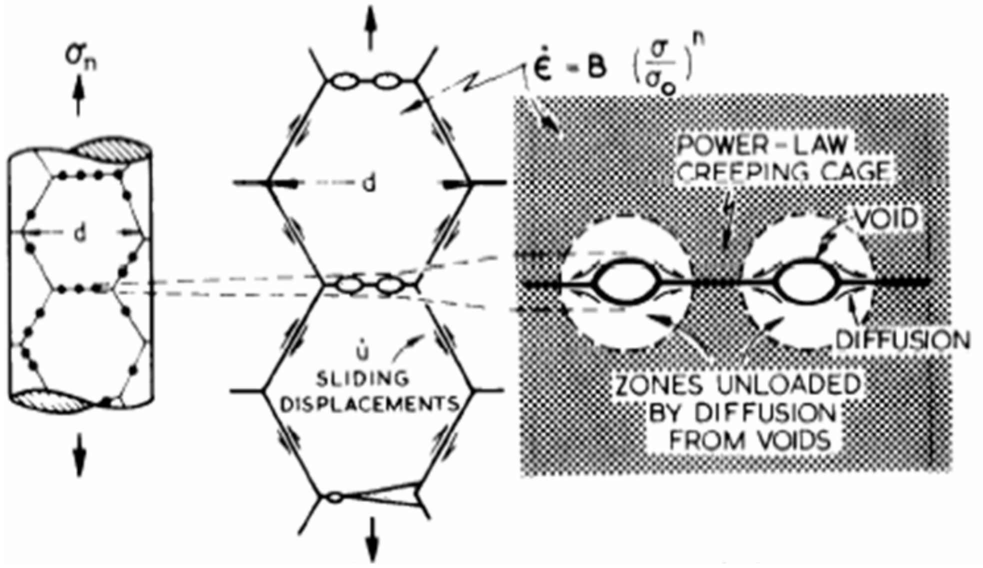

(a) (b) (c)

Fig. 1.11 Schematic representation of intergranular creep controlled fracture. Grain boundary sliding simulates (a) grain and (b) boundary voids (c) they grow by diffusion [4].

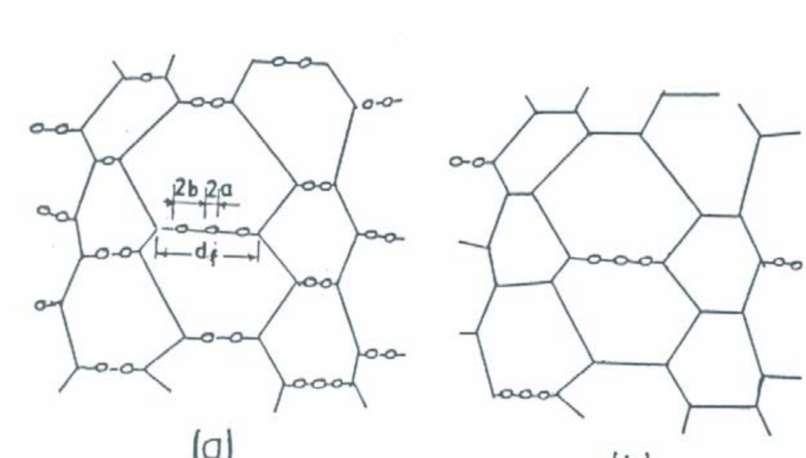

Fig. 1.12 A schematic diagram showing cavities growing on isolated grain boundary facets (a) heavily cavitated (b) slightly cavitated polycrystal. The growth is constrained [19].

Further, growth can be unconstrained or constrained [19] as illustrated in Fig. 1.12. For the case of unconstrained growth, as discussed above, cavities are present on all of the grain boundaries in the solid and are free to grow to the point of complete fracture (assumption (b)). For constrained cavity growth, cavities are present only on isolated boundaries. Here cavity growth on the cavitated grain displacements associated with the cavitation has to be accommodated by corresponding displacement in the matrix. Consequently, cavity growth may be limited entirely by the creep flow of the matrix, but cavitation is still by diffusion.

Another type of constraint has been considered by Dyson [19]. In a perfect grain boundary, vacancies are produced by grain boundary dislocations moving in such boundaries (assumption c)). In engineering alloys containing high densities of grain boundary particles, grain boundaries are not perfect vacancy sources. Under these circumstances two possible mechanisms arise:

(a) vacancy growth is controlled by the movement of intrinsic and extrinsic grain boundary dislocations [20].

(b) dislocations climbing in the grain boundaries originate entirely from matrix and grain-boundary dislocation sources created during dislocation creep. Growth will consequently be limited by the availability of dislocation sources and we have source-controlled vacancy growth [21].

Needleman and Rice [22] explained the enhanced cavity growth based on interaction between the diffusive transfer of matter from cavity surface and the plasticity of matrix. The principal effect is that creep deformability of the grains allows the matter diffused from cavity surface to be accommodated by local separations of the adjoining grains in the vicinity of the cavity. This shortens the effective diffusion path length and results in higher rates of cavity growth than would be the case if either diffusional or plasticity controlled flow of matter acted in isolation.

1.5 Creep damage

The origins of tertiary creep are progressive damage processes including the formation, growth and coalescence of cavities on grain boundaries, coarsening of precipitates and environmental effects. The cavities may nucleate earlier during the creep process, possibly at primary creep stage, Fig. 1.2. The growth of cavities weakens the material's load-bearing capacity. The coalescence of cavities or propagation of micro-cracks leads to the final fracture. Continuum damage mechanics, introduced by Kachanov [23], has been widely used for characterizing the evolution of the material damage during tertiary creep.

1.5.1 Creep damage evaluation

1.5.1.1 Kachanov-Rabotnov Model

The phenomenological creep-damage equations developed by L.M. Kachanov [23] and Rabotnov [24] consist of an internal scalar damage variable which characterizes the creep damage of the material. Specifying the initial cross-section area of a specimen by A_0 and the area covered by cavities as A, the Kachanov's continuity is defined as follows [25];

$$\omega = \frac{A}{A_0}; 0 \le \omega \le 1 \qquad (1.1)$$

$$\psi = 1 - \omega = \frac{A_0 - A}{A} \qquad (1.2)$$

where ψ is the continuity function, which is a positive and continuously decreasing function. The value $\psi = 1$ ($\omega = 0$) means the virgin material, whereas, $\psi = 0$ ($\omega = 1$) corresponds to the fracture (completely damaged cross-section).

Rabotnov [24] assumed that the creep rate is a function of stress and current damage state as

$$\dot{\varepsilon}_c = \dot{\varepsilon}_c(\sigma, \omega)$$

Furthermore, the damage processes also can be reflected in evolution form

$$\dot{\omega} = \dot{\omega}(\sigma, \omega)$$

$$\dot{\varepsilon}_c = \frac{A\sigma^n}{(1-\omega)^\phi} \tag{1.3}$$

$$\dot{\omega} = \frac{B\sigma^\chi}{(1-\omega)^\phi}\,. \tag{1.4}$$

When the damage is zero (virgin material), the creep rate equation (Eq. 1.3) leads to the Norton's power law.

$$\dot{\varepsilon}_s = A\sigma^n \tag{1.5}$$

Setting $\chi = n$ the first equation can be written as; $\dot{\varepsilon}_c = A\sigma_{eff}^n$

where $\sigma_{eff} = \sigma/(1-\omega)$ is the so-called net-stress or effective stress. In this case, the equation represents the Norton-Bailey secondary creep law for the description of tertiary stage of creep deformation.

Lemaitre and Chaboche [26] proposed the effective stress concept to formulate constitutive equations for damaged materials based on available constitutive equation for "virgin" materials.

For a constant stress, the damage evolution (Eq. 1.4) can be integrated as follows

$$\int_0^{\omega_{cr}} (1-\omega)^\phi \, d\omega = \int_0^{t_r} B\sigma^\chi \, dt$$

where t_r is the rupture life and ω_{cr} is the critical damage (= 1). The integration leads to the following expression

$$t_r = \frac{1}{B(1+\phi)\sigma^{\chi}} \tag{1.6}$$

This equation relates the rupture life with stress and can be expressed as

$$t_r = M\sigma^{-m} \tag{1.7}$$

where, m is the slope (χ) of the uniaxial creep rupture plot and $M = 1/B(1+\phi)$.

The creep damage as a function of time can be represented as

$$\omega = 1 - \left(1 - \frac{t}{t_r}\right)^{1/(1+\phi)} \tag{1.8}$$

This equation incorporated in strain rate equation and integration leads to the following relation

$$\varepsilon_c = \frac{A\sigma^{(n-\chi)}}{B(n-\phi-1)}\left\{\left[1 - \frac{t}{t_r}\right]^{\frac{\phi+1-n}{\phi+1}} - 1\right\} \tag{1.9}$$

By setting t = t_r the creep strain before the fracture, i.e. $\varepsilon_c^r = \varepsilon_c^r(t_r)$, can be calculated as

$$\varepsilon_c^r = \frac{A\sigma^{(n-\chi)}}{B(\phi+1-n)} \tag{1.10}$$

Solving Eqs. 1.7, 1.5 and 1.10 gives a expression as

$$\varepsilon_c^r = \frac{\dot{\varepsilon}_s t_r}{1 - \dfrac{n}{\phi+1}} \tag{1.11}$$

$$\dot{\varepsilon}_s \times t_r = \frac{A}{B(1+\phi)}\sigma^{(n-\chi)} \tag{1.12}$$

In a special case, if $n = \chi$, then,

$$\dot{\varepsilon}_s \times t_r = \frac{A}{B(1+\phi)} \tag{1.13}$$

This is the Monkman-Grant relationship [27] which states, that for a given material the product of the steady state creep rate and the time to fracture is a material constant. It can be noticed that the Monkman-Grant relationship follows from the Kachanov- Rabotnov model if the slopes of the steady state creep rate vs. stress and the stress vs. time to fracture dependencies coincide in the double logarithmic scale. In this case, the creep strain before the creep fracture (creep ductility) should be stress independent, as it follows from the Eq. 1.11.

1.5.1.2 Physically based continuum damage mechanics model

Physically-based continuum creep damage mechanics (CDM) is a multi-state variable formulation for creep rate that has its origin in the single-state variable description of tertiary creep introduced by Kachanov [23] and Rabotnov [24]. However, CDM differs considerably in detail from the original empirical concept of Kachanov / Rabatnov and additionally considers primary creep, with secondary creep and damage due to different microstructural damages. Whether the resultant secondary creep rate is close or not in magnitude to a steady state rate depends on specific circumstances.

Ashby et al. [28], Dyson [29] and Dyson et al. [30] identified four broad categories of creep damage due to (i) loss of external section, (ii) loss of internal section, (iii) degradation of microstructure and (iv) gaseous environmental attack, Fig. 1.13. Each category was found to contain several micro-mechanisms.

CREEP DAMAGE CATEGORY	DAMAGE MECHANISM		DAMAGE PARAMETER	DAMAGE RATE	CREEP RATE
Strain-Induced	Cavity Nucleation Control; Growth Constrained	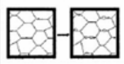	$D_N = \frac{\pi d^2 N}{4} = \omega$	$\dot{\omega} = \frac{k_N}{\varepsilon_u}\dot{\varepsilon}$	$\dot{\varepsilon} = \dot{\varepsilon}_0 \sinh\left[\frac{\sigma(1-H)}{\sigma_0(1-\omega)}\right]$
	Cavity Growth Controlled by Creep-Constraint	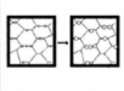	$D_N = \frac{\pi d^2 N}{4} = \omega$ $D_G = \left(\frac{r}{\ell}\right)^2$	$\dot{\omega} = o$ $\dot{D}_G = \frac{d}{2\ell D_G}\dot{\varepsilon}$	$\dot{\varepsilon} = \dot{\varepsilon}_0 \sinh\left[\frac{\sigma(1-H)}{\sigma_0(1-\omega)}\right]$
	Dynamic Subgrain Coarsening	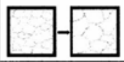	$D_{sg} = 1 - \left(\frac{r_{sg,i}}{r_{sg}}\right)$	$\dot{D}_{sg} = (1-D_{sg})\frac{\dot{r}_{sg}}{r_{sg}}$	?
	Multiplication of Mobile Dislocations		$D_d = \frac{\rho}{\rho_i} - 1$	$\dot{D}_d = C\dot{\varepsilon}$	$\dot{\varepsilon} = \dot{\varepsilon}_0(1+D_d)\sinh\left[\frac{\sigma(1-H)}{\sigma_0}\right]$
Thermally-Induced	Particle-Coarsening	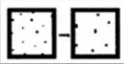	$D_p = 1 - \frac{P_i}{P}$	$\dot{D}_p = \frac{K_p}{3}(1-D_p)^4$	$\dot{\varepsilon} = \dot{\varepsilon}_0 \sinh\left[\frac{\sigma(1-H)}{\sigma_0(1-D_p)}\right]$
	Depletion of Solid-Solution Elements		$D_s = 1 - \frac{\bar{c}_t}{c_0}$	$\dot{D}_s = K_s D_s^{1/3}(1-D_s)$	$\dot{\varepsilon} = \frac{\dot{\varepsilon}_0}{(1-D_s)}\sinh\left[\frac{\sigma(1-H)}{\sigma_0}\right]$
Environmentally-Induced	Fracture of Surface Corrosion Product		$D_{cor} = \frac{2x}{R}$	$\dot{D}_{cor} = \frac{1}{R}\left(\frac{K_c\dot{\varepsilon}}{\varepsilon^*}\right)^{1/2}$	$\dot{\varepsilon} = \dot{\varepsilon}_0 \sinh\left[\frac{\sigma(1-H)}{\sigma_0(1-D_{cor})}\right]$
	Internal Oxidation	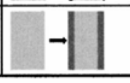	$D_{ox} = \frac{2x}{R}$	$\dot{D}_{ox} = \frac{K_{ox}}{R^2 D_{ox}}$	$\dot{\varepsilon} = \dot{\varepsilon}_0 \sinh\left[\frac{\sigma(1-H)}{\sigma_0(1-D_{ox})}\right]$

Fig. 1.13 Schematic diagram showing creep damage mechanisms and associated governing equations [30].

Strain induced damage

Grain boundary cavitation, dynamic sub-grain coarsening and mobile dislocation multiplication have all been identified as belonging to this category. Two types of creep cavitation mechanisms are discussed. In one, cavity nucleation is assumed to be rapid compared to growth and a fixed density of cavities is allowed to grow until coalescence occurs followed by rupture. The more usual case is when nucleation occurs continuously throughout creep life. This is a difficult problem to quantify in general, but specific cases are easier to analyze and are also important. Under service stressing, it is possible to provide a simplified analysis because cavity growth rates will be sufficiently rapid compared to matrix creep rates that constraint growth will always prevail. Subgrains do not form in many commercial alloys, but their strain controlled growth in tempered martensitic steels has been judged by to have an important role in controlling creep strain rate acceleration in tertiary creep, and thus in determining creep life. Although subgrains can and do grow by thermally induced processes, the strain induced mechanism appears to be faster.

Thermally induced damage:

Thermally induced damage can occur in some materials by coarsening of a constant volume fraction of particles or dissolution of precipitate particles. These particles add creep strength to the material. Coarsening of particles increases the creep rates during creep deformation and leads to creep damage in the material.

Environmentally induced damage:

The distinguishing feature of environmentally induced damage is that the damage rate is inversely related to the size of the component. This kind of damage could result from oxidation or corrosive environment. This results in cracking and exposure of new material for further attack leading to reduction in creep life.

1.6 Multiaxial state of stress

In the design and creep life prediction of elevated temperature components, extensive use is made of test data generated on laboratory samples under uniaxial stress. However, the components experience multiaxial state of stress as a result of change in geometry, inhomogeneous microstructure as in weld joint [31] and also due to the mode of loading during service. In order to assess the life of such components, it is necessary to establish the effective stress criteria governing creep and rupture under multiaxial stress conditions and to be able to interpret them in terms of uniaxial test data. In addition, the redistribution of stresses occurring during creep must be taken into account.

The following assumptions are made in predicting the creep life under multiaxial state of stress [32].

(1) Constant volume is maintained during creep

$$\dot{\varepsilon}_1 + \dot{\varepsilon}_2 + \dot{\varepsilon}_3 = 0 \tag{1.14}$$

(2) the principal shear strain rates are proportional to the principal shear stresses

$$\frac{\dot{\gamma}_1}{\tau_1} = \frac{\dot{\gamma}_2}{\tau_2} = \frac{\dot{\gamma}_3}{\tau_3} = 2\psi \tag{1.15}$$

where ψ is a constant and $\dot{\gamma}_1$, $\dot{\gamma}_2$ and $\dot{\gamma}_3$ are shear strain rates and τ_1, τ_2 and τ_3 are respective principal shear stresses and are defined as

$$\tau_1 = \frac{1}{2}(\sigma_2 - \sigma_3),\ \tau_2 = \frac{1}{2}(\sigma_3 - \sigma_1) \text{ and } \tau_3 = \frac{1}{2}(\sigma_1 - \sigma_2)$$

$$\gamma_1 = \varepsilon_2 - \varepsilon_3,\ \gamma_2 = \varepsilon_3 - \varepsilon_1 \text{ and } \gamma_3 = \varepsilon_1 - \varepsilon_2$$

Combining these two results leads to the relations

$$\dot{\varepsilon}_{ij} = \psi(\sigma_{ij} - \sigma_m)$$

where

$$\psi = \frac{3\bar{\dot{\varepsilon}}}{2\sigma_{vm}} \text{ and } \sigma_m = \frac{1}{2}(\sigma_1 + \sigma_2 + \sigma_3)$$

(3) the effective strain rate is related to the effective stress in the same way as in the uniaxial loading, e.g.

$\bar{\dot{\varepsilon}} = f_1(t) f_2(\sigma_{vm})$ where σ_{vm} is the von-Mises stress and is defined as,

$$\sigma_{vm} = \frac{1}{\sqrt{2}}\sqrt{(\sigma_1 - \sigma_2)^2 + (\sigma_2 - \sigma_3)^2 + (\sigma_3 - \sigma_1)^2}$$

Therefore,

$$\dot{\varepsilon}_{ij} = \frac{3}{2} f_1(t) \frac{f_2(\sigma_{vm})}{\sigma_{vm}} (\sigma_{ij} - \sigma_m) \tag{1.16}$$

The constitutive relations under steady state conditions for multiaxial state of stress can be defined as

$$\dot{\varepsilon}_{ij} = \frac{3}{2}\frac{f_2(\sigma_{vm})}{\sigma_{vm}}\sigma'_{ij} \tag{1.17}$$

where, σ'_{ij} is the deviatoric stress components ($\sigma'_{ij} = (\sigma_{ij} - \sigma_m)$)

In case of Norton's law relation as stress function,

$f_2(\sigma_{vm}) = A\sigma_{vm}^n$ the creep rate equation becomes,

$$\dot{\varepsilon}_{ij} = \frac{3}{2}A\sigma_{vm}^{n-1}\sigma'_{ij} \tag{1.18}$$

Creep strain rate including one damage variable can be expressed in the following form

$$\dot{\varepsilon}_c = \frac{3}{2}A\left(\frac{\sigma_{vm}}{1-\omega}\right)^{n-1}\frac{\sigma'_{ij}}{1-\omega} \tag{1.19}$$

and damage rate can be defined in terms of representative stress

$$\dot{\omega} = \frac{B\sigma_{rep}}{(1-\omega)^{\phi}} \tag{1.20}$$

1.6.1 Types of multiaxial testing

Various techniques have been developed to test materials under multi-axial creep conditions [33]. Examples of multi-axial specimens for creep testing are: thin-walled pipes subjected to axial force and torque, tubes under internal pressure, two- and three-dimensional cruciform specimens subjected to axial forces, circumferentially notched specimens subjected to axial force.

Geometrical representation of yield surface in three dimensional state of stress (σ_1, σ_2 and σ_3) in plane stress condition is shown in Fig. 1.14 [34].

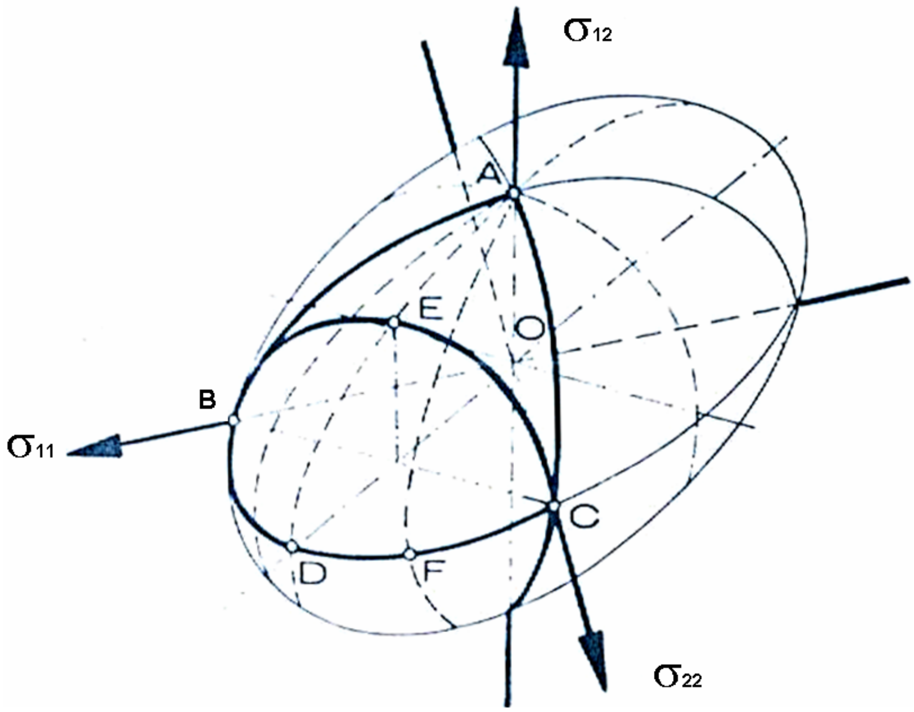

Fig. 1.14 The von-Mises potential surface for an isotropic body under plane stress conditions [34].

Ellipses formed by intersection of the ellipsoid with the appropriate planes represent different ways of stressing which may be realized experimentally:

AB or AC: tension-torsion of thin tubular specimens

BDC: tension-internal pressure of thin tubular specimens, tension of cruciform specimens

AD or AF: torsion-internal pressure of thin tubular specimens

Point A: torsion of thin tubular specimens.

1.6.1.1 Tubes with internal pressure

In pressurized tubes or pipes a multiaxial state of stress exists, which changes with time from the initial elastic state to a stationary state distribution and subsequently redistributes during tertiary creep. The tubes with internal pressure can also be tested by superimposing axial load [35]. The internal pressure is usually produced by steam or inert gas but in some cases liquid sodium provides the pressure whereas in others corrosive process gases are used. In case of maximum principal stress governing behavior, the simple thin wall elastic calculation should be made ($P = \sigma t / r$) even for thick walled specimens if *n* (stress exponent) is unknown. For known values of *n*, the maximum hoop stress after redistribution should be used to determine the internal pressure. Conversely for von-Mises stress controlled behavior, the thin wall elastic solution ($P = 2\sigma t / \sqrt{3}\, r$) should be made if *n* is unknown (*P* is pressure, *r* is the radius, *t* is the thickness and σ is the stress). For known values of *n*, the maximum equivalent stress after redistribution should be used. The advantage of carrying out creep tests under internal pressure is that pipes of same dimensions can be tested and improved design and remnant life assessment can be made and multiaxial stress rupture criteria can be determined. However, the disadvantage is that the experimental setup would be of larger size and safety due to higher internal pressure would be a concern.

1.6.1.2 Tension-torsion of thin tubular specimens

Biaxial testing on thin walled pipes is carried out by applying torsional load along with axial load [34]. Axial load is applied through the lever mechanism. Torque is applied to the test piece through the torque disc. Special care is required for imposing the defined stress state to the specimen. Following precautions should be made while testing under tension-torsion testing.

1. The surface effects should not dominate in the behaviour of specimens. In order to avoid this, the ratio of surface area to volume of the specimen must be as small as possible.

2. Specimen must not be too thick in order to avoid a stress gradient through the thickness; and
3. The appropriate ratio of thickness to external diameter must be achieved to avoid premature buckling.

1.6.1.3 Cruciform specimen

The problem associated with tube testing (viz. rotation of principal stress plane due to shear deformation and buckling etc.) can be overcome by use of cruciform specimens [36]. The design of such a specimen consists of series of limbs extending from each edge of a thinned central square section. These limbs prevent the lateral constraint on the central test section. This kind of specimens can be used for testing in tension-tension quadrant and tension-compression quadrant of two dimensional stress states.

1.6.1.4 Notched specimens

The most widely used technique for introducing multiaxial state of stress into a specimen is by subjecting the circumferentially notched bar subjected to axial tensile load [37- 45]. The constraint to radial deformation provided by the shank introduces a state of multiaxial state of stress in the notch region which depends upon the notch geometry and creep properties of the material [43].

1.6.1.4.1 Stresses around notch

The stresses vary significantly across the notch. Bridgman developed a semi-empirical analysis in terms of radius of curvature of the neck and the radius of the minimum cross-section [46]. The expression for the three components of stresses can be expressed as

Von-Mises stress, $$\sigma_{vm} = \sigma_{nom}\left[\left(1+\frac{2r}{a}\right)\ln\left(1+\frac{a}{2r}\right)\right]^{-1} \quad (1.21)$$

Radial and hoop (tangential) stress, $$\sigma_{11} = \sigma_{33} = \sigma_{vm}\ln\left[1+\frac{1}{2}\frac{a}{r}\left(1-\frac{x^2}{a^2}\right)\right] \quad (1.22)$$

Axial stress, $$\sigma_{22} = \sigma_{vm}\left\{1+\ln\left[1+\frac{1}{2}\frac{a}{r}\left(1-\frac{x^2}{a^2}\right)\right]\right\} \quad (1.23)$$

where, a is the minimum notch section radius, x is the radial distance and r is the notch root radius. Hayhurst et al. [45] carried out FE analysis under creep conditions and observed that the stress distribution for the notched specimens with shallow notch and ductile material (high stress exponent) and shallow notch matches the Bridgman's analysis which considers elastic-perfectly plastic deformation.

1.7 Effect of notch on creep behaviour

1.7.1 Stress redistribution

Different creep rates across the notch root because of continuous change in cross-sectional area impose constraint to creep deformation to maintain the strain continuity. The stresses around the notch redistribute during creep deformation and approach to a stationary state condition [43]. Hayhurst et al. [45] studied the stress redistribution around circumferential semicircular U and V-notches. Stationary state stress distributions for the circular U-notch were found to be relatively smooth; whereas for V-notch, the stress distribution was non-uniform and peak developed adjacent to the notch tip where plain strain condition prevailed. Time required to attain the stationary state for V-notches was found to be much higher than that for U-notches. The degree of constraint imposed on the materials depends on the kind of notch introduced and the profile of notch root and ductility of the material [44,45]. Both V- and U-notches are incorporated in the cylindrical creep specimen to study the effect of constraint on creep behaviour [45]. Circumferential V-notches are found to exhibit higher degree of constraint than that of circumferential U-notches [45]. For laboratory experiments to study the effect of constraint on creep deformation and fracture, U-notches are preferred over the V-notches, since the U-notches produce creep cavitation over a relatively larger volume assisting the post test investigation [47]. Webster et al. [43,48] observed that for each notch geometry, there is a skeletal point where the stresses are almost constant irrespective of the value of stress exponent '*n*' in Norton's law relating steady state creep rate ($\dot{\varepsilon}_s$) with applies stress as $\dot{\varepsilon}_s = A\sigma^n$, with *A* and *n* are material constants. The stresses at the skeletal point have been used to characterize the deformation and failure of material under multiaxial creep conditions.

1.7.2 Notch Strengthening and weakening

The presence of notches may exhibit notch creep strengthening or weakening depending on the notch shape and acuity (ratio of radius minimum cross section to radius of notch root), testing conditions and the material ductility [38-41,49-53]. Notch strengthening is expected when the high axial stresses across the notch throat plane redistributes quickly below the applied stress. This kind of behaviour is typically observed in ductile materials. However, the notch weakening is expected in situations where the very high axial stresses due to the presence of notch redistribute very slowly and the local accumulated strain exceeds the limit which is required for fracture before attaining the stationary state across the notch root. This behaviour is typically observed in brittle materials.

McLean et al. [49] re-plotted the experimental data of Davis and Manjoine [50] and studied the effect of notches on creep behaviour of different materials having varying ductilities. Figure 1.15 shows the rupture life of different notches with notch acuity ratio. The ordinate is the ratio of the 1000 h notch rupture strength to the 1000 h plain specimen rupture strength. All the four materials showed notch strengthening for shallow notches, however, with increase in notch sharpness, three of the four materials showed notch weakening. The stresses redistribute with time under creep and attain the stationary condition and remain stable. The von-Mises stress in the shallow notches (up to 4) decreases with creep exposure and reaches below the net stress leading to notch strengthening.

The analytical calculations carried out by Hayhurst et al. [42] indicated that the creep strain accumulation would be larger for sharper notches as compared to shallow notches. Thus beyond some critical notch acuity, the accumulated strain may exceed locally that required for fracture before attaining the stationary state. The more is the material ductile, the sharper the notch must be before such transient effects intervene.

Studies carried out on Nimonic 80A under triaxial state of stress introduced by notch and reported notch strengthening [38]. The fracture at higher stresses was observed to initiate at the centre of the specimens (inside-out) and at the notch root (outside-in) at relatively lower stresses. Multiaxial creep response of 2.25Cr-1Mo steel was studied by Al-Faddagh et al. [39]. Material exhibited notch strengthening under tested conditions and was attributed to the decrease in von-Mises stress at the skeletal point with increase in notch acuity ratio. However, progressive increase in hydrostatic stress was found to be responsible for the saturation in strengthening.

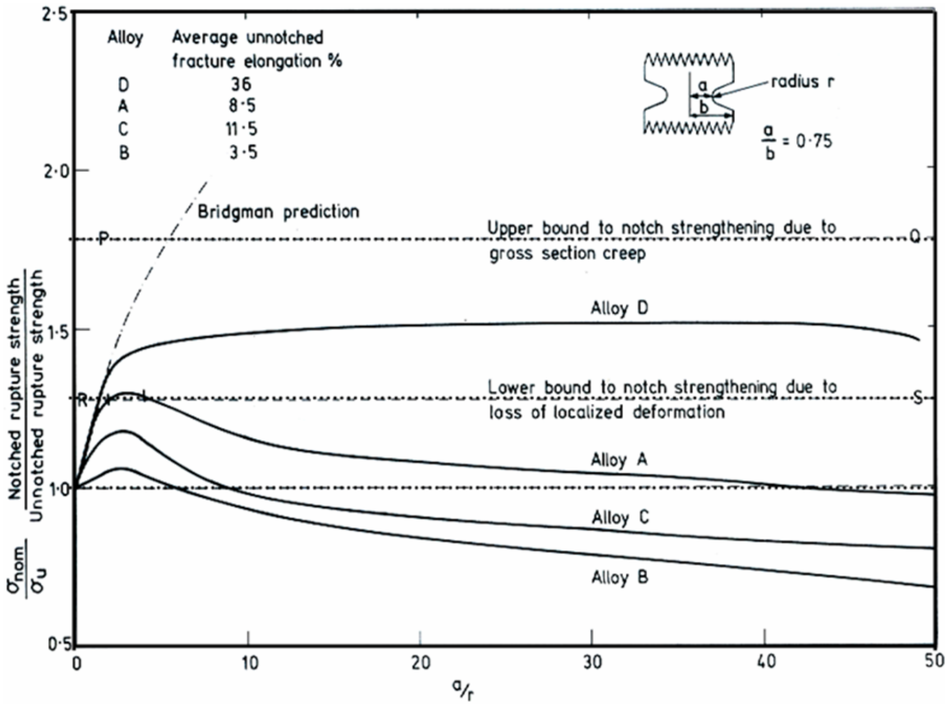

Fig. 1.15 Notch strengthening as a function of notch sharpness for four different alloys [49]. Alloy A, B and C are refractalloy with various heat treatments to give different mechanical properties and Alloy D is 12Cr-3W steel.

Eggeler et al. [41] carried out the multiaxial creep studies on tempered and untempered P91 steel. The steel exhibited notch strengthening for both tempered and untempered conditions. The fracture mode in tempered P91 was ductile in nature and brittle in untempered condition. The authors commented on the possibility of notch weakening that could happen at the relatively lower stress. Ng et al. [40] studied the effect of notch on 0.5Cr-0.5Mo-0.25V. The steel showed notch strengthening for shallow notches and tendency towards notch weakening for sharper notches [40]. The studies carried out on alloy X-750 by Pandey et al. [51] reported notch strengthening under the testing conditions. The cracking in the specimens was found to shift systematically from centre of notch at the high stresses towards notch root at lower stresses. Webster et al. [52] carried out studies on notched specimens of beta processed titanium alloy Ti5331s and observed notch strengthening in the material. Similar observations were made by Kwon et al. on 2.25Cr-1Mo and Durehete 1055 steels [53].

1.7.3 Creep rupture life prediction under multiaxial state of stress

The creep rupture life under uniaxial loading can be expressed as a function of the applied stresses as:

$$t_f = M\sigma^{-m} \tag{1.24}$$

where, *M* and *m* are parameters that characterize the damage evolution in the material. However, Hayhurst and Leckie [54] pointed out that Eq. (1.24) does not correctly predict creep rupture of notched bars even if the nominal stress in the notch is used in the expression. The creep rupture life versus stress equation was further modified to account for different components of stresses in multiaxial state of stress. The stress-rupture life relation can be used to describe multiaxial behaviour by replacing the stress with representative stress, which is given below

$$t_f = M{\sigma_{rep}}^{-m} \tag{1.25}$$

The representative stress, σ_{rep}, is defined as the stress applied in the uniaxial plain bar specimen which has the same creep rupture life as the notched bar specimen. A notched specimen is said to be notch weakening if $\sigma_{rep} > \sigma_{net}$ and notch strengthening if $\sigma_{rep} < \sigma_{net}$.

Many researchers have worked to establish to define the representative stress in terms of stress components [55-58]. Sdobyrev [55] proposed a relationship of creep rupture life with stress for describing the multiaxial behaviour

$$t_r = A\{\lambda\sigma_1 + (1-\lambda)\sigma_{vm}\}^{-\chi} \tag{1.26}$$

where A and χ are material constants. However, the prediction of rupture life found to be significantly different for biaxial tension with the above mentioned relationship. Johnson et al. [56,57] conducted biaxial creep tests on aluminum alloy and pure copper, and showed that the rupture life can be related to the octahedral shear stress and maximum principal stress criteria respectively. Hayhurst [58] carried out the creep tests on an aluminum alloy under bi-axial stress conditions and observed similar trends. Hayhurst [58] commented that the rupture behaviour of copper and aluminum alloys can be considered as representing the two extreme stress sensitive rupture. The behaviour of other creep resistant alloys falls between the two extremes. Hayhurst [58] further proposed that the isochronous rupture surface can be described in terms of combination of the maximum principal stress, von-Mises stress and hydrostatics stress,

$$t_r = M(\alpha\sigma_1 + \beta\sigma_{vm} + \gamma\sigma_m)^{-\chi} \tag{1.27}$$

where α, β, and γ are constants. The loci of constant time to rupture in stress space can be represented as shown in Fig. 1.16.

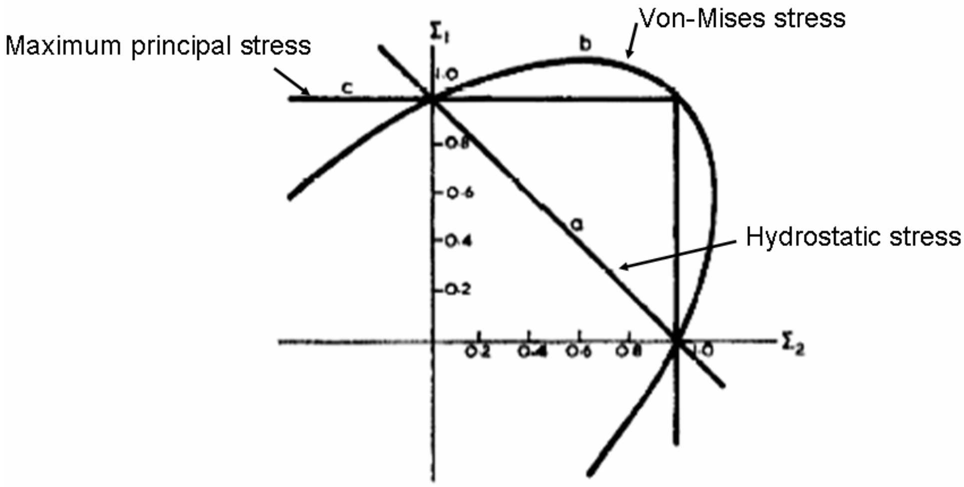

Fig. 1.16 Loci of constant rupture life considering different failure criteria [58].

The constant β was found to very small and the equation was further modified [59]

$$t_r = M\left(\alpha\sigma_1 + (1-\alpha)\sigma_{vm}\right)^{-\chi} \tag{1.28}$$

Typical values of α for Aluminum, Copper and 316 SS were found to be 0.0, 0.7 and 0.75 respectively [60].

A different form of stress rupture criterion was proposed by Cane [61]. The contributions of different stresses is given by the following expression

$$t_r = M\sigma_1^{-\gamma}\sigma_{vm}^{\gamma-m} \tag{1.29}$$

The exponent γ was found to vary in the range 1.5- 3.0 for commonly used low alloy ferritic steels. This approach was adopted for the validation of code of practice for different low alloy ferritic steels [62].

Nix et al. [63] proposed a new concept to predict the creep rupture life under multiaxial state of stress. The creep rupture life could be predicted from the uniaxial creep data by using the principal facet stress as a creep rupture parameter.

$$\sigma_{rep} = 2.24\sigma_1 - 0.62(\sigma_2 + \sigma_3) \tag{1.30}$$

where, σ_1 is the maximum principal stress and σ_2 and σ_3 are intermediate and minimum principal stresses respectively. The parameter could predict the creep life for those materials which mainly fail by creep cavitation viz. 2.25Cr-1Mo steel, Nimonic 80, 316 stainless steels and copper. The model fails to predict creep rupture life for aluminum alloy, in which failure is controlled by von-Mises stress.

Huddleston [64] proposed a model for multiaxial creep rupture strength which involved three stress state parameters and two material parameters.

$$\sigma_{rep} = \frac{3}{2}\sigma'\left(\frac{2\sigma_{vm}}{2\sigma'}\right)^a \exp\left[b\left(\frac{J_1}{S_s} - 1\right)\right] \tag{1.31}$$

where J_1 is the first invariant of the stress tensor ($J_1 = \sigma_1 + \sigma_2 + \sigma_3$), S_1 is the deviatoric stress ($S_1 = \sigma_1 - J_1/3$) and S_s is defined as $S_s = \sqrt{\sigma_1^2 + \sigma_2^2 + \sigma_3^2}$ and a and b are the material parameters. The model could correlate the multiaxial creep rupture life for 304 stainless steel. However, the data of ferritic steels could not be truly represented by the model [65].

1.7.4 FE analysis coupled with Continuum damage mechanics

Finite element analysis coupled with continuum damage mechanics (FE-CDM) has been extensively used for prediction of mechanical properties and especially for estimating stress distribution and damage evolution around the notches under creep conditions [66-74]. Single damage variable (based on Kachanov model) was used to predict the creep rupture life of plain and notched specimens of Titanium and nickel base superalloys by Hyde et al [74]. Comparison of creep life of notched specimen was found to be in good agreement with the experimental results. The damage was found to reach critical limit at the centre for nickel base superalloy, whereas, it was at the notch root for titanium base alloy. Othman et al. [75] carried out FE-CDM analysis on single and double circumferential U- notches and observed that the rupture life of the double notched specimen was within 5% variation with the single notched specimens. Othman et al. [69] considered two damage variables for tertiary softening considering (i) grain boundary cavity nucleation and growth and (ii) the multiplication of mobile dislocations softening due to tertiary creep and hardening due to the multiplication of dislocations during creep. Hall and Hayhurst [76] used FE-CDM to predict creep rupture life of ferritic steel weldments. Analysis carried out by Hyde et al. [67] on welded pipes and notched specimens using one damage variable (based on Kachanov model) and three damage variables [77,78] revealed that the analysis with single parameter over-estimated the creep rupture life of the material.

1.7.5 Effect of constraint on creep deformation

The presence of notch imposes constraint on the structure. The degree of constraint depends on combination of material property, specimen geometry and stress level. Ewing [79] theoretically investigated the onset of plane strain plastic flow in notched plates under tension based on slip line field theory. The critical width for a given neck and notch shape was defined as the minimum width that just permits deformation to be localized at the neck without decrease in constraint factor. The critical width is defined as:

$$w_c = a/2(2\exp(x)-1) - R(\exp(x)-1)^2 \tag{1.32}$$

where R is the notch radius and *a* is the neck width.

$$x = \min[\beta, \ln(1 + a/2R)] \tag{1.33}$$

and $\beta = \frac{1}{2}\pi - \alpha$, where α is the half notch angle.

The critical width can be calculated based on the relation given by Szczepiński et al. [80]. The critical width for round notched bars can be defined as

$b/a = \sqrt{H/h}$

where *a* and *b* are minimum diameter of notch and maximum diameter of un-notched portion, respectively. *H* and *h* are minimum width of notch and maximum width of un-notched portion of bar, respectively.

The constraint factor as per the Bridgman criteria defined as

$$f = \left(1 + \frac{R}{a}\right)\ln\left(1 + \frac{a}{4R}\right) \tag{1.34}$$

Kim et al. [81] carried out the fully plastic analysis of notched bars using FE analysis considering elastic-perfectly plastic material and compared the constraint imposed due to different notch geometries. According to Miller [82], the constraint factor for deep and sharp notches has a limit of 2.85. Hayhurst et al. [42] studied the FE analysis of effect of constraint on creep behaviour of subcritical and supercritical notches. In relatively shallow supercritical notches, the stresses were relatively uniform occupying around 50% of notch throat. However, the relatively sharper supercritical notches had sharp variation of stresses across the notch. This was found to be due to the constraint to radial deformation provided by the shoulders of the notch which led to higher radial and tangential components of stress. In order to maintain the compatibility of flow across the notch, the axial stress raised in the notched region. The authors concluded that the shallow supercritical notches can be used for metallographic examination due to relatively larger volume subjected to uniform stress distribution across the notch.

1.7.6 Effect of Multiaxial state of stress on Ductility

The failure under multiaxial state of stress is associated with the creep cavity nucleation and their growth which depends on the distribution of stresses across the notch. Increase in hydrostatic stress leads to an apparent reduction in the ductility. A number of models [83] have been proposed to account for this dependence and are generally based on the growth of a void in a deforming medium. These models show that the void growth rate is a function of the ratio between the hydrostatic stress (σ_m) and the von-Mises stress (σ_{vm}). This ratio, (σ_m / σ_{vm}), is often known as the triaxiality. The analytical work performed by McClintock [84], Rice and Tracey [85], indicated the exponential amplification of the growth rate of microvoids with stress triaxiality in elastic-perfectly plastic materials. Cocks and Ashby [86] carried out the approximate calculations of the grain boundary cavity growth rates of creeping material under multiaxial state of stress and its effect on creep ductility. The model proposed by Rice and Tracey [85] is based on hole growth by the rigid plastic deformation of surrounding matrix. The model proposed by Rice and Tracey and Cocks and Ashby can be represented by the following expressions, respectively:

$$\frac{\varepsilon_f^*}{\varepsilon_f} = \frac{0.521}{\sinh\left(\dfrac{3\sigma_m}{2\sigma_{vm}}\right)} \tag{1.35}$$

$$\frac{\varepsilon_f^*}{\varepsilon_f} = \sinh\left[\frac{2}{3}\left(\frac{n-1/2}{n+1/2}\right)\right] \Big/ \sinh\left[2\left(\frac{n-1/2}{n+1/2}\right)\frac{\sigma_m}{\sigma_{vm}}\right] \tag{1.36}$$

where $\varepsilon_f^* / \varepsilon_f$ is the ratio of multiaxial to uniaxial creep ductility and *n* is the creep stress exponent.

Spindler [87] analyzed the models described by Hales [88] the creep ductility based on different void growth models viz. plastic hole growth, diffusion controlled cavity growth and constrained cavity growth, Fig. 1.17. At relatively lower stresses, the local deformation due to the growth of intergranular voids exceeds the deformation rate of the surrounding material. As a result the stresses are redistributed such that the cavitating boundaries transverse to the maximum principal stress unload until the local strain rate due to cavitation equals the remote strain rate due to the applied stress. The lower plateau indicates ductility based on the constrained cavity growth. The voids on grain boundaries subjected to tensile stresses experience a gradient of chemical potential of vacancies. Vacancies migrate under the influence of this gradient and cause the voids to grow. The upper plateau, which is shown in Fig. 1.17, is determined from the failure of constant strain rate tensile tests. The failure in this region is controlled by plastic hole growth mechanisms.

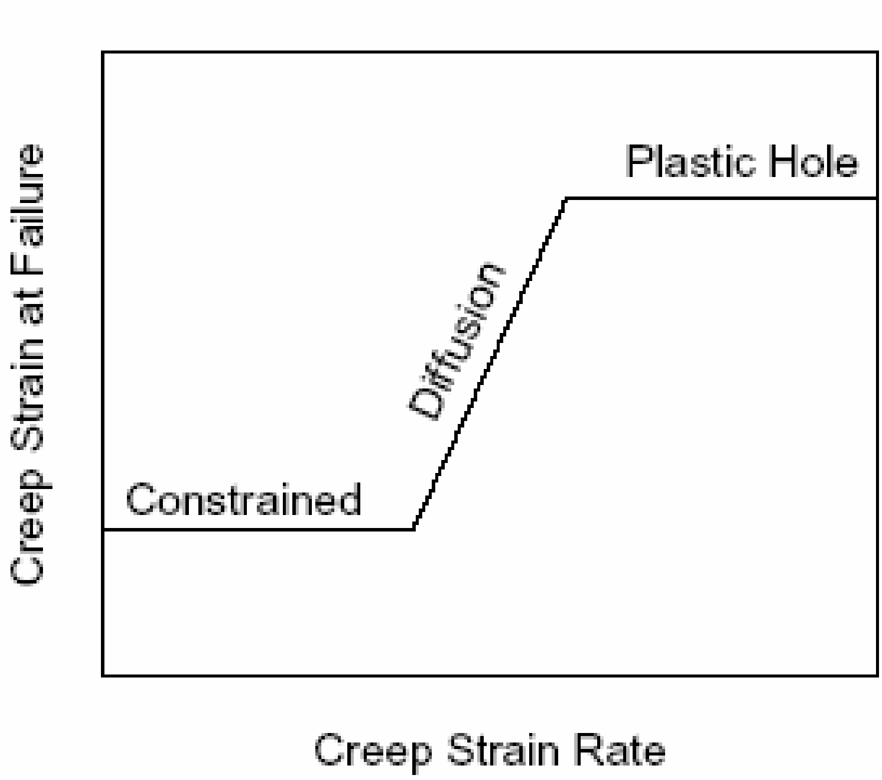

Fig. 1.17 Schematic of the effect of failure mechanism on creep ductility [87].

1.8 Ferritic steels used in high temperature applications

Good thermo-physical properties, high temperature oxidation resistance and mechanical properties and cost effectiveness compared to austenitic stainless steels are the main reasons for selection of ferritic steels as a structural material for steam generators of Prototype Fast Breeder Reactor (PFBR) at Kalpakkam, India, and fossil power plants and heat transport systems. In early 1950s, continuous demand for energy resulted in evolution of 2.25Cr-1Mo steel designated as ASTM Grade 22. This steel was widely used in fossil power plants as well as many heat transport systems. Subsequently, 9Cr-1Mo (ASTM Grade 9) steel was developed to improve high temperature oxidation resistance. The chart (Fig. 1.18) shows process of evolution of ferritic steels with base composition of 2 wt.% Cr, 9 wt.% Cr and 12 wt.% Cr with 10^5 h creep rupture strength at 600°C. Since then, continual drive to increase operating temperature of conventional fossil-fired power plants to increase thermal efficiency and reduce CO_2 emission led to the development of several ferritic steels with improved elevated temperature strengths and oxidation resistance. Evolution of steels (Fig. 1.18), began with T22 and T9 and 12%Cr steels with 10^5 h creep-rupture strengths at 600°C of about 35MPa, has resulted in increasing operating steam temperatures and pressures.

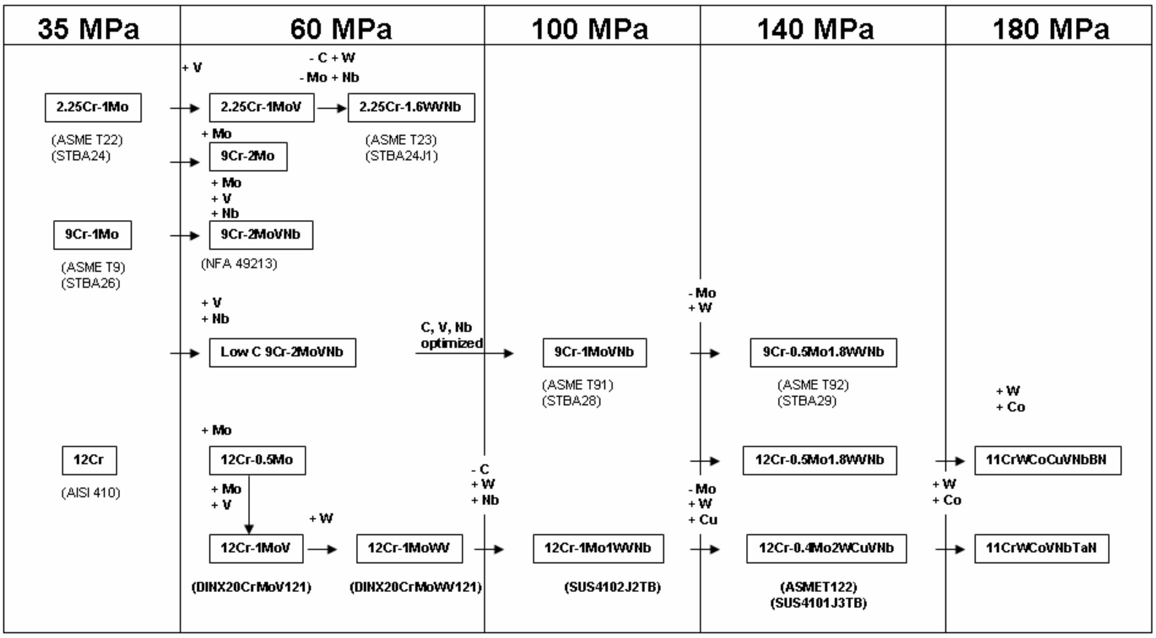

Fig. 1.18 Development of ferritic steels for boiler applications [89].

The increase in chromium content was to increase oxidation resistance of the material. Three generations of steels have been introduced since the introduction of T22, T9, 12Cr steel, and steels of fourth generation are in the development stage (Fig. 1.18). With increasing operating temperatures to 600°C, emphasis shifted from 2.25 to 9 and 12 wt.% Cr for better oxidation and corrosion resistance. Chromium is a ferrite stabilizer, and with increase from 9 to 12, it was necessary to add austenite stabilizers to achieve complete austenitisation to obtain 100% martensitic structure.

The metallurgical details of the steels used in the investigation are given below:

1.8.1 2.25Cr-1Mo steel

Microstructure of any ferritic steel formed on cooling from austenite is given by its time temperature transformation diagram. 2.25Cr-1Mo steel is used in various conditions including annealed, normalized + tempered and quenched + tempered. The microstructure of annealed steel is predominantly ferrite with some gross carbide area (that sometimes appears as pearlite) and possibly bainite. Normalized 2.25Cr-1Mo steel contains ferrite and bainite with the amount of bainite increasing with carbon to nearly 100% of the structure for carbon levels greater than about 0.12 wt. %. Quenched 2.25Cr-1Mo steel has the potential to contain martensite.

The mechanical properties of 2.25Cr-1Mo steel depend primarily on the carbide type, size, morphology and distribution. Baker and Nutting [90] have described the general sequence of carbides formed in both quenched and normalized 2.25Cr-1Mo steel during tempering. Prior to tempering, the microstructure contains epsilon carbides which can be described as $Fe_{2.4}C$. This precipitate appears alone in the martensitic structure but is accompanied by cementite formed homogeneously from diffuse zones. Mo_2C has considerable solubility for other alloying elements, especially chromium, and should probably be referred to as M_2C. At this point, the carbide sequence splits with the formation of Cr_7C_3 (generally denoted as M_7C_3) and $M_{23}C6$ (chromium rich carbide). The M_7C_3 probably nucleates at the M_2C / matrix interface while the M23C6 nucleates and grows at grain boundaries as large spheroidal particles. The last carbide to form, M_6C, grows at the expense of all other carbides and is believed to be the equilibrium precipitate in 2.25Cr-1Mo steel.

After normalizing, the ferrite is free of any carbide. The first precipitate to appear in the ferrite during tempering is acicular M_2C particles which develop from diffuse zones in the matrix similar to those observed in the bainite. This carbide persists in the ferrite, showing no tendency to transform to any of the other metastable carbides observed in the other micro-constituents. Eventually, M_6C forms in the ferrite and the M_2C begins to dissolve.

1.8.2 9Cr-1Mo steel

In recent years, 9Cr-1Mo steel has become an important material in the power generating industries. Good creep properties combined with adequate oxidation / corrosion resistance have led to the use of this material at temperatures of 550° C and above [91]. Also under irradiation, high chromium martensitic steels are superior to their austenitic counterparts in terms of void swelling, thermal and irradiation creep and thermal fatigue properties. The material is commonly used in normalized and tempered condition. The material has martensitic microstructure with a high density of transformation dislocations after heat treatment. Normalizing and tempering heat treatments produce tempered martensitic structure with carbides decorating both the prior austenitic grain boundaries and martensitic lath boundaries. The general sequence of carbide formation in 9Cr-1Mo steel has been reported [92] as

$$Fe_3C \rightarrow M_7C_3 \rightarrow M_{23}C_6$$

M_2X types of carbides/nitrides are also reported in the intragranular region. Senior et al. [93] from their extensive TEM studies have indicated that the population of the precipitates on the prior austenite grain boundaries and on the martensitic lath boundaries is almost exclusively $M_{23}C_6$ while the population of precipitates within the laths consists of appreciable quantities of both $M_{23}C_6$ and Cr_2N particles.

1.8.3 Modified 9Cr-1Mo steel

9Cr-1Mo steel, modified with alloying additions of niobium and vanadium is extensively used as a structural material at elevated temperatures in fossil-fired power plants. Interest in this steel stems primarily due to its proposed use for tubing in the reheater and superheater portions and as a thick-section tube plate material in the steam generators of LMFBRs. The selection of modified 9Cr-1Mo steel for steam generator application is based principally on its high thermal conductivity and low thermal expansion coefficient, coupled with a good resistance to stress corrosion cracking in water-steam systems compared to austenitic stainless steels and better monotonic tensile and creep strength at elevated temperatures compared with the 9Cr-1Mo steel. The good weldability and microstructural stability over very long periods of exposure to high temperature service conditions and consequent improvements in the creep strength are other attractive features that favored the selection of modified 9Cr-1Mo for steam generator applications.

This steel is commonly used in the normalized and tempered condition. The normalizing treatment is usually performed at 1040°C/1 h followed by air cooling, while tempering is carried out at 760°C/1 h followed by air cooling. Austenisation during the normalizing dissolves most of the secondary phases (carbides/nitrides/carbonitrides) and the austenite transforms into martensite with a lath morphology during the cooling phase. Tempering of martensite results in the precipitation of $M_{23}C_6$ carbides especially on the lath boundaries and prior austenite grain (PAG) boundaries. The microstructure of this class of steels is therefore made up of several scales (Fig. 1.19), the most predominant of which is the PAG structure that forms during the normalizing treatment. Depending on the heat treatment, the size of the PAG varies between 10 and 50 μm. Inside each PAG boundary, packets of laths form during the martensitic transformation associated with air-cooling following austenisation. Inside the laths, subgrains form during the tempering treatment. The dominant precipitates in the alloy are large (60- 150 nm) $M_{23}C_6$ particles that are mainly on lath boundaries and prior-austenite grain boundaries. The V and Nb give rise to a fine distribution of small (20- 80nm) MX type precipitates (V, Nb) (C, N) [95]. Addition of Nb also helps in improving the properties by promoting nucleation of finely distributed $M_{23}C_6$ carbides and by aiding grain refinement, whereas V enters the carbide particles and retards their growth. The alloy derives its strength in normalized and tempered condition, from carbides like NbC, VC and $M_{23}C_6$ on sub-boundaries and from the tempered martensitic laths with high dislocation densities. In addition, C and Cr could also form fine precipitates of nitrides within the ferrite matrix contributing to further strengthening [96]. Molybdenum is a solid solution strengthener and acts as a retardant for dislocation recovery/recrystallisation.

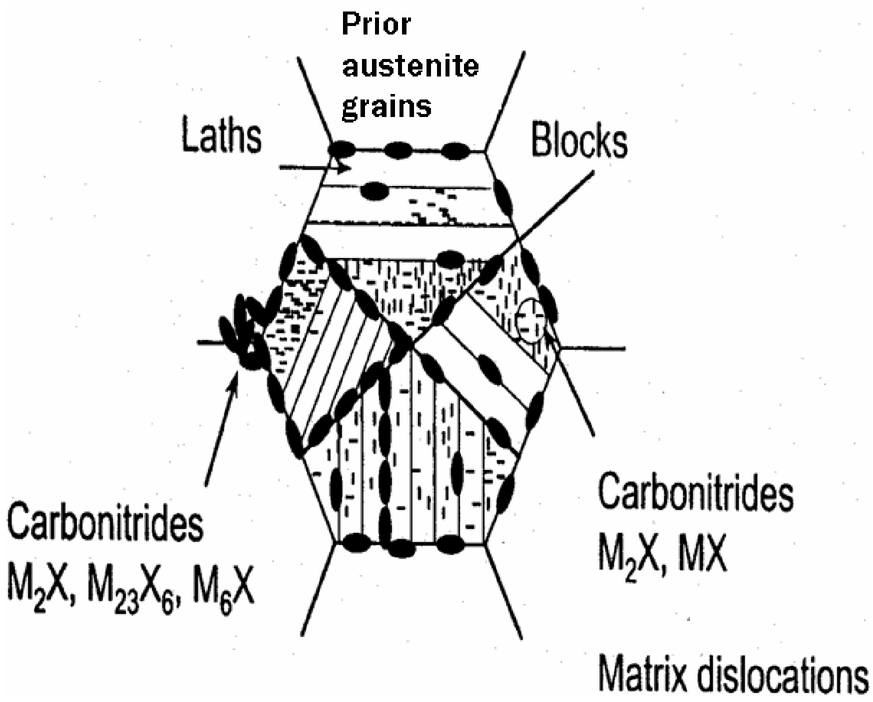

Fig. 1.19 Schematic representation of non-uniform precipitation states in tempered martensitic 9-12% Chromium steels [94].

1.9 Scope of the work

The preceding literature survey clearly brought out the importance of multiaxial state of stress on creep behaviour of materials in high temperature applications. Various techniques have been adopted for introducing multiaxial state of stress in specimen for carrying out the effect of multiaxiality on creep behaviour at laboratory scale. Incorporation of circumferential U-notch in cylindrical specimens is widely used to introduce different states of multiaxial stresses. Among the ferritic steels used in power plants, most widely used materials are 2.25Cr-1Mo, 9Cr-1Mo and modified 9Cr-1Mo steels. Stresses in the notched specimens are generally complex in nature. Finite element analysis is widely used for estimating the stresses across the notch for predicting the creep rupture life under multiaxial state of stress.

In this investigation, it is planned to study in detail, the effect of multiaxial state of stress on creep behaviour of ferritic steels. The work plan is as follows:

- Materials for investigation: 2.25Cr-1Mo, 9Cr-1Mo and modified 9Cr-1Mo steels.
- Method of introduction of multiaxiality: Circumferentially U-notch in cylindrical specimens with various notch root radius ranging from 5 mm to 0.25 mm to vary the multiaxial state of stress.
- Creep test: Temperature- 873 K, stress range- 90 to 230 MPa.
- Fractographic and creep cavitation studies: Scanning electron microscopy (SEM).
- Estimation of stresses across the notch: Finite element analysis incorporating individual steel's deformation characteristics.

- Creep damage evolution with creep exposure: Finite element analysis coupled with continuum damage mechanics.
- Creep life prediction: Finite element analysis based on concept of representatives stress and skeletal point.

CHAPTER 2

EXPERIMENTAL PROCEDURES AND MATERIALS

Experimental procedures and materials

2.1 Introduction

Experimental details pertaining to the creep under uniaxial and multiaxial state of stress and fractographic studies are described in this chapter. Creep tests were carried out on 2.25Cr-1Mo, 9Cr-1Mo and modified 9Cr-1Mo steels on plain specimens at 873 K. Creep tests were also carried out on circumferentially U- notched specimens at different stress levels and at 873 K to understand the effect of multiaxial state of stress on creep rupture behaviour of the steels. FE analysis was carried out for assessing the stress distribution across the notch throat plane. FE Analysis coupled with continuum damage mechanics was also carried out to understand the damage evolution across the notch throat plane and predict the creep rupture life of the steels. Tensile tests were carried out on these steels to incorporate the elasto-plastic behaviour in FE analysis. The details pertaining to analysis of stationary state stress distribution and VUMAT subroutine written for damage evolution and prediction of creep rupture life is described in this chapter.

2.2 Materials

Materials used in the present investigation are 2.25Cr-1Mo, 9Cr-1Mo and modified 9Cr-1Mo steel. Chemical compositions of the steels used are given in Table 2.1. The 12 mm thick plates were received in normalized and tempered heat treated condition. The heat treatment given to different steels is given in Table 2.2.

2.3 Tensile tests

Tensile tests were carried out on plain specimens of 2.25Cr-1Mo, 9Cr-1Mo and modified 9Cr-1Mo steels. Figure 2.1 shows the specimen design used for the testing. The tensile tests were carried out in air at 873 K employing a strain rate of 3×10^{-3} s^{-1} using Hung Ta 2402 model screw driven system. Test temperature was controlled within ± 2K throughout the test. During the test, load-displacement data was recorded and logged in a data logger. Since no strain gauge extensometer was employed, the specimen extension was considered as corresponding cross head movement.

Table 2.1 Chemical compositions of the steels (wt. %)

Material \ Element	2.25Cr-1Mo steel	9Cr-1Mo steel	modified 9Cr-1Mo steel
C	0.06	0.1	0.092
Si	0.18	0.49	0.39
Mn	0.48	0.46	0.45
P	0.008	0.008	<0.005
S	0.008	0.002	0.004
Cr	2.18	8.36	8.8
Mo	0.93	0.93	0.93
V	-	-	0.23
Nb	-	-	0.08
N	-	-	0.033
Fe	Bal.	Bal.	Bal.

Table 2.2 Heat treatment procedures for different steels under investigation

Material	Normalizing	Tempering
2.25Cr-1Mo Steel	1223 K for 15 min followed by air cooling	1003 K for 60 min followed by air cooling
9Cr-1Mo Steel	1223 K for 15 min followed by air cooling	1053 K for 120 min followed by air cooling
modified 9Cr-1Mo Steel	1313 K for 1 hour followed by air cooling	1033 K for 1 hour followed by air cooling

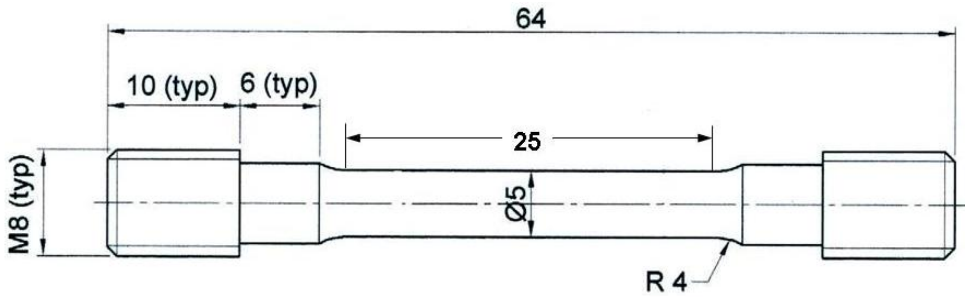

Fig. 2.1 Specimen design for tensile testing (all dimensions in mm).

2.4 Creep tests

2.4.1 Plain specimens

Creep tests were carried out on plain specimen of 2.25Cr-1Mo, 9Cr-1Mo and modified 9Cr-1Mo steels in air using constant load creep testing machines at 873 K. Drawing of the specimen used for creep experiments is shown in Fig. 2.2. Creep tests on all the steels were carried out in the stress range 90 - 230 MPa. The pictorial view of the machines used for creep testing is shown in Fig. 2.3. The test temperature was controlled within ± 2K over the entire gauge length throughout the test. The creep elongation was measured continuously during the test by extensometer and digital dial gauge arrangement. All tests were continued till fracture.

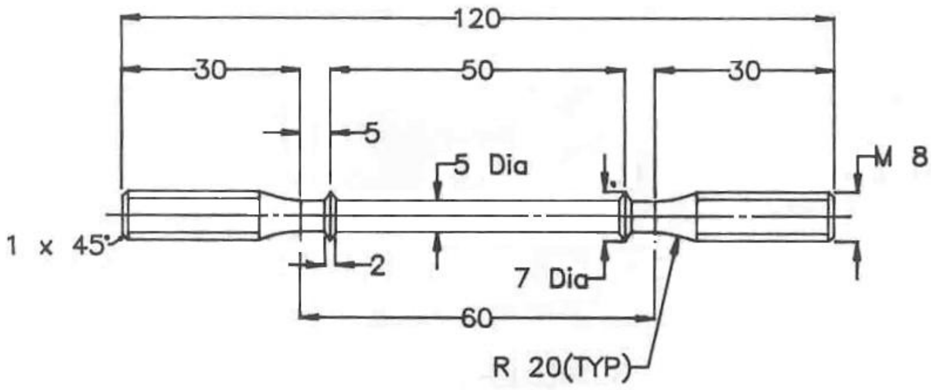

Fig. 2.2 Specimen design for creep testing of plain specimen (all dimensions in mm).

Fig. 2.3 Photograph of the creep machines used for investigation.

2.4.2 Notched specimens

Creep tests were also carried out on notch specimen of all the steels at net applied stresses (σ_{net}, stress applied to the minimum cross section in notch) ranging from 110 - 230 MPa and at 873 K. Circumferentially U-notches with various notch root radii, keeping the minimum diameter of the specimen constant (5 mm), similar to plain specimen, were introduced in the cylindrical specimens of the steels. The geometry of the notched specimens along with photograph is illustrated in Fig. 2.4.

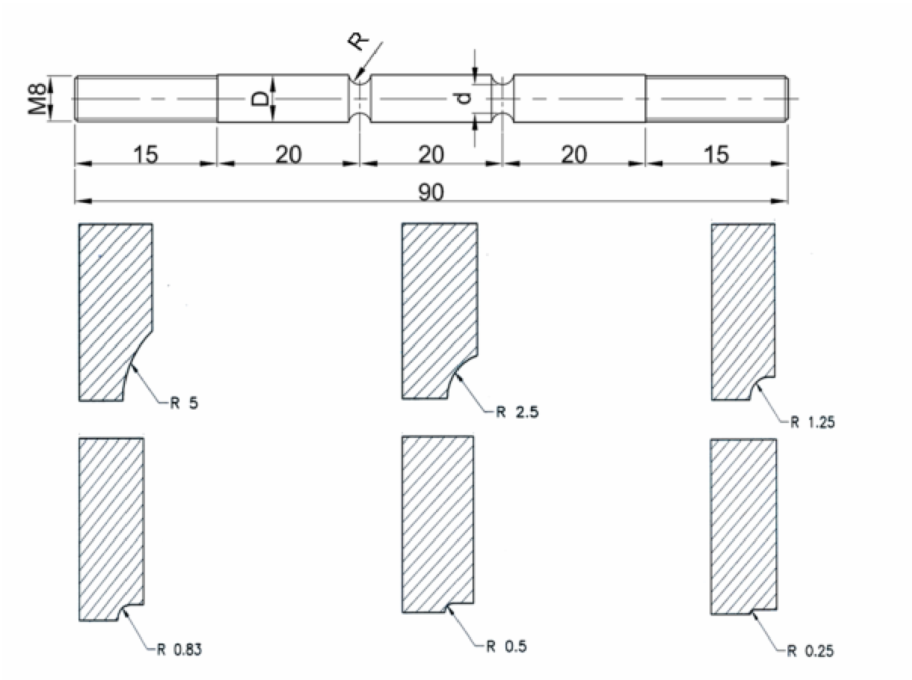

Fig. 2.4 Notched creep test specimen details (all dimensions are in mm) along with photograph of the specimens.

The notch acuity ratio (ratio of notch throat diameter to notch root radius) has been varied from 1 to 20 by changing the notch root radius (5 mm, 2.5 mm, 1.25 mm, 0.83 mm, 0.5 mm and 0.25 mm) and keeping the notch throat diameter to 5 mm, Table 2.3.

Table 2.3 Dimensions of different notch geometries of the notched specimens

D	d	R	Notch acuity ratio (d/R)
8.35 mm	5.00 mm	5.00 mm	1
		2.50 mm	2
		1.25 mm	4
		0.83 mm	6
		0.50 mm	10
		0.25 mm	20

The ratio of diameter of parallel portion of specimen to notch throat diameter (D/d) was fixed at 1.67 [42]. The variation of notch acuity ratio (d/R) from 1 to 20 resulted in an elastic stress concentration factor ranging from 1 to 3.4. Two notches were provided in each specimen so that the un-failed notch could be utilized for post creep test metallographic investigations. The notches were sufficiently apart (≈ 20 mm) to avoid the interference of stress fields between them [70]. Tests on notched specimens were carried out in such a way that net applied stress acting in the notch throat plane was equal to the nominal stress on plain specimen.

2.5 Finite element analysis

Finite element analysis of stress distribution across the notch throat plane during creep exposure was carried out to understand creep rupture behaviour of the notched specimens. 2D axisymmetric analysis was carried out due to geometrical and loading symmetry, using quadrilateral elements employing ABAQUS 6.10 finite element solver [97]. Appropriate boundary conditions were incorporated in the model, Fig. 2.5. The nodes along line AB were restrained in Y-direction and nodes along AD were restrained in X-direction. The uniform stress was applied on line CD.

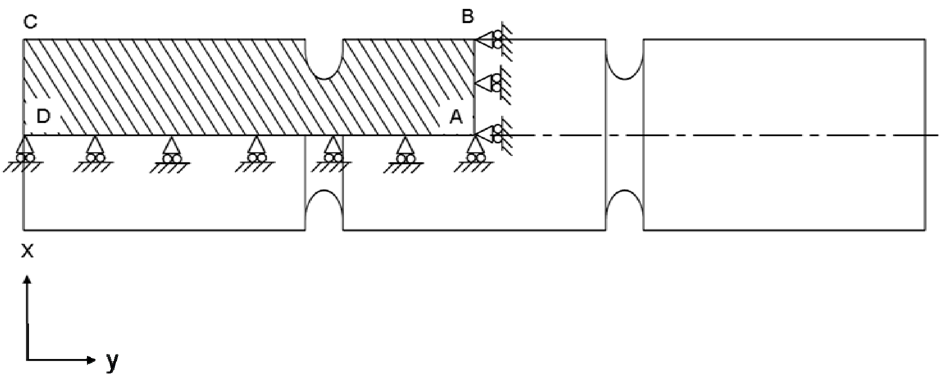

Fig. 2.5 Finite element model geometry used for analysis along with boundary conditions.

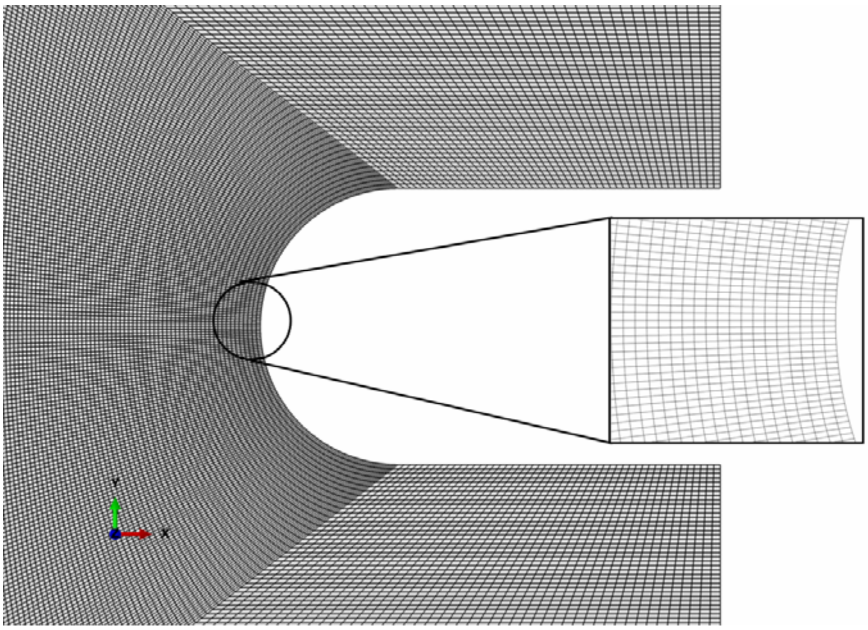

Fig. 2.6 Typical finite element mesh used in analysis (notch root radius = 0.5 mm).

The analysis was carried out implementing elasto-plastic-creep behaviour of the materials. The elasto-plastic behaviour was incorporated in the model using Hollomon equation ($\sigma_t = K\varepsilon_p^{\;n'}$) and creep behaviour using Norton's creep law relating the steady state creep rate with applied stress ($\dot{\varepsilon}_s = A\sigma^n$). Von-Mises yield criterion has been used for occurrence of yielding in the steels. The material was assumed to deform elastically or elasto-plastically depending on the notch root radius and net applied stress initially, followed by creep deformation. Typical mesh used in the FE analysis is shown in Fig. 2.6. The element size was reduced at and close to the notch root and elastic analysis was used to ensure that the mesh configuration was sufficiently refined near the notch root to predict the theoretical elastic stress concentration factor at the notch root [98]. The FE analysis was continued till the stress redistribution across the notch throat plane attained a stationary state condition. The stress redistribution was considered to attain stationary state condition when the creep strain in the material at the notch throat plane reached the elastic strain, as stated by Calladine [99].

2.6 Continuum damage mechanics

In order to understand the damage evolution in the material under multiaxial state of stress, it is necessary to include the tertiary stage of creep deformation in the material model. Continuum damage mechanics, proposed by Kachanov [23], has been widely accepted and used for predicting the tertiary creep behaviour of the materials. This approach has been used in the present investigation to estimate the creep damage across the notch throat plane.

Creep deformation rate component under multiaxial state of stress can be defined by [74],

$$\dot{\varepsilon}_{c\,ij} = \frac{3}{2} A \left(\frac{\sigma_{vm}}{1-\omega} \right)^{n-1} \frac{\sigma_{ij}^{'}}{1-\omega} \tag{2.1}$$

where A and n are coefficients in Norton's law, σ_{vm} is the von-Mises stress, σ'_{ij} is the deviatoric stress component and ω is the damage parameter varying from 0 to 1 indicating virgin and fully damaged material respectively. The creep damage rate as a function of representative stress and current damage is given by

$$\dot{\omega} = \frac{B\sigma_{rep}^{\chi}}{(1-\omega)^{\phi}} \tag{2.2}$$

where B, ϕ and χ are material constants and σ_{rep} is the representative stress. The representative stress has been defined based on models as proposed by Cane [61], Hayhurst et al. [37] and Nix et al. [63]. The representative stress can be expressed, based on the above models respectively as

$$\sigma_{rep} = \sigma_1^{\gamma/m}\sigma_{vm}^{(m-\gamma)/m} \tag{2.3.1}$$

$$\sigma_{rep} = \alpha\sigma_1 + (1-\alpha)\sigma_{vm} \tag{2.3.2}$$

$$\sigma_{rep} = 2.24\sigma_1 - 0.62(\sigma_2 + \sigma_3) \tag{2.3.3}$$

where m, α and γ are material constants, σ_1 σ_2 and σ_3 are the maximum, intermediate and minimum principal stresses respectively and σ_{vm} is the von-Mises stress. The representative stress reduces to the maximum principal stress for $\gamma = m$ ($\alpha = 1$) and to the von-Mises stress for $\gamma = 0$ ($\alpha = 0$).

The creep strain and damage rate equations (Eqs. 2.1 and 2.2) under uniaxial stress converges to the following expressions respectively [74]

$$\dot{\varepsilon}_c = A\left(\frac{\sigma}{1-\omega}\right)^n \tag{2.4}$$

and $$\dot{\omega} = \frac{B\sigma^{\chi}}{(1-\omega)^{\phi}} \tag{2.5}$$

For a constant stress, the damage evolution (Eq. 2.5) can be integrated as follows

$$\int_0^{\omega_{cr}} (1-\omega)^{\phi} d\omega = \int_0^{t_r} B\sigma^{\chi} dt$$

where t_r is the rupture life and ω_{cr} is the critical damage (= 1). The integration leads to the following expression

$$t_r = \frac{1}{B(1+\phi)\sigma^{\chi}} \tag{2.6}$$

The experimental creep rupture lives at different stresses can be fitted to the above equation to obtain the constants χ, B and ϕ. The slope of the plot in log-log scale is given by -χ and the intersection is $B(1+\phi)$. The values of B and ϕ can be obtained by trial and error or optimization procedures [100] for minimum deviation in predicting the creep strain and rupture life.

Integration of damage rate equation (Eq. 2.5) gives the following expression for damage evolution

$$\omega = 1 - \left[1 - B(1+\phi)\sigma^{\chi} t\right]^{1/(1+\phi)} \tag{2.7}$$

Incorporating the above equation (Eq. 2.7) in strain rate equation (Eq. 2.4) and integration leads to the following relation

$$\varepsilon_c = \frac{A\sigma^{(n-\chi)}}{B(n-\phi-1)} \left\{ \left[1 - B(1+\phi)\sigma^{\chi} t\right]^{\frac{\phi+1-n}{\phi+1}} - 1 \right\} \tag{2.8}$$

The Eq. 2.8 has been used for prediction of creep strain as a function of creep exposure of the materials under uniaxial loading at different stresses. The Eqs. (2.1 - 2.3) have been used in predicting creep deformation and rupture behaviour of material under multiaxial state of stress employing ABAQUS finite element solver. A user material subroutine VUMAT was written in FORTRAN and implemented in the ABAQUS Explicit for calculating the stresses, creep strains, damage in the notched specimen. The subroutine VUMAT allowed incorporating the material laws (strain and damage rate equations, their integration and updating). The explicit analysis used Euler forward integration method and due to stability issues, the time increment was very small. The advantage of carrying out explicit analysis using VUMAT is that applying the explicit integration is simple and straightforward. However, the disadvantage of explicit scheme is that it is conditionally stable if time increment becomes large. The material properties were defined within the subroutine. VUMAT subroutine was first tested for predicting the creep strain and rupture life of plain specimens before implementing it for predicting the rupture life under multiaxial state of stress. VSPRINC utility subroutine was used within VUMAT for calculating the maximum principal stress at each integration point which was used for estimating representative stress along with von-Mises stress. The rate equations were solved and increment of variables was calculated and at the end of increment all the variables were updated and passed on to main program. The program was terminated when the calculated damage reaches to a limit of 0.5 at any element. As the damage parameter increased beyond this value, the accelerated creep rate led to severe distortion of the elements. The steps involved in the VUMAT subroutine are given in the Fig. 2.7.

2.7 Fractographic studies

Fractography of fractured surface of tensile and creep tested samples was carried out using a CamScan 3200 Scanning Electron Microscope (SEM). Specimen preparation consisted of sectioning and ultrasonic cleaning in methyl alcohol for 15 minutes of the fractured samples prior to examination. SEM was also used to study the creep cavitation in un-failed notch of creep tested samples. Un-failed notches of creep-ruptured notched specimens were sectioned longitudinally and polished mechanically up to 0.25 µm surface finish to carry out SEM to understand the creep damage behaviour. The samples were etched by 2 % Nital (2 ml nitric acid and 98 ml methyl alcohol) for 2.25Cr-1Mo steel and Villela's reagent (1 gm picric acid, 5 ml concentrate HCl and 100 ml methyl alcohol) for 9Cr-1Mo steel and modified 9Cr-1Mo steel respectively.

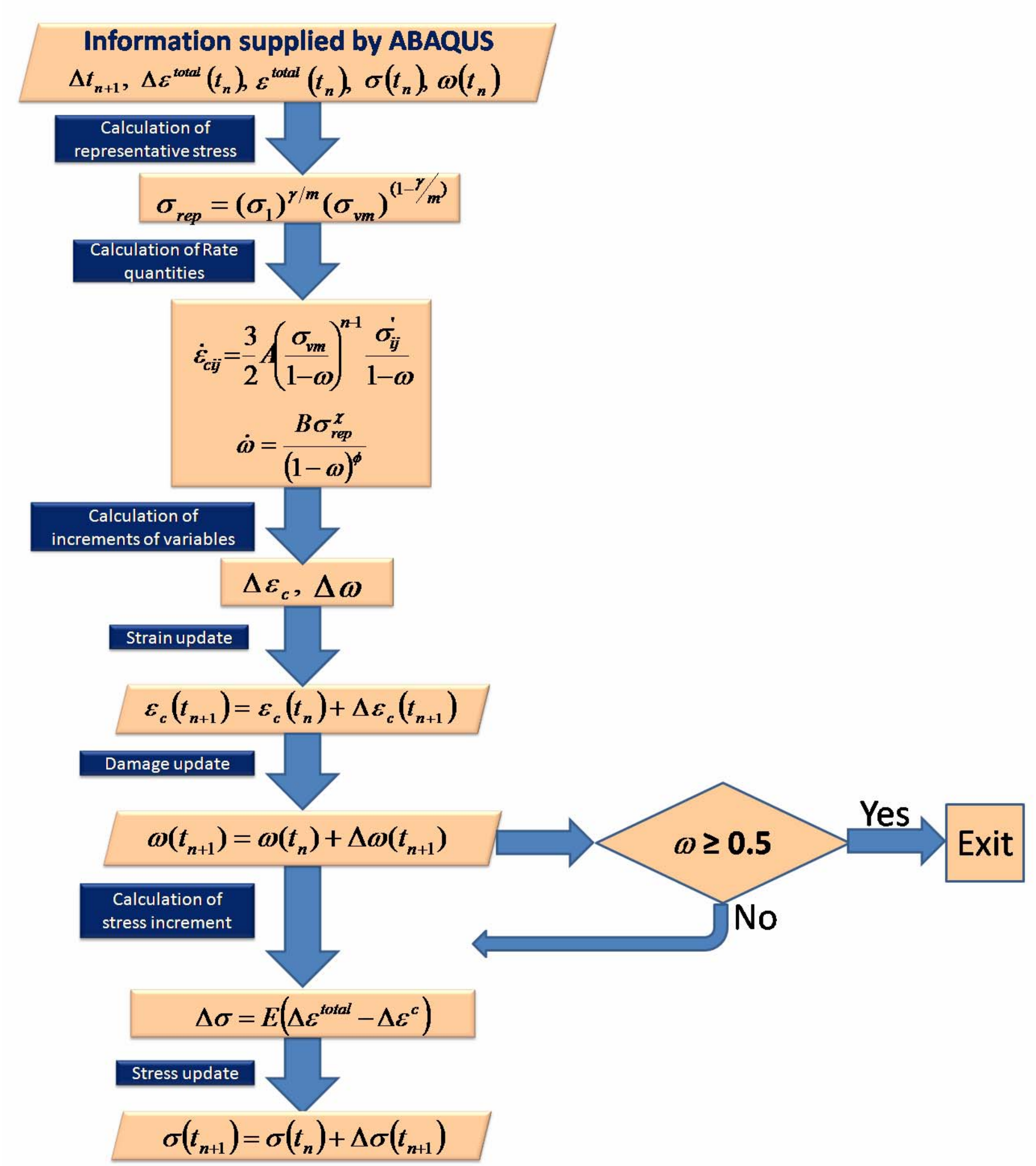

Fig. 2.7 Flow chart for user-subroutine VUMAT implemented in ABAQUS.

CHAPTER 3

UNIAXIAL CREEP BEHAVIOUR

Uniaxial creep behaviour

3.1 Introduction

In order to interpret the creep behaviour of different grades of ferritic steels under multiaxial state of stress, it is important to understand the response of these steels under uniaxial tensile and creep conditions. The deformation characteristics of these steels would also help in understanding of damage evolution and prediction of creep rupture life under multiaxial state of stress. Uniaxial tensile and creep behaviour of 2.25Cr-1Mo, 9Cr-1Mo and modified 9Cr-1Mo steels have been discussed in this chapter.

3.2 Tensile deformation

The tensile tests were carried out on plain specimens in air at 873 K employing a strain rate of 3×10^{-3} s^{-1} on the steels. Tensile curves of the steels are shown in Fig. 3.1. Yield stress of the materials was found to be in the increasing order of 2.25Cr-1Mo, 9Cr-1Mo and modified 9Cr-1Mo steel. True stress - true plastic strain behaviour of the steels at 873 K are shown in Fig. 3.2. Hollomon relation [101], $\sigma_t = K\varepsilon_p{}^{n'}$; where, σ_t is the true stress, ε_p is true plastic strain, K is the strength coefficient and n' is the strain hardening exponent, has been used to describe plastic flow behaviour of the steels. The values of K and n' obtained for different steels from log-log plot between true stress and true plastic strain are shown in Table 3.1. Typical cup and cone type transgranular ductile fracture was observed for all the steels.

3.3 Creep deformation

Creep tests were carried out on plain specimens of 2.25Cr-1Mo, 9Cr-1Mo and modified 9Cr-1Mo steels at 873 K over a uniaxial stress range of 90 - 230 MPa. Table

3.2 summarizes the uniaxial creep properties of the steels. The creep curves of the steels at 873 K over wide range of stresses are shown in Fig. 3.3. The creep deformation of the steels was characterized by a small instantaneous strain on loading, a transient primary stage, a secondary stage, followed by a prolonged tertiary creep regime. A short transient and a prolonged tertiary stage indicated that the strain hardening in the material rapidly recovered at such a high homologous temperature. In normalized and tempered ferritic steels, the occurrence of transient creep has been reported to be the consequence of movement and annihilation of high dislocation density that are introduced in the material during bainite/martensite transformation on normalization heat treatment [102]. Loss of creep strength due to the microstructural instability of the material on creep exposure is considered as the main cause of early onset of tertiary stage during creep deformation [102]. Comparison of creep curves of the steels obtained at 150 MPa and 873 K is shown in Fig. 3.4. The modified 9Cr-1Mo steel exhibited higher creep deformation and rupture strength than both the 2.25Cr-1Mo and 9Cr-1Mo steels. The 2.25Cr-1Mo and 9Cr-1Mo steels possessed comparable creep rupture strength. The variations of steady state creep rate ($\dot{\varepsilon}_s$) with applied stress (σ) of the steels are shown in Fig. 3.5. The variations follow Norton's law, a power law relation of the form, $\dot{\varepsilon}_s = A\sigma^n$, where A is a constant and n is the stress exponent. The coefficients in Norton's law for the steels are given in Table 3.3. The 2.25Cr-1Mo steel was found to have lowest creep deformation strength and modified 9Cr-1Mo steel had highest creep deformation strength among the three ferritic steels. The observed stress exponent values in the range 6-13 indicate that dislocation creep would have been the creep deformation mechanism in the steels over the investigated stress range and 873 K [103-105].

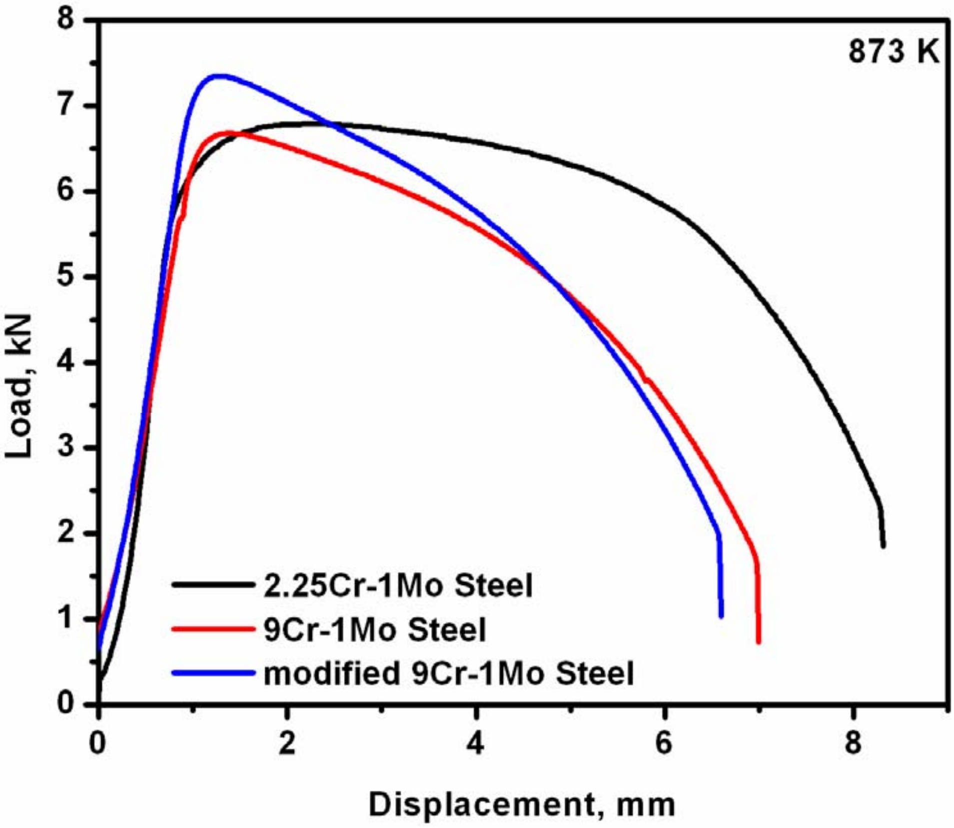

Fig. 3.1 Tensile curves obtained at 873 K of the steels.

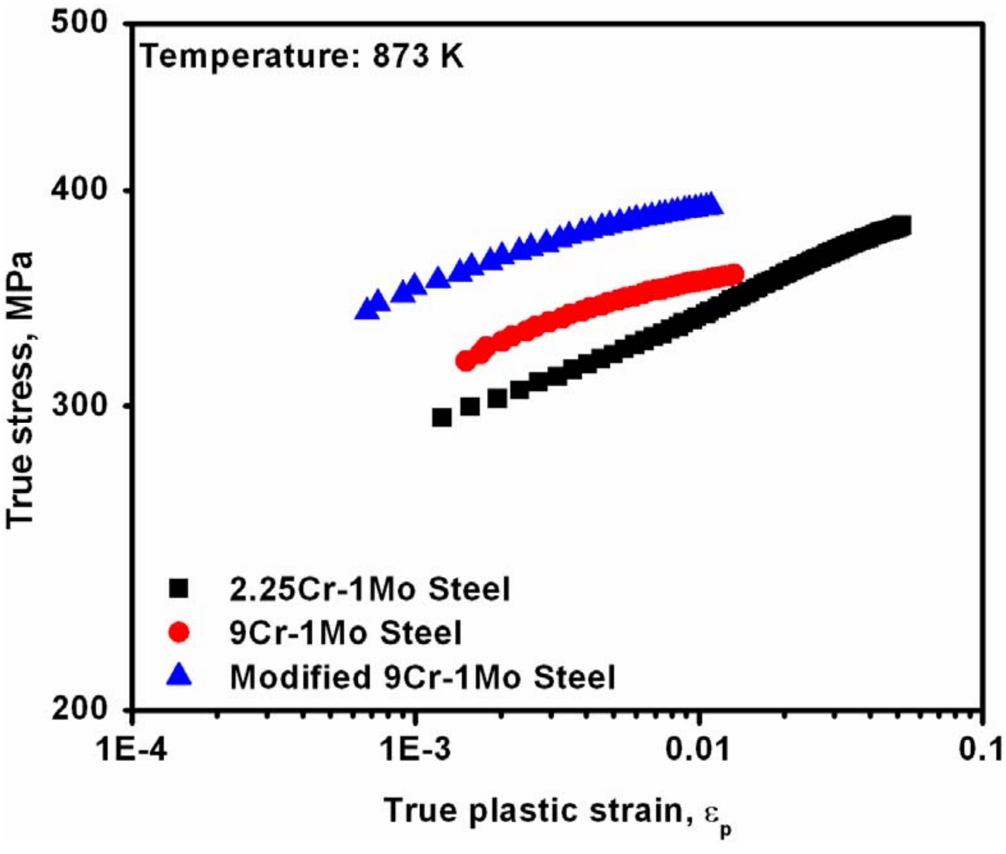

Fig. 3.2 True stress - true plastic strain plot of the steels.

Table 3.1 Tensile properties of different ferritic steels under investigation at 873 K

Material	Yield stress, MPa	Ultimate tensile stress, MPa	Elongation, %	Reduction in area, %	Strength coefficient, K	Strain hardening exponent, n′
2.25Cr-1Mo Steel	290	354	32.75	91.62	474.24	0.073
9Cr-1Mo Steel	310	340	33.72	92.45	445.65	0.049
modified 9Cr-1Mo Steel	350	374	30.88	90.19	489.78	0.048

Table 3.2 Creep deformation and rupture properties of different ferritic steels at 873 K

Material	Stress, MPa	Steady state creep rate, h^{-1}	Rupture life, h	Elongation, %	Reduction in area, %
2.25Cr-1Mo steel	210	1.02×10^{-2}	4.8	38.6	94.5
	170	2.20×10^{-3}	26.2	37.9	93.5
	150	1.08×10^{-3}	55.3	38.2	89.8
	130	4.21×10^{-4}	152.1	36.5	90.8
	110	2.22×10^{-4}	353.5	36.5	89.7
	90	5.21×10^{-5}	1619.2	36.1	72.1
9Cr-1Mo steel	210	2.64×10^{-2}	3.2	31.2	92.5
	170	6.04×10^{-3}	17.6	33.4	92.1
	150	1.45×10^{-3}	60.8	37.2	91.2
	130	8.46×10^{-4}	129.6	35.1	90.1
	110	1.04×10^{-4}	730.2	32.1	86.4

	230	1.18×10^{-2}	4.6	22.3	89.3
	210	3.85×10^{-3}	14.9	25.6	88.9
modified 9Cr-1Mo steel	190	1.28×10^{-3}	35.6	14.4	88.2
	170	1.25×10^{-4}	363.8	18.3	87.1
	150	6.52×10^{-5}	744.9	24.1	84.3

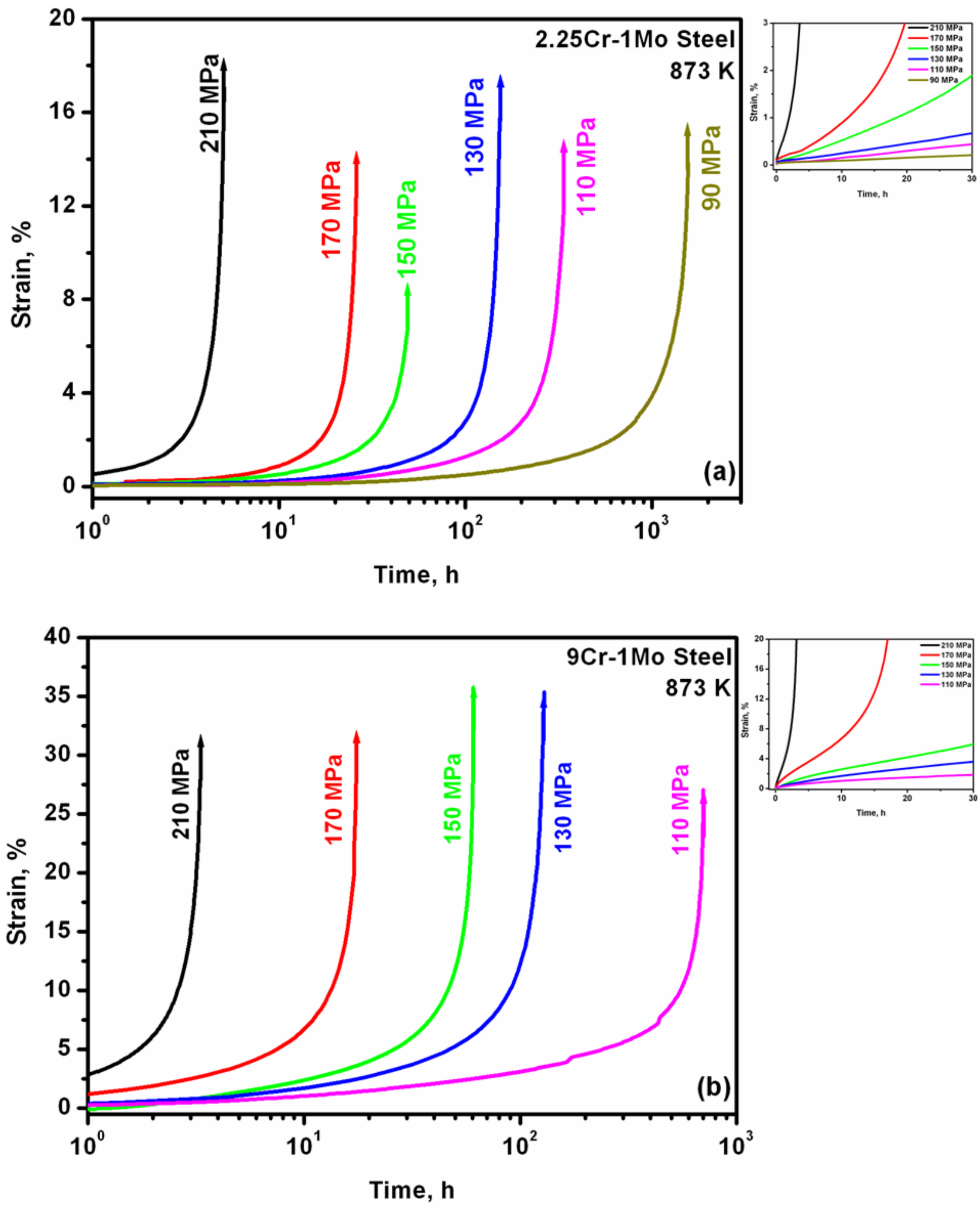

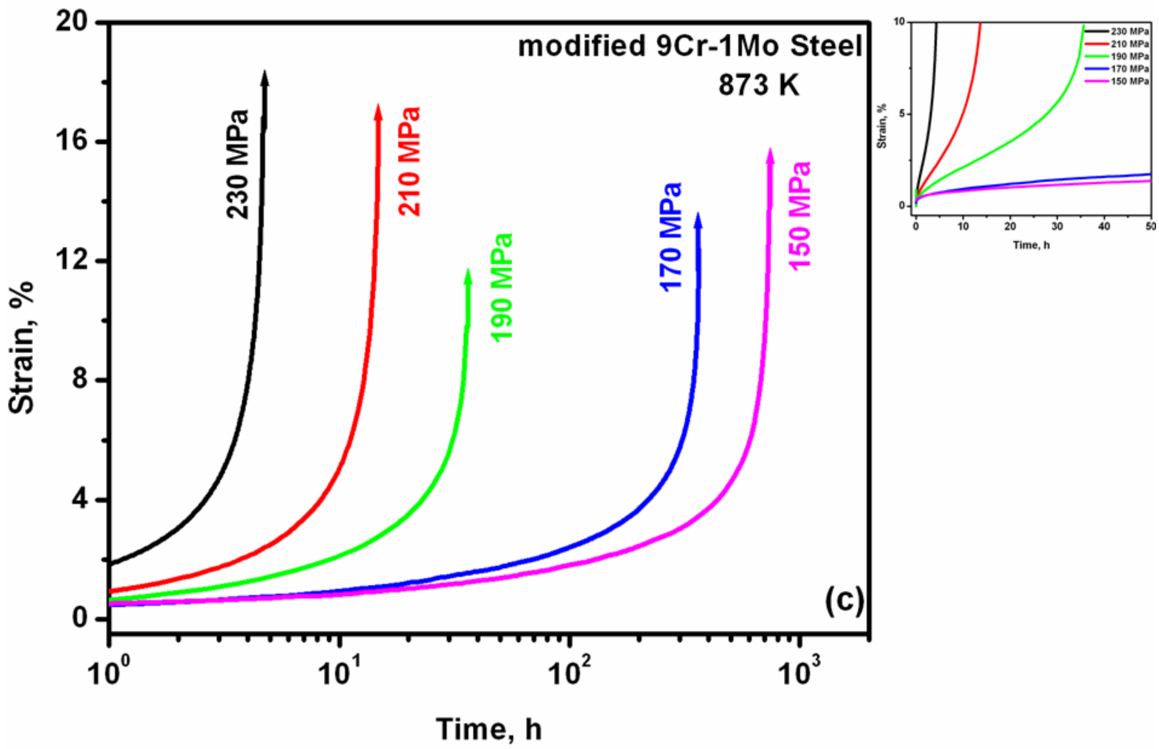

Fig. 3.3 Variations of creep strain as a function of creep exposure time of the steels creep tested over a stress range at 873 K for (a) 2.25Cr-1Mo, (b) 9Cr-1Mo and (c) modified 9Cr-1Mo steels. Also shown in the right are the initial portions of the creep strain with time.

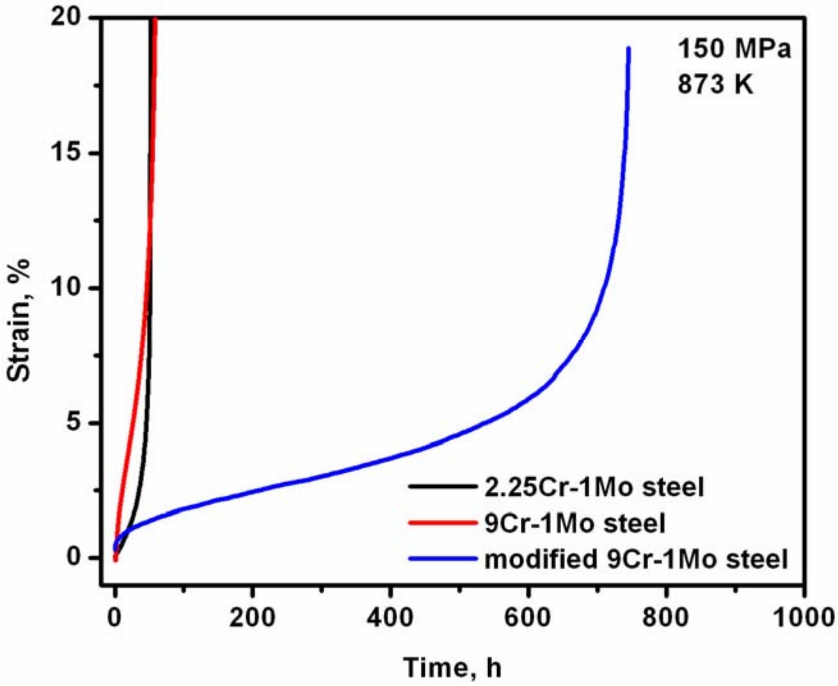

Fig. 3.4 Comparison of creep curves of the investigated steels (150 MPa, 873 K).

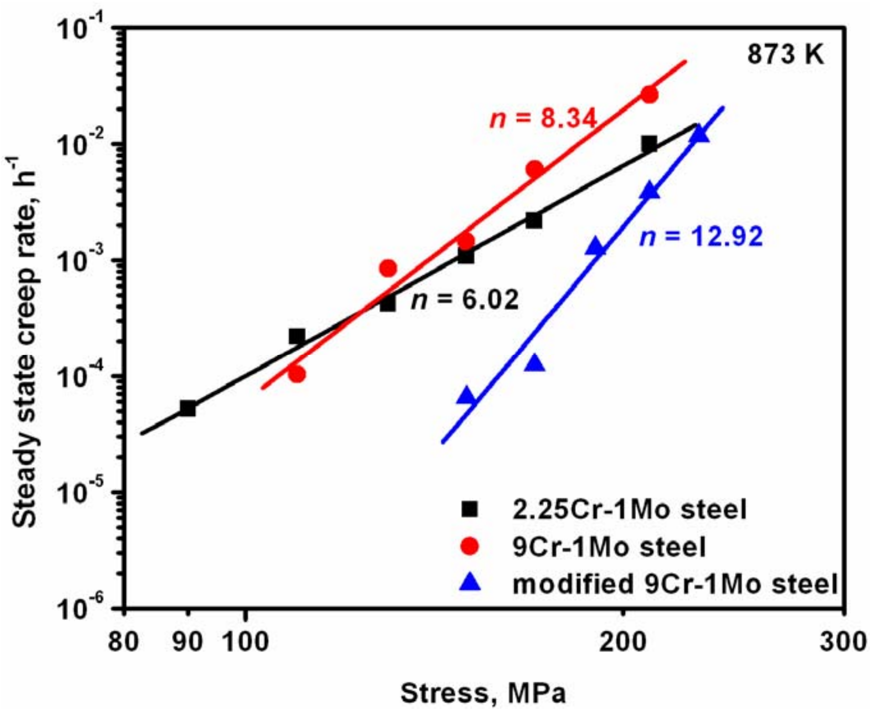

Fig. 3.5 Comparison of steady state creep rate of the steels as a function of applied stress, creep tested at 873 K.

Table 3.3 The coefficients in power-laws governing the stress dependencies of steady state creep rate $\dot{\varepsilon}_s = A\sigma^n$ and rupture life $t_r = M\sigma^{-m}$ for different ferritic steels creep tested at 873 K

Material	*A*	*n*	*M*	*m*
2.25Cr-1Mo steel	9.17×10^{-17}	6.02	1.89×10^{16}	6.69
9Cr-1Mo steel	1.27×10^{-21}	8.34	4.37×10^{19}	8.24
modified 9Cr-1Mo steel	3.57×10^{-33}	12.92	1.36×10^{30}	12.47

Detailed microstructural analysis carried out by Baker and Nutting [90] explained the strengthening mechanism in these steels. The Cr-Mo ferritic steels derive their high-temperature strength from the solid solution strengthening, phase-transformation-induced dislocation substructure, and intra- and inter-granular metal-carbonitride precipitates. The most effective creep strengthening in 2.25Cr-1Mo steel results from the fine dispersion of semicoherent acicular Mo_2C precipitates [90]. However, the Mo_2C precipitates are relatively less stable against thermal and creep exposures and are eventually replaced by M_6C precipitates through the intermediate precipitation of M_7C_3 and $M_{23}C_6$ carbides [90]. The chromium-rich $M_{23}C_6$ precipitates observed in 9Cr-1Mo steel on grain and subgrain boundaries are reported to be too coarse (>100 nm) to prevent the movement of dislocation, but effective in stabilizing the subgrain structures against instability on thermal and creep exposures; thus, they indirectly contribute to strengthening [106]. In modified 9Cr-1Mo steel, intragranular precipitation of (V,Nb)(C,N) carbonitrides impart high creep strength to the steel [92]. The undissolved primary Nb(C,N) particles act as nucleating centers for $M_{23}C_6$ to increase its density, and also the dissolved vanadium in the chromium-rich $M_{23}C_6$ increases its stability against thermal and creep exposures. Thus, the $M_{23}C_6$ precipitates are more effective in modified 9Cr-1Mo steel than in 9Cr-1Mo steel in stabilizing the phase-transformation-induced dislocation substructure against thermal and creep exposures. The observed differences in creep deformation strength of the steels (Fig.3.5) are considered due to the differences in the prevailed strengthening mechanism in the steels.

3.4. Creep rupture life and damage

The variation of rupture life (t_r) of the steels with applied stress (σ) is shown in a double-logarithmic plot in Fig. 3.6. Rupture life was found to decrease with increase in applied stress and obeyed a power law relation as $t_r = M\sigma^{-m}$, where M and m are the stress coefficient and the stress exponent respectively. The stress dependence of rupture life exhibited negative slope. Similar absolute values of n (relating minimum creep rate with applied stress) and m (relating applied stress with creep rupture life) (Table 3.3) for all the steels suggest that the creep deformation and fracture processes are controlled by same mechanism [103].

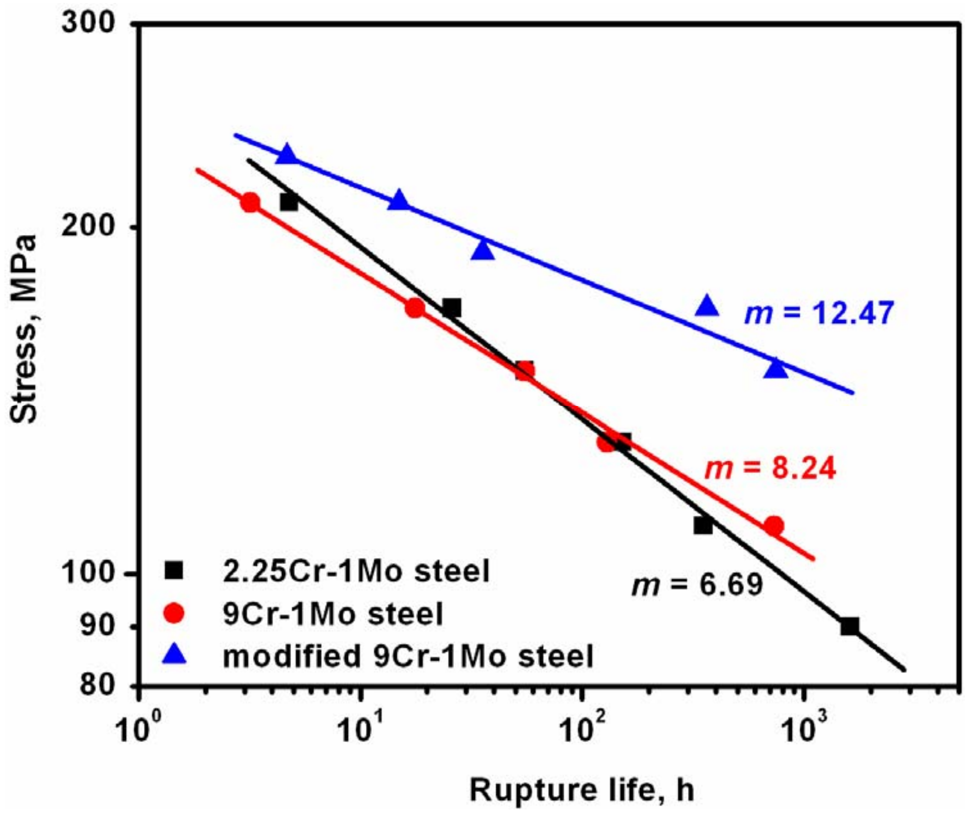

Fig. 3.6 Comparison of creep rupture life of the steels as a function of applied stress, creep tested at 873 K.

The steady state creep rate ($\dot{\varepsilon}_s$) and rupture life (t_r) of materials are often related through the Monkman-Grant relationship, $\dot{\varepsilon}_s^{\alpha} t_r = C$, where α is a constant close to unity and C is the Monkman-Grant constant [27]. The applicability of the Monkman-Grant relationship for different steels in the investigation is shown in Fig. 3.7. It confirms that the same mechanism is being responsible for the creep deformation and fracture of the steels under investigation. The investigation has clearly brought out the uniqueness of Monkman-Grant relationship between creep rate and rupture life of materials, in spite of steels having different strength. The values of α and C were found out to be 0.99 and 0.063 respectively. Low value of Monkman-Grant constant

'*C*' indicated small contribution of transient primary strain to overall creep strain and the majority of creep strain accumulation was during the tertiary stage of creep deformation [107].

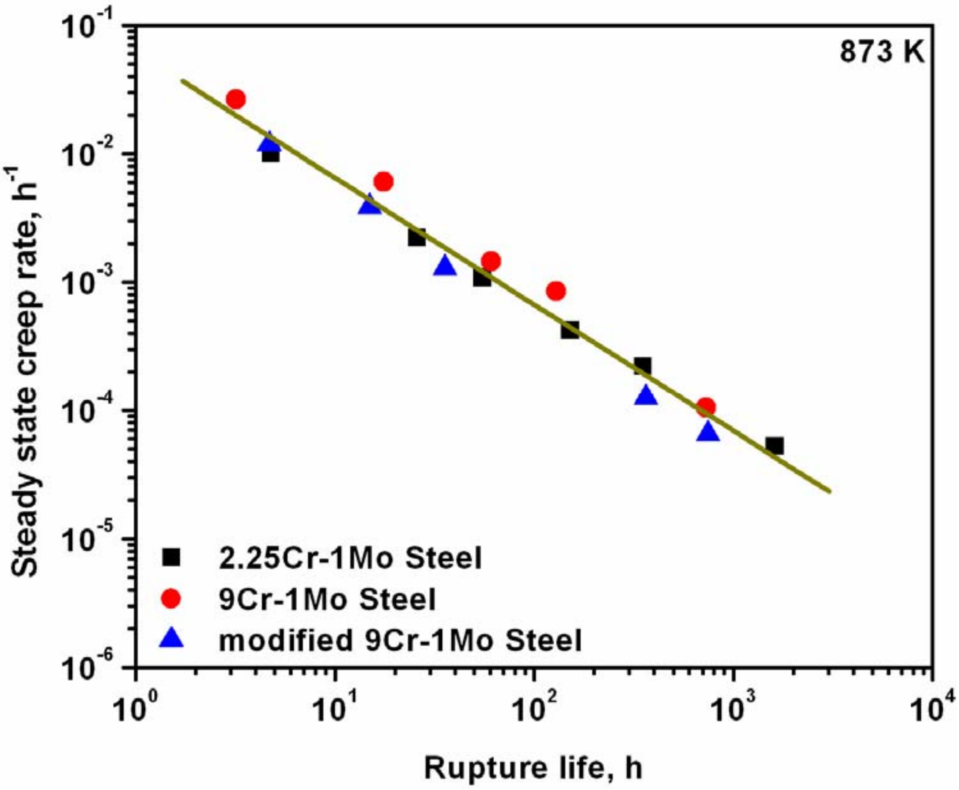

Fig. 3.7 Variation of steady state creep rate with rupture life of the steels, exhibiting the validity of Monkman-Grant relation for the steels.

3.5 Time to onset of tertiary stage of creep deformation and creep damage tolerance

The analysis of tertiary stage of creep deformation of the steels has been carried out based on the onset of tertiary creep deformation. The time to onset of tertiary stage 't_{ot}' was measured from creep curve as the time at which the creep rate started increasing from the steady state. The variation of 't_{ot}' with rupture life is shown in Fig. 3.8.

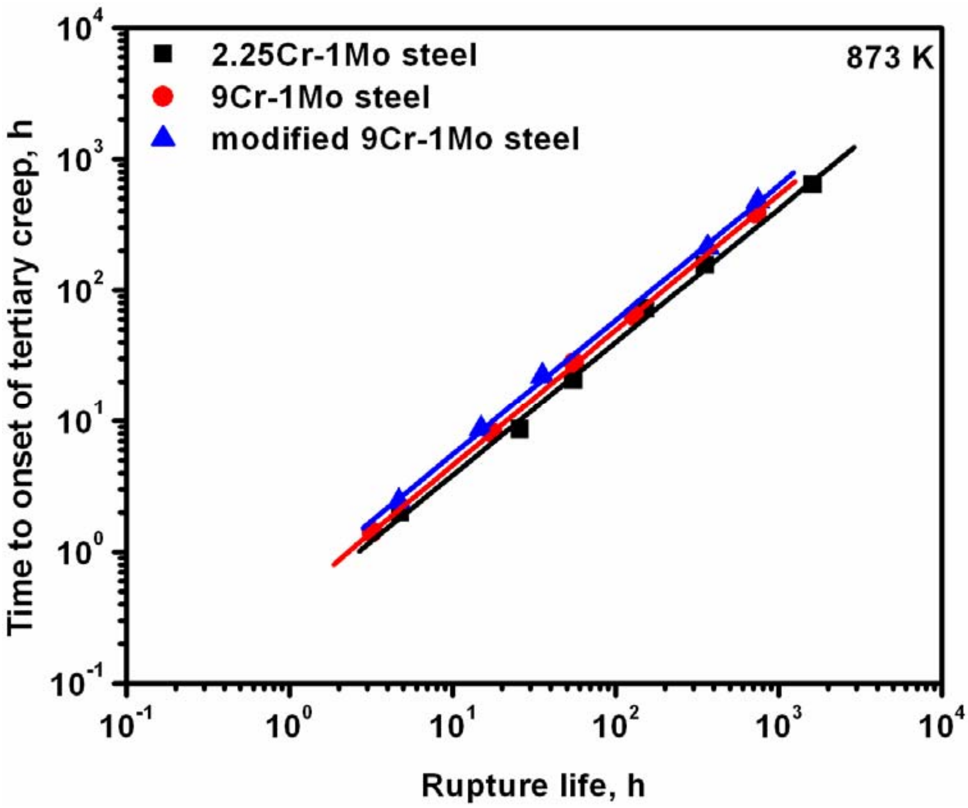

Fig. 3.8 Variations of time to onset of tertiary stage of creep deformation as a function of creep rupture life for the steels.

It followed a linear equation of the form t_{ot} = f . $t_{r,}$ where ‘f’ is a constant. The value of constant ‘f’ was found to be around 0.37, 0.52 and 0.63 for 2.25Cr-1Mo, 9Cr-1Mo and modified 9Cr-1Mo steel respectively. This indicates that the 2.25Cr-1Mo, 9Cr-1Mo and modified 9Cr-1Mo steels respectively spent about 63 %, 48 % and 37 % of their creep rupture life in the tertiary stage of deformation. The extensive tertiary creep in terms of both the time spent and accumulation of large creep strain observed in these steels is in agreement with the observations made by Choudhary et al. [103]. Early onset of tertiary stage of creep deformation is due to various kinds of damage accumulation in the material on creep exposure like intergranular creep cavitation, mechanical instability owing to neck formation, internal oxidation and microstructural degradation such as the coarsening of precipitate particles and recovery of dislocation substructures. Based on CDM approach, an indication of the damage process initiating tertiary creep is provided by the creep damage tolerance parameter defined as $\lambda = \varepsilon_f / \dot{\varepsilon}_s . t_r$, where ε_f is strain to failure, $\dot{\varepsilon}_s$ is steady state creep rate and t_r is rupture life [28,108,109]. Each damage micro-mechanism acting alone results in a characteristic shape of the creep curve and a corresponding characteristic value of λ [28,108,109]. It has been predicted that for values of λ between 1.5 to 2.5, the tertiary stage of creep deformation is due to the growth of creep cavities by diffusive transfer of atoms from cavity surface on to the grain boundary; whereas it can be as high as 4 or more when microstructural degradation causes the damage in the material. Thus the materials, which are microstructurally stable and display only limited tertiary stage under the imposed test conditions, exhibit $\lambda < 2$; whereas $\lambda > 2$ is observed in the materials where tertiary stage of creep deformation starts because of the microstructural instability. Figure 3.9 shows the variation of creep damage tolerance factor λ with rupture time for all the steels. The value of λ was found to decrease with rupture life from around 7.8 to around 4.5 for 2.25Cr-1Mo steel, Fig. 3.9(a). Such high value of λ for 2.25Cr-1Mo steel indicates coarsening of precipitates and dislocation substructures as the dominant damage mechanism operating during creep. Detailed TEM studies carried out by Chaudhuri et al. [110] on creep exposed 2.25Cr-1Mo steel revealed that softening was more affected by the coarsening of carbides than that of dislocation density. The bainitic 2.25Cr-1Mo steel derives its creep strength mainly from metastable intragranular acicular Mo_2C carbide [105]. Precipitation sequence in bainitic 2.25Cr-1Mo steel has been studied by Baker and Nutting [90]. With thermal and creep exposure, the metastable Mo_2C carbide dissolves and leads to the precipitation of chromium rich $M_{23}C_6$ and molybdenum rich

M_6C intergranular carbides with the consequence of decrease in creep deformation and rupture strength.

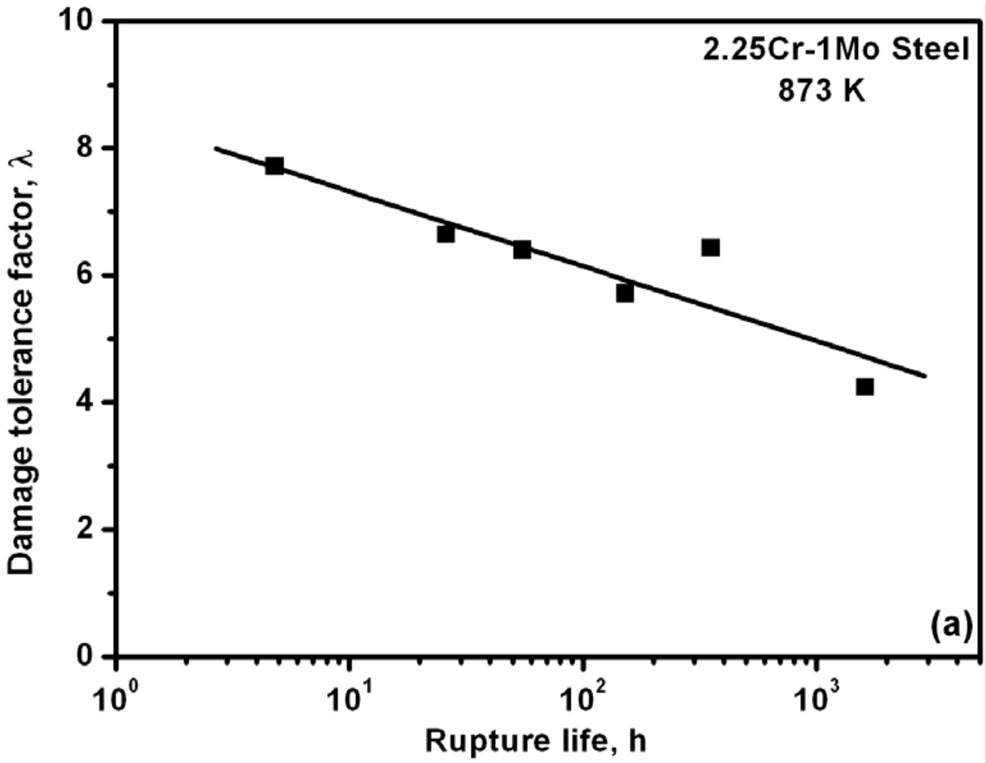

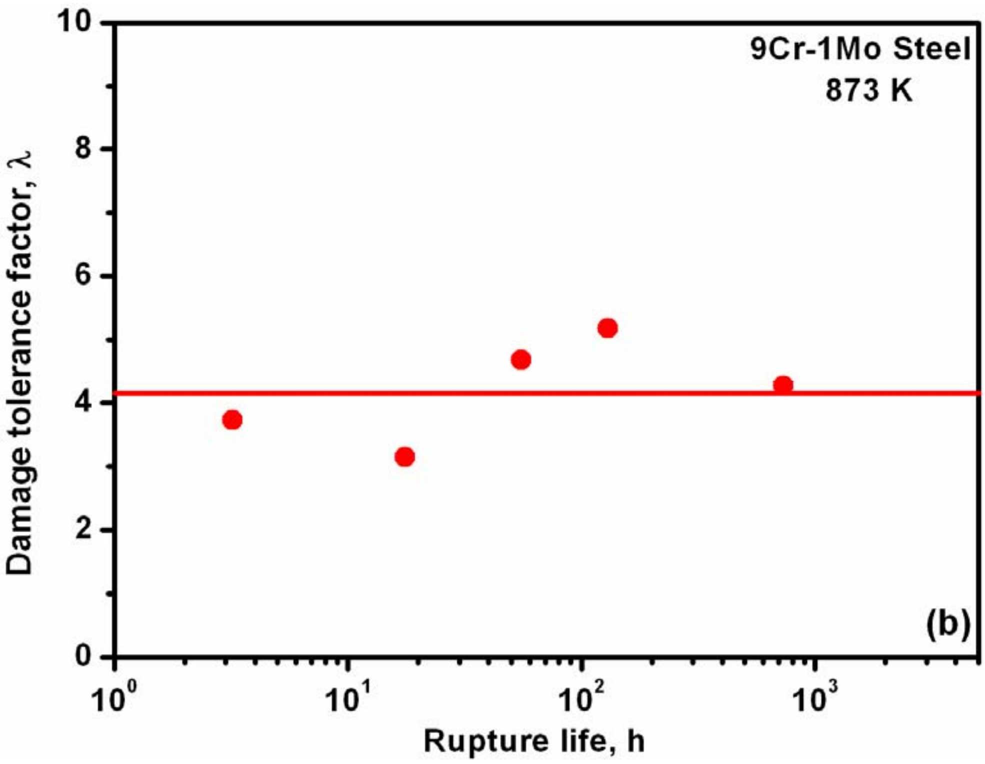

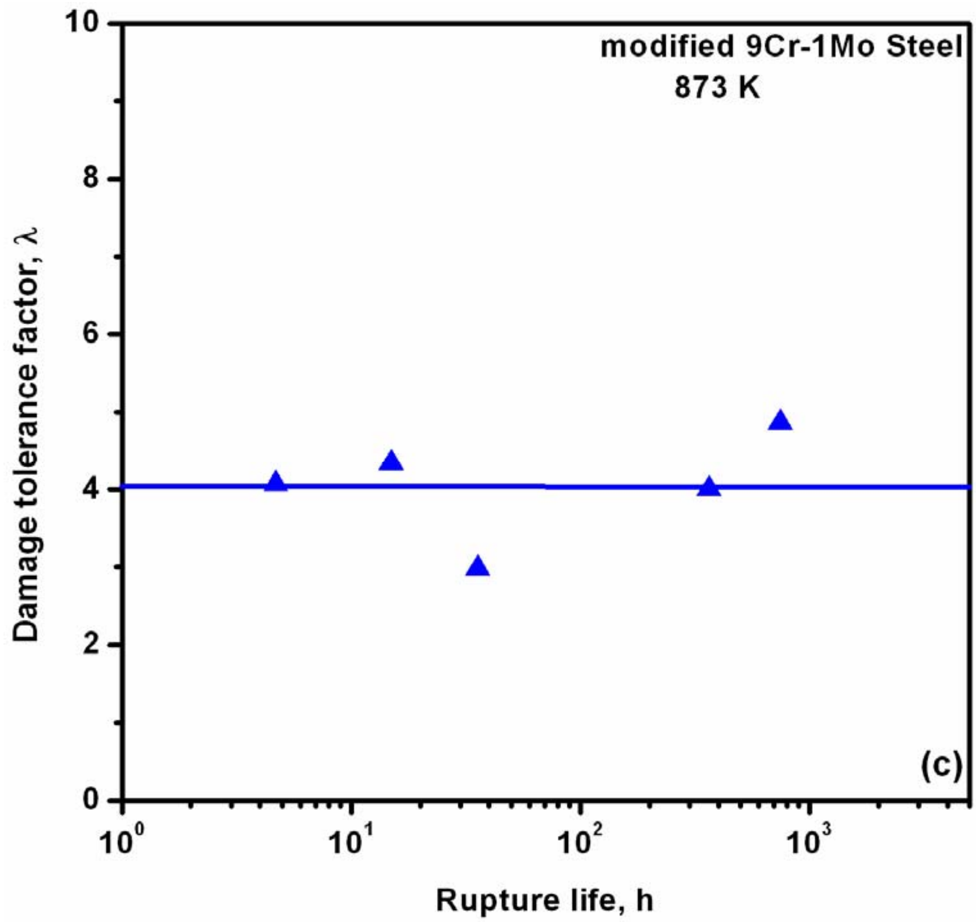

Fig. 3.9 Variation of damage tolerance factor with rupture life for (a) 2.25Cr-1Mo, (b) 9Cr-1Mo and (c) modified 9Cr-1Mo steels.

The decrease in values of λ indicates the tendency towards intergranular failure on long-term creep exposure, under multiaxial state of stress as in notch specimen or microstructurally inhomogeneous weld joint. Type IV cracking in 2.25Cr-1Mo steel weld joint is an example of creep cracking under multiaxial state of stress imposed by microstructural inhomogeneity [31]. The value of damage tolerance factor was found to be 4.2 and 4 for 9Cr-1Mo and modified 9Cr-1Mo steels respectively, Fig. 3.9(b) and 3.9(c). Choudhary et al. [103,111] attributed the high λ values in 9Cr-1Mo and modified 9Cr-1Mo steels to microstructural degradation in terms of the coarsening of precipitates, decrease in dislocation density and dislocation cells/subgrain coarsening. The high creep damage tolerance factor observed for 2.25Cr-1Mo, 9Cr-1Mo and modified 9Cr-1Mo steel is generic in nature and microstructural degradation is the dominant damage mechanism in Cr-Mo steels [103,107,111].

The variations of creep rupture ductility (% reduction in area) as a function of rupture life is shown in Fig. 3.10. The creep rupture ductility was found to be almost independent of rupture life for 9Cr-1Mo and modified 9Cr-1Mo steels over the stresses under investigation. However, the creep ductility was found to decrease with creep exposure for 2.25Cr-1Mo steel.

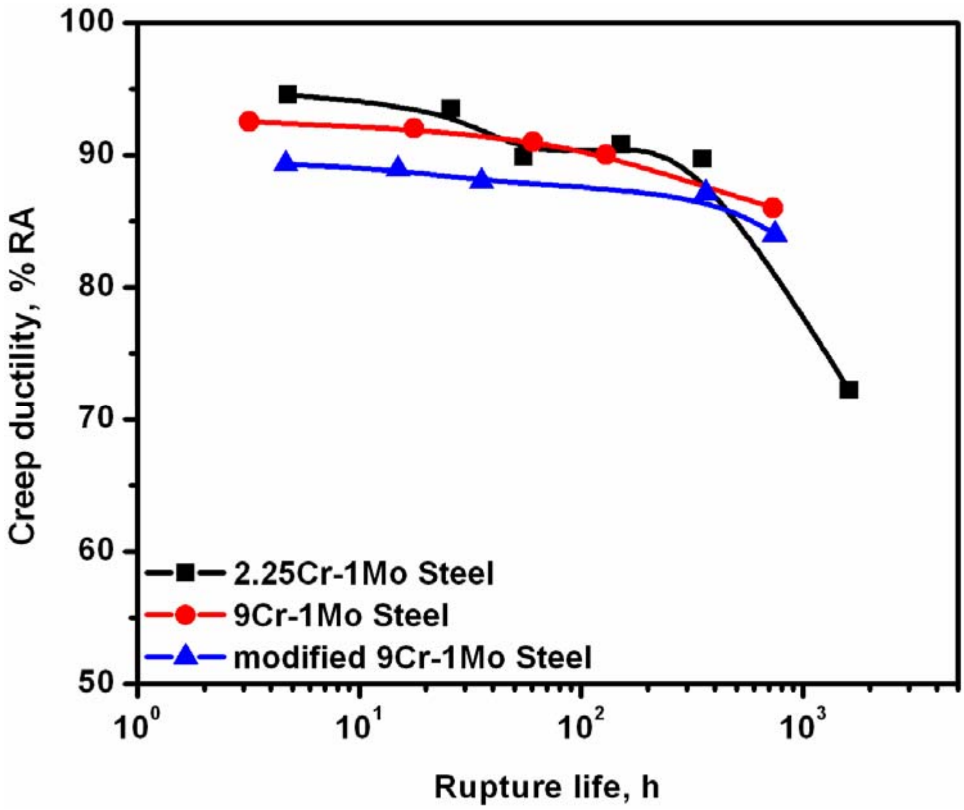

Fig. 3.10 Comparison of creep rupture ductility (% reduction in area) as a function of creep rupture life for the steels at 873 K.

Scanning electron microscopy (SEM) examination of the fracture surfaces of the creep ruptured specimens revealed transgranular fracture characterized by dimples resulting from coalescence of microvoids (Fig. 3.11) at all stresses and for all the steels studied in the present investigation. Optical metallographic examination of the creep ruptured specimens also revealed transgranular fracture with no evidence of intergranular creep cavitation. However, shape and size of dimples was found to vary depending on the material. It was very fine in 9Cr-1Mo steel, whereas coarser in case of 2.25Cr-1Mo and modified 9Cr-1Mo steels.

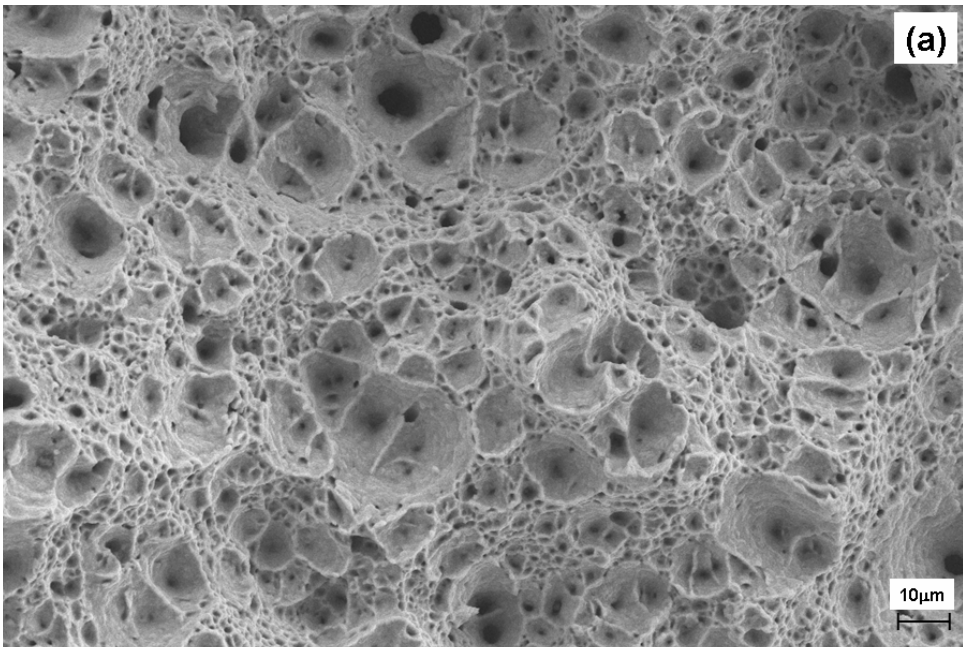

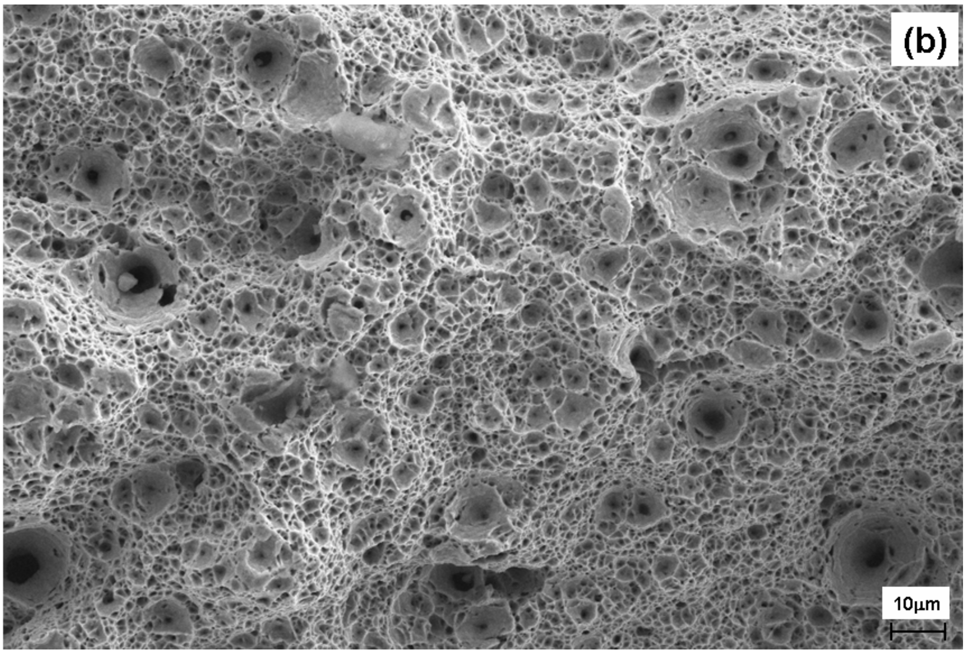

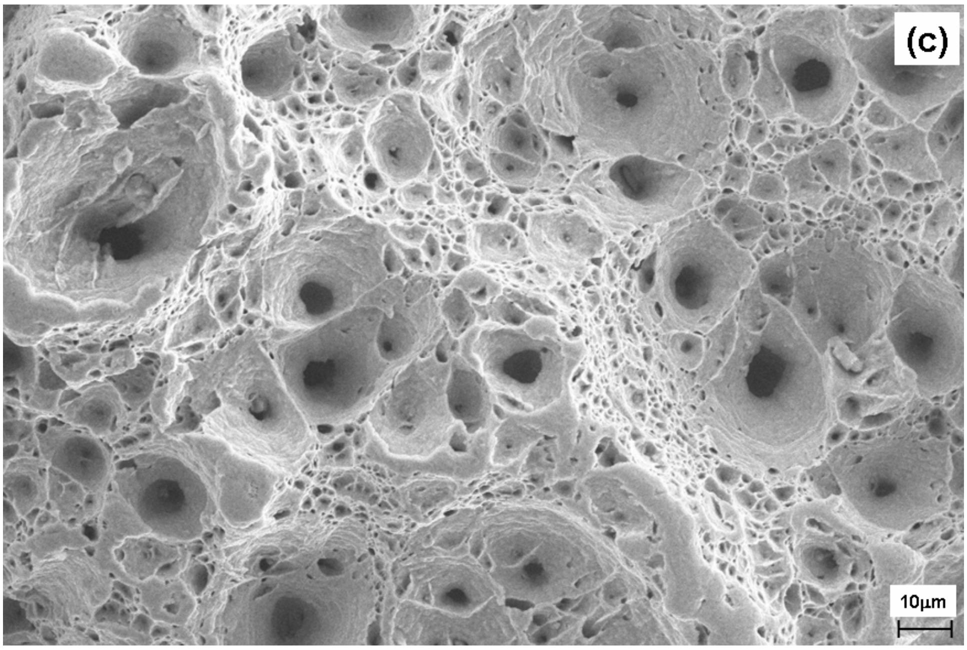

Fig. 3.11 SEM fractographs showing ductile fracture at 150 MPa and 873 K in the (a) 2.25Cr-1Mo, (b) 9Cr-1Mo and (c) modified 9Cr-1Mo steels.

3.6 Conclusions

Based on the creep deformation and fracture behaviour studies of 2.25Cr-1Mo, 9Cr-1Mo and modified 9Cr-1Mo steels at 873 K over a stress range of 110-230 MPa, following conclusions have been drawn.

1. The creep deformation of the steels was well characterized by a small instantaneous strain on loading, brief transient primary and secondary stages, followed by a prolonged tertiary creep regime.
2. The modified 9Cr-1Mo possessed more creep strength (lower creep deformation rate and higher rupture life) than the 2.25Cr-1Mo and 9Cr-1Mo steels.
3. The variations of steady state creep deformation rate of the steels with applied stress followed Norton's law.

4. Monkman-Grant relationship between steady state creep rate and rupture life was obeyed by the steels. The same equation was found to be followed by all the steels.
5. Creep damage of the steels under uniaxial stress was found to be due to microstructural degradation, with no evidences of intergranular creep cavitation over the stress range investigated.

CHAPTER 4

EFFECT OF NOTCH ON CREEP RUPTURE BEHAVIOUR

Effect of notch on creep rupture behaviour

4.1 Introduction

The 2.25Cr-1Mo steel was found to have lowest creep deformation strength and modified 9Cr-1Mo steel possessed highest creep deformation strength among the three ferritic steels under uniaxial creep conditions as discussed in Section 3.3. In this chapter, the effect of notch on creep rupture behaviour of these steels has been discussed. The strengthening observed in these steels in presence of notch and the fractographic observations have been explained based on FE analysis of stress distribution across the notch throat plane. Tensile and creep deformation characteristics of individual steel have been incorporated in the FE analysis.

4.2 Creep rupture life of the steels in presence of notch

Creep tests were carried out on the notched specimens of the steels having notch root radius of 1.25 mm at the stress levels ranging from 110 - 230 MPa and 873 K. A pictorial view of the notches of acuity ratio 4 in the notched specimen is shown in Fig. 4.1. The net applied stress (σ_{net}) at notch throat plane was same as that of applied stress (σ) in case of plain specimen. The creep rupture lives of notched specimens were found to be higher than those of the plain specimens, exhibiting strengthening in the presence of notch in all the steels, Fig. 4.2. Table 4.1 summarizes the creep rupture properties of the steels for the notch root radius of 1.25 mm.

The rupture life of notched specimen increased with decrease in net applied stress and obeyed a power law relation ($t_r = M'\sigma^{m'}$) as in case of plain specimens, where M' and m' are the stress coefficient and the stress exponent respectively. Table 4.2 shows the values of the constants of the steels in presence of notch and are compared with those of plain specimens. Stress sensitivity of rupture life of the steels decreased in presence of notch and the decrease was more for modified 9Cr-1Mo and least for 2.25Cr-1Mo steel. The extents of strengthening in presence of notch in the different steels as functions of net applied stress and rupture life of plain specimen are shown in Fig. 4.3 and Fig. 4.4 respectively. The extent of strengthening in presence of notch was found to increase in the order of 2.25Cr-1Mo, 9Cr-1Mo and modified 9Cr-1Mo steel. The increase in strengthening was comparable for the 9Cr-1Mo and 2.25Cr-1Mo steels. However, significant increase in strengthening was observed in modified 9Cr-1Mo steel. Eggeler et al. [41] studied the effect of notch on creep behaviour of 9Cr-1Mo steel and observed strengthening in the steel. The strengthening effect was found to decrease with the decrease in applied stress and increase in rupture life for all the steels, as depicted by decrease in slopes of plots in Figs. 4.3 and 4.4 with decrease in stress and increase in rupture life respectively. Studies carried out by Dyson et al. [38] on notched specimens of Nimonic 80A indicated notch strengthening. Al-Faddagh et al. [39] and Al-Abed et al. [62] also reported similar observations of notch strengthening for 2.25Cr-1Mo steel. However, Ng et al. [40] reported that the 0.5Cr-0.5Mo-0.25V steel (tempered bainitic steel) showed notch strengthening for shallow notches and tendency towards notch weakening for sharper notches. Notch strengthening has also been observed in modified 9Cr-1Mo steel by Wasmer et al. [112].

Variations of creep rupture ductility of the steels (% reduction in area) in presence of notch as a function of rupture life are shown in Fig. 4.5 and compared with those of plain specimen. Presence of notch decreased the creep rupture ductility of the steels significantly. The 2.25Cr-1Mo steel suffered more reduction in ductility in presence of notch than the other two steels.

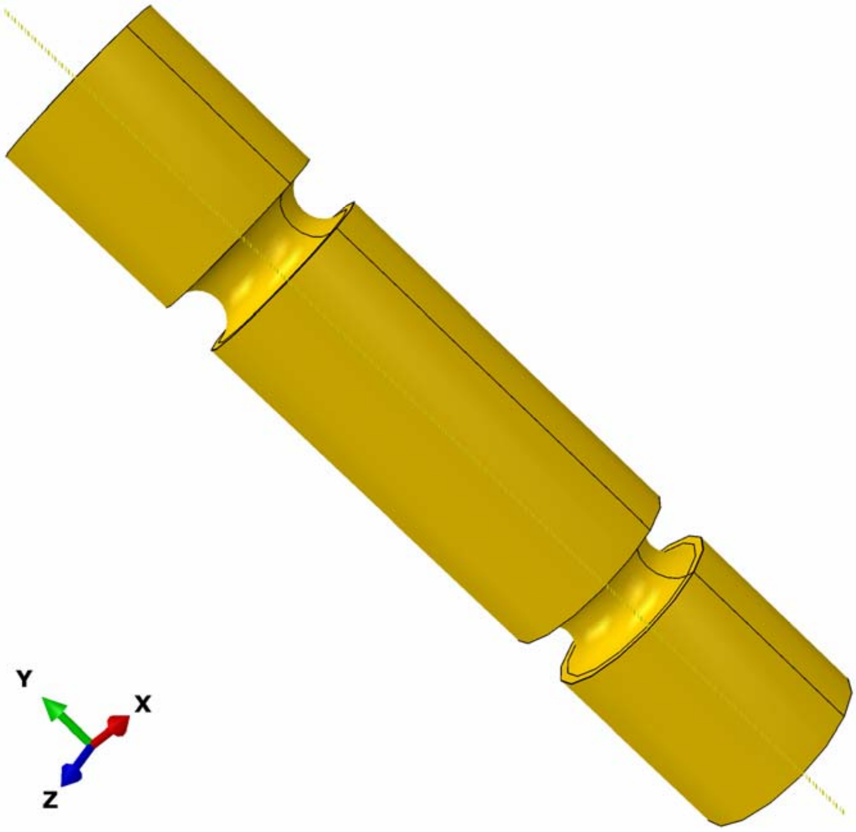

Fig.4.1 Drawing showing the geometry of creep specimen having two notches.

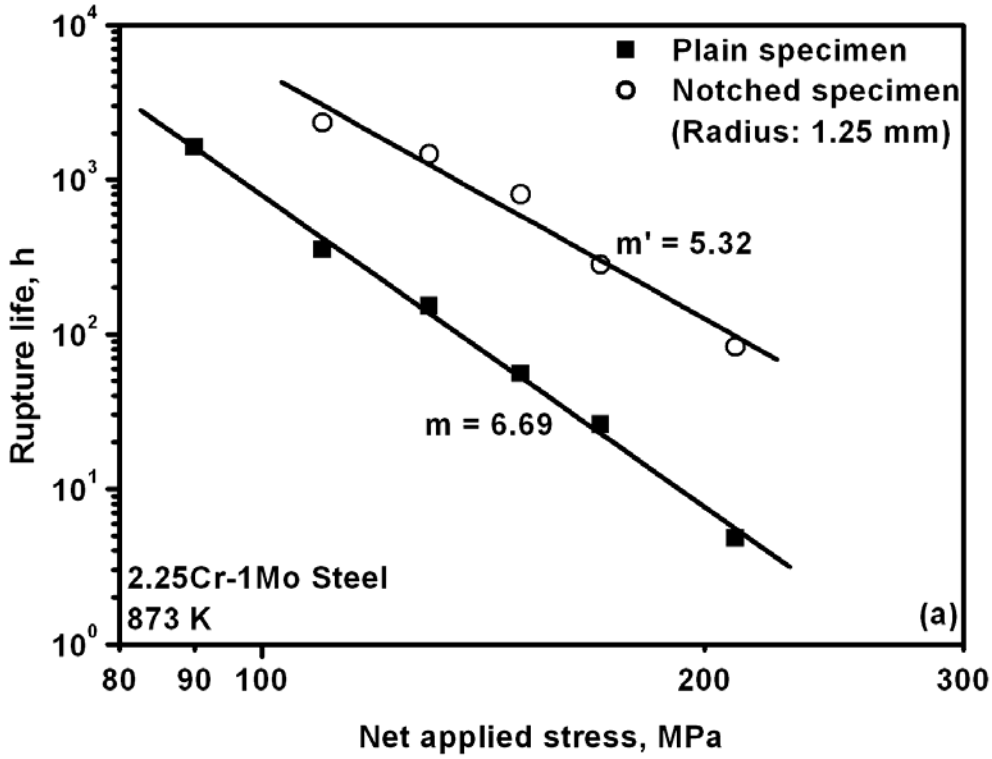

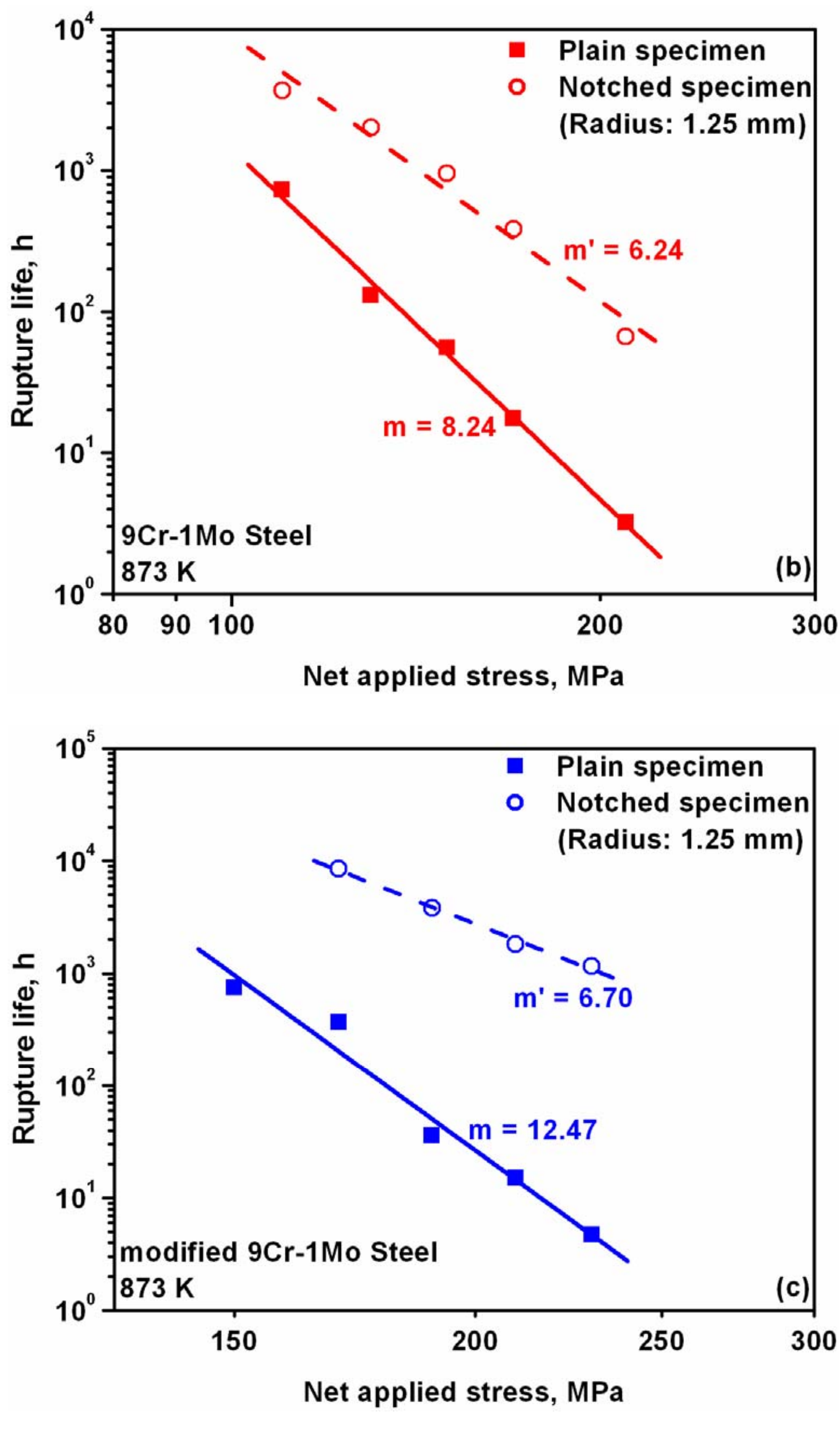

Fig. 4.2 Variation of creep rupture life as a function of net applied stress for (a) 2.25Cr-1Mo, (b) 9Cr-1Mo and (c) modified 9Cr-1Mo steels.

Table 4.1 Creep rupture properties of the steels in presence of notch with notch radius (1.25 mm) or notch acuity ratio of 4, over the stress range 110 - 230 MPa and 873 K

Material	**Stress, MPa**	**Rupture life, h**	**Reduction in area, %**
2.25Cr-1Mo steel	210	83.2	65.5
	170	282.4	50.3
	150	803.5	40.2
	130	1460.4	33.1
	110	2324.1	20.0
9Cr-1Mo steel	210	66.9	75.8
	170	385.8	59.3
	150	947.6	45.5
	130	2007.4	32.2
	110	3695.8	20.4
modified 9Cr-1Mo steel	230	1161.3	52.6
	210	1821.4	41.9
	190	3790.1	36.8
	170	8555.3	33.5

Table 4.2 Comparison of coefficients of rupture life versus net applied stress plots for the steels

Material	**Plain specimens**		**Notched specimens**	
	M	m	M'	m'
2.25Cr-1Mo steel	1.89×10^{16}	6.69	2.19×10^{14}	5.32
9Cr-1Mo steel	4.37×10^{19}	8.24	2.69×10^{16}	6.24
modified 9Cr-1Mo steel	1.36×10^{30}	12.47	7.08×10^{18}	6.70

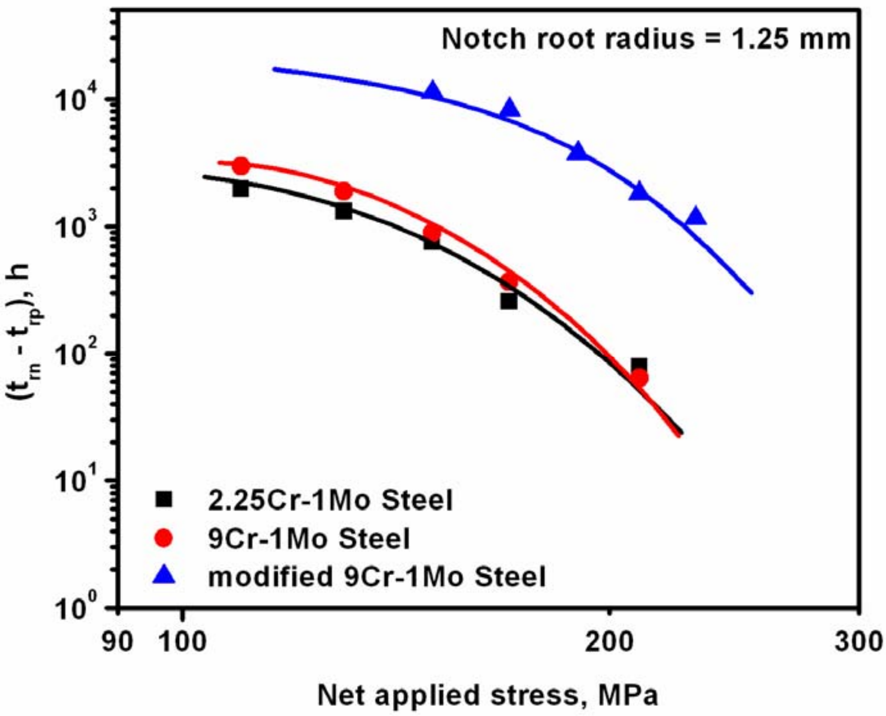

Fig. 4.3 Variations of notch strengthening (t_{rn} - t_{rp}) (difference between time to rupture with and without notch) as a function of net applied stress for 2.25Cr-1Mo, 9Cr-1Mo and modified 9Cr-1Mo steels.

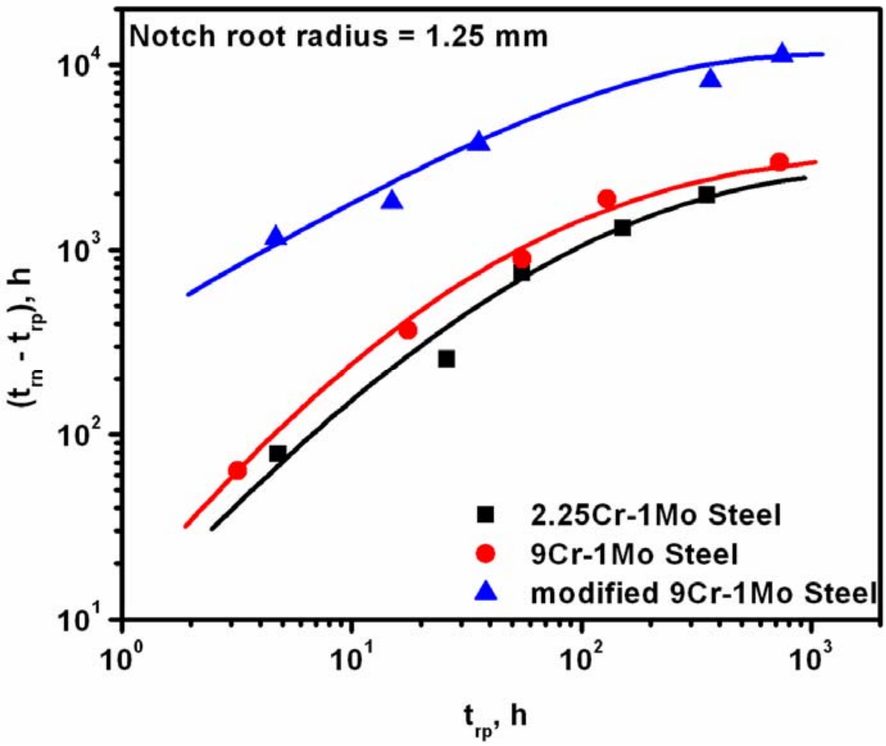

Fig. 4.4 Variations of notch strengthening (t_{rn} - t_{rp}) (difference between time to rupture with and without notch) as a function of rupture life of plain specimen for 2.25Cr-1Mo, 9Cr-1Mo and modified 9Cr-1Mo steels.

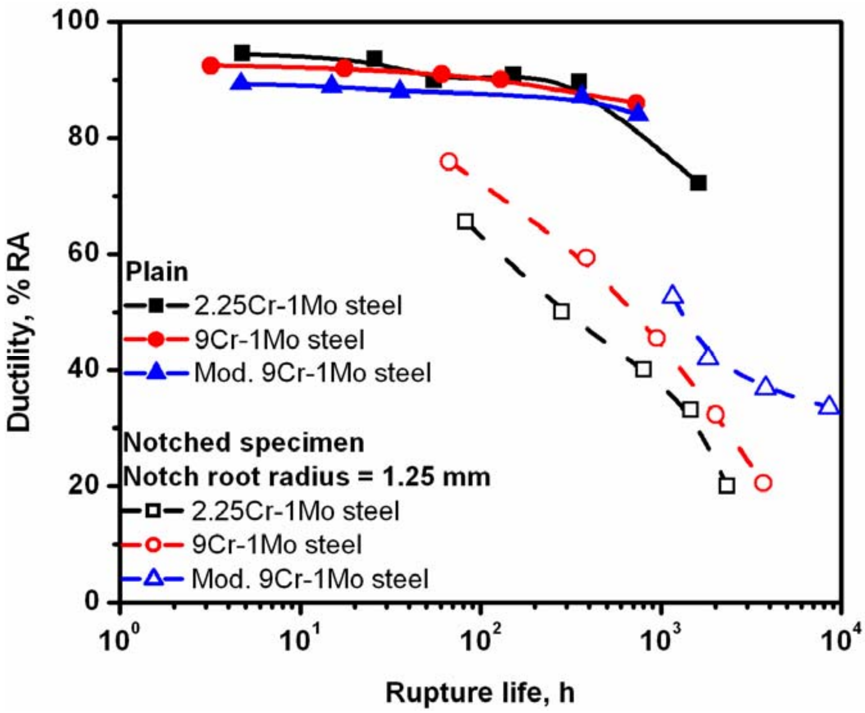

Fig. 4.5 Variations of creep ductility as a function of rupture life for plain and notched specimen for the steels.

4.3 Fracture behaviour of the steels in presence of notch

Predominantly transgranular dimple failure was observed in the notched specimens of the steels at relatively higher applied stresses (Fig. 4.6(a) and 4.6(b)), as in the plain specimens, Fig. 3.11. Shear lip, resulting in cup and cone type of failure, caused by final mechanical instability at the notch root region was observed, Fig. 4.6(a). This indicated that the failure began at the central location of the notched specimen and propagated towards the notch root. Similar view of crack propagation from centre of notch throat plane to notch root has been reported by several investigators [38,62]. Width of the shear lip zone was found to decrease with decrease in applied stress. The shape and size of the dimples in the failed notched specimens were found to depend on the applied stress and the location in the failed surface. Dimples around the central location of the notch throat plane were relatively bigger in

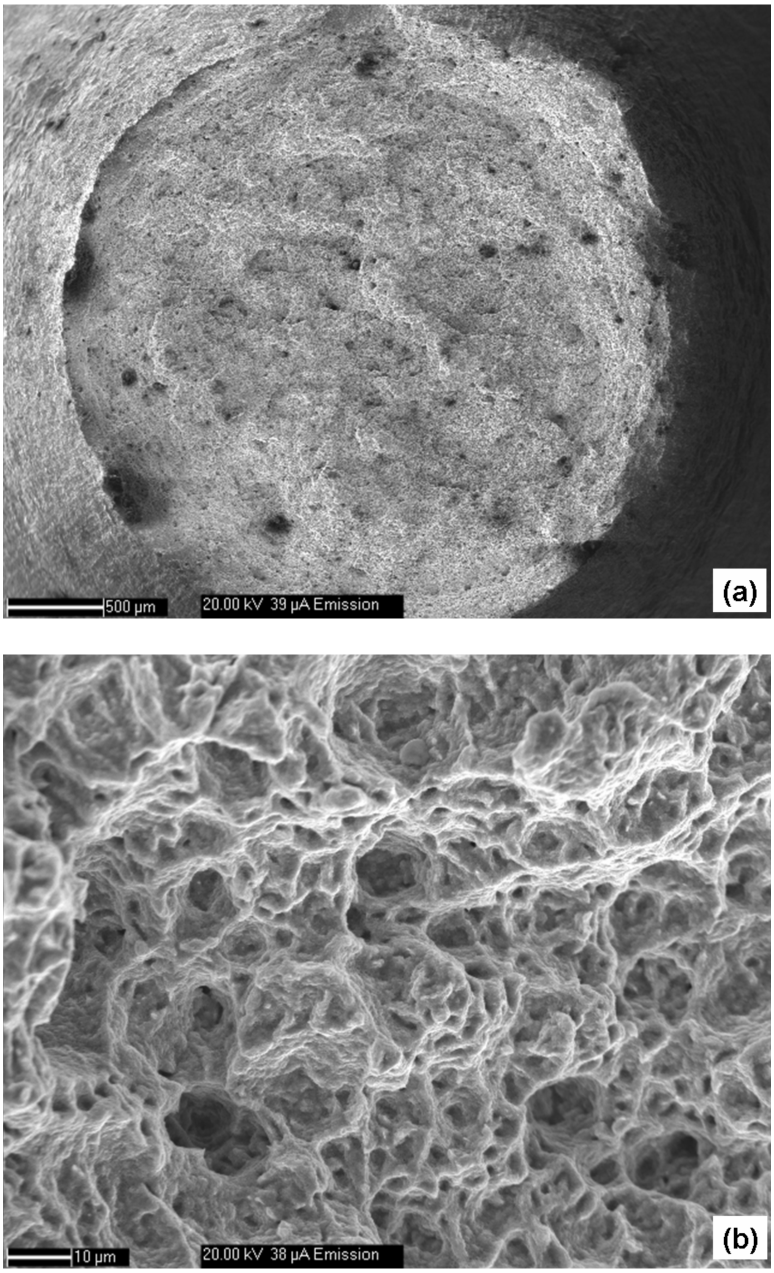

Fig. 4.6 (a) Typical cup and cone fracture with (b) dimpled ductile fracture appearance observed in notched specimen (notch root radius = 1.25 mm) at relative higher stresses (210 MPa, 873 K) in 2.25Cr-1Mo steel.

size and deeper (Fig. 4.7(a)) than those near to the notch root (Fig. 4.7(b)). This indicates that the voids at the central location of notch throat would have grown appreciably by stress perpendicular to it leading to cup and cone type of fracture at relatively higher stresses. At relatively lower applied stresses, evidences of intergranular creep failure were also observed in 2.25Cr-1Mo at close to notch root, Fig. 4.8. Eggeler et al. [41] have also reported intergranular creep cavitation at the notch root for relatively lower applied stresses, suggesting a cross over for relatively lower stresses which may lead to notch weakening kind of behaviour in the steel. Studies carried out on 2.25Cr-1Mo steel by Kwon et al. [53] indicated damage initiation near the notch root for Modified Bridgman type of notch indicating creep cavitation. The studies carried out on alloy X-750 by Pandey et al. [51] showed notch strengthening in the material for the testing conditions. They observed that the crack initiation site moved systematically from notch centre at high stresses towards the notch root at relatively lower stresses. For the notch of root radius 1.25 mm and over the investigated stress range no evidence of creep cavitation was observed in the 9Cr-1Mo and modified 9Cr-1Mo steels, indication that these steels are more resistant to creep cavitation under multiaxial state of stress than the 2.25Cr-1Mo steel.

4.4 FE analysis of stress distribution across the notch throat plane

The steels under investigation exhibited notch strengthening under creep conditions, extent of which was found to depend on the material. Finite element analysis of stress distribution across the notch throat plane during creep exposure was carried out to understand the difference in notch strengthening of the materials. The FE analysis was carried out on incorporating elasto-plastic-creep behaviour of the materials. The tensile behaviour was incorporated using Hollomon equation ($\sigma_t = K{\varepsilon_p}^{n'}$) whereas creep behaviour using Norton's creep law relating the steady state creep rate with applied stress ($\dot{\varepsilon}_s = A\sigma^n$).

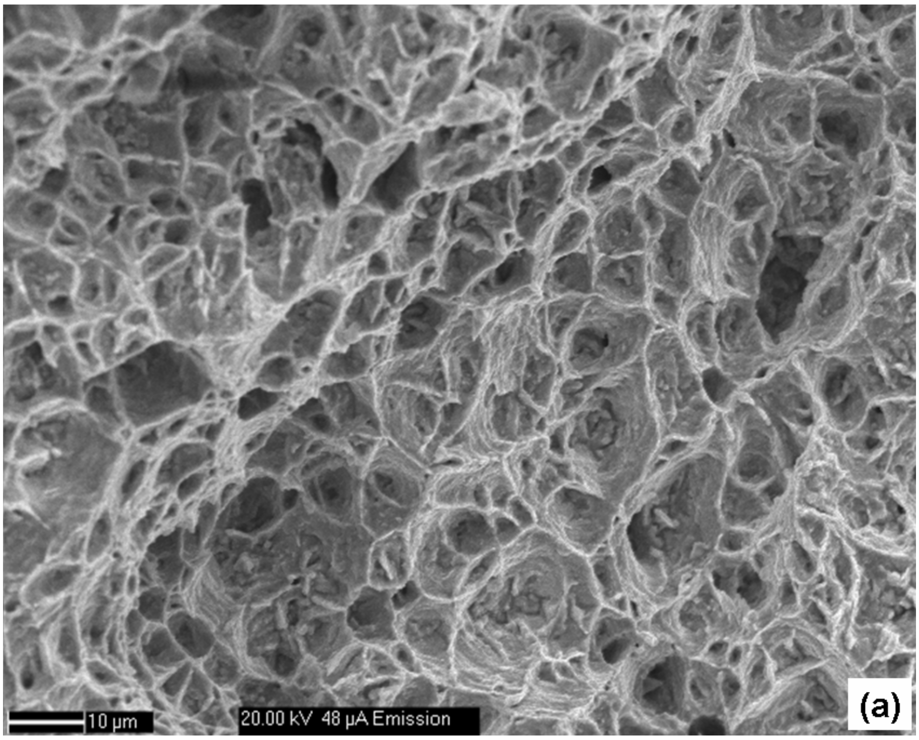

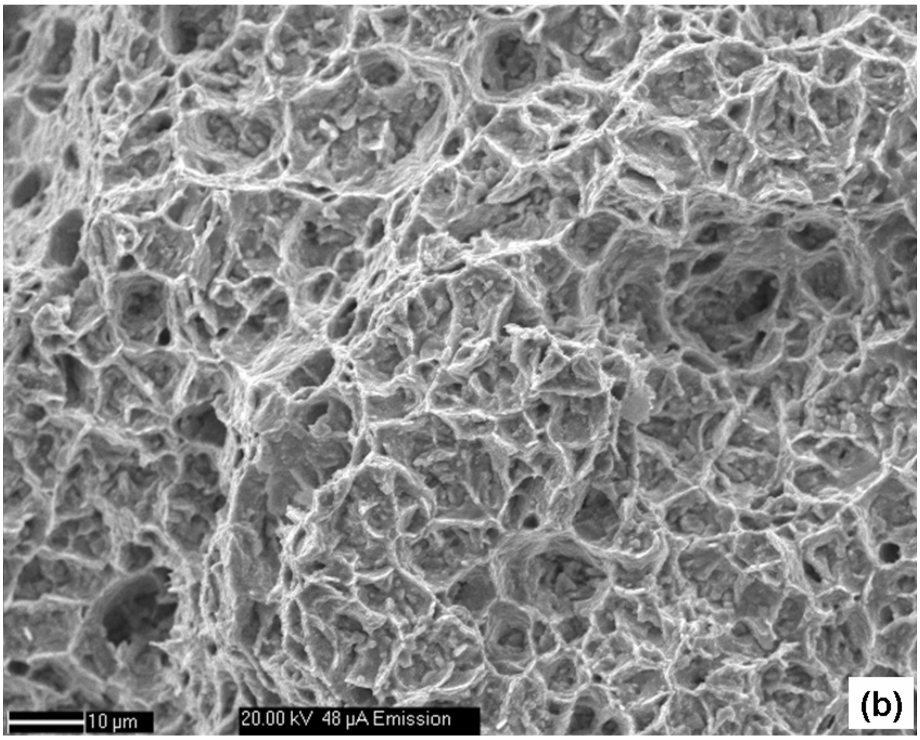

Fig. 4.7 (a) Relatively deep dimpled fracture at the central region of notch throat plane (b) relatively shallow dimpled fracture at the notch root region of notch throat plane, in notched specimen (notch root radius = 1.25 mm) at relative lower stresses (130 MPa, 873 K) in 9Cr-1Mo steel.

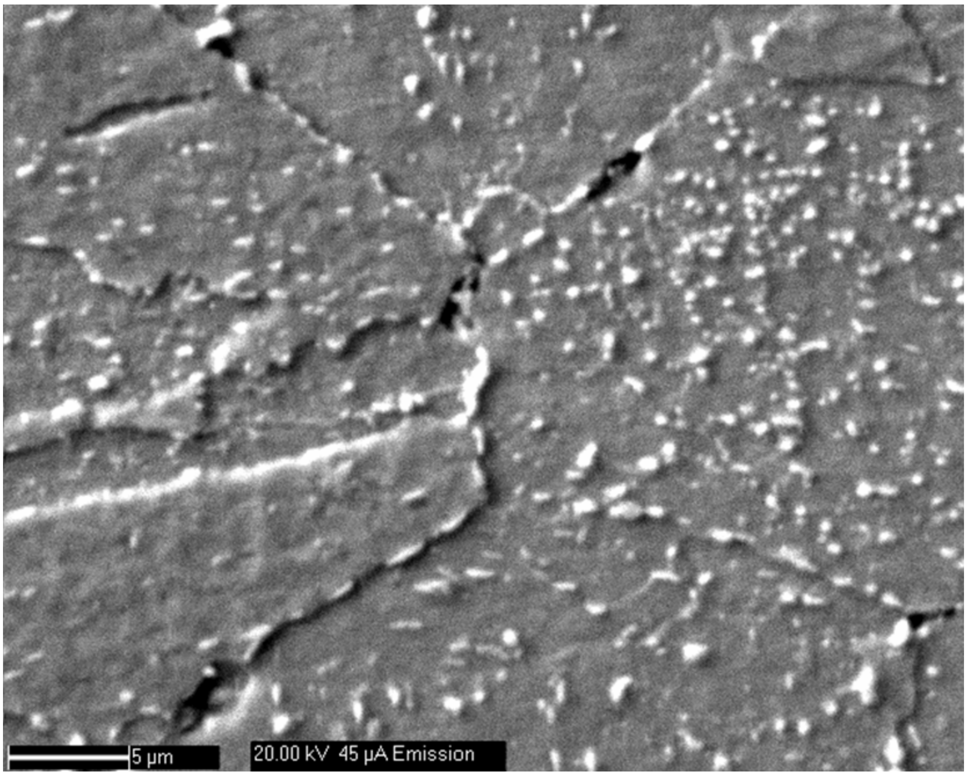

Fig. 4.8 Intergranular creep cavitation observed in notched specimen of notch root radius of 1.25 mm, 130 MPa and 873 K.

4.4.1 Distribution of axial stresses on initial loading

On initial loading under multiaxial state of stress the material will under go elastic deformation followed by plastic deformation. Von-Mises yield criterion has been used for onset of yielding in the steels during loading. Von-Mises stress under multiaxial state of stress is defined as

$$\sigma_{vm} = \sqrt{\frac{(\sigma_1 - \sigma_2)^2 + (\sigma_2 - \sigma_3)^2 + (\sigma_3 - \sigma_1)^2}{2}}$$

where σ_1, σ_2 and σ_3 are the maximum, intermediate and minimum principal stresses respectively. Variations of axial (maximum principal stress) and von-Mises stress distributions across the notch throat plane for notch root radius of 1.25 mm for the steels immediately after loading are shown in Fig. 4.9(a) and 4.9(b) respectively. The axial stress at the central region of notch throat plane was significantly lower than that of net applied stress (210 MPa), Fig. 4.9(a). The von-Mises stress, governing the yielding in material, was higher than the yield stress for 2.25Cr-1Mo (290 MPa) and 9Cr-1Mo (310 MPa) steels at the notch root, Fig. 4.9(b) resulting in localized yielding. Localized yielding at the notch root region resulted in decrease in stress at the notch root for 2.25Cr-1Mo and 9Cr-1Mo steels. However, for modified 9Cr-1Mo steel, stress concentration at the notch root was lower the yield stress (350 MPa) resulting in no reduction in the developed stresses.

4.4.2 Distribution of stresses during creep deformation

Stress redistribution across the notch during creep exposure has been reported by several investigators [44,45,48,113]. The difference in creep rates across the notch leads to stress redistribution across the notch throat plane during creep exposure. As creep deformation takes place, regions of high stress shed load to the regions of lower stresses due to the high stress sensitivity of creep deformation rate (Fig. 3.5). Under creep condition, stress redistribution across the notch was found to change with creep exposure and approached to a stationary state [45]. Pictorial views of distribution of stationary state radial (σ_{11}), axial (σ_{22}) and hoop (σ_{33}) stresses across the notch are shown in Fig.4.10; whereas variations of the stresses across the notch throat plane for different fractions of time to reach stationary state are shown in Fig. 4.11 for 2.25Cr-1Mo steel at 210 MPa. The stresses were normalized with respect to the net applied stress. The stresses across the notch especially across the notch throat plane were found to vary in a complex way. The radial stress arose from the elasto-plastic-creep deformation was found to be significantly lower than the net applied stress (Fig. 4.11(a)). The stress was higher at the central region of notch throat plane and decreased towards the notch root. The stress redistribution during creep exposure led

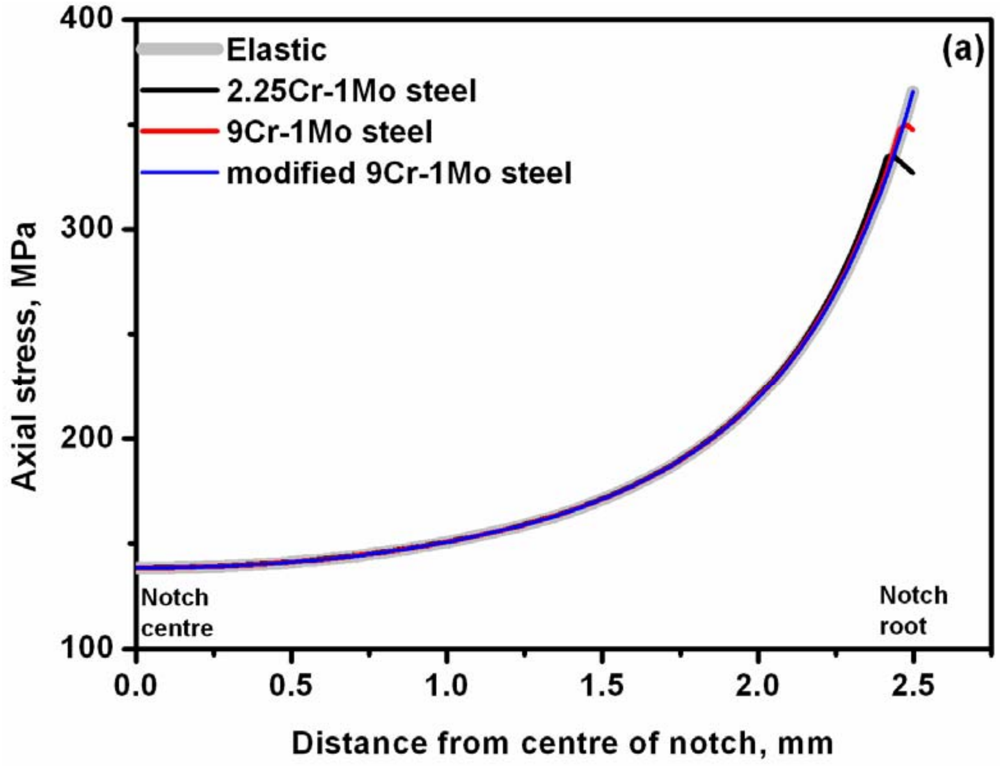

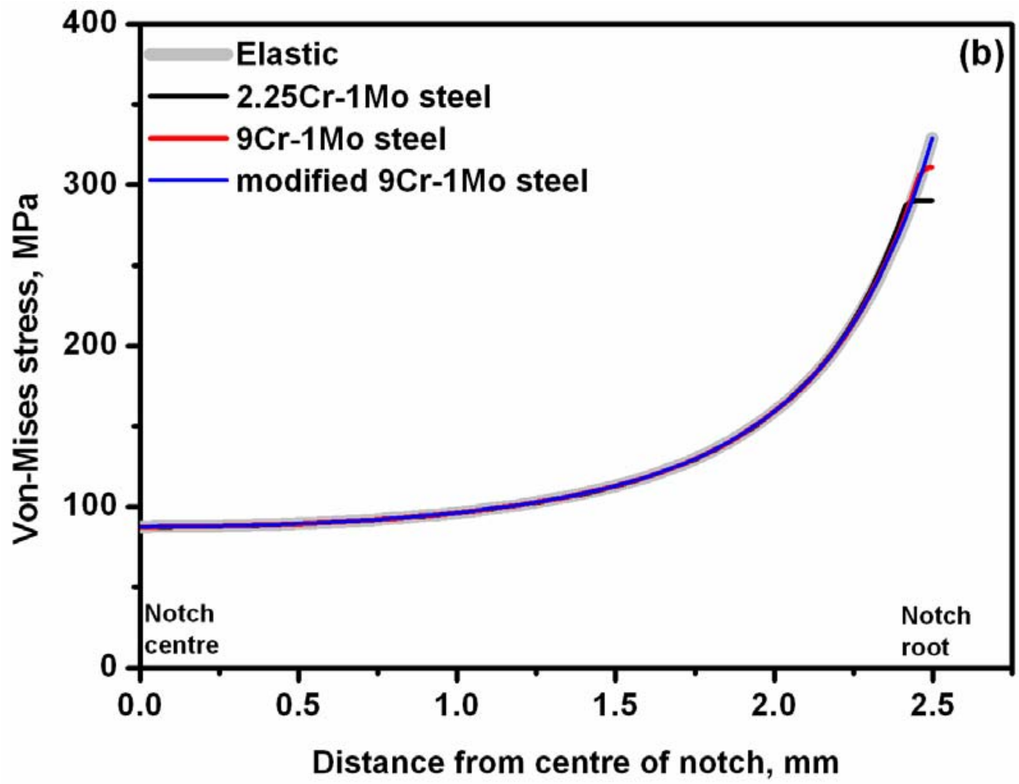

Fig. 4.9 Variations of (a) axial and (b) von-Mises stresses across the notch throat plane as a function of distance from notch centre for all the steels at 210 MPa.

to increase in the radial stress. The axial stress was found to be significantly higher at the notch root than that around the centre of notch throat plane after elasto-plastic-creep deformation (Fig. 4.11(b)). With creep exposure, the axial stress at the centre of notch throat plane increased whereas it decreased at the notch root. The stationary state distribution of axial stress showed a maximum between the centre of notch and notch root and had a value higher than the net applied stress. After elasto-plastic deformation, the hoop stress was significantly lower than the net applied stress (Fig.4.11(c)). With creep exposure, the hoop stress increased around the central region of notch and decreased at notch root. The hoop stress exhibited maxima similar to axial stress after attaining the stationary state and had a value lower than the net applied stress.

4.4.2.1 Effect of localized plastic deformation on stationary state stress distribution

The distributions of stationary state axial (maximum principal) and von-Mises stresses considering both elastic-creep and elasto-plastic creep behaviour of 2.25Cr-1Mo steel at a net applied stress of 210 MPa across the notch throat plane are shown in Fig. 4.12(a) and 4.12(b) respectively. It can be concluded that localized plastic deformation at the notch root does not play significant role in the distribution of stresses across the notch throat plane during creep exposure. Similar behaviour has been observed for 9Cr-1Mo steel and modified 9Cr-1Mo steel.

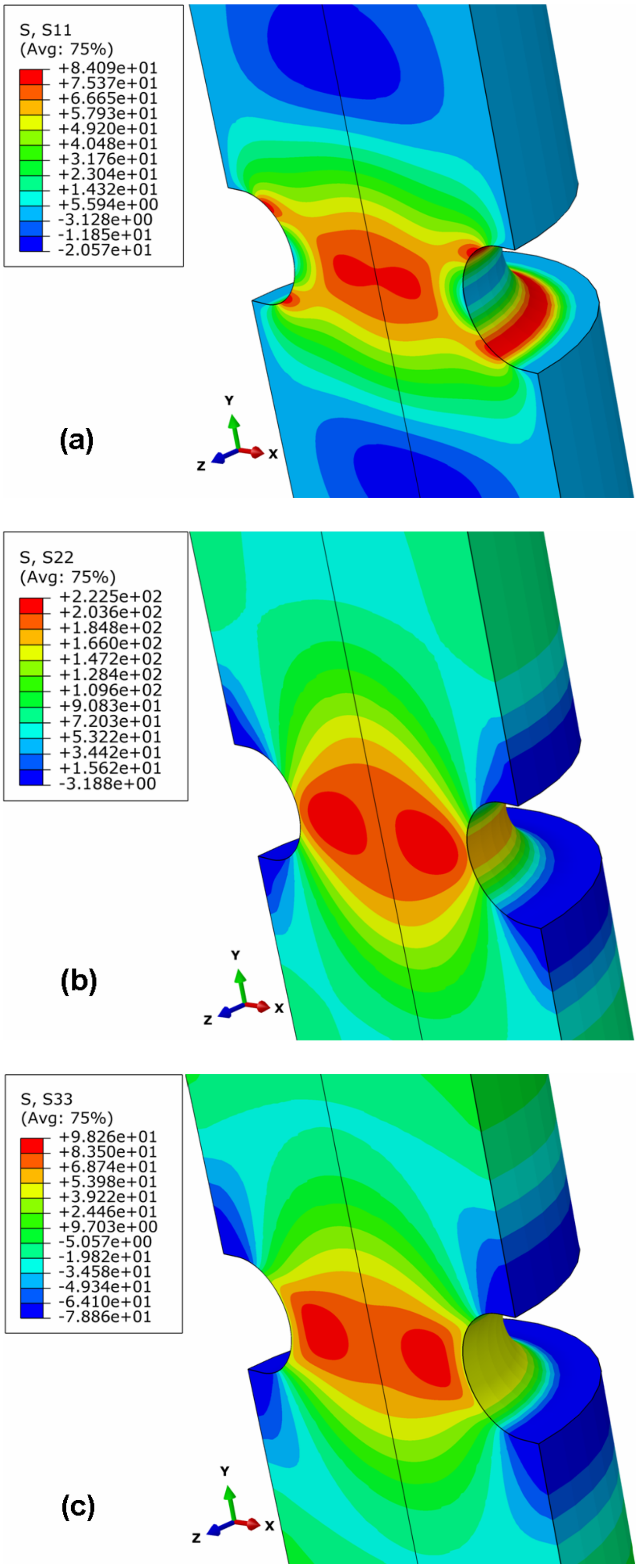

Fig. 4.10 Pictorial views of stationary state stress variation across the notch; (a) radial stress, (b) axial stress and (c) hoop stresses.

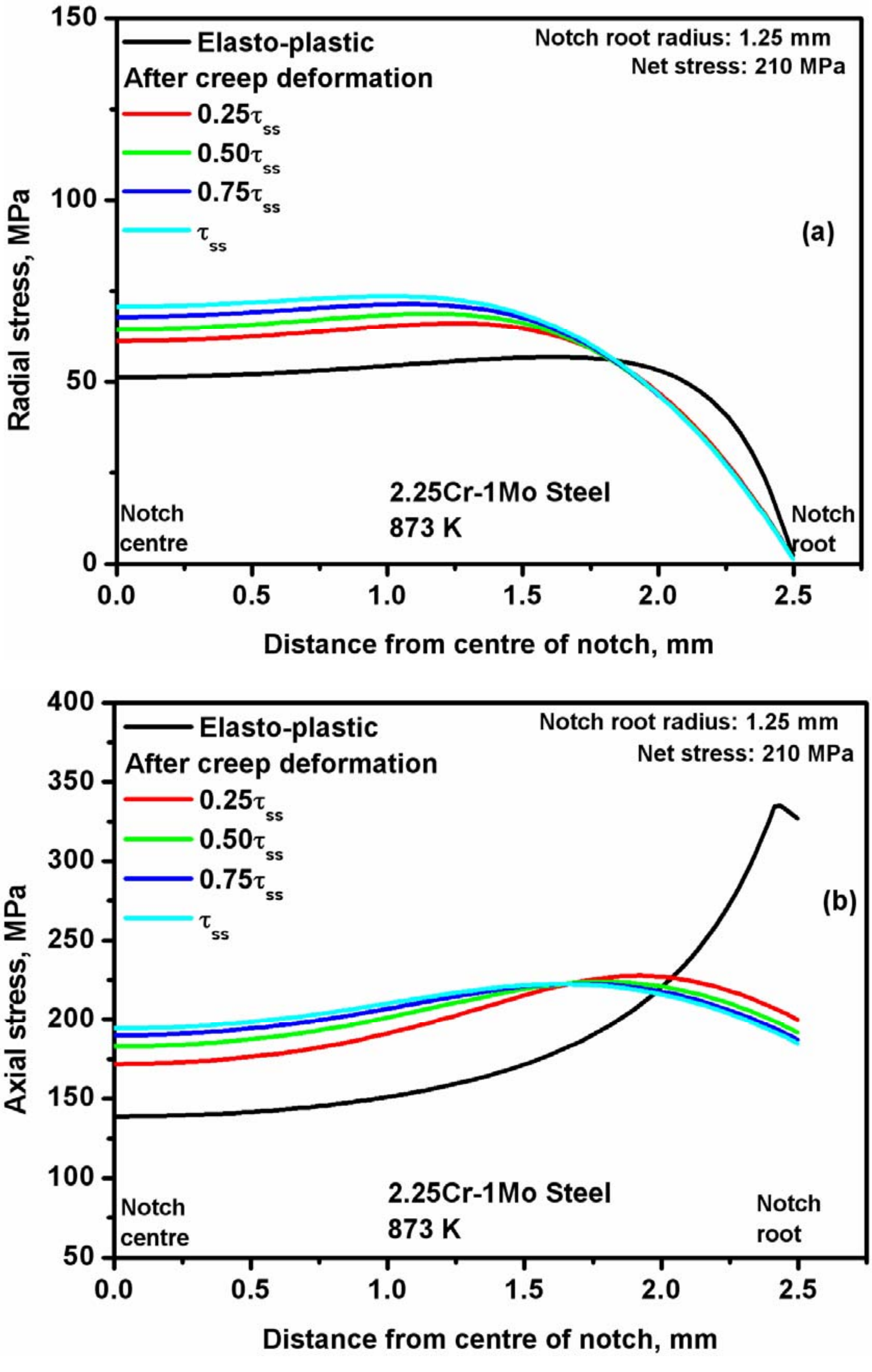

Elasto-plastic
After creep deformation
0.25τss
0.50τss
0.75τss
τss
Notch root radius: 1.25 mm
Net stress: 210 MPa
(a)
2.25Cr-1Mo Steel
873 K
Notch centre
Notch root
Radial stress, MPa
Distance from centre of notch, mm
Elasto-plastic
After creep deformation
0.25τss
0.50τss
0.75τss
τss
Notch root radius: 1.25 mm
Net stress: 210 MPa
(b)
2.25Cr-1Mo Steel
873 K
Notch centre
Notch root
Axial stress, MPa
Distance from centre of notch, mm

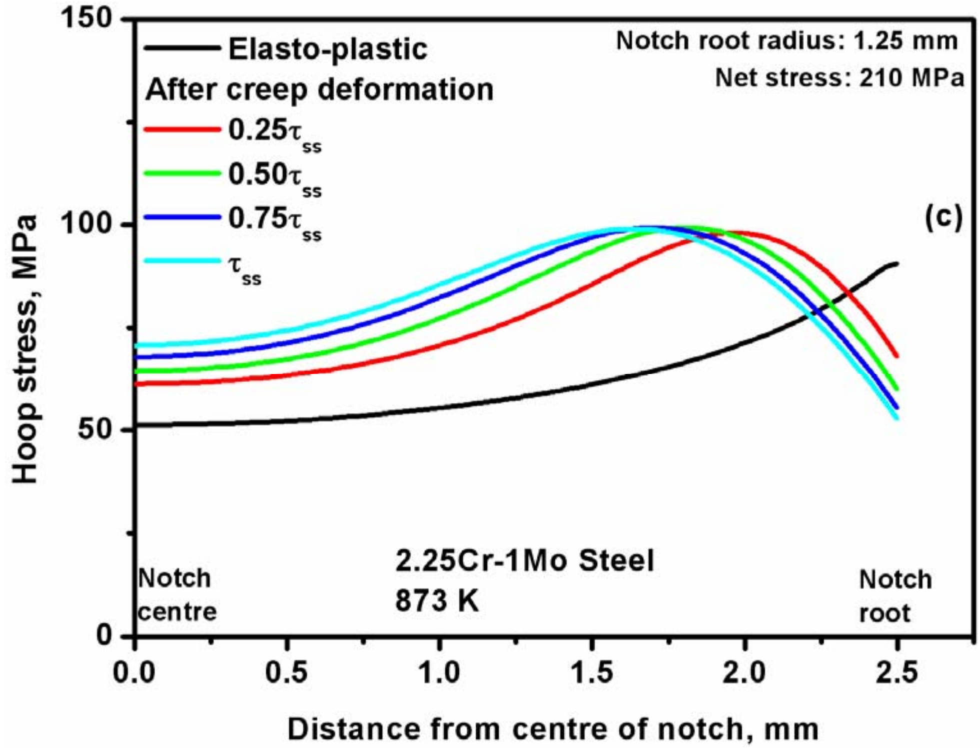

Fig. 4.11 Redistribution of normalized (a) radial, (b) axial and (c) hoop stresses across the notch throat plane as a function of creep exposure.

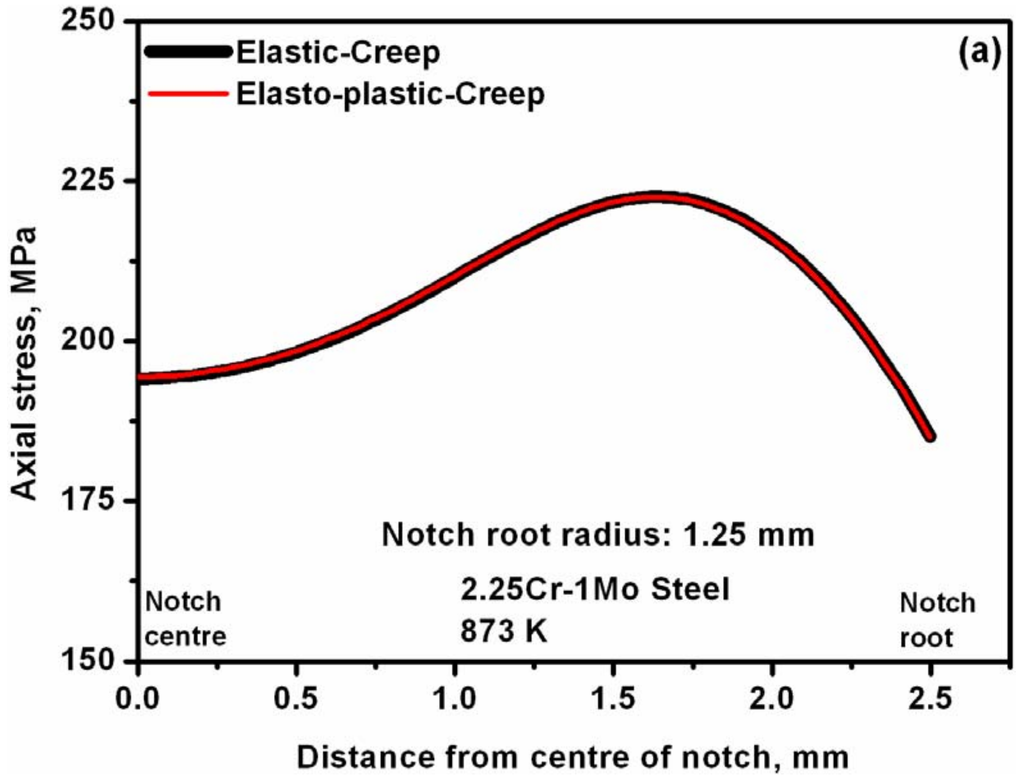

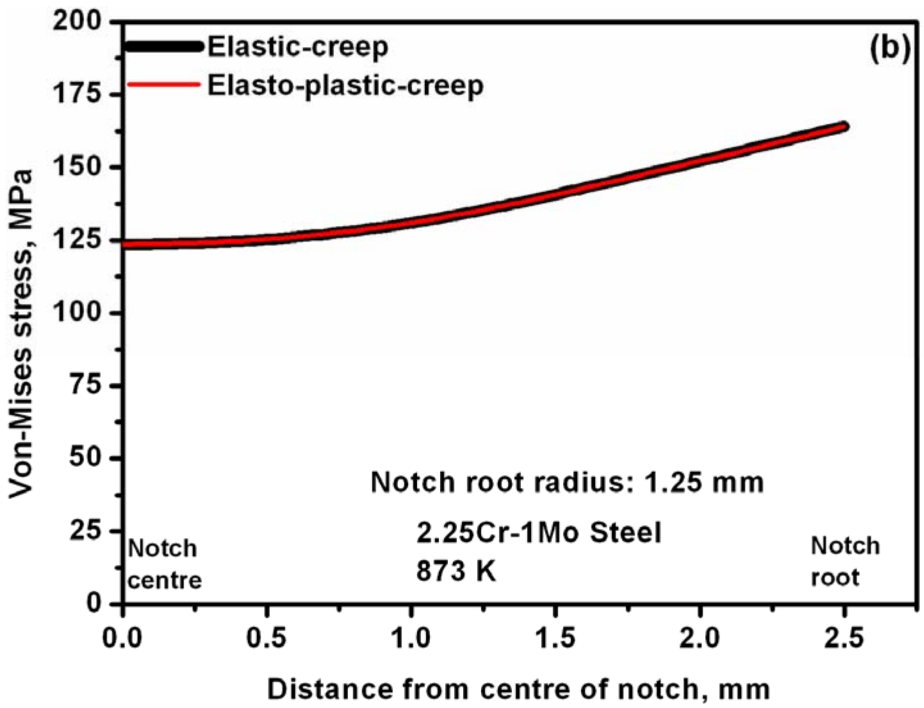

Fig. 4.12 FE analysis of stress distribution across the notch throat plane (a) axial (maximum principal) and (b) von-Mises stresses, considering elastic-creep and elasto-plastic-creep behaviour of 2.25Cr-1Mo steel, 210 MPa.

4.5 Role of different components of multiaxial state of stress on creep deformation and cavitation

Creep cavitation in materials proceeds with the nucleation of creep cavities and their growth followed by linkage into discrete cracks leading to failure. Nucleation of creep cavity in Cr-Mo ferritic steels under constrained conditions has been discussed by Cane [47], Goyal et al. [31] and Perrin et al. [114]. Nucleation of creep cavity is associated with the stress concentration around grain boundary irregularities like grain boundary triple point, ledges, particles etc., which is produced by inhomogeneous plastic deformation around them. Since the shear stress is required for the plastic deformation to occur, von-Mises stress plays a major role in creep cavity nucleation [63]. However, stability of the nucleated creep cavities is decided by

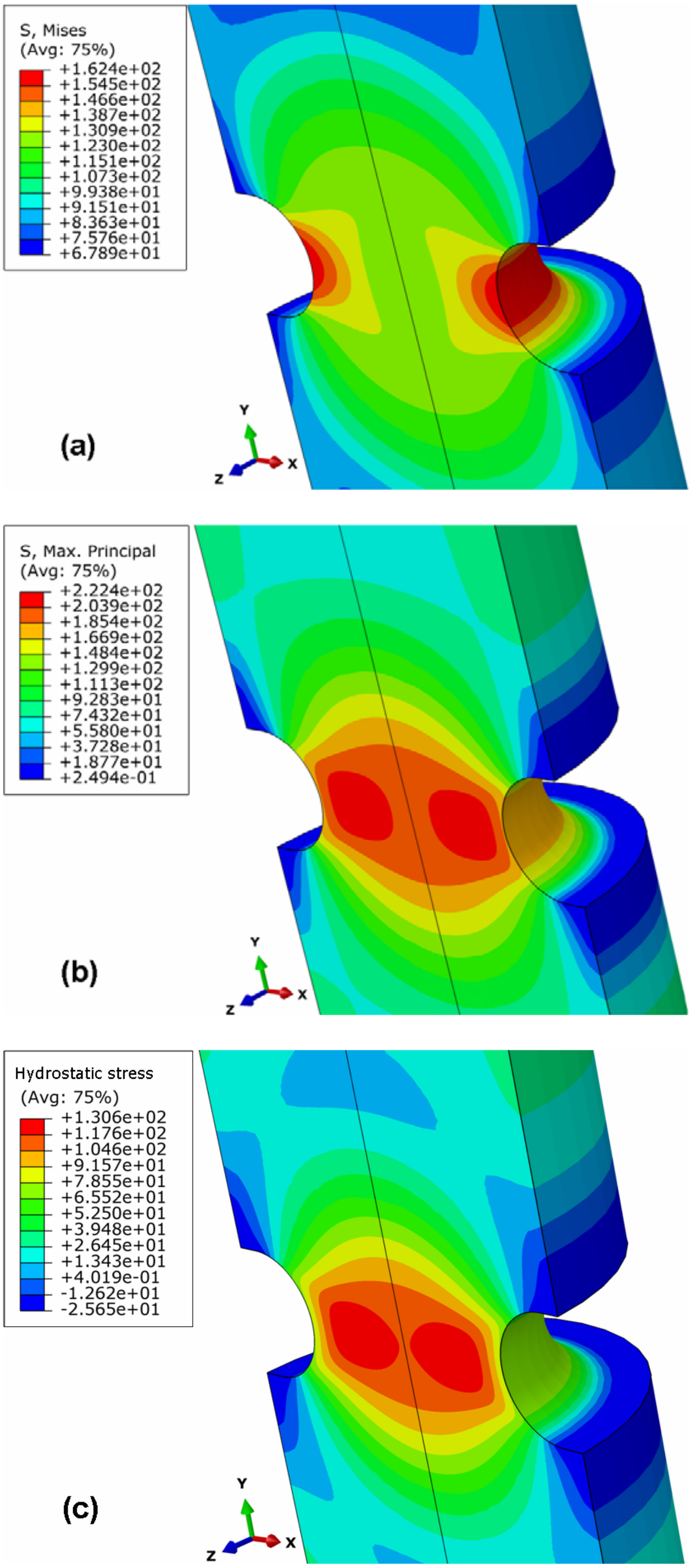

Fig. 4.13 Pictorial views showing the finite element analysis of stress distribution across the notch specimen of notch acuity ratio 1.25 for creep testing at 210 MPa and 873 K, (a) von-Mises stress, (b) maximum principal stress and (c) hydrostatic stress.

the maximum principal stress as the critical cavity size r_c, which can avoid the sintering, is governed by $r_c = 2\gamma_c / \sigma_1$, where γ_c is the surface energy and σ_1 is the maximum principal stress. For the growth of existing creep cavity, it has to attain the critical size otherwise the cavity will sinter.

The nucleated stable creep cavity can grow basically by two mechanisms: (i) plasticity controlled growth [12,13,31] and (ii) stress-directed flow of atoms (diffusive growth) [17]. Cavity can grow in presence of hydrostatic stress. Cavity growth by plasticity controlled by von-Mises stress occurs as a result of creep deformation of the matrix surrounding the grain boundary cavity in the absence of vacancy flux [4]. The von-Mises stress will assist the cavity growth by inducing plasticity whereas cavity growth by stress directed flow of atom will be controlled by maximum principal stress. The cavity growth at high temperatures can also be driven by the hydrostatic component of the stress state, as in the case of high temperature ductile fracture. The pictorial views of the stationary state von-Mises stress, maximum principal stress and hydrostatic stress distributions across the notch, as estimated by finite element analysis, are shown in Figs. 4.13(a), Fig. 4.13(b) and Fig. 4.13(c) respectively. Pictorials show complex distribution of the stress across the notch and maximum variation of the stresses occurred across the notch throat plane.

4.5.1 Notch strengthening and cavitation in 2.25Cr-1Mo steel – effect of multiaxial state of stress

Creep deformation and cavitation behaviour of 2.25Cr-1Mo steel under multiaxial state of stress has been assessed based on the distribution of the von-Mises, principal and hydrostatic stresses across the notch throat plane. Variations of the stationary state von-Mises, maximum principal and hydrostatic stresses across the notch throat plane are shown in Fig. 4.14. The von-Mises stress was found to remain below the net applied stress and increased towards notch root. Maximum principal stress was found to be lower than net applied stress at the centre and root of notch and showed a maximum value which was more than the net applied stress. The behaviour of hydrostatic stress under stationary state condition across the notch throat plane was similar to that of principal stress but the maximum value of the hydrostatic stress remained below the net stress.

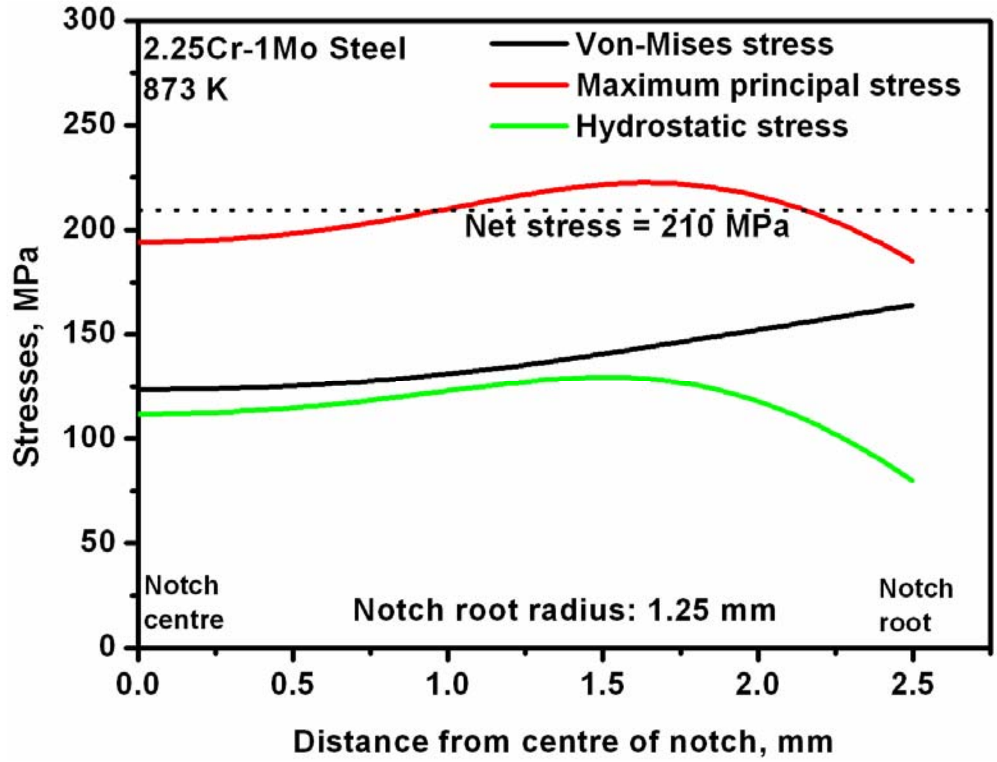

Fig. 4.14 Distribution of von-Mises, maximum principal and hydrostatic stresses across the notch throat plane after attaining the stationary state.

The decrease in von-Mises stress below the net applied stress after stress redistribution leads to the strengthening in 2.25Cr-1Mo steel in presence of notch (Fig. 4.2(a)) [49]. Variation of stresses across the notch throat plane for different net applied stresses is shown in Fig. 4.15. At all the applied stresses, the von-Mises stress decreased below the applied stress (Fig. 4.15(b)); whereas the peak values in the maximum principal stress was more than the net applied stresses. Figure 4.3 revealed that the extent of strengthening in presence of notch decreased with decrease in net applied stress and tends to saturate at relatively lower applied stresses. The decrease in stationary state von-Mises stresses compared to that in the plain specimen (net applied stress) across the notch throat plane is shown in Fig. 4.16(a) for different net applied stresses. The von-Mises stress across the notch throat plane deceased with net applied stress, indicating that the extent of strengthening in presence of notch decreases with decrease in applied stresses. The difference of maximum principal stress with respect to net applied stress across the notch throat plane at different applied stresses is shown in Fig. 4.16(b). The maximum principal stress was less than net stress at the notch central region whereas more at near the notch root region. Presence of high principal stress coupled with relatively higher von-Mises stress near to the notch root region is expected to nucleate and stabilized intergranular creep cavity. However, under higher net applied stresses resulting in relative less creep rupture life, nucleated creep cavity would have little time to grow by diffusive transfer of atoms from cavity surface to grain boundary for inducing creep cavitation. Thus predominantly ductile dimple failure in notch specimens was observed at higher applied stresses (Fig. 4.6 and Fig. 4.7). At lower applied stresses causing relatively longer creep rupture life, evidences of intergranular creep cavitation was observed near to the notch root region (Fig. 4.8).

4.6 Material dependency of notch strengthening

The presence of notch was found to increase the creep rupture life of the steels (Fig. 4.2). The extent of strengthening was comparable for 2.25Cr-1Mo and 9Cr-1Mo steels. However, modified 9Cr-1Mo steel exhibited more extensive strengthening than that of the other two steels (Fig. 4.3).

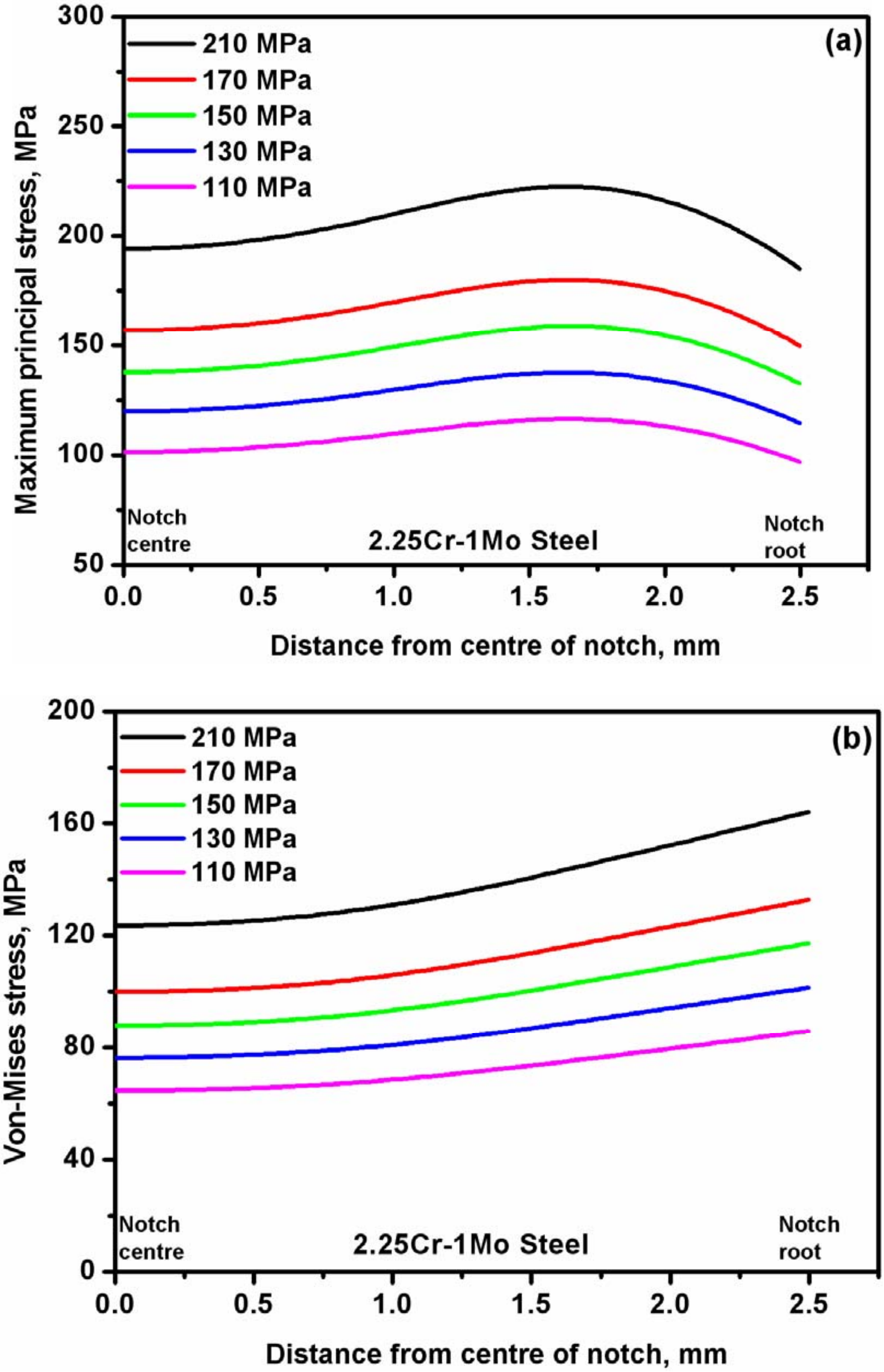

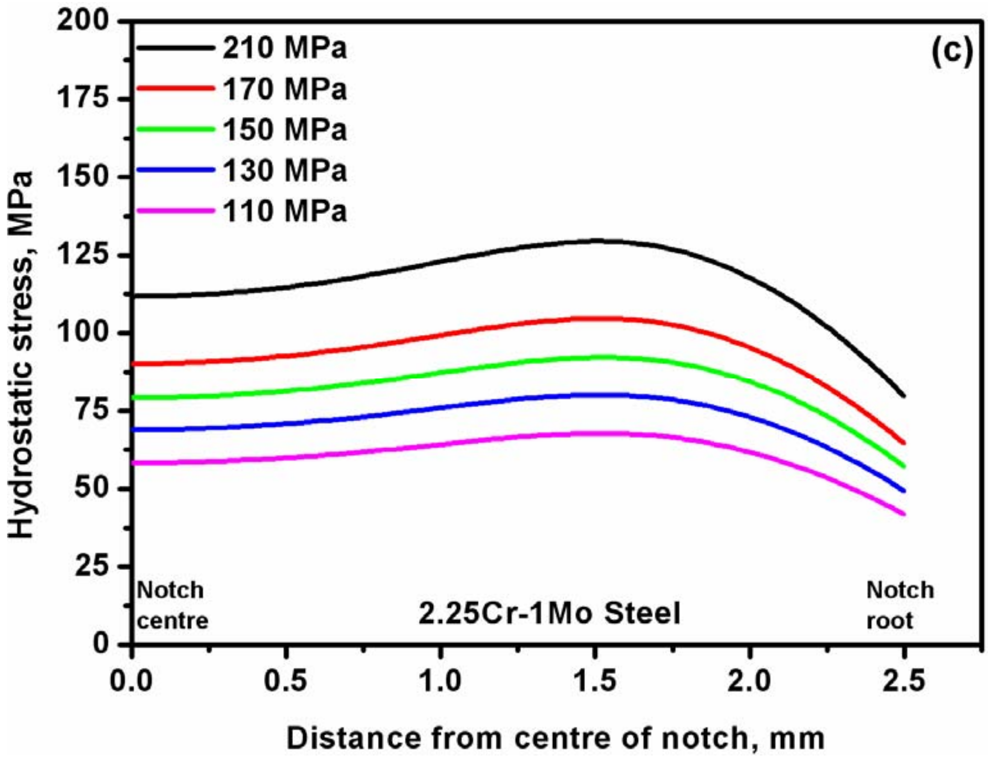

Fig. 4.15 Variations of difference in (a) maximum principal (b) von-Mises and (c) hydrostatic stresses across the notch throat plane for different net applied stresses.

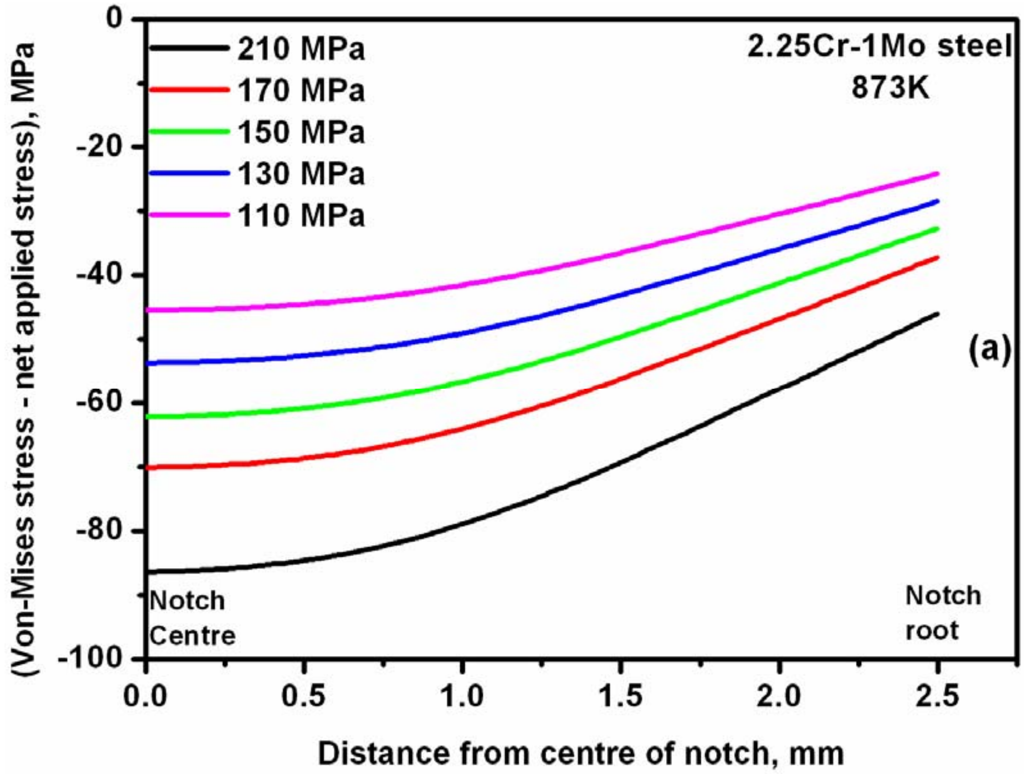

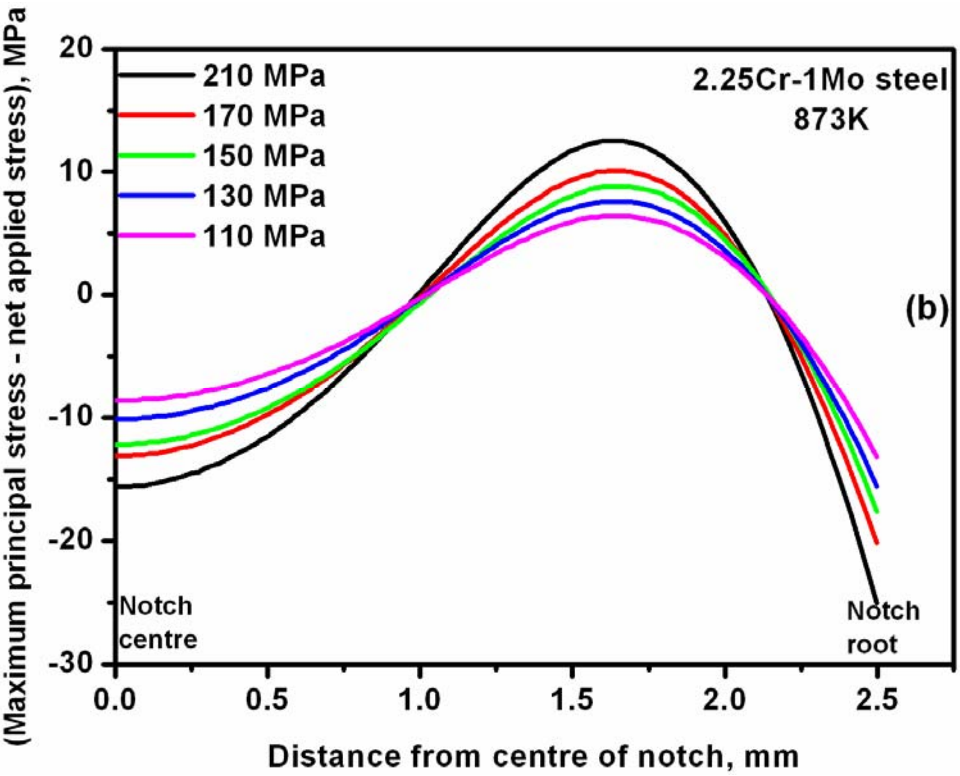

Fig. 4.16 Variation of difference in (a) von-Mises and (b) maximum principal stresses with respect to net applied stress across the notch throat plane for different net applied stresses.

To assess the different extent of notch strengthening in different steels, FE analysis of stress distribution across the notch throat plane was carried out on incorporating the tensile and creep deformation properties of the individual steels. Tensile flow and creep deformation characteristics of the steels are discussed in Sections 3.2 and 3.3 respectively. The relaxation of maximum principal and von-Mises stresses at the notch root for different steels are shown in Fig. 4.17. The time for relaxation has been normalized with the time to reach stationary state for the steels. The stresses relaxed with creep exposure at different rates and to a different extents depending upon the materials. The relaxation was relatively faster for modified 9Cr-1Mo steel and slowest for 2.25Cr-1Mo steel, because of higher stress sensitivity of creep deformation in modified 9Cr-1Mo steel (n = 12.92) than that in 2.25Cr-1Mo (n = 6.02) and 9Cr-1Mo steels (n = 8.34) (section 3.3). This is reflected in the difference in the steady state variation of maximum principal, von-Mises and hydrostatic stress variations across the notch throat plane. The variations of maximum principal, von-Mises and hydrostatic stresses normalized with respect to yield stress of individual steel are shown in Fig. 4.18.

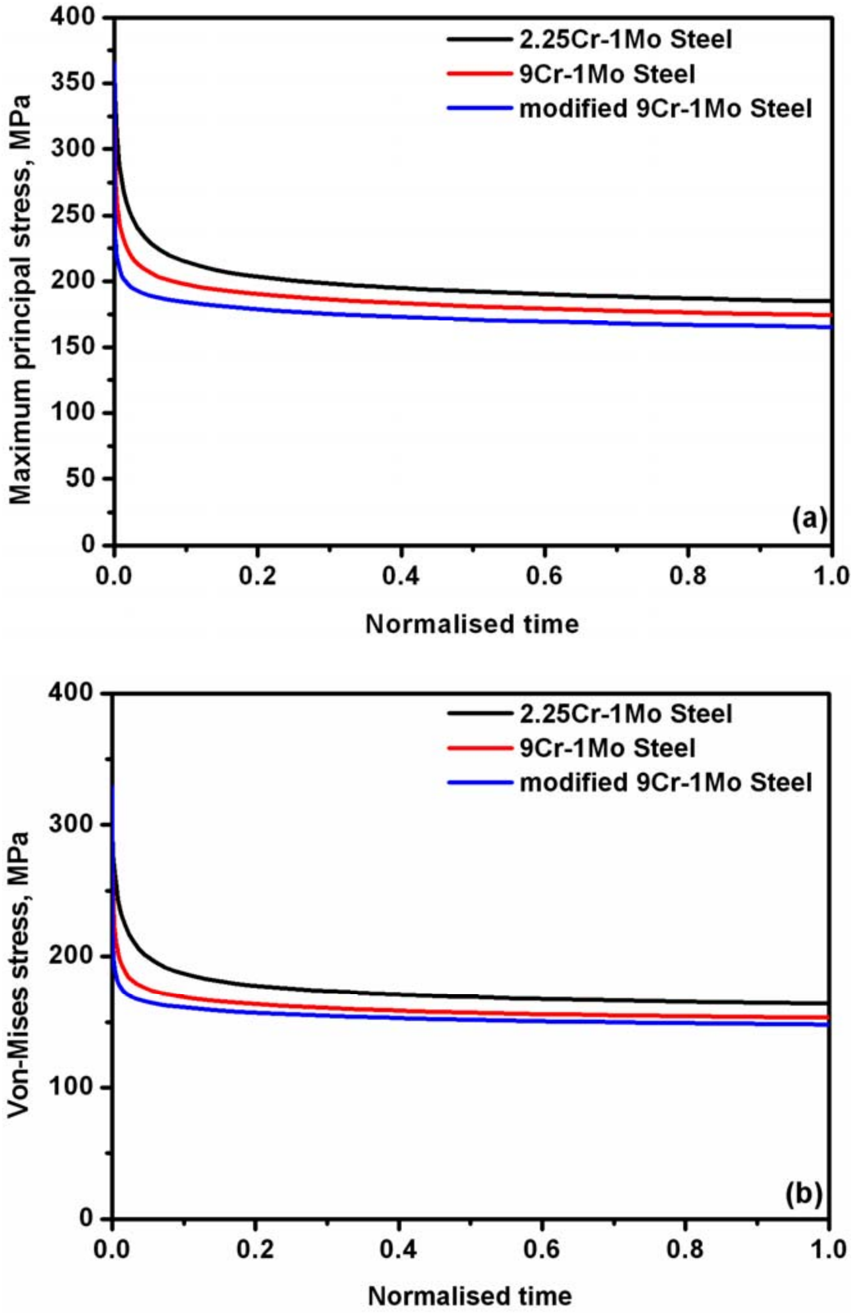

Fig. 4.17 Relaxation of (a) maximum principal and (b) von-Mises stresses at the notch root as a function of creep exposure for different steels at 210 MPa.

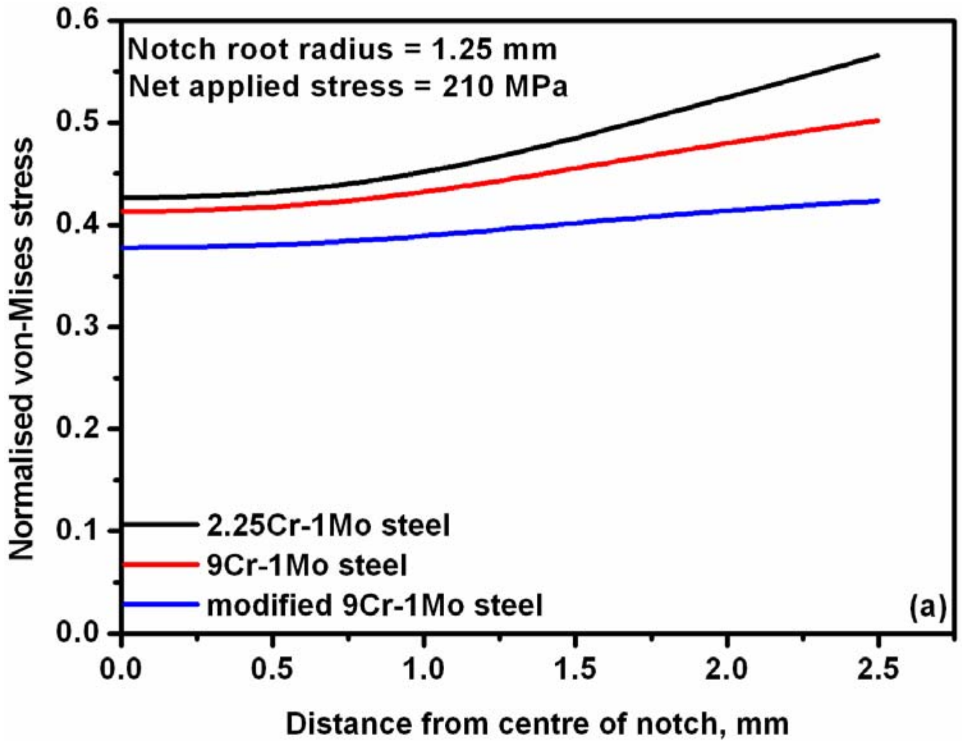
Notch root radius = 1.25 mm
Net applied stress = 210 MPa
Normalised von-Mises stress
2.25Cr-1Mo steel
9Cr-1Mo steel
modified 9Cr-1Mo steel
(a)
Distance from centre of notch, mm
0.0
0.5
1.0
1.5
2.0
2.5
0.1
0.2
0.3
0.4
0.5
0.6

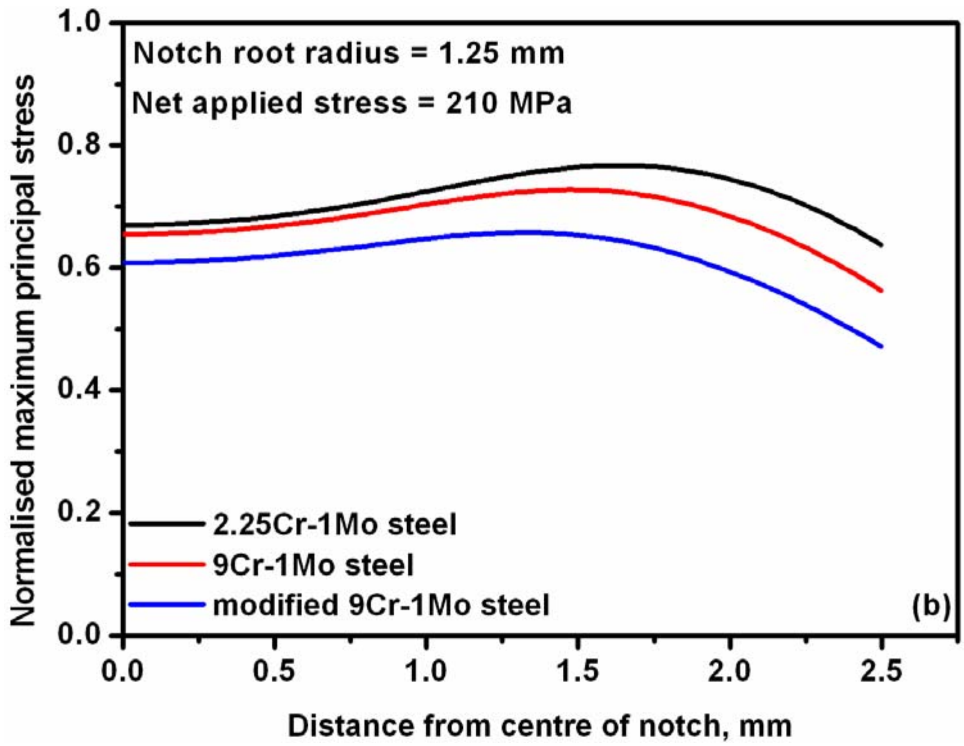
Notch root radius = 1.25 mm
Net applied stress = 210 MPa
Normalised maximum principal stress
2.25Cr-1Mo steel
9Cr-1Mo steel
modified 9Cr-1Mo steel
(b)
Distance from centre of notch, mm
0.0
0.5
1.0
1.5
2.0
2.5
0.2
0.4
0.6
0.8
1.0

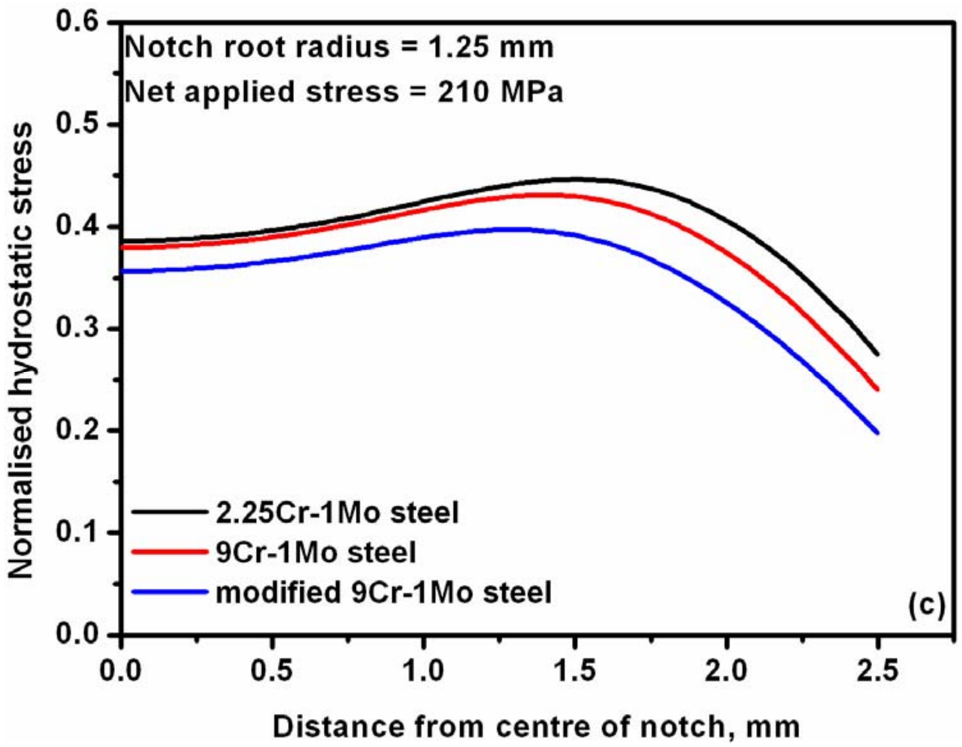

Fig. 4.18 Distribution of normalized (a) von-Mises, (b) maximum principal and (c) hydrostatic stresses across the notch throat plane after attaining the stationary state in 2.25Cr-1Mo, 9Cr-1Mo and modified 9Cr-1Mo steels.

The normalized stresses were found to be in the increasing order of modified 9Cr-1Mo, 9Cr-1Mo and 2.25Cr-1Mo steel. Higher stresses across the notch throat plane in 2.25Cr-1Mo steel results from the lack of stress relaxation (Fig. 4.17) than in other two steels. This implies that at a given net applied stress 2.25Cr-1Mo steel would spend most of its life time in higher stress than in modified 9Cr-1Mo steel, resulting in lower notch strengthening (Fig. 4.3).

4.7 Conclusions

Following conclusions have been drawn based on the studies on the effect of multiaxial state of stress introduced by notch of root radius 1.25 mm on creep rupture strength of 2.25Cr-1Mo, 9Cr-1Mo and modified 9Cr-1Mo steels, creep tested at 873

K over a stress range 110 - 230 MPa and distribution of stresses across the notch based on finite element analysis:

1. Multiaxial state of stress introduced incorporating notch in uniaxial specimen led to increase in creep rupture life of the steels. The increase in creep rupture life decreased with decrease in applied stress and tends to saturate at lower applied stress.
2. The increase in creep rupture strength under multiaxial state of stress was comparable for 2.25Cr-1Mo and 9Cr-1Mo steels whereas significantly more for modified 9Cr-1Mo steel.
3. Creep ductility of the steels decreased under multiaxial state of stress, which became more significant at lower applied stress. The reduction in creep rupture strength was more for 2.25Cr-1Mo steel and less for modified 9Cr-1Mo steel.
4. Under the investigated multiaxial state of stress, the steels failed predominantly in ductile mode with some evidences of intergranular creep failure especially on long-term creep exposure. The 2.25Cr-1Mo steel was more prone to intergranular creep cavitation than both the 9Cr-steels.
5. Finite element distribution of stress across the notch revealed that stress distribution across the notch altered with creep exposure and attained a stationary state.
6. The von-Mises stress across the notch throat plain was less than the net applied stress and progressively increased from notch centre to notch root. The maximum principal stress showed a maximum value between notch centre and root and the maximum value was more than net applied stress.

7. The reduction in von-Mises stress across the notch throat plane under multiaxial state of stress increased the creep rupture life of the steels. Higher reduction led to more creep rupture strength in modified 9Cr-1Mo steel than that in other two steels. The lower extent of von-Mises stress reduction with decrease in applied stress led to tendency of saturation at lower stress.
8. Presence of relatively higher maximum principal stress close to the notch root region was found to promote intergranular creep cavitation at notch root region. Relatively higher maximum principal stress in 2.25Cr-1Mo than that in the 9Cr-steels revealed higher susceptibility to intergranular creep cavitation in 2.25Cr-1Mo steel than in 9Cr-1Mo and modified 9Cr-1Mo steels.

CHAPTER 5

EFFECT OF NOTCH SHARPNESS ON CREEP RUPTURE BEHAVIOUR

Effect of notch sharpness on creep rupture behaviour

5.1 Introduction

Creep rupture life of the steels was found to increase in presence of notch, indicating notch strengthening behaviour as discussed in Section 4.2. The effects of different multiaxial state of stresses on creep rupture behaviour of 2.25Cr-1Mo, 9Cr-1Mo and modified 9Cr-1Mo ferritic steels have been discussed in this chapter. The different multiaxial state of stresses across the notch throat plane were generated by varying the notch root radius (notch sharpness) from 5 mm to 0.25 mm, resulting in notch acuity ratio (ratio of notch throat diameter to notch root radius) in the range 1 - 20. Creep tests were carried out on the notched specimens of all the steels at net applied stresses in the range 110 - 230 MPa at 873 K. FE analysis of stress distribution across the notch throat plane was carried out to understand the effect of different multiaxial state stresses on the creep strengthening and fracture behaviour of the steels.

5.2 Effect of notch sharpness on creep rupture life

Multiaxial state of stress was found to influence the creep rupture life of the steels appreciably. Table 5.1 summarizes the creep properties of notched specimens of the steels having different notch acuity ratios. The rupture lives of the steels for all the notch acuity ratios were higher than plain specimen indicating notch strengthening, Fig. 5.1. The rupture life of notched specimen increased with decrease in net applied stress for a given notch acuity ratio and obeyed a power law relation ($t_r = M'\sigma^{m'}$) as in case of plain specimens, where M' and m' are the stress coefficient and the stress exponent respectively. Table 5.2 shows the values of the constants of the steels in presence of notch. Stress sensitivity of rupture life of the steels decreased with increase in notch sharpness and tends to saturate. The decrease was more for modified 9Cr-1Mo and least for 2.25Cr-1Mo steel, Fig. 5.2. The rupture life increased with notch sharpness (notch acuity ratio) for all the steels as shown in Fig. 5.3. The strengthening was found to saturate with increase in notch acuity ratio in all the steels (Fig. 5.3). The extent of strengthening with notch acuity ratio was found to depend on the material. It was in the increasing order of 2.25Cr-1Mo, 9C-1Mo and modified 9Cr-1Mo steel, Fig. 5.4. With increase in notch acuity ratio, the strengthening increased more rapidly in modified 9Cr-1Mo steel that that in 2.25Cr-1Mo and 9Cr-1Mo steels. The increase in strengthening with notch acuity ratio was comparable for 2.25Cr-1Mo and 9Cr-1Mo steels. The effect of notch acuity ratio on creep rupture life has been investigated by Al-Faddagh et al. [39] on 2.25Cr-1Mo steel. The material exhibited strengthening and was found to saturate for higher notch acuity ratios as observed in the present investigation. Studies carried out by Al-Abed et al. [62] on 2.25Cr-1Mo steel showed notch strengthening in the steel.

The variations of creep rupture ductility (% reduction in area or % RA) of the notched specimens as a function of notch acuity ratio for the steels are shown in Fig. 5.5. Creep rupture ductility of the steels decreased significantly with increase in notch acuity ratio and tends to saturate at higher notch acuity ratio. Effect of notch acuity ratio on creep rupture ductility at a net applied stress of 210 MPa is shown in Fig. 5.6 for the steels. The 9Cr-1Mo steel exhibited relatively more ductility than 2.25Cr-1Mo steel whereas the modified 9Cr-1Mo the least for a given notch acuity ratio. The increase in notch sharpness decreased the rupture ductility to a greater extent in modified 9Cr-1Mo steel and less extent in 9Cr-1Mo steel.

Table 5.1(a) Creep rupture properties of 2.25Cr-1Mo steel

Notch acuity ratio	**Net applied stress, MPa**	**Rupture life, h**	**Creep ductility, %RA**
0 (Plain specimen)	210	4.8	94.5
	170	26.2	93.5
	150	55.3	89.8
	130	152.1	90.8
	110	353.5	89.7
	90	1619.2	72.1
1	210	22.8	83.2
	170	92.3	79.0
	150	206.2	76.0
	130	467.3	64.0
	110	946.5	60.0
2	210	42.8	79.7
	170	150.4	70.2
	150	342.9	63.9
	130	616.4	57.5
	110	1716.8	47.0
4	210	83.2	65.5
	170	282.4	50.3
	150	803.5	40.2
	130	1460.4	33.1
	110	2324.1	20.0
6	210	88.1	56.7

	170	343.5	41.3
	150	743.1	32.0
	130	972.2	24.3
	110	3108.9	13.1
10	210	156.3	46.2
	170	534.1	36.0
	150	969.1	25.0
	130	1719.4	20.0
	110	3070.2	10.1
20	210	161.5	39.7
	170	548.7	25.1
	150	914.4	18.0
	130	1890.1	12.2
	110	3421.2	2.7

Table 5.1(b) Creep rupture properties of 9Cr-1Mo steel

Notch acuity ratio	Net applied stress, MPa	Rupture life, h	Creep ductility, %RA
0 (Plain specimen)	210	3.2	92.5
	170	17.6	92.1
	150	60.8	91.2
	130	129.6	90.1
	110	730.2	86.4
1	210	19.3	87.0
	170	84.2	78.0

	150	167.1	67.6
	130	799.2	52.7
	110	2396.8	41.9
2	210	23.3	82.0
	170	127.2	70.0
	150	547.5	55.1
	130	1643.5	42.2
	110	2008.4	32.6
4	210	66.9	75.8
	170	385.8	59.3
	150	947.6	45.5
	130	2007.4	32.2
	110	3695.8	20.4
6	210	80.1	68.2
	170	639.5	42.1
	150	1107.6	30.3
	130	2069.9	17.1
	110	3895.5	11.1
10	210	89.6	61.3
	170	586.3	30.0
	150	1489.7	13.6
	130	2014.4	12.6
	110	3501.5	7.9
20	210	169.8	50.1
	170	696.2	16.3

	150	1183.6	10.6
	130	1752.3	6.4
	110	3318.7	2.8

Table 5.1(c) Creep rupture properties of modified 9Cr-1Mo steel

Notch acuity ratio	**Net applied stress, MPa**	**Rupture life, h**	**Creep ductility, %RA**
0 (Plain specimen)	230	4.6	89.3
	210	14.9	88.9
	190	35.6	88.2
	170	363.8	87.1
	150	744.9	84.3
1	230	53.4	81.9
	210	105.2	81.4
	190	1533.8	74.1
	170	1892.5	68.2
	150	7871.1	62.0
2	230	95.7	78.8
	210	922.3	64.4
	190	1186.4	55.1
	170	3472.2	48.0
	150	15925	41.1
4	230	1161.3	52.6
	210	1821.4	41.9
	190	3790.1	36.8

	170	8555.3	33.5
6	230	2376.0	30.3
	210	2334.7	21.0
	190	5302.4	18.1
10	230	2082.8	14.0
	210	5640.4	10.2
20	230	3006.5	8.0
	210	4186.5	5.1

Table 5.2 Comparison of coefficients of rupture life versus net applied stress plots for the steels at different notch acuity ratios

Notch acuity ratio	**2.25Cr-1Mo steel**		**9Cr-1Mo steel**		**Modified 9Cr-1Mo steel**	
	M′	**m′**	**M′**	**m′**	**M′**	**m′**
1	8.62×10^{14}	5.82	7.44×10^{18}	7.59	1.14×10^{30}	11.98
2	5.73×10^{14}	5.64	3.29×10^{18}	7.34	4.41×10^{27}	10.77
4	2.19×10^{14}	5.32	2.69×10^{16}	6.24	7.20×10^{18}	6.69
6	1.75×10^{14}	5.27	4.10×10^{15}	5.83	2.49×10^{13}	4.27
10	8.27×10^{12}	4.59	1.15×10^{15}	5.57	1.51×10^{29}	10.95
20	1.73×10^{13}	4.73	4.79×10^{12}	4.46	1.18×10^{12}	3.64

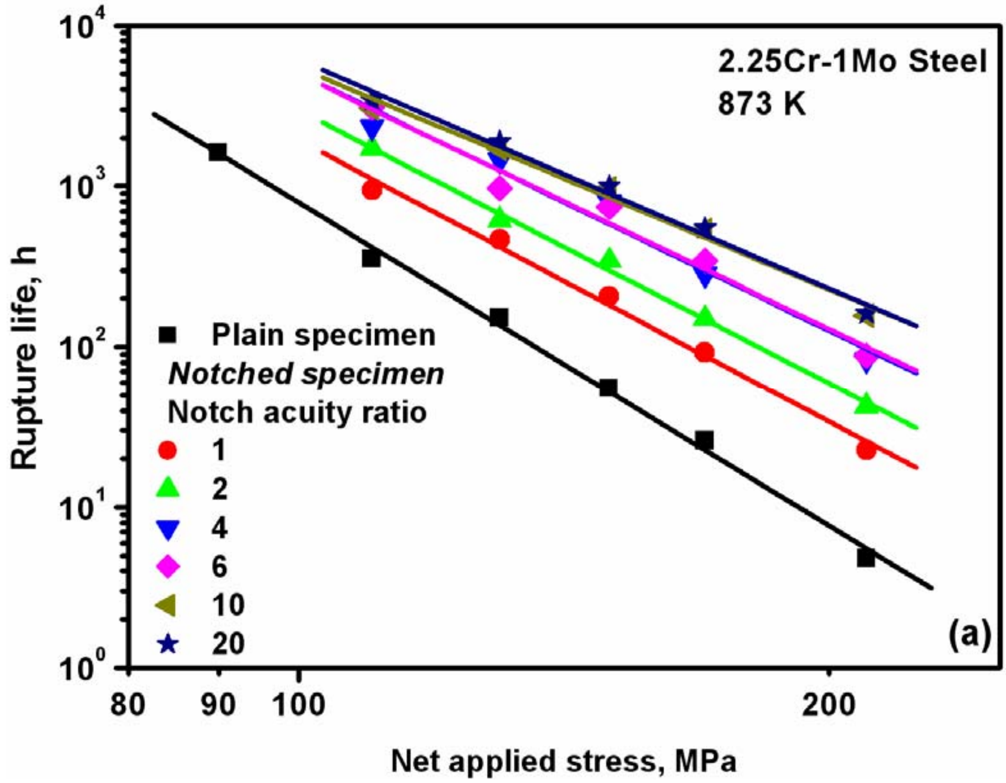
2.25Cr-1Mo Steel
873 K
Rupture life, h
Plain specimen
Notched specimen
Notch acuity ratio
1
2
4
6
10
20
(a)
Net applied stress, MPa

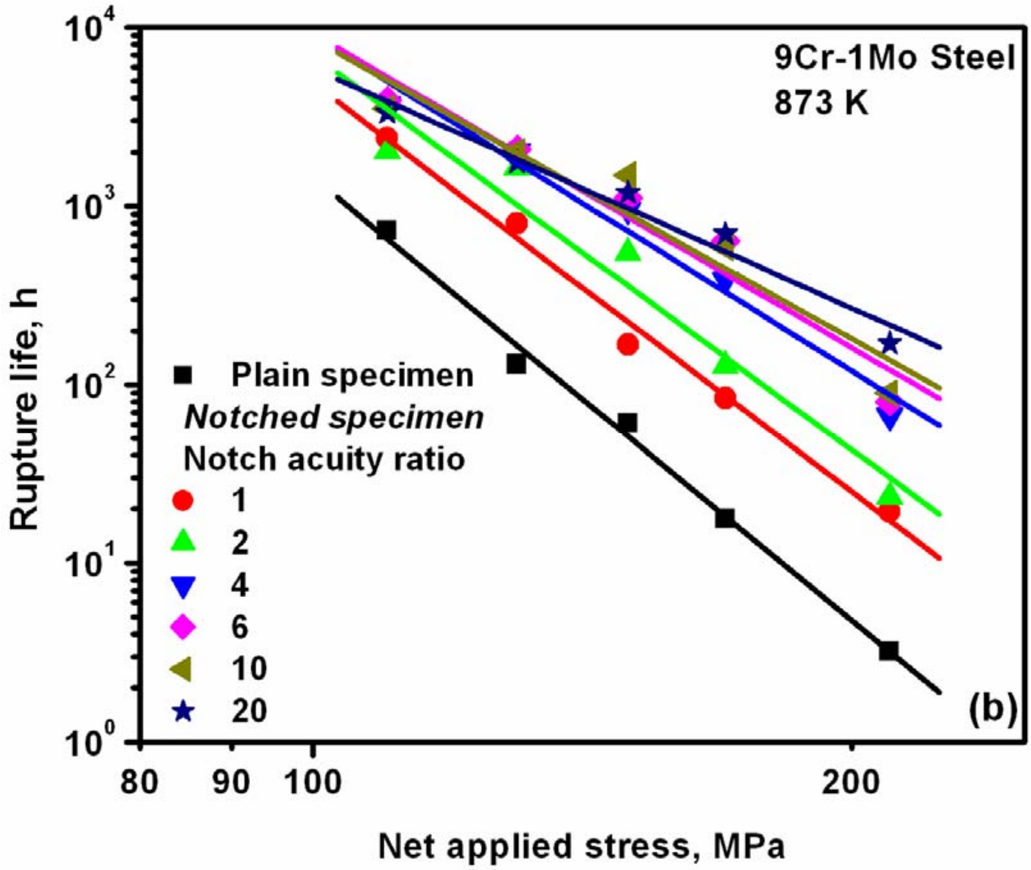
9Cr-1Mo Steel
873 K
Rupture life, h
Plain specimen
Notched specimen
Notch acuity ratio
1
2
4
6
10
20
(b)
Net applied stress, MPa

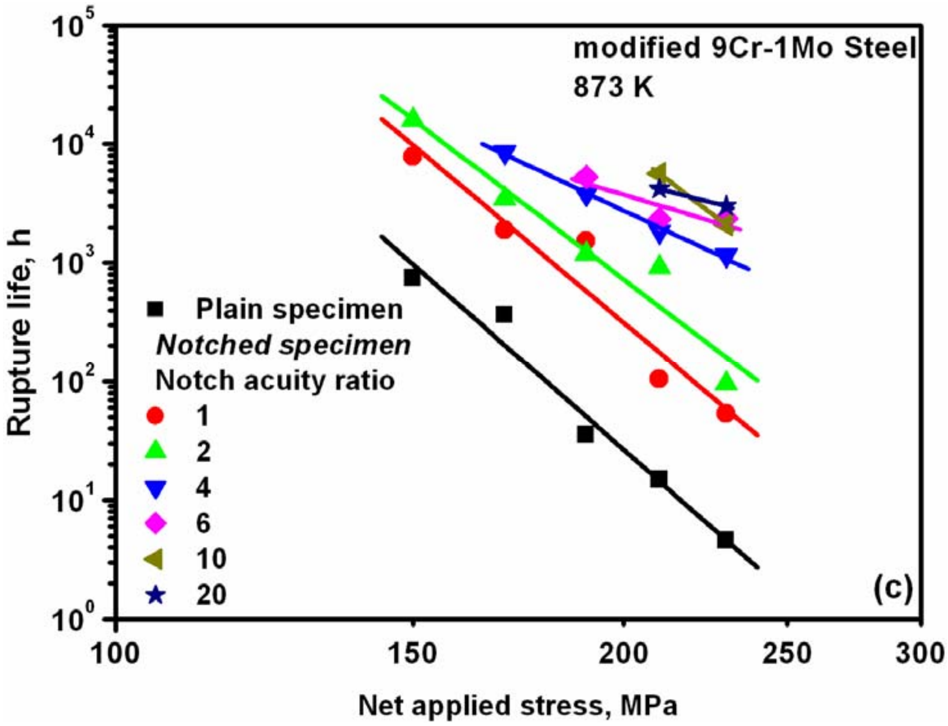

Fig. 5.1 Variation of rupture life in presence of notch of different notch acuity ratios as a function of net applied stress for (a) 2.25Cr-1Mo, (b) 9Cr-1Mo and (c) modified 9Cr-1Mo steels.

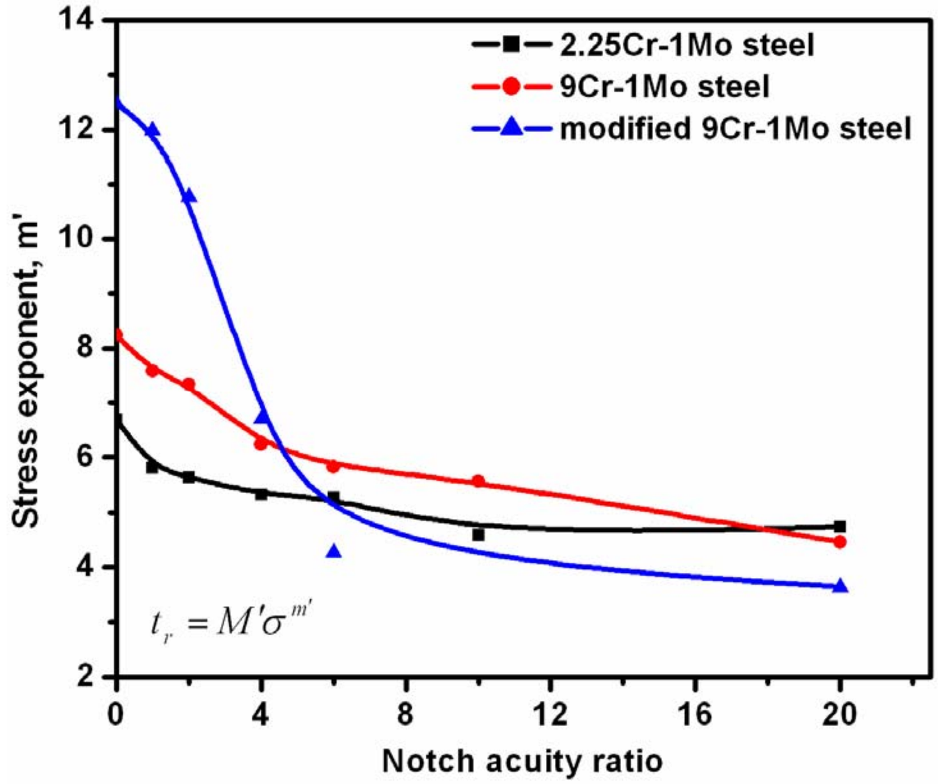

Fig. 5.2 Variation of stress exponent (m′) as a function of notch acuity ratio for the steels.

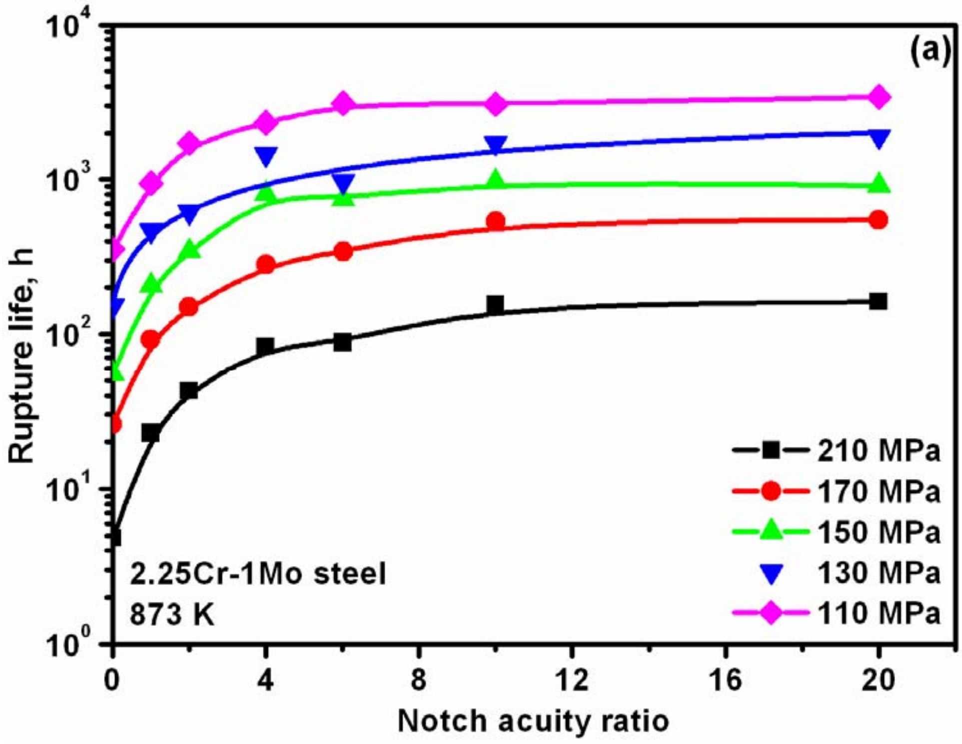
(a)
Rupture life, h
Notch acuity ratio
210 MPa
170 MPa
150 MPa
130 MPa
110 MPa
2.25Cr-1Mo steel
873 K

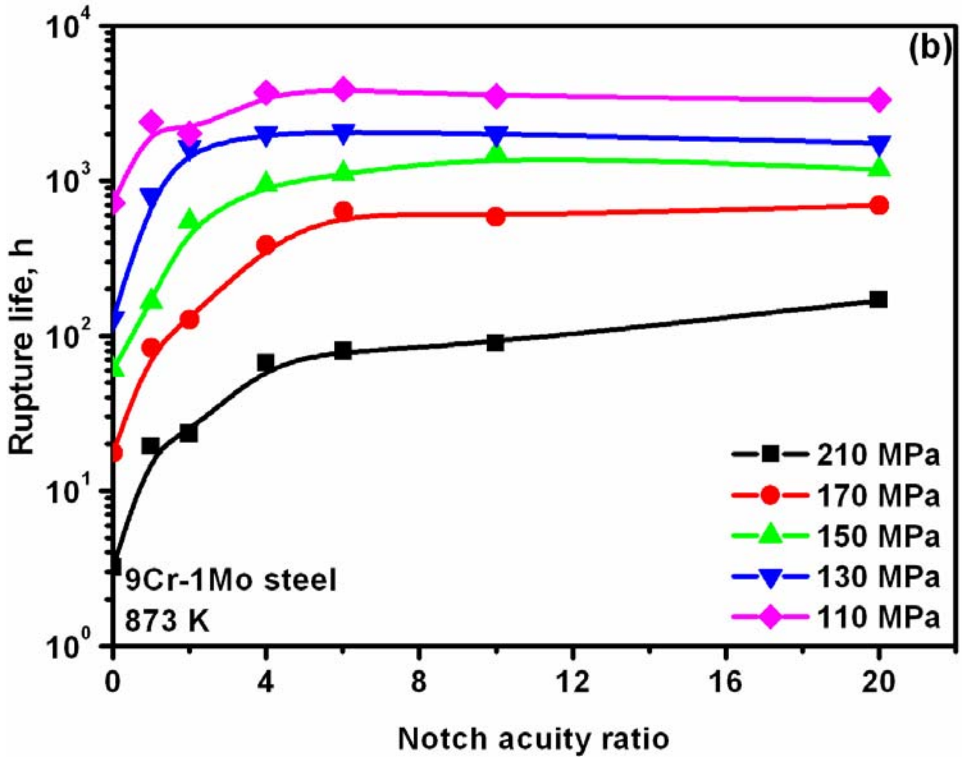
(b)
Rupture life, h
Notch acuity ratio
210 MPa
170 MPa
150 MPa
130 MPa
110 MPa
9Cr-1Mo steel
873 K

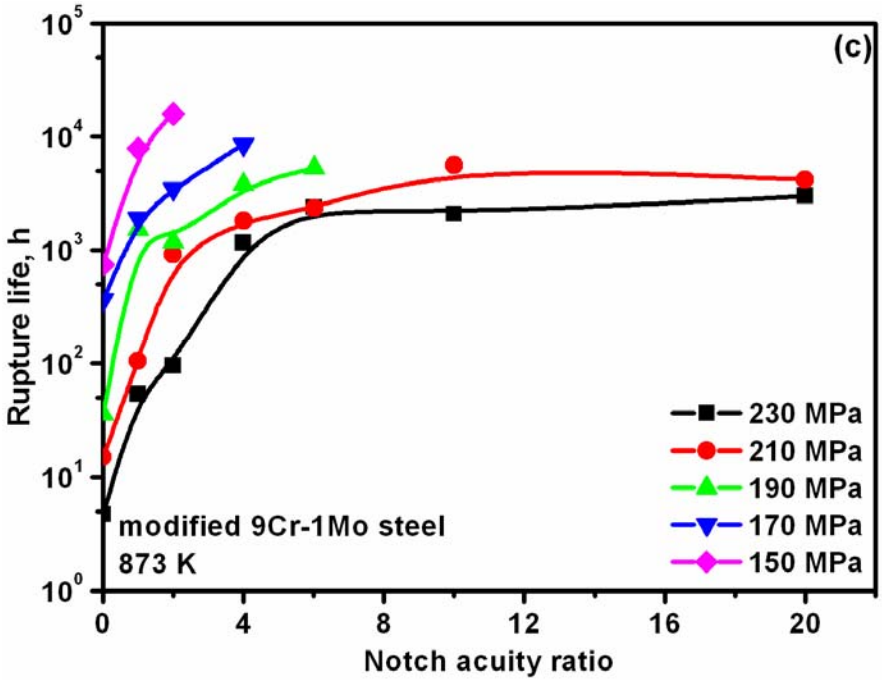

Fig. 5.3 Variation of rupture life as a function of notch acuity ratio at 873 K for (a) 2.25Cr-1Mo, (b) 9Cr-1Mo and (c) modified 9Cr-1Mo steel.

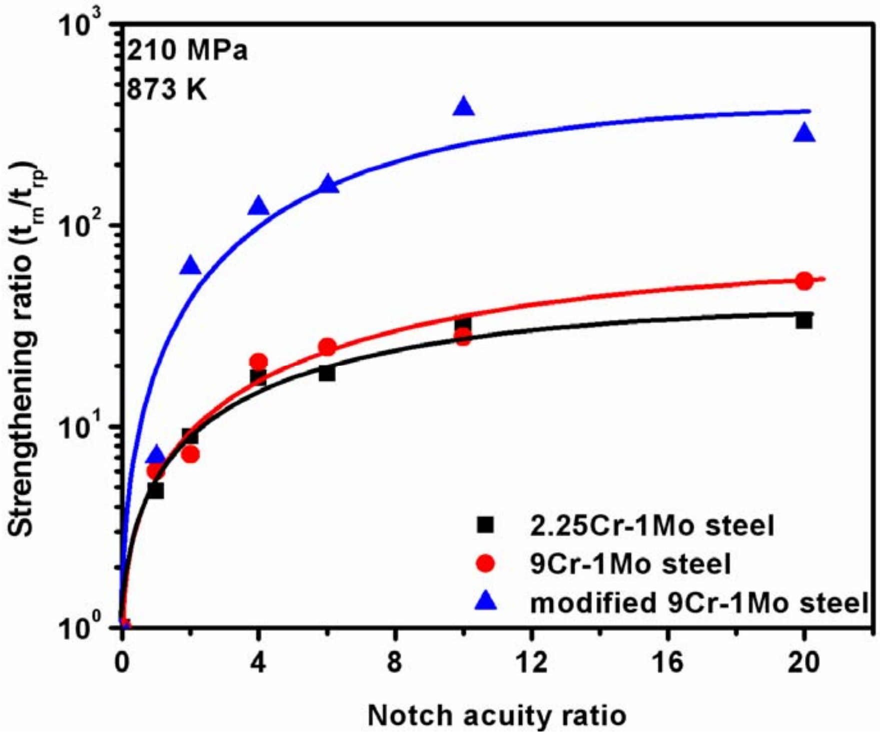

Fig. 5.4 Comparison of strengthening in different steels as a function of notch acuity ratio at 210 MPa and 873 K.

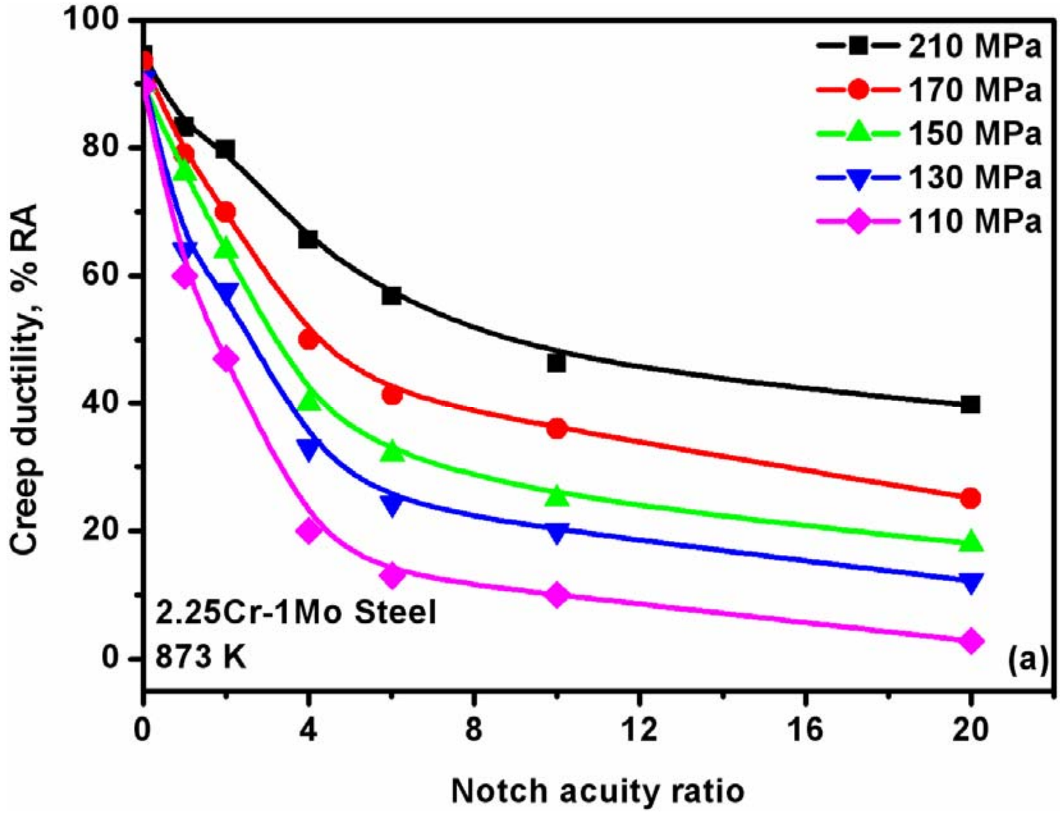

Creep ductility, % RA
Notch acuity ratio
210 MPa
170 MPa
150 MPa
130 MPa
110 MPa
2.25Cr-1Mo Steel
873 K
(a)

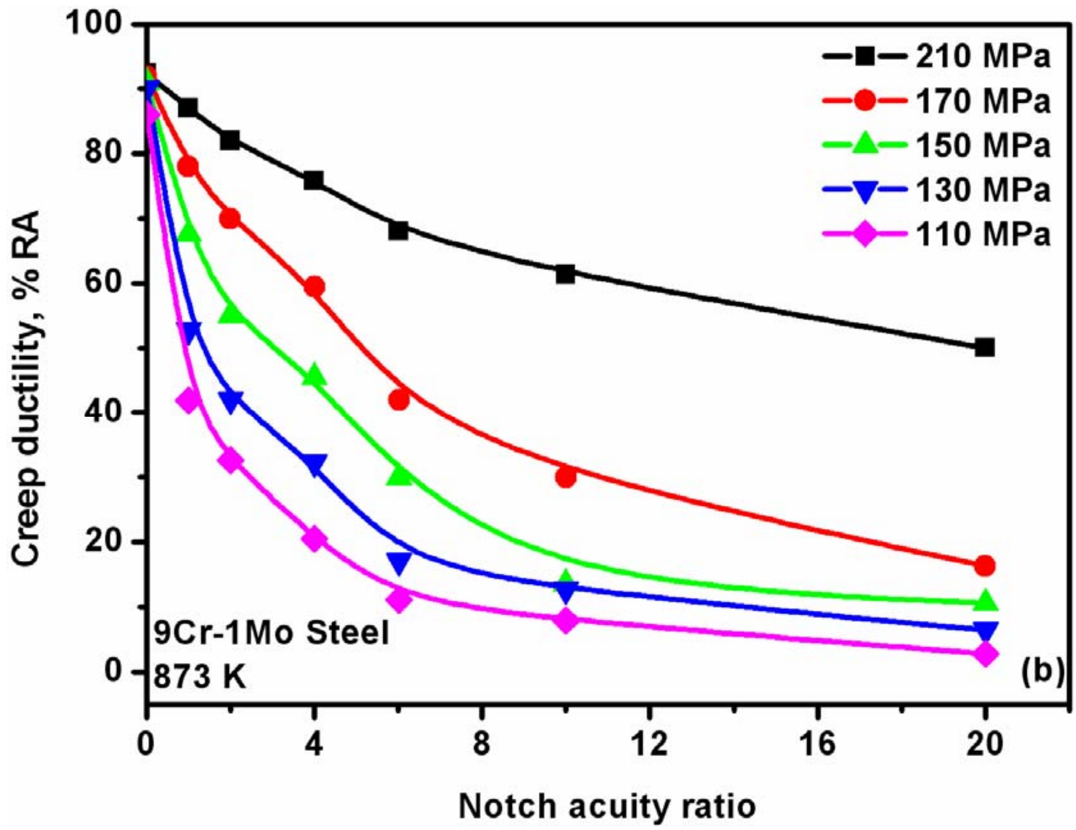

Creep ductility, % RA
Notch acuity ratio
210 MPa
170 MPa
150 MPa
130 MPa
110 MPa
9Cr-1Mo Steel
873 K
(b)

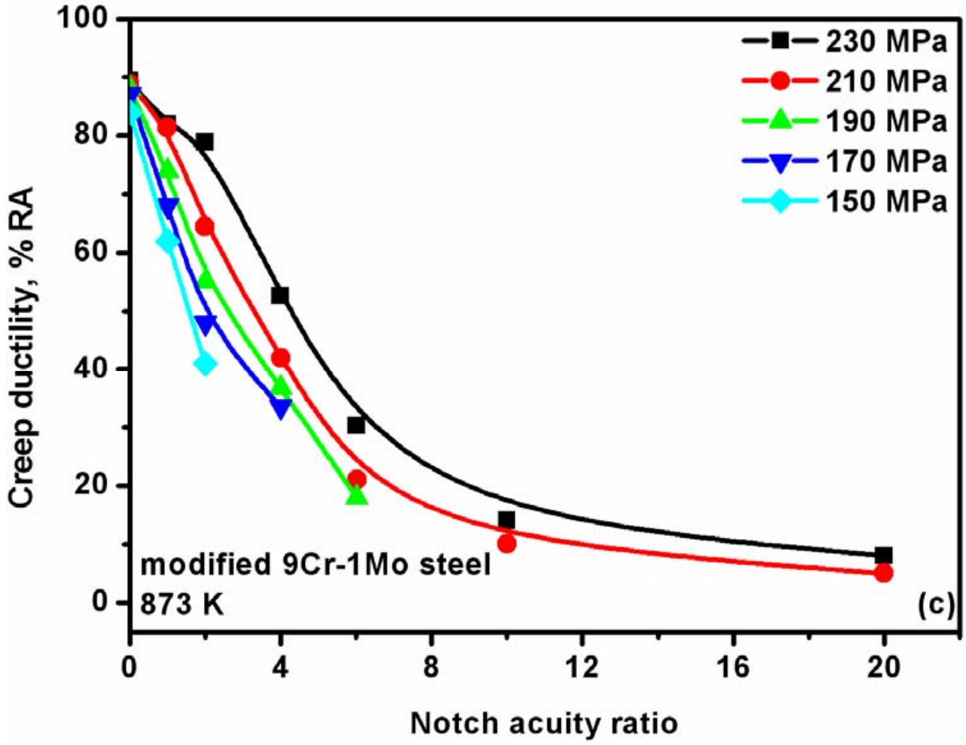

Fig. 5.5 Variation of creep ductility (in % reduction in area) as a function of notch acuity ratio for (a) 2.25Cr-1Mo, (b) 9Cr-1Mo and (c) modified 9Cr-1Mo steel.

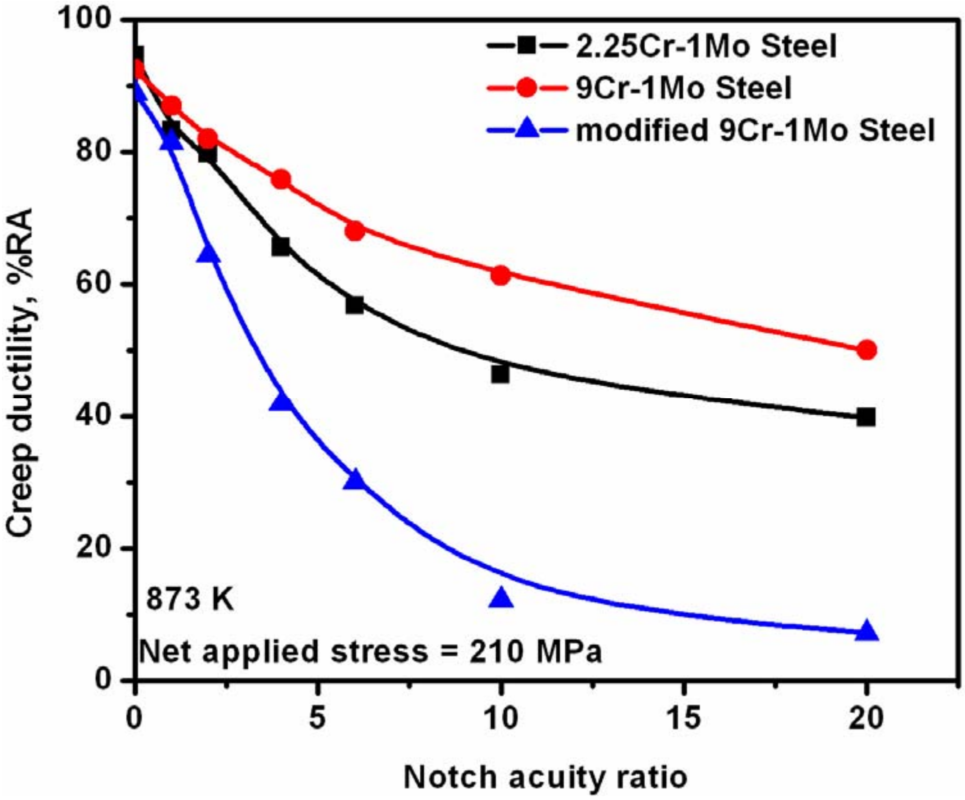

Fig. 5.6 Variation of creep ductility as a function of notch acuity ratio for the steels at 210 MPa and 873 K.

5.3 Effect of notch sharpness on fracture appearance

Detailed fractographic studies have been carried out on creep tested notched specimens of all the steels. SEM investigations of the fracture surfaces of the creep ruptured notched specimens of all the steels showed significant variation in the appearance depending on the notch acuity ratio and net applied stress. Low magnification image of fractured surface of creep ruptured notched specimen having notch acuity ratio of 1 (notch root radius = 5 mm) is shown in Figs. 5.7 for 2.25Cr-1Mo steel creep tested at 150 MPa and 873 K. Shear-lip type of failure of the notched specimen was observed for notches of relatively lower notch acuity ratio < 4, as in plain specimen. Shear-lip, characteristic of cup and cone type of failure, was caused by final mechanical instability around the notch root as can be seen from Fig. 5.7.

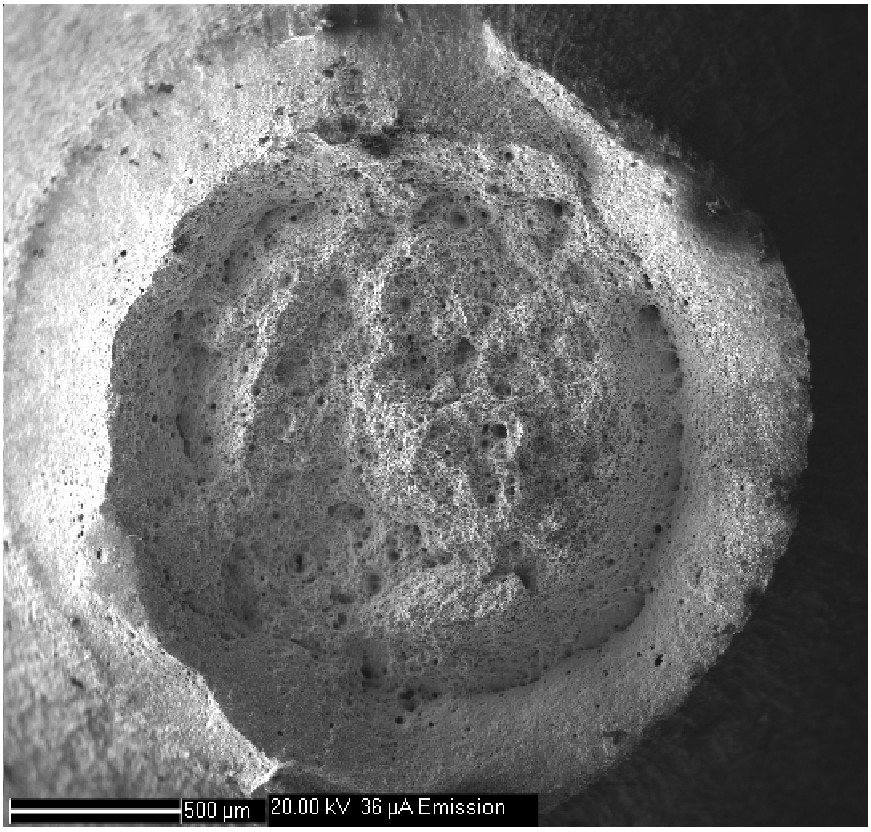

Fig. 5.7 Typical cup and cone fracture with shear lip observed in notch specimen for relative shallow notches (Notch acuity ratio = 1.0, 150 MPa, 873 K) for 2.25Cr-1Mo steel.

This suggests that the failure initiated at the central region of the notch throat plane by plasticity-induced intragranular ductile dimple failure mode (Fig. 5.8(a)) and propagated towards the notch root. Rapid propagation of transgranular crack resulted in shallow dimple appearance of the fractured surface in the shear lip zone (Fig. 5.8(b)).

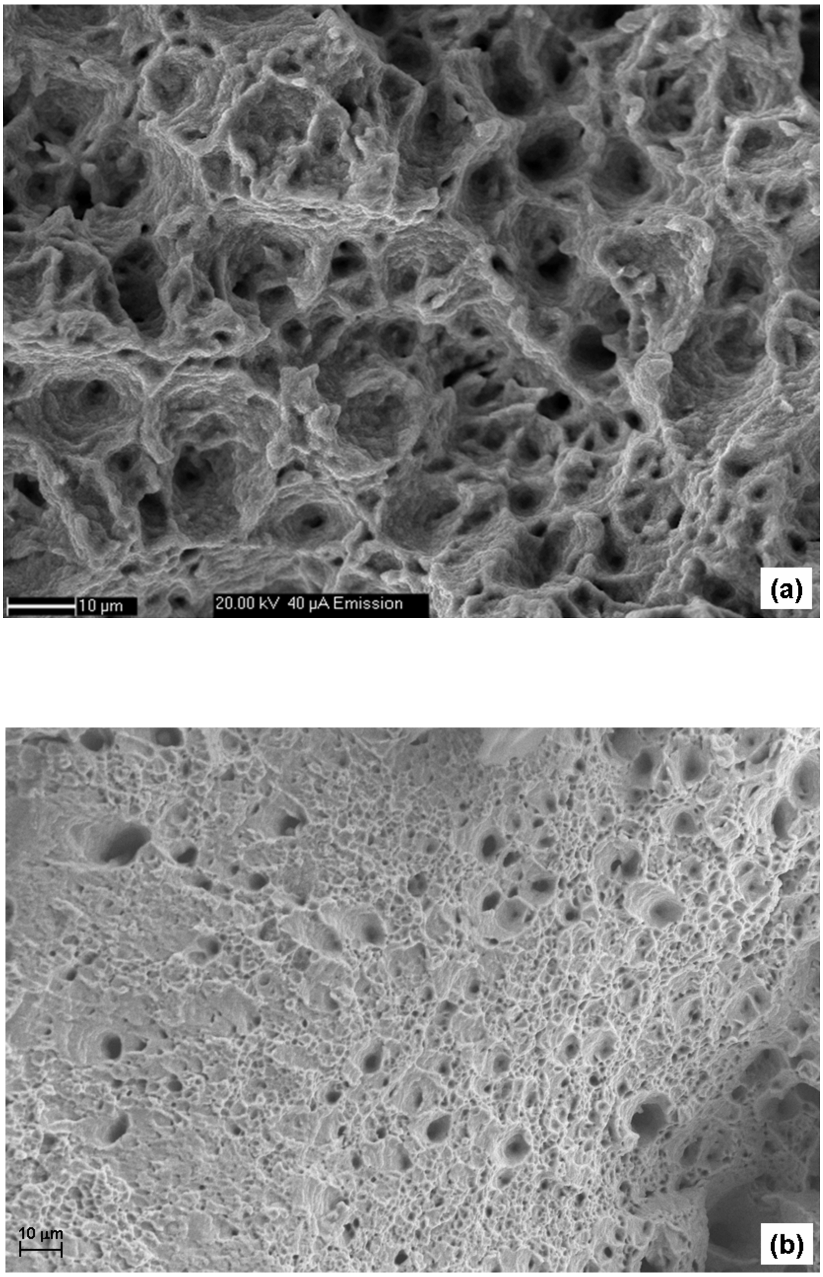

Fig. 5.8 Typical transgranular ductile fracture observed in notch specimen at (a) central region (b) shear lip for relative shallow notches (Notch acuity ratio = 1.0, 150 MPa, 873 K) in 2.25Cr-1Mo steel.

For relatively sharper notches of notch acuity ratio ≥ 4, quite appreciable change in fracture appearance was observed. Low magnification SEM fractograph of the fracture surface is shown in Fig. 5.9 for notch acuity ratio of 20 (notch root radius = 0.25 mm) creep tested at 150 MPa and 873 K. SEM micrograph close to notch root clearly shows intergranular creep cavitation (Fig. 5.10(a)) whereas the ductile dimple fracture (Fig. 5.10(b)) around the central region of notch throat plane. These evidences clearly indicate that creep cavitation would have started from the notch root region and propagated towards the central region leading to ductile dimple failure by plastic instability at the central region. SEM micrograph of the longitudinal section of un-failed notch of the creep ruptured specimen for notch acuity ratio of 10 is shown in Fig. 5.11. The figure clearly revealed that the creep crack initiation occurred at the notch root and propagated towards the central region of notch throat plane. The observed changes in overall fracture appearance of 2.25Cr-1Mo steel for different notch acuity ratios and creep tested at different stresses is shown schematically in Fig. 5.12. The fracture behaviour of 2.25Cr-1Mo steel under multiaxial state of stress progressively shifted from the fracture appearance depicted in Fig. 5.12(a) to Fig. 5.12(b) i.e., predominantly dimple ductile appearance to predominantly intergranular creep cavitation appearance with increase in notch acuity ratio and decrease in net applied stress. The SEM quantitative fractographic analysis of ductile dimple appearance with notch acuity ratio for all the net applied stresses is shown in Fig. 5.13. Increase in notch sharpness was found to impart greater extent of creep embrittlement in the steel than that by decrease in applied stress.

SEM macro-fractography of the creep ruptured notched specimens of 9Cr-1Mo steel having notch root radius of 2.5 mm and 0.25 mm, creep tested at 150 MPa, 873 K are shown in Fig. 5.14(a) and (b) respectively. Shear lip, resulting from the cup

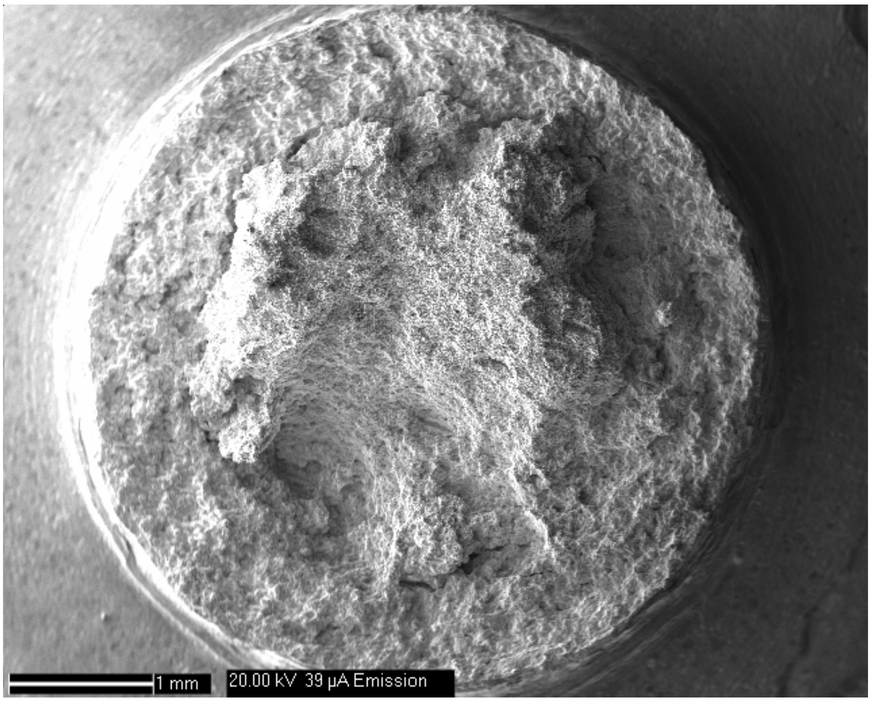

Fig. 5.9 Low magnification fractograph of relatively sharper notch (Notch acuity ratio = 20, 150 MPa, 873 K) in 2.25Cr-1Mo steel.

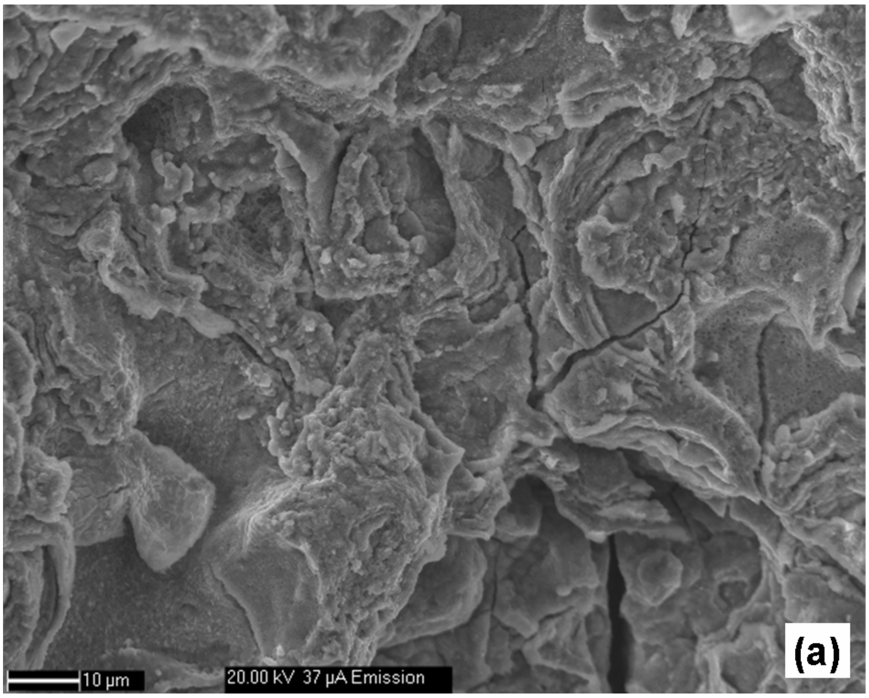

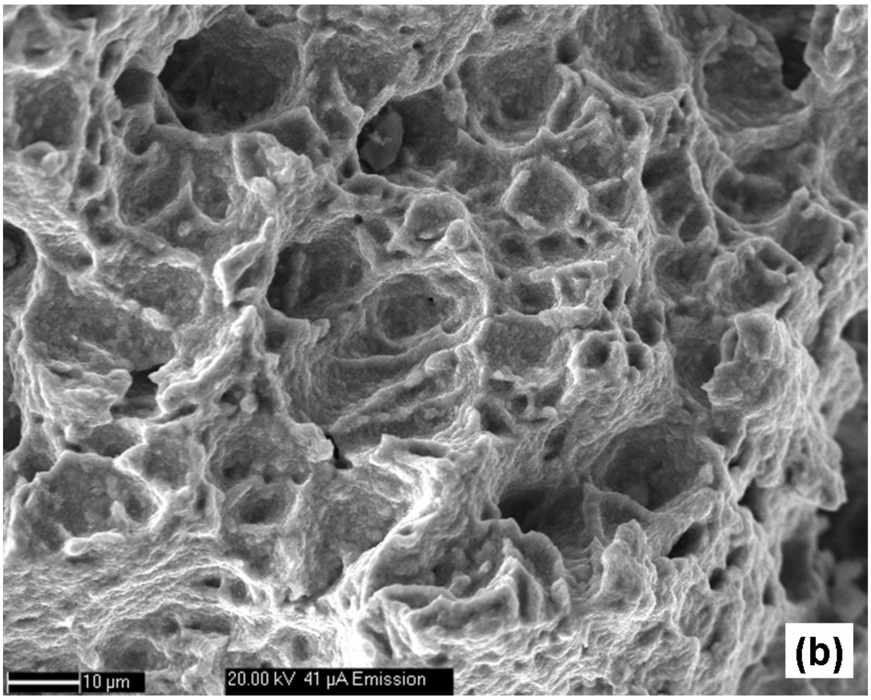

Fig. 5.10 (a) creep cavitation induced brittle fracture near notch root (b) transgranular ductile fracture near the central region of notch throat plane (Notch acuity ratio = 20, 150 MPa, 873 K) in 2.25Cr-1Mo steel.

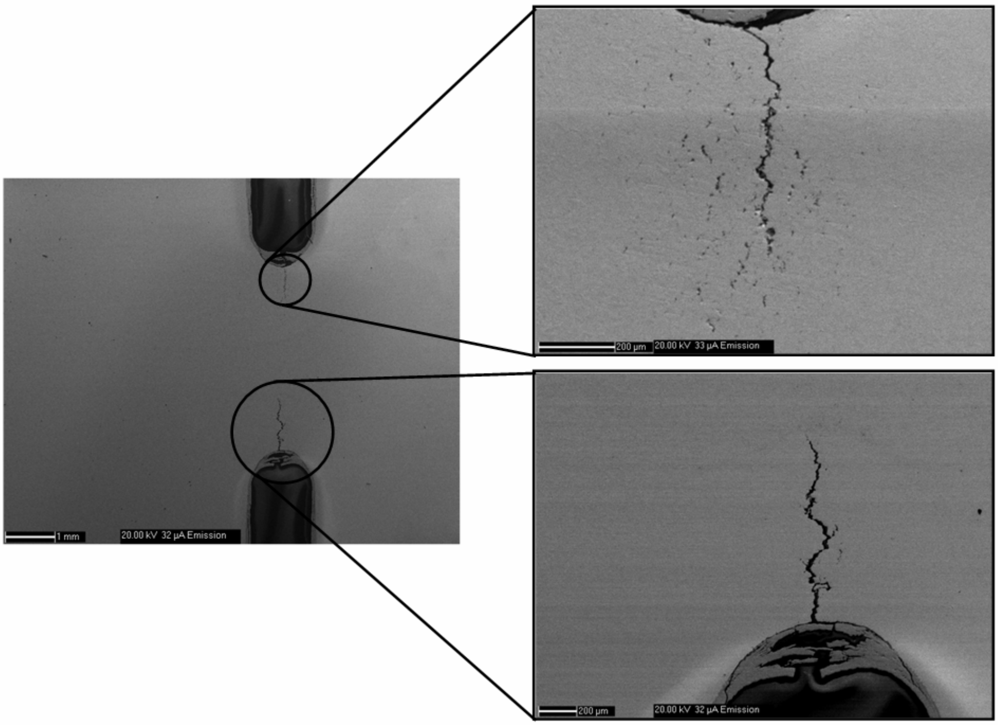

Fig. 5.11 Nucleation of crack at the notch root observed in notch specimen at relative sharper notches (Notch acuity ratio = 10, 150 MPa, 873 K) in 2.25Cr-1Mo steel.

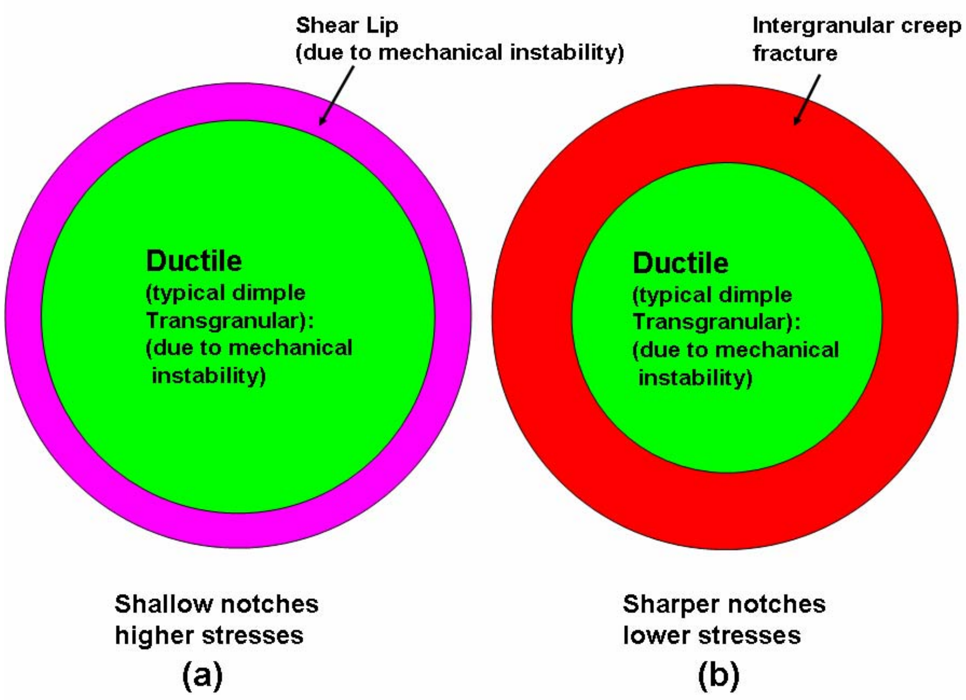

Fig. 5.12 Schematic diagrams showing the change in appearance of fracture mode with notch sharpness and net applied stress.

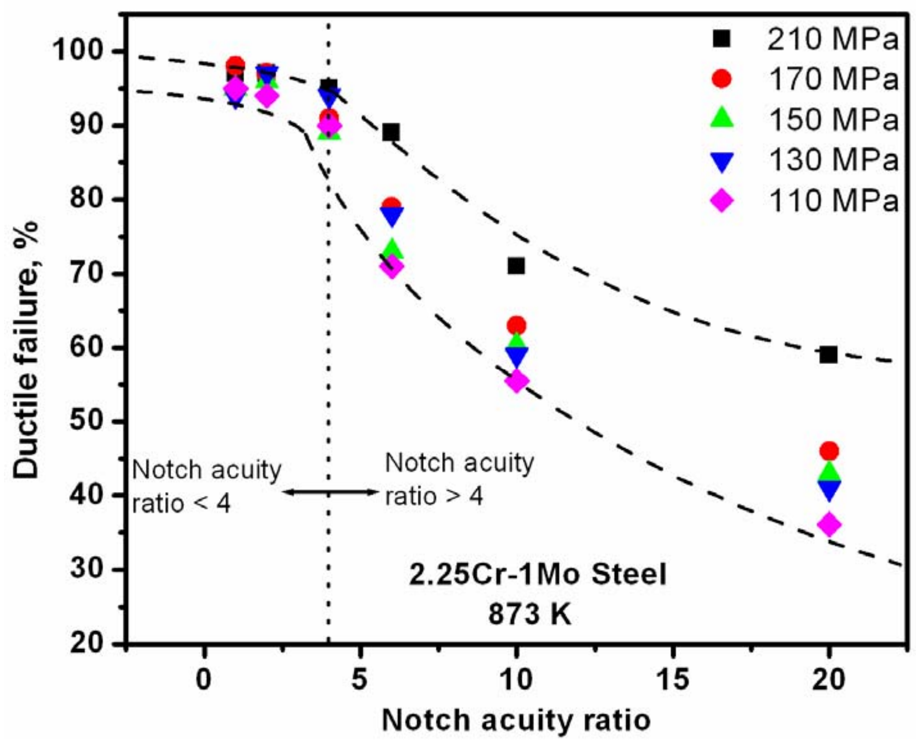

Fig. 5.13 Variations of % ductile fracture appearance as a function of notch acuity ratio at different net applied stresses in 2.25Cr-1Mo steel.

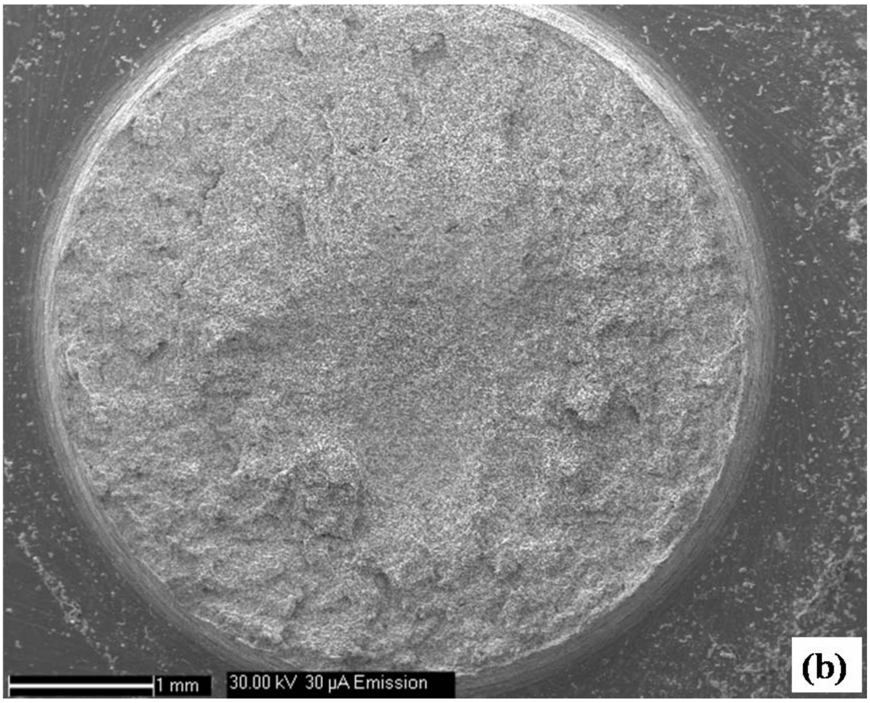

Fig. 5.14 SEM micrographs of 9Cr-1Mo steel (a) Typical cup and cone fracture with shear lip observed in notched specimen at relative shallow notches (notch radius of 2.5 mm) and (b) mixed mode fracture for relatively sharper notches (notch radius of 0.25 mm) at 150 MPa, 873 K.

and cone type of ductile failure, caused by final mechanical instability at the notch root, was observed for relatively shallow notches, Fig. 5.14(a), whereas, predominantly brittle failure with significantly less reduction in ductility was observed for specimens having relatively sharper notches with high acuity ratio Fig. 5.14(b). SEM fractographs at central and notch root location of the creep fractured notched specimen of notch root radius of 0.25 mm are shown in Fig. 5.15(a) and (b) respectively. Transgranular ductile dimple appearance was observed in the central region (Fig. 5.15(a)) whereas brittle intergranular appearance was observed around the notch root region (Fig. 5.15(b)). Isolated intergranular creep cavitation near the notch root was observed in the polished surface of the un-failed notch of notched specimen (Fig. 5.15(c)). Even though both the 2.25Cr-1Mo and 9Cr-1Mo steels exhibited comparable notch strengthening (Fig. 5.4), the fracture appearance in 9Cr-1Mo showed relatively more ductile dimple appearance for a given net applied stress and notch acuity ratio than that of 2.25Cr-1Mo steel. This is reflected in higher creep rupture ductility of the 9Cr-1Mo steel than that of the 2.25Cr-1Mo steel in presence of notch (Fig. 5.6). The numerical analysis for damage development in the notched specimens carried out by Yue et al. [115] showed that creep damage would be more at the central region for relatively shallow notches and at the notch root for relatively sharper notches. Fracture appearance in modified 9Cr-1Mo steel was similar to those in other two steels but the prevalence of intergranular creep cavitation appearance was more than that in 2.25Cr-1Mo and 9Cr-1Mo steel for a given applied stress and notch acuity ratio. Creep deformation resistance of modified 9Cr-1Mo steel was significantly more than other two steels (Fig. 3.4). Longer creep rupture life in modified 9Cr-1Mo steel than those in 2.25Cr-1Mo and 9Cr-1Mo steels facilitated the nucleated creep cavities to grow leading to intergranular creep cavitation with lower rupture ductility (Fig. 5.6). Extensive creep cavitation was observed in the modified 9Cr-1Mo especially at higher notch acuity ratio and lower applied stress stresses (Fig. 5.16).

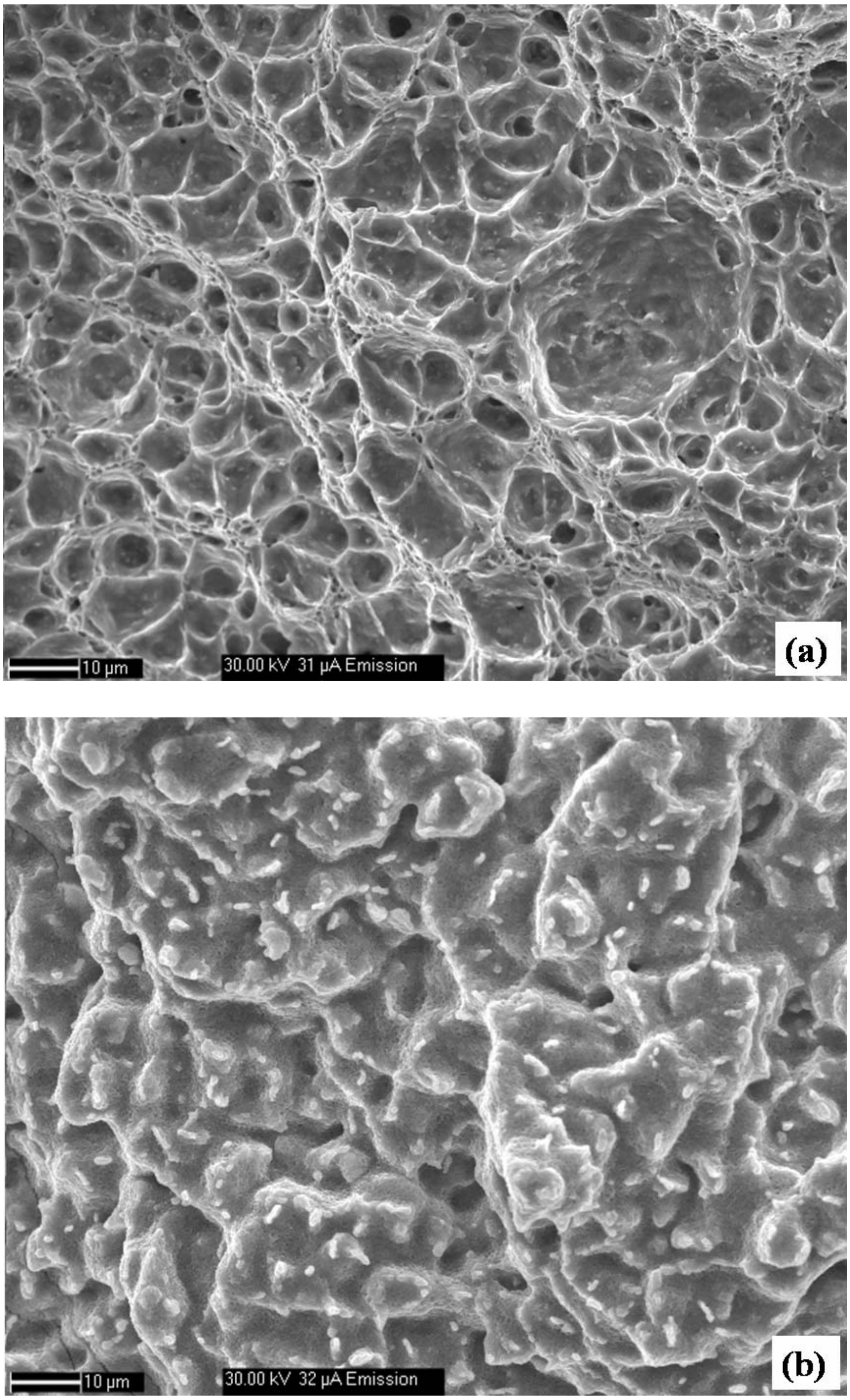

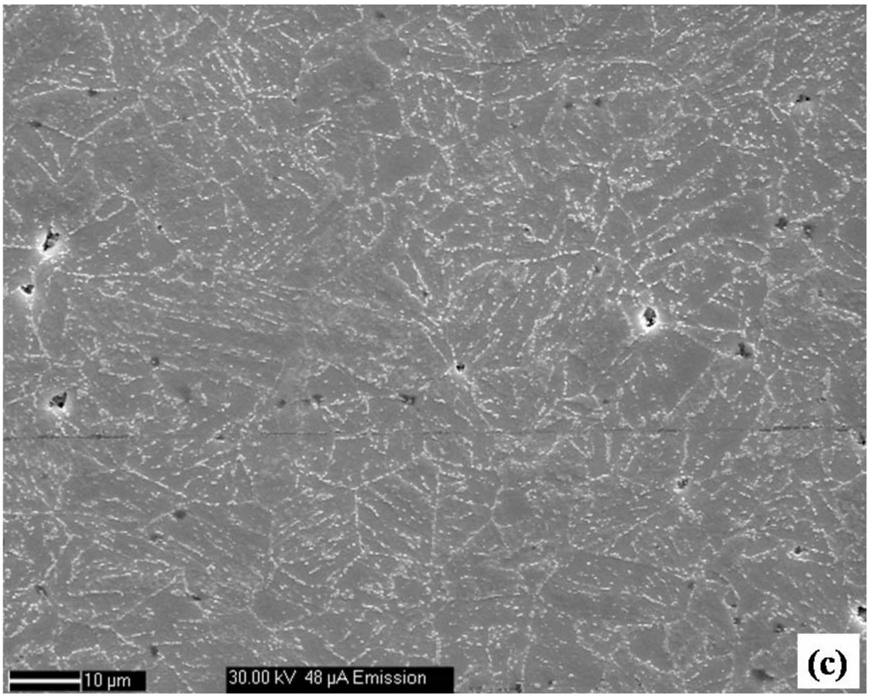

Fig. 5.15 SEM micrographs of 9Cr-1Mo steel (a) Ductile transgranular fracture at central region, (b) brittle intergranular fracture associated with (c) creep cavitation at notch root for relatively sharper notches (notch radius 0.25 mm) at 150 MPa, 873 K.

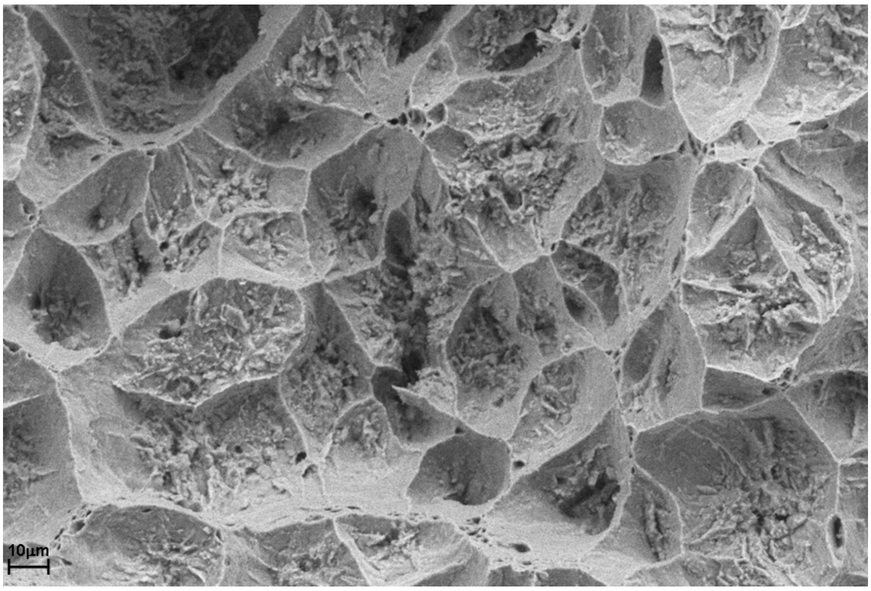

Fig. 5.16 Creep cavitation in modified 9Cr-1Mo steel creep tested at 873 K, 170 MPa and notch acuity ratio of 1.25 mm.

5.4 Finite element analysis to assess the notch strengthening and fracture behaviour

Creep rupture life of the steels increased in presence of notch, extent of which increased with notch acuity ratio and was found to depend on material's deformation properties. The fracture appearance depended appreciably on the notch acuity ratio, changed from transgranular failure to intergranular creep failure with increase in notch acuity ratio. The assessment of notch strengthening and fracture behaviour has been carried out using FE analysis and is discussed in subsequent sections.

5.4.1 Effect of notch acuity ratio on stress distribution

FE analyses of stress distribution across the notch throat plane were carried out considering material's (i) elastic properties, (ii) elastic and time independent plastic properties and (iii) elasto-plastic and time dependent creep properties in the FE models. 2D axisymmetric analysis was carried out using 4 noded quadrilateral elements employing ABAQUS 6.10 finite element solver incorporating appropriate boundary conditions.

5.4.1.1 Elastic and elasto-plastic behaviour

Initially, mesh sensitivity analysis was carried out to assess the dependency of mesh size on stress distribution across the notch throat plane. The material was assumed to deform elastically in the analysis. The axial stress distribution across the notch throat plane for notches of different notch acuity ratios for 2.25Cr-1Mo steel after elastic deformation is shown in Fig. 5.17. The stress concentration at the notch root increased sharply with the increase in notch acuity ratio. The FE mesh was refined in the notch root region to an extent that the axial stress estimated at the notch root was in agreement with the theoretical elastic stress calculated based on Peterson's equation [98], indicating the adequacy of mesh size refinement for the FE analysis.

Effect of plastic behaviour of the material in the stress distribution across the notch throat plane was also assessed considering material's elasto-plastic deformation behaviour. Plastic deformation was not found to initiate at the notch root in the notched specimen for notch acuity ratios of 1 and 2 due to lack of adequate stress concentration. The plastic deformation and plastic zone at the notch root increased with further increase in notch acuity ratio, Fig. 5.18. Localized plastic deformation decreased the intensity of stress in the notch root region for relatively sharper notches and the peak in stress shifted to subsurface [52]. Plastic deformation was not found to take place in case of 9Cr-1Mo steel and modified 9Cr-1Mo steel up to the notch acuity ratio of 4 for the stresses under investigation.

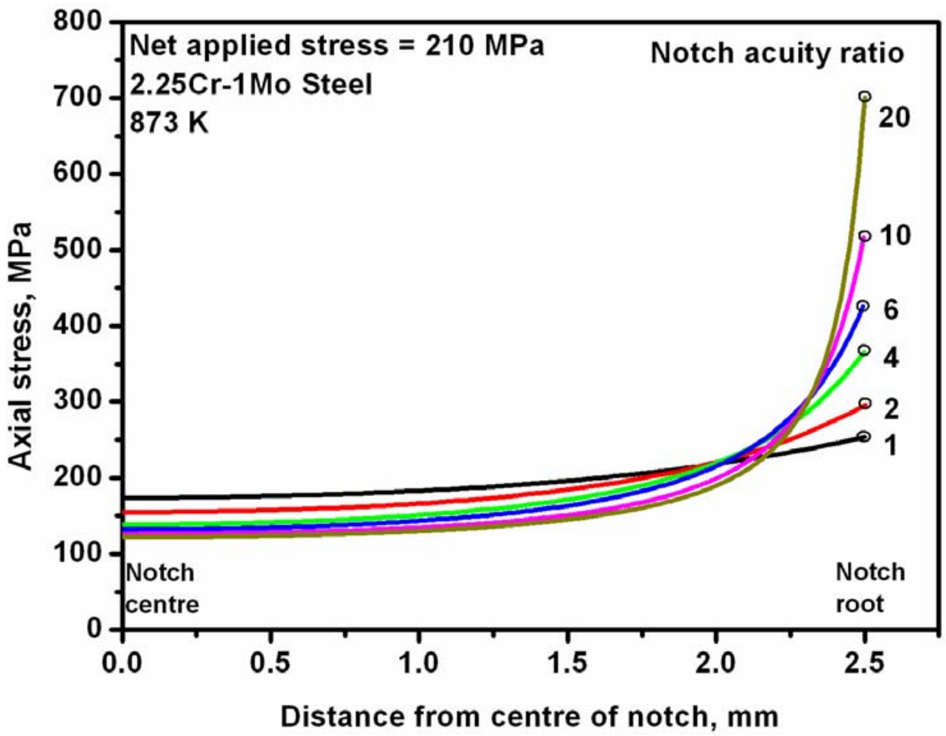

Fig. 5.17 Variation of axial stress across the notch throat plane as a function of notch acuity ratio (open circle symbol indicates the stress corresponding to elastic stress concentration factor).

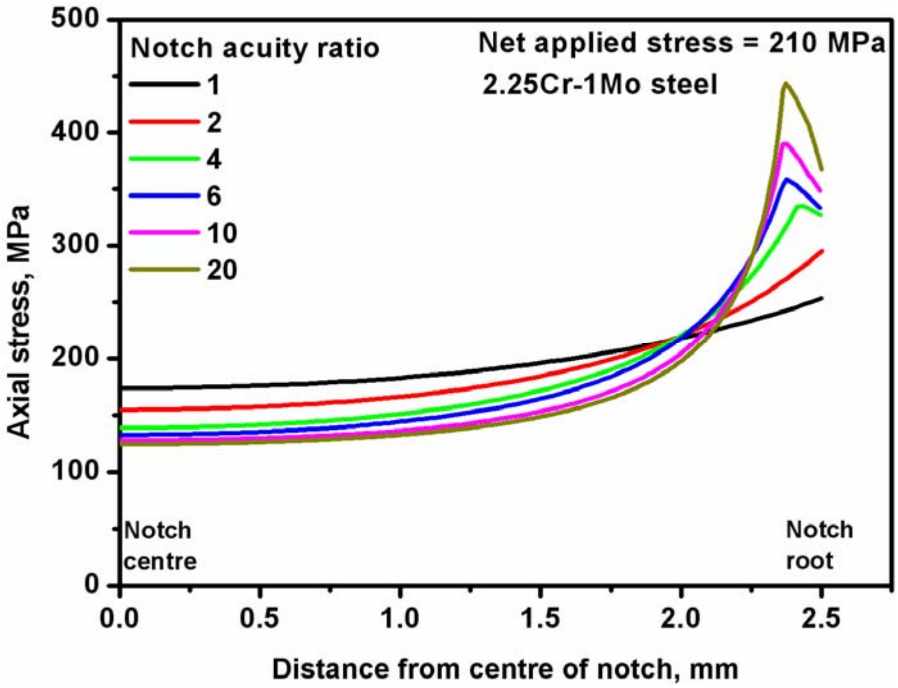

Fig. 5.18 Variation of axial stress across the notch throat plane after elastic/elasto-plastic deformation depending on the notch acuity ratio for 2.25Cr-1Mo steel.

5.4.1.2 Elasto-plastic-creep behaviour

FE analysis of stress distribution across the notch throat plane in 2.25Cr-1Mo steel during creep deformation has been carried out on incorporating material's time independent (plastic) and time dependent (creep) behavior in the model. The material was considered to undergo elastic/elasto-plastic deformation followed by creep deformation in the analysis.

The difference in creep rates across the notch throat plane leads to stress redistribution during creep exposure. As creep deformation takes place, regions of high stress shed load to the regions of lower stresses due to the stress sensitivity to creep deformation. The distribution of axial stress across the notch throat plane with creep exposure for two notch acuity ratios of 2 and 10 are shown in Fig. 5.19. Under creep condition, stress distribution across the notch throat plane was found to change with creep exposure and approached to a stationary state. The pattern of stress distribution across the notch throat plane was found to depend on the notch acuity ratio. The value of axial stress increased progressively at the central region of notch throat plane and decreased at the notch root region for all the notches investigated. In the central region of notch throat plane, the axial stress became progressively more than the net applied stress for relatively shallow notches, whereas, it remained below net applied stress for relatively sharper notches. Near the notch root region, the axial stress was below the net applied stress for all the notches. The variation in axial stress across the notch throat plane showed a maxima (Fig. 5.19) and it had value more than the net applied stress for all the notch acuity ratios. The redistribution of radial and hoop stresses was also found to occur during creep deformation.

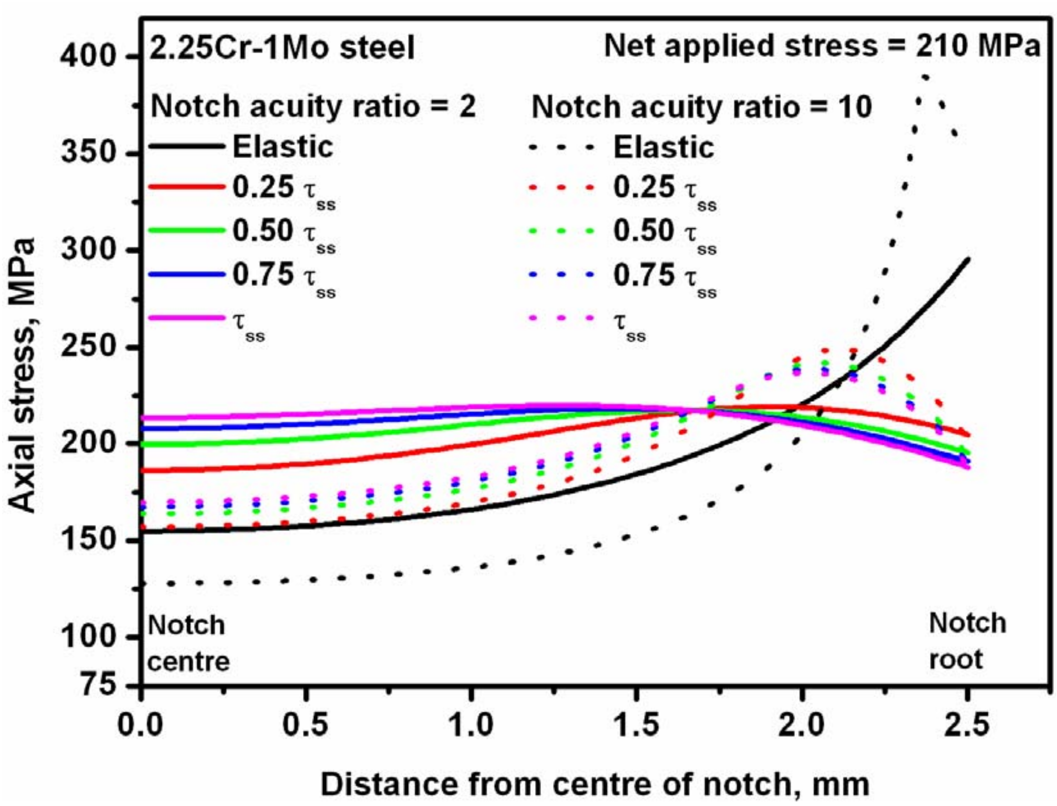

Fig. 5.19 Redistribution of axial stress across the notch throat plane with creep exposure for 2.25Cr-1Mo steel and notch acuity ratios of 2 and 10 at 210 MPa (τ_{ss} represents the time to reach stationary state).

As mentioned in Chapter 4, the maximum principal, von-Mises and hydrostatic stresses play significant roles in creep deformation and cavitation of materials. The variations of von-Mises stress across the notch in 2.25Cr-1Mo steel for notch acuity ratio of 1, 4 and 10 at 210 MPa are shown in Fig. 5.20. Significant variation in the stress was observed depending on the notch sharpness. For shallow notches (Fig. 5.20(a)), the von-Mises stress was uniform across the notch, whereas, it was concentrated at the notch root for relatively sharper notches (Fig. 5.20(b) and (c)). Fig. 5.21 and Fig. 5.22 show the variation of maximum principal and hydrostatic stresses for notch acuity ratio of 1, 4 and 10 at 210 MPa. The stresses were not uniform across the notch and concentrated at the central region of notch for relatively shallow notches (Fig. 5.21(a)) and close to notch root for sharper notches (Fig. 5.21(b) and (c)). Similar distribution was observed for hydrostatic stress, Fig. 5.22. The variations of stationary state distribution of these stresses across the notch throat plane and the effect of notch acuity ratio for 2.25Cr-1Mo steel at 210 MPa has been assessed and are shown in Fig. 5.23. The von-Mises across the notch throat plane was found to decrease with increase in notch acuity ratio, Fig. 5.23(a). The variation in von-Mises stress across the notch throat plane was not found to change appreciably for relatively shallow notches (notch acuity ratio < 4). However, in relatively sharp notches (notch acuity ratios ≥ 4), the von-Mises stress increased gradually at the notch root region however remained below the net stress for all the notch acuity ratios investigated. The variation in maximum principal stress across the notch throat plane showed a maxima (Fig. 5.23(b)) and it had value more than the net applied stress for all notch acuity ratios. The maxima in principal stress increased with notch acuity ratio and its position progressively shifted towards the notch root region.

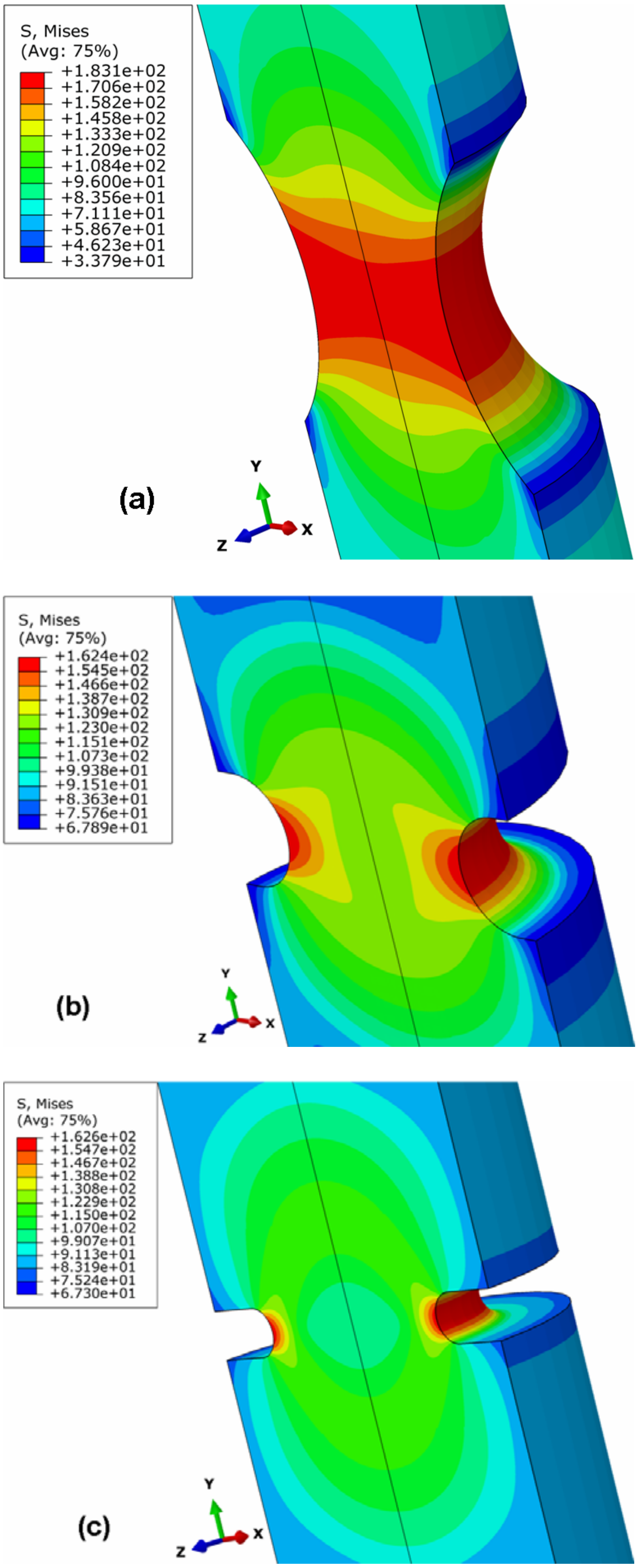

Fig. 5.20 Pictorial view of the von-Mises stress for the notch acuity ratios of (a) 1, (b) 4 and (c) 10 after attaining the stationary state at 210 MPa for 2.25Cr-1Mo steel.

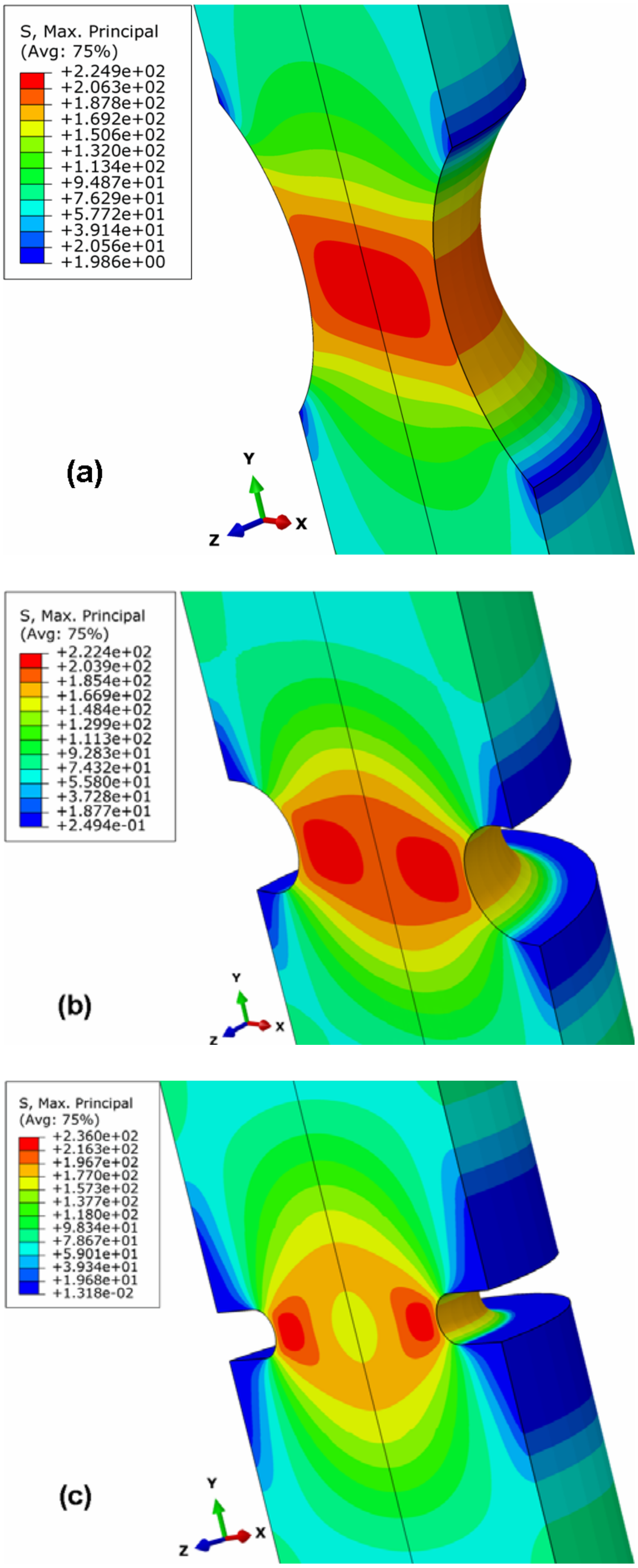

Fig. 5.21 Pictorial view of the maximum principal stress for the notch acuity ratios of (a) 1, (b) 4 and (c) 10 after attaining the stationary state at 210 MPa for 2.25Cr-1Mo steel.

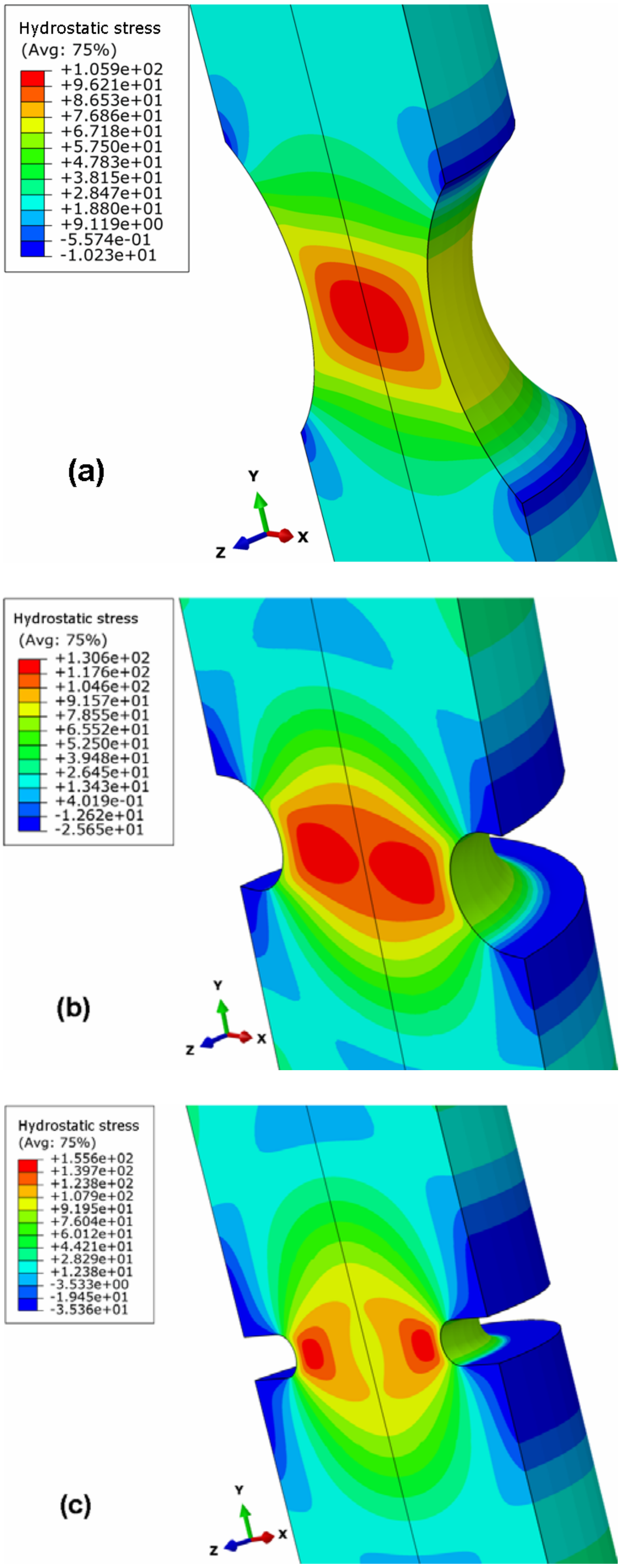

Fig. 5.22 Pictorial view of the hydrostatic stress for the notch acuity ratios of (a) 1, (b) 4 and (c) 10 after attaining the stationary state at 210 MPa for 2.25Cr-1Mo steel.

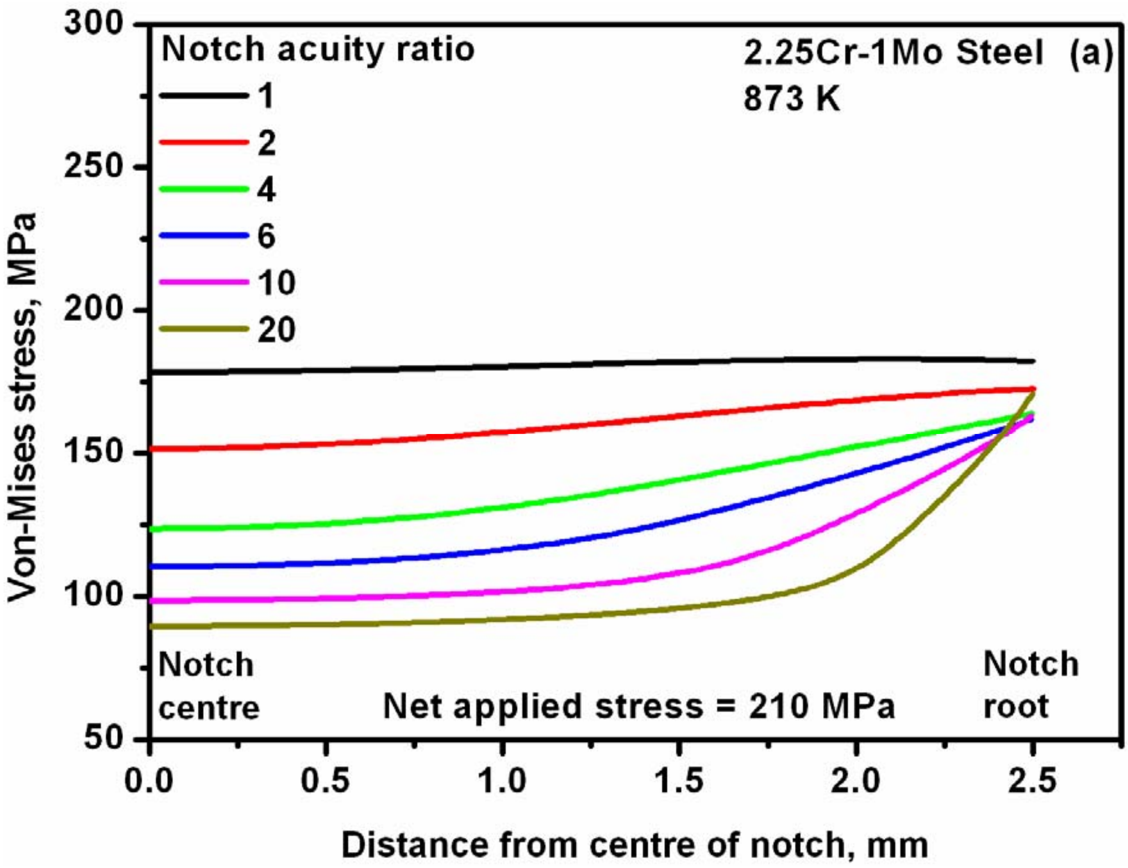
Notch acuity ratio
1
2
4
6
10
20
2.25Cr-1Mo Steel (a)
873 K
Von-Mises stress, MPa
Notch centre
Net applied stress = 210 MPa
Notch root
Distance from centre of notch, mm
300
250
200
150
100
50
0.0
0.5
1.0
1.5
2.0
2.5

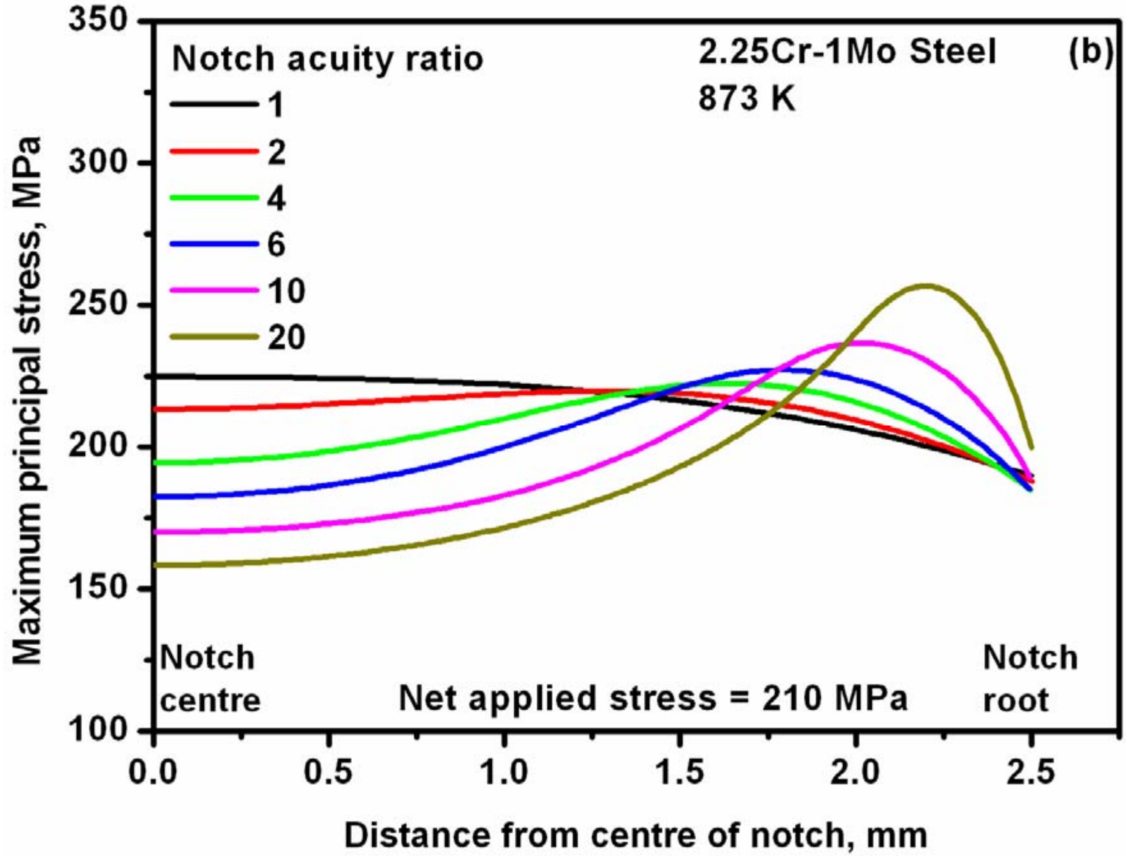
Notch acuity ratio
1
2
4
6
10
20
2.25Cr-1Mo Steel (b)
873 K
Maximum principal stress, MPa
Notch centre
Net applied stress = 210 MPa
Notch root
Distance from centre of notch, mm
350
300
250
200
150
100
0.0
0.5
1.0
1.5
2.0
2.5

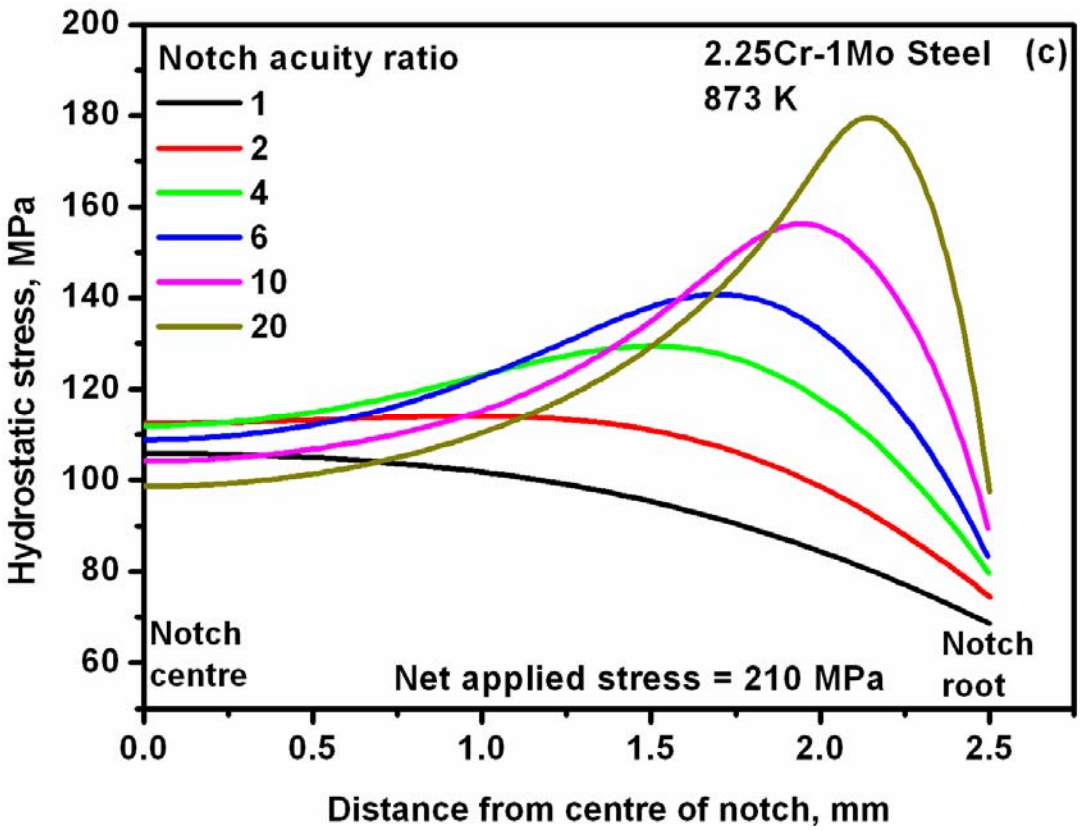

Fig. 5.23 Variation of (a) maximum principal (b) hydrostatic and (c) von-Mises stress across the notch throat plane as a function of notch acuity ratio for 2.25Cr-1Mo steel at 210 MPa and 873 K.

Similar variation in hydrostatic stress across the notch throat plane for different notch acuity ratios was observed (Fig. 5.23(c)). It is worth noting that the maximum value of the hydrostatic stress remained below the net stress for all the notch acuity ratios investigated.

5.4.2 Assessment of notch strengthening in the steels

Creep rupture strengthening observed in the steels in presence of notch (Fig. 5.1) and effect of notch acuity ratio on the extent of strengthening (Fig. 5.3) have been assessed based on the stationary state stress distributions across the notch throat plane. Creep deformation in the materials is governed by the shear stresses (von-Mises stress). The extent of notch strengthening has been explained based on the variation of von-Mises stress with notch acuity ratio. The von-Mises stress remained below the net applied stress after stress redistribution (Fig. 5.23(a)) for all the notch acuity ratios and resulted in notch strengthening as observed experimentally (Fig. 5.1). The decrease in von-Mises stress with increase in notch acuity ratio led to higher notch strengthening with increase in notch acuity ratio. The reduction in von-Mises stress is also reflected in the reduction in ductility of the notched specimens with increase in notch acuity ratio (Fig. 5.6). The saturating tendency of von-Mises stress with increase in notch acuity ratio would have been the cause for saturation of notch strengthening at higher notch acuity ratio.

Notch strengthening was found to be comparable for 2.25Cr-1Mo and 9Cr-1Mo steel; however, modified 9Cr-1Mo steel exhibited pronounced notch strengthening (Fig. 5.4). FE analysis incorporating individual material's properties has been carried out to assess the strengthening effect in different steels. The variations of normalized von-Mises, maximum principal and hydrostatic stresses across the notch for the steels at 210 MPa and notch acuity ratio of 10 are shown in Fig. 5.24, 5.25 and 5.26 respectively. The stresses were normalized with respect to yield stress of individual steel. The stress distributions across the notch were found to vary significantly and depend on the material considerably. The comparisons of stationary state normalized von-Mises, maximum principal and hydrostatic stresses across the notch throat plane for the steels are shown in Fig. 5.27(a), (b) and (c) respectively for notches of acuity ratio of 2 and 10. The von-Mises stress across the notch throat plane was in the decreasing order of 2.25Cr-1Mo, 9Cr-1Mo and modified 9Cr-1Mo steels. Lower von-Mises stress in modified 9Cr-1Mo steel than that of 2.25Cr-1Mo and 9Cr-1Mo steels resulted in higher notch strengthening in modified 9Cr-1Mo steel.

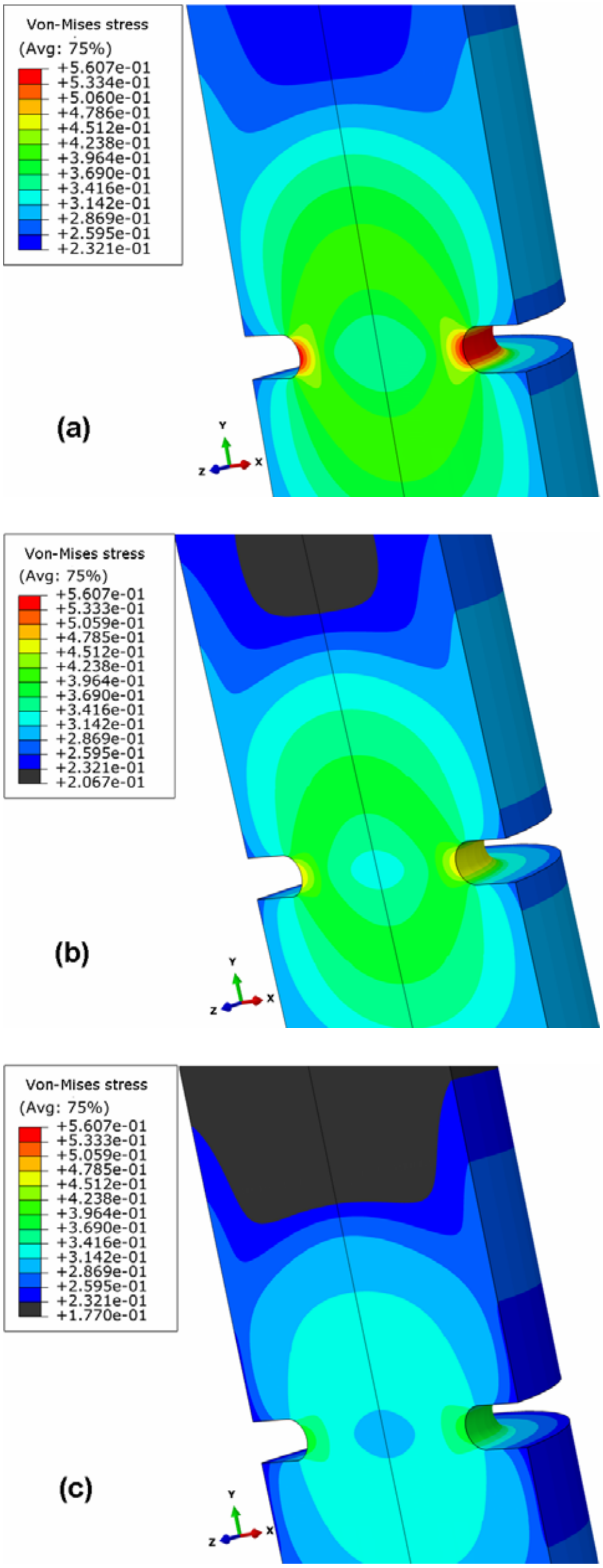

Fig. 5.24 Effect of material on the distribution of normalized von-Mises stress across the notch of acuity ratio 10 at 210 MPa for (a) 2.25Cr-1Mo, (b) 9Cr-1Mo and (c) modified 9Cr-1Mo steels (stresses were normalized with respect to yield stress of the material).

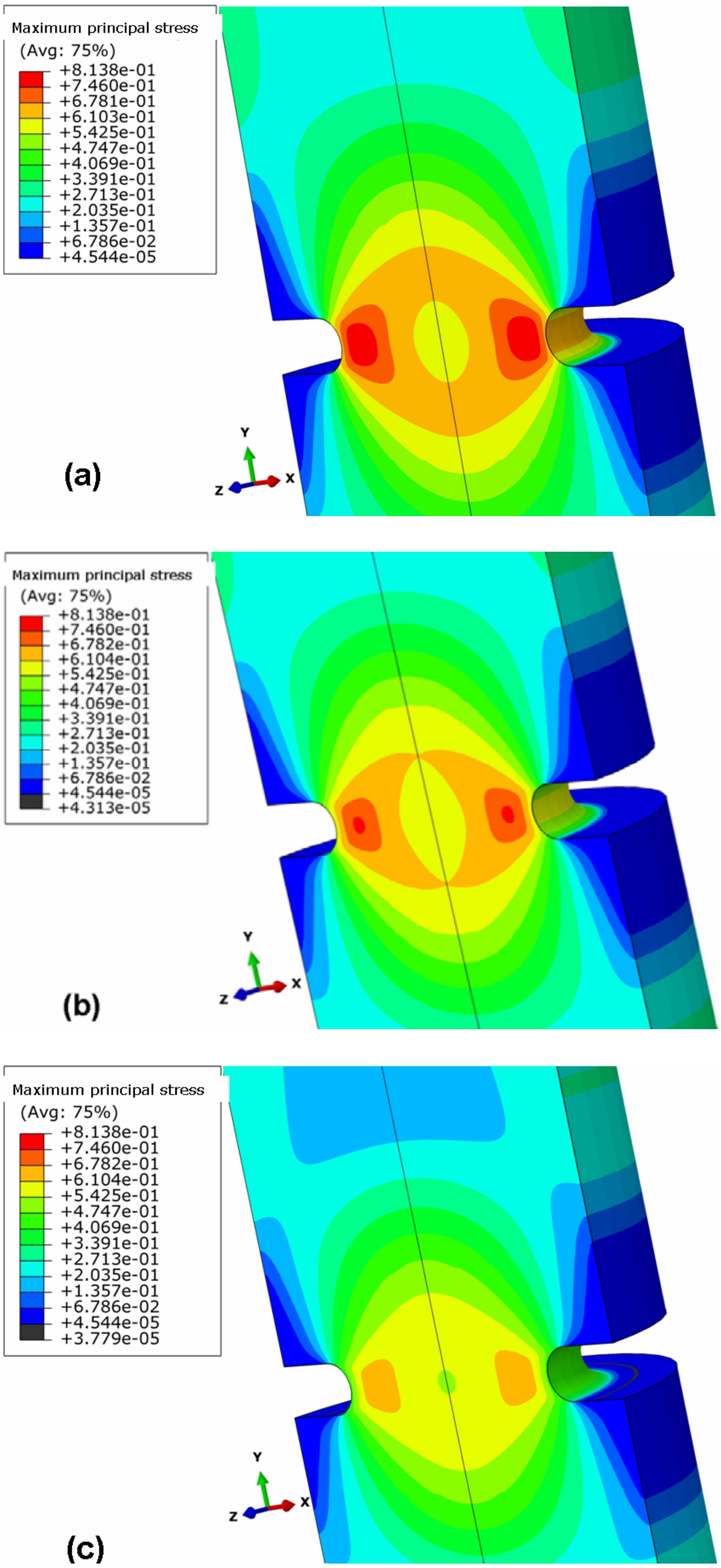

Fig. 5.25 Effect of material on the distribution of normalized maximum principal stress across the notch of acuity ratio 10 at 210 MPa for (a) 2.25Cr-1Mo, (b) 9Cr-1Mo and (c) modified 9Cr-1Mo steels.

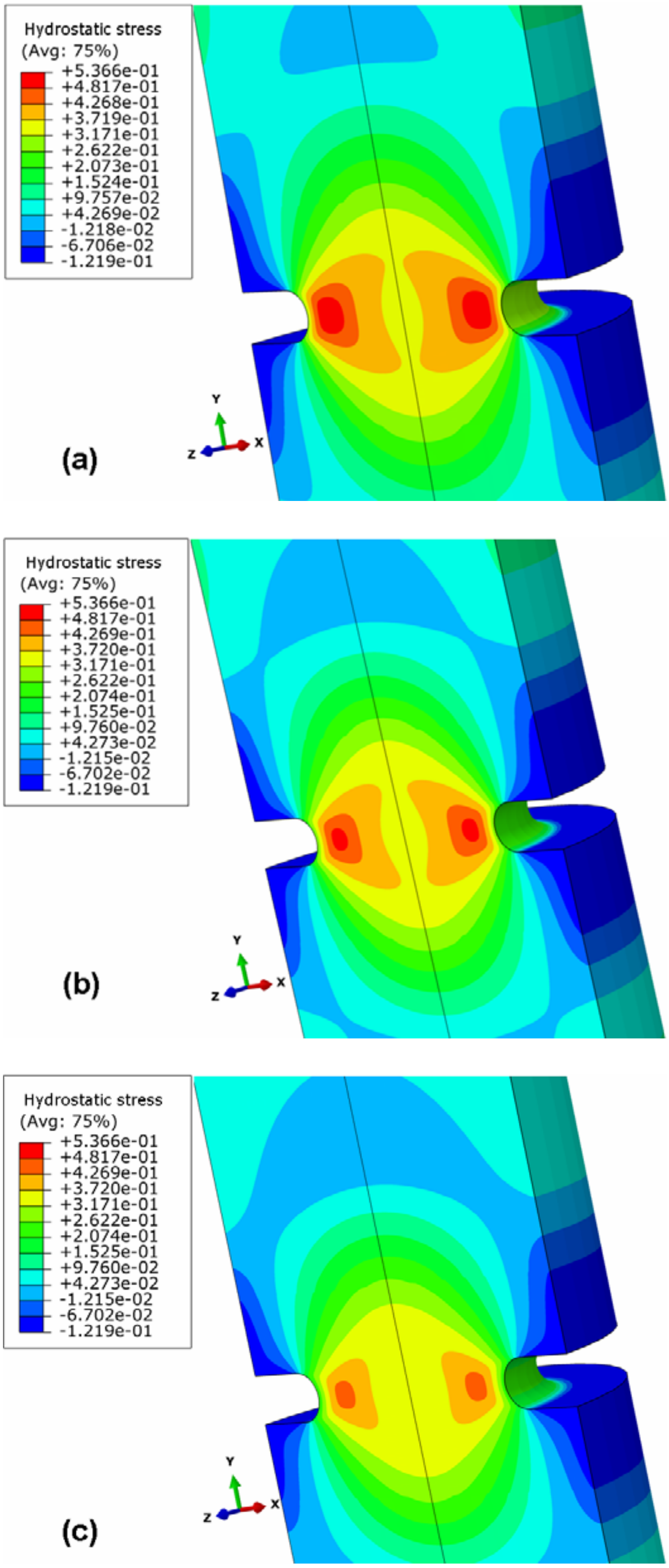

Fig. 5.26 Effect of material on the distribution of normalized hydrostatic stress across the notch of acuity ratio 10 at 210 MPa for (a) 2.25Cr-1Mo, (b) 9Cr-1Mo and (c) modified 9Cr-1Mo steels.

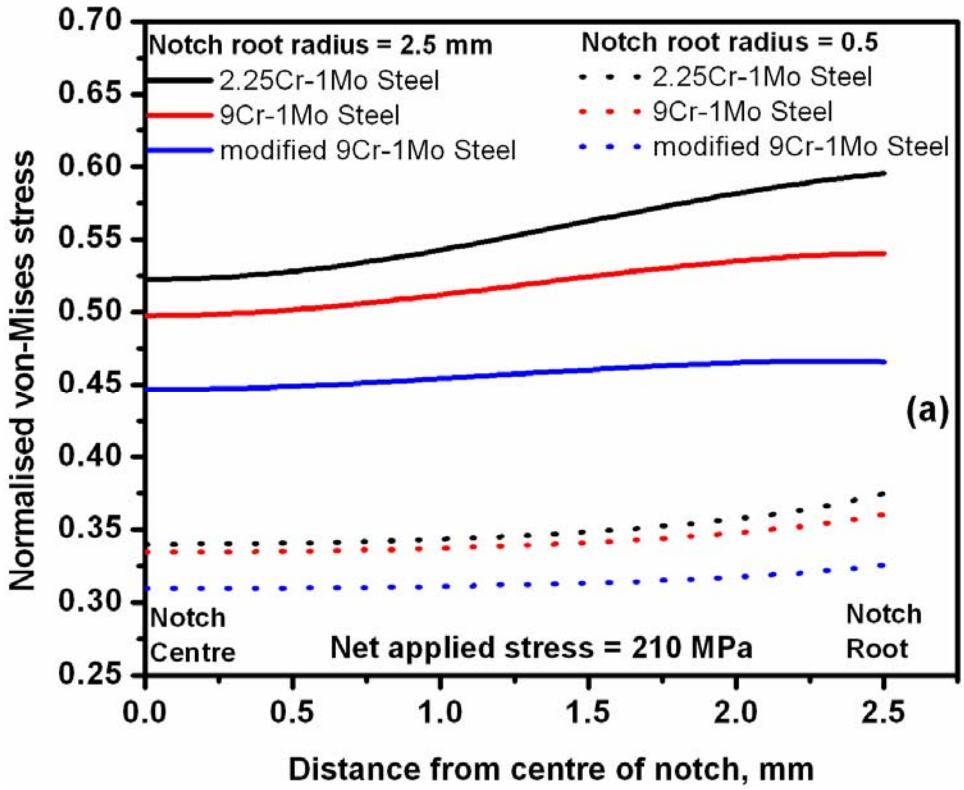
Notch root radius = 2.5 mm
2.25Cr-1Mo Steel
9Cr-1Mo Steel
modified 9Cr-1Mo Steel
Notch root radius = 0.5
2.25Cr-1Mo Steel
9Cr-1Mo Steel
modified 9Cr-1Mo Steel
(a)
Notch Centre
Net applied stress = 210 MPa
Notch Root
Normalised von-Mises stress
Distance from centre of notch, mm
0.70
0.65
0.60
0.55
0.50
0.45
0.40
0.35
0.30
0.25
0.0
0.5
1.0
1.5
2.0
2.5

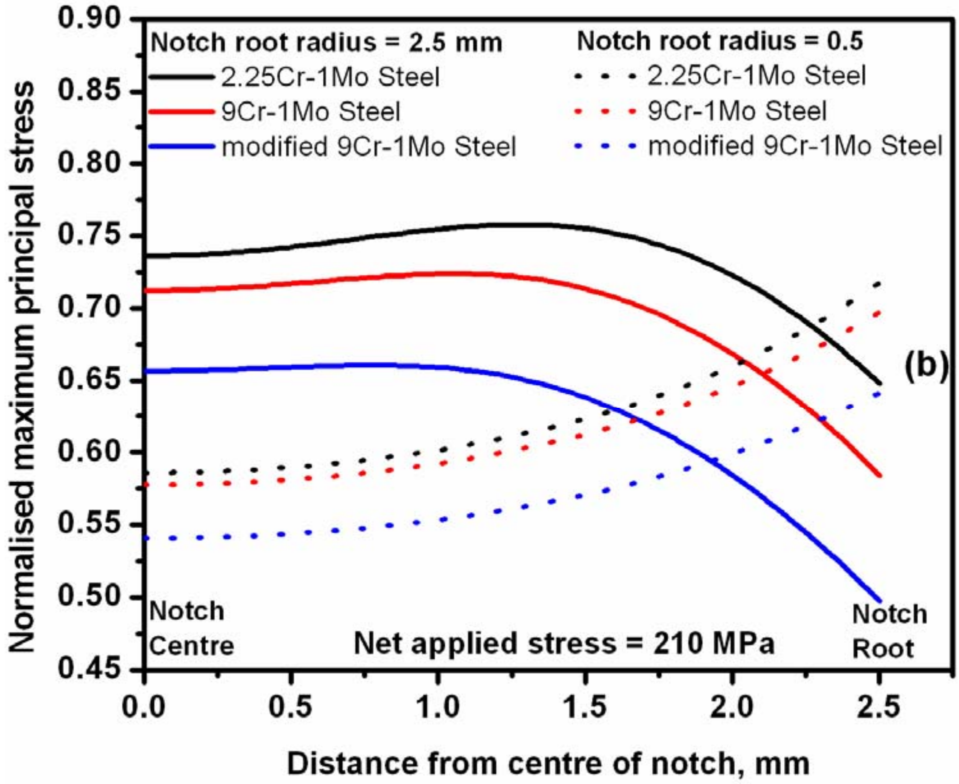
Notch root radius = 2.5 mm
2.25Cr-1Mo Steel
9Cr-1Mo Steel
modified 9Cr-1Mo Steel
Notch root radius = 0.5
2.25Cr-1Mo Steel
9Cr-1Mo Steel
modified 9Cr-1Mo Steel
(b)
Notch Centre
Net applied stress = 210 MPa
Notch Root
Normalised maximum principal stress
Distance from centre of notch, mm
0.90
0.85
0.80
0.75
0.70
0.65
0.60
0.55
0.50
0.45
0.0
0.5
1.0
1.5
2.0
2.5

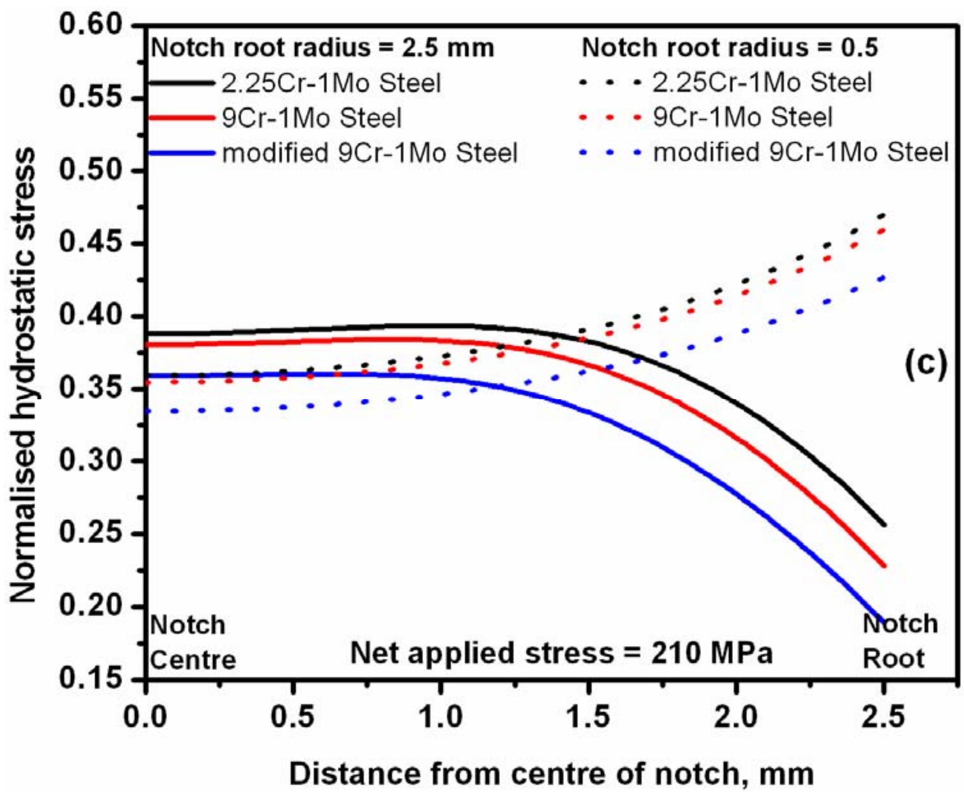

Fig. 5.27 Variation of normalized (a) maximum principal (b) hydrostatic and (c) von-Mises stresses across the notch throat plane for all the steels and notch root radii of 2.5 and 0.5 mm at 210 MPa and 873 K.

The von-Mises stress decreases significantly with increase in notch acuity ratio for all the steels. Larger extent of decrease in von-Mises stress with notch acuity ratio in all the steels increased the notch strengthening to greater extent. The relaxation of axial stress of 210 MPa at the notch root for two different notch acuity ratios (4 and 10) is shown in Fig. 5.28 for the steels. The time for relaxation has been normalized with the time to reach stationary state for the steels. The stress was found to relax with creep exposure at different rate and to a different extent depending upon the material and notch sharpness (notch acuity ratio). The stress relaxation was relatively faster for modified 9Cr-1Mo steel especially for sharper notches and slower for 2.25Cr-1Mo steel, because of higher stress sensitivity of creep deformation in modified 9Cr-1Mo steel than that in 2.25Cr-1Mo and 9Cr-1Mo steels (section 3.3). Numerical analysis carried out by Yue et al. [115] revealed that the stress redistribution would be faster for brittle materials than that of ductile materials as observed in this investigation. Dyson et al. also observed the saturation in strengthening for 2.25Cr-1Mo steel at high notch acuity ratios. They indicated that the decrease in von-Mises stress resulted in notch strengthening in the steel, as observed experimentally in the present investigation (Fig. 5.1).

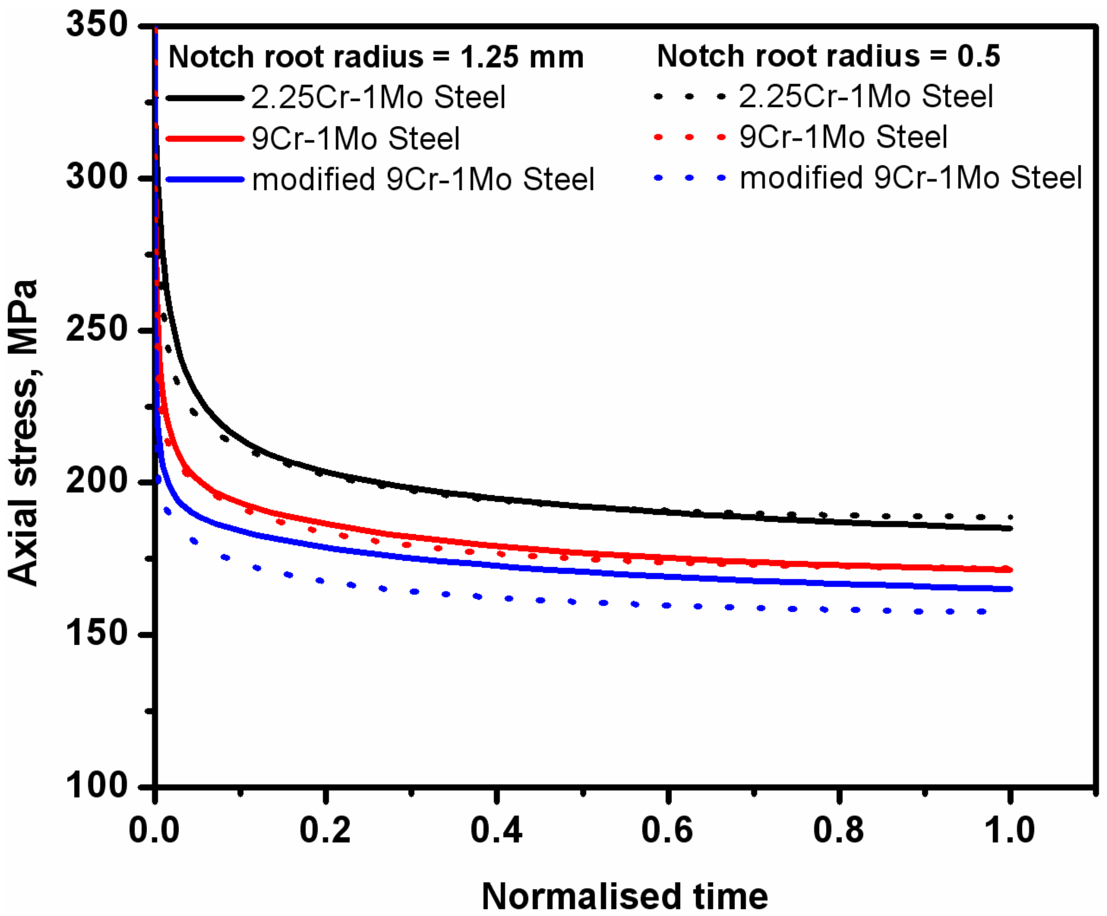

Fig. 5.28 Variation of axial stress as a function of normalized time to attain stationary state for all the steels at net applied stress of 210 MPa.

5.4.3 Assessment of variation in fracture appearance

Creep failure in materials occurs either by plasticity induced intragranular cavity nucleation and growth resulting in ductile dimple fracture appearance or by intergranular creep cavitation leading to brittle fracture appearance. Creep cavitation proceeds with the nucleation of creep cavities and their growth followed by linkage into discrete cracks leading to final failure. Intergranular creep cavity nucleation is generally associated with stress and strain concentrations at the discontinuities, such as precipitates, ledges, grain boundary triple points, etc. Nucleation of creep cavity under constrained condition imposed by (i) presence of notch in specimen and (ii) microstructural inhomogeneity, as in ferritic steel weldment, has been discussed extensively by Cane [47] and Goyal et al. [31] respectively. The importance of von-Mises stress in the nucleation of creep cavity has been reported by Nix et al. [6]. For the relatively shallow notches (notch acuity ratio < 4), the presence of relatively high and uniform von-Mises stress across notch throat plane (Fig. 5.23(a)) is expected to produce more or less uniform creep cavity nucleation across the notch throat plane. Growth of the nucleated creep cavity is influenced by the triaxial state of stress. The hydrostatic stress plays a significant role in cavity growth under constrained conditions. Presence of high hydrostatic stress at the central region of notch throat plane (Fig. 5.23(c)) would have caused preferential growth of the nucleated cavities. Thus, even though, nucleation of creep cavities occurred through out the notch throat plane of shallow notch, the cavities at the central region of notch throat plane would have grown faster. At some critical strain, plastic deformation becomes localized at the ligament between the cavities causing them to rupture by mechanical instability. This result in cavities coalescence and fracture follows. This mechanism becomes important under high strain-rate conditions as in the shallow notch, where significant strain is realized. Fracture surface with dimple appearance, Fig. 5.8(a), supports the view of above creep cavitation mechanism in the relatively shallow notches.

For relatively sharper notches (notch acuity ratio ≥ 4), von-Mises stress at the notch root region was found to be maximum, Fig. 5.23(a). As the nucleation of creep cavities is controlled by von-Mises stress through plastic deformation, nucleation of creep cavities is expected to be more in the notch root region. High principal stress along with high hydrostatic stress (Fig. 5.23(b) and 5.23(c)) would have led to the growth of the nucleated cavities at the near notch root region (Fig. 5.11). The cavity growth by principal stress occurs by diffusive transfer of material from cavity surface to the grain boundary [17]. The fracture surface appearance is expected to be intergranular as observed (Fig. 5.10(a)). Coalescence of the creep cavities would have led to the propagation of crack from the notch root region towards the central region of the notch throat plane. Final failure of the ligament at the central region of notch throat plane would have occurred due to mechanical instability, resulting in ductile dimple fracture appearance (Fig. 5.10(b)).

The factors that influence the creep fracture behaviour of material under triaxial state of stress as in notched specimen has been studied by Wu et al. [44]. The factors described are maximum principal stress and its location, strain at notch root, local vs. global events, hydrostatic stress and stress triaxiality. Among them, the most relevant factor has been suggested as the stress triaxiality. The stress triaxiality (ST) has been defined as [44]

$$ST = \frac{\sigma_m}{\sigma_{vm}} = \left(\frac{\sigma_1 + \sigma_2 + \sigma_3}{3} \right) \frac{1}{\sigma_{vm}} \tag{12}$$

The distribution of ST across the notch throat for notch acuity ratio of 2 and 10 are shown in Fig. 5.29(a) and (b) respectively.

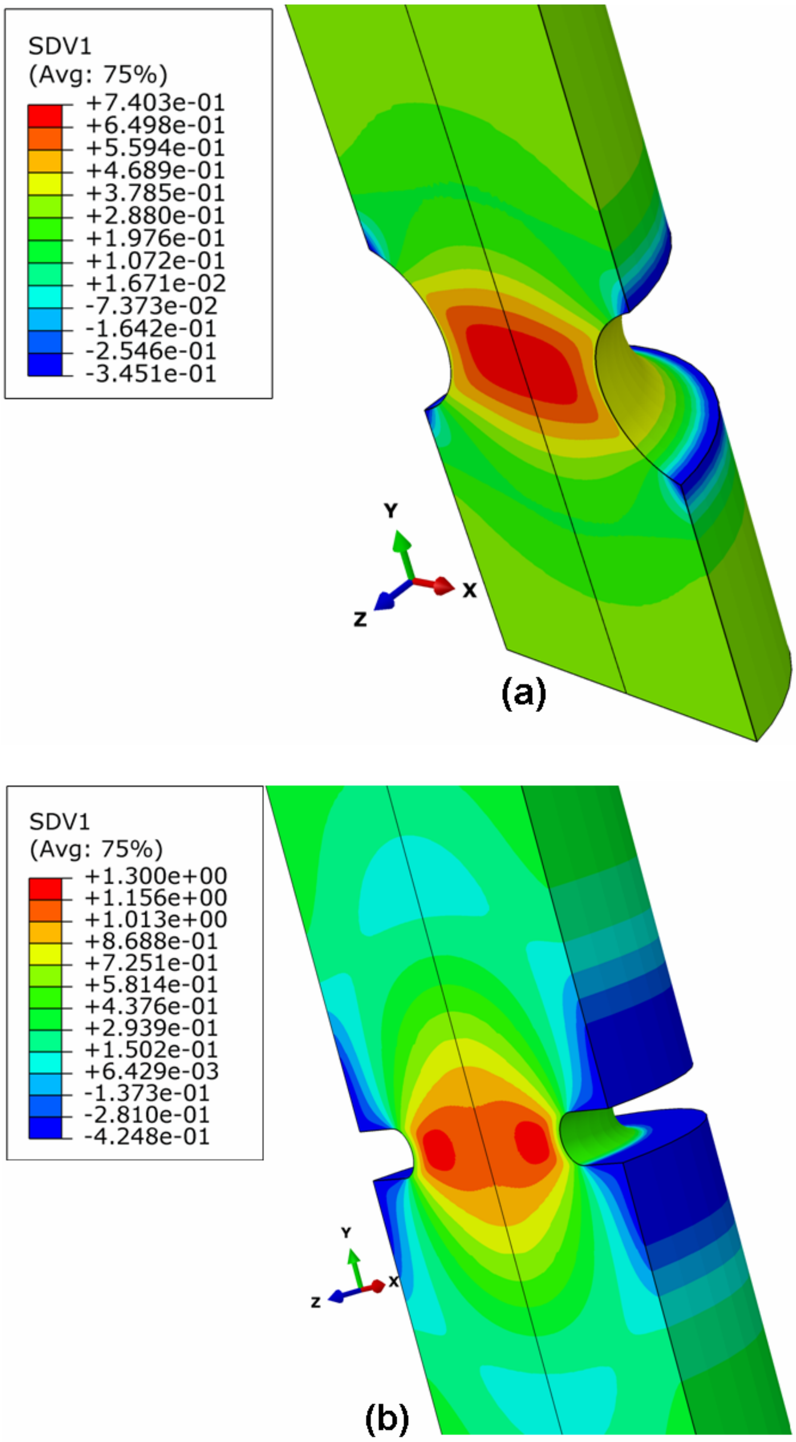

Fig. 5.29 Contour plots of stress triaxiality for notch acuity ratios of (a) 2 and (b) 10 after attaining the stationary state for 2.25Cr-1Mo steel at 210 MPa.

The stress triaxiality was found to be maximum at the central location of notch throat plane for the relatively shallow notches. The magnitude of the maximum value of ST increased and location shifted towards notch root with increase in sharpness of notch. If stress triaxiality is assumed to be the most important indicator of deformation under multiaxial state of stress, the fracture surface appearance indicated a higher void nucleation and growth near central region of notch for the relatively shallow notches, (Fig. 5.29(a)) and creep cavitation induced brittle fracture near notch root for the relatively sharper notch (Fig. 5.29(b)). Similar experimental observations are reported by Dyson et al. in Nimonic 80 [38] and Al-Abed et al. in 2.25Cr-1Mo steel [62] under multiaxial state of stress.

The prevalence of intergranular creep cavitation appearance in modified 9Cr-1Mo steel was more than that in 2.25Cr-1Mo and 9Cr-1Mo steel for a given applied stress and notch acuity ratio (Fig. 5.16). As discussed earlier, the stress triaxiality plays a significant role in governing the creep failure behaviour of materials. Distribution of stress triaxiality across the notch throat plane for notch acuity ratio of 10 at 210 MPa is shown in Fig. 5.30 for the steels. Stress triaxiality was normalized by yield stress to bring the effect of deformation characteristics of the individual steel into account. Maximum value of stress triaxiality was found to be in the decreasing order of 2.25Cr-1Mo, 9Cr-1Mo and modified 9Cr-1Mo steels. Relatively higher values of stress triaxiality have resulted in more creep cavitation in 2.25Cr-1Mo steel, as observed (Fig. 5.30(a)) with lower reduction in rupture ductility (Fig. 5.6). However, even though the presence of lower stress triaxiality for modified 9Cr-1Mo steel is expected to yield lower creep cavitation, the observed higher prevalence of intergranular brittle fracture appearance in the steel might be due to longer creep exposure (Fig. 5.16), which has facilitated the nucleated creep cavities to grow leading to intergranular creep cavitation with lower rupture ductility (Fig. 5.6).

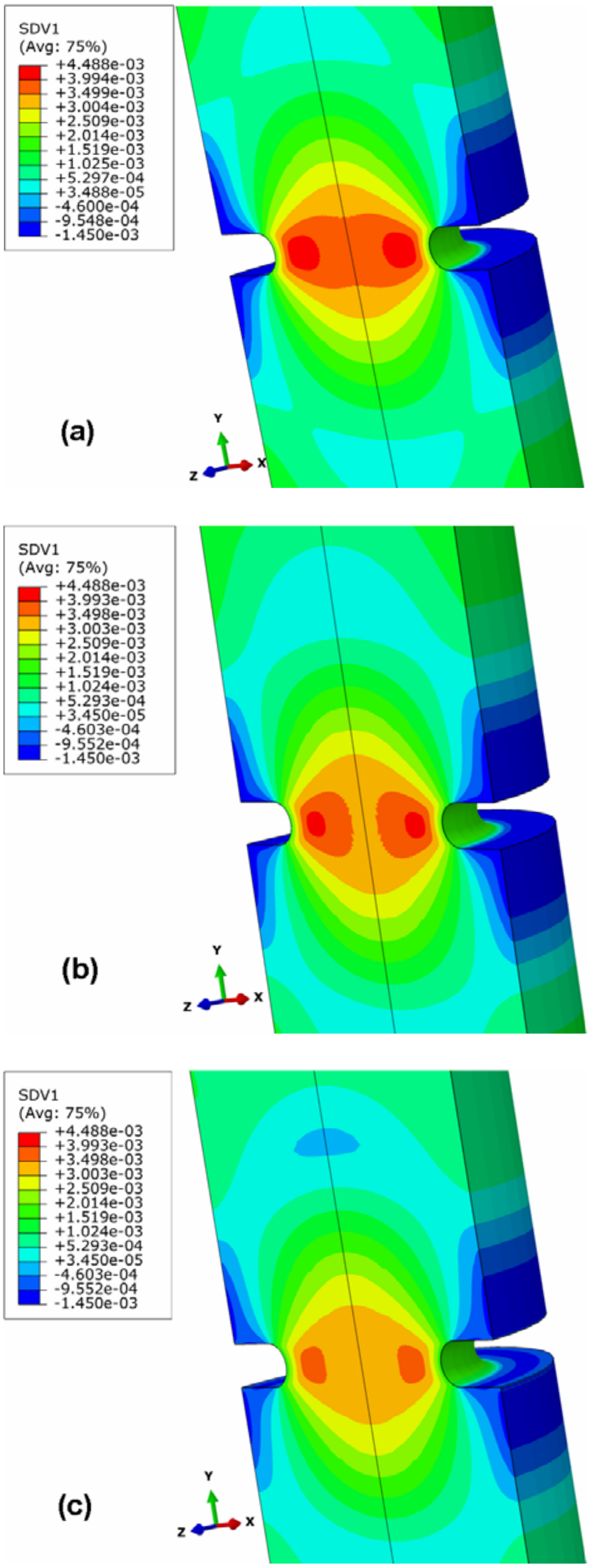

Fig. 5.30 Pictorial view of normalized stress triaxiality in notched specimens for (a) 2.25Cr-1Mo (b) 9Cr-1Mo and (c) modified 9Cr-1Mo steels at 210 MPa for a notch radius of 0.5 mm.

5.5 Conclusions

Based on the studies of creep rupture behaviour of 2.25Cr-1Mo, 9Cr-1Mo and modified 9Cr-1Mo steels under multiaxial state of stresses introduced by incorporation of notches with different sharpness in round specimens of the steels and finite element analysis of stress distribution across the notches, following conclusions have been made.

1. Presence of notch increased the creep rupture strength of the steels. With increase in notch sharpness creep rupture strength of the steels increased and tend to saturate for higher sharpness.
2. The extent of strengthening with notch sharpness was comparable for 2.25Cr-1Mo and 9Cr-1Mo steels; whereas the modified 9Cr-1Mo steel exhibited greater extent of strengthening.
3. The creep rupture ductility of the steels decreased in presence of notch and the extent of decrease was more for sharper notches. In presence of notch, the 9Cr-1Mo steel possessed more creep rupture ductility whereas modified 9Cr-1Mo steel the least.
4. Creep failure mode of the steels was found to change with notch sharpness. The failure mode changed from predominantly ductile dimple to mixed mode with the prevalence of brittle intergranular creep cavitation along with dimple with increase in notch sharpness. The 9Cr-1Mo steel was found to be less prone to creep cavitation than the other two steels.
5. The reduction in von-Mises stress across the notch throat plane, its higher extent for sharper notches, increased the creep rupture strength of the steels in presence of notches, which was more for sharper notches. The stress reduction was more for modified 9Cr-1Mo steel and least for 2.25Cr-1Mo, resulting in

more notch-strengthening in modified 9Cr-1Mo steel than in 2.25Cr-1Mo and 9Cr-1Mo steels.

6. Presence of higher maximum principal and hydrostatic stresses coupled with high von-Mises stress at the notch root region for relatively sharper notches resulted in intergranular creep cavitation at the notch root region.

CHAPTER 6

CREEP LIFE PREDICTION UNDER MULTIAXIAL STATE OF STRESS

Creep life prediction under multiaxial state of stress

6.1 Introduction

Structural components operating at high temperatures are subjected to creep damage, which results from the formation, growth and coalescence of cavities and also from the enhanced microstructural degradation in the form of coarsening of precipitates and dislocation substructure under stress [6]. The components are generally designed based on uniaxial creep data. However, the components experience multiaxial state of stress as a result of change in geometry, inhomogeneous microstructure as in weld joint [31,71] and also due to the mode of loading during service. In order to assess the life of such components, it is important to predict the creep rupture life of the component under multiaxial state of stress which influences the creep damage accumulation appreciably. The strengthening and fracture behaviour observed in the steels under investigation has been discussed in Section 5.2 and 5.3. This chapter will describe the concept of representative stress for predicting the creep rupture life under multiaxial state of stress. Further, FE analysis coupled with continuum damage mechanics has been utilized to assess the creep damage evolution under multiaxial state of stress to predict the creep rupture strength of the steels.

6.2 Representative stress concept

The creep rupture life of material under multiaxial state of stress depends on creep deformation and cavitation. The mechanisms associated with the creep deformation and cavitation has been discussed extensively under uniaxial and triaxial state of stresses by Nix [6] and Nix et al. [63], Cane [47] and Goyal et al. [31]. The creep rupture life under uniaxial loading is expressed in terms of the applied stress as

$$t_r = M\sigma^{-m} \tag{6.1}$$

where, m is the slope of the uniaxial creep rupture plot. Creep rupture life under multiaxial state of stress can also be described by an equation similar to uniaxial loading on incorporating a representative stress as

$$t_r = M\sigma_{rep}^{-m} \tag{6.2}$$

The representative stress, σ_{rep}, is defined as the stress applied to the uniaxial plain specimen, which would result in the same creep rupture life as that of notched specimen. If $\sigma_{rep} > \sigma_{\mathrm{net}}$ (where σ_{net} is the net applied stress in the notched specimen), the presence of notch decreases the rupture life of material and causes notch weakening; whereas, if $\sigma_{rep} < \sigma_{net}$, the presence of notch increases the rupture life of material resulting in notch strengthening.

Creep rupture under multiaxial state of stress depends on the components of stress viz., maximum principal stress, hydrostatic stress and von-Mises stress in governing the creep deformation and cavitation. It is widely reported that the (i) von-Mises stress controls the deformation and creep cavity nucleation processes [63], (ii) the maximum principal and hydrostatic stress control the continuum cavity growth whereas (iii) the maximum principal stress controls the stress directed diffusion controlled intergranular cavity growth [63]. The relative contribution of each of the stresses to representative stress in governing the creep rupture life under multiaxial state of stress depends on the material's deformation and fracture response to the stresses.

Many relationships are available in literature for multiaxial stress rupture criteria (MSRC) [65]. In the present investigation, the approaches proposed by Cane [61], Sdobyrev [55] and Hayhurst [58] and Nix et al. [63] have been used and compared for their suitability for estimation of representative stress for ferritic steels.

Extensive studies carried out by Cane [61] on 2.25Cr-1Mo steel revealed that the creep deformation and rupture of the material under multiaxial state of stress is predominantly governed by different stress components. The model proposed by Cane assumes that the cavity growth is constrained by the matrix deformation under multiaxial state of stress. The matrix deformation and creep cavitation are function of von-Mises and maximum principal stresses. The rupture life under multiaxial state of stress is represented as [61]

$$t_r = M\sigma_1^{-\gamma}\sigma_{vm}^{\gamma-m} \tag{6.3}$$

where γ is the material parameter, m is the stress sensitivity of rupture life (Eq. 6.1), σ_1 and σ_{vm} are maximum principal and von-Mises stress respectively. The representative stress in this criterion is defined as

$$\sigma_{rep} = \sigma_1^{\gamma/m}\sigma_{vm}^{(m-\gamma)/m} \tag{6.4}$$

The relative contributions of maximum principal and von-Mises stresses are determined by γ/m. When γ/m is close or equal to 0, the multiaxial stress rupture behaviour is predominantly controlled by von-Mises stress. If γ/m is close or equal to 1, the maximum principal stress predominantly governs the multiaxial stress rupture life. For 0<γ/m<1, the rupture life is governed by both the maximum principal and von-Mises stresses. In this model, creep deformation and cavitation are interdependent in governing the creep rupture life of material under multiaxial state of stress.

Sdobyrev [55] and Hayhurst [58] proposed the representative stress as the addition of maximum principal and von-Mises stresses with α as a parameter relating the contribution of each stress in creep fracture. The representative stress in this case is defined as

$$\sigma_{rep} = \alpha\sigma_1 + (1-\alpha)\sigma_{vm} \tag{6.5}$$

where α is the material constant. The relative contributions of each stress on rupture life of notched specimen are determined by α. The value of $\alpha = 1$ indicates that the creep rupture is controlled by maximum principal stress; whereas, $\alpha = 0$ indicates that the creep rupture is governed by von-Mises stress. In this model, the contribution of each stress is assumed to influence the creep deformation and cavitation independent of each other. Hayhurst et al. [60], based on the experimental data, established the value of α as 0.0, 0.7 and 0.75 for aluminum alloy, copper and 316 stainless steels respectively.

In another approach, Nix et al. [63] has proposed the concept of principal facet stress governing the multiaxial state of stress. The basis for principal facet stress lies on the fact that the creep cavitation occurs on the grain boundaries perpendicular to the principal stress. The principal facet stress is defined by the combination of principal stresses as

$$\sigma_{rep} = 2.24\sigma_1 - 0.62(\sigma_2 + \sigma_3) \tag{6.6}$$

where, σ_1 is the maximum principal stress and σ_2 and σ_3 are intermediate and minimum principal stresses respectively. This model is especially applicable when the material is prone to creep cavitation.

FE analysis of stress distribution across the notch throat plane, as discussed in Chapters 4 and 5, clearly revealed that the stresses vary significantly across the notch throat plane during creep exposure and attained the stationary state. In such a case, it is difficult to identify the location in notch throat plane at which the stresses should be considered in defining the representative stress for creep rupture life prediction. Webster et al. [48] and Hayhurst and Webster [43], based on FE analysis, have introduced the concept of skeletal point in notch throat plane for determining the representative stress.

6.3 Skeletal point concept

The skeletal point is the location in notch throat plane for a given notch geometry, where the variation of stress across the notch throat plane for different stress exponent '*n*' in Norton's law, intersects. The stresses estimated at this point have been implemented to characterize the creep deformation, damage and failure behaviour of materials under multiaxial state of stress by many investigators [71,60,75-78]. In the present investigation, the stress at the skeletal point has been used for predicting the creep rupture of 2.25Cr-1Mo, 9Cr-1Mo and modified 9Cr-1Mo steels under multiaxial state of stress introduced in plain specimen on incorporating notches of different notch acuity ratio.

In order to obtain the skeletal point stresses, FE analysis of stress distribution across the notch throat plane was carried out for various values of stress exponent '*n*' in Norton's law ($\dot{\varepsilon}_s = A\sigma^n$) ranging from 1 to 10 for net applied stress of 200 MPa. The value of coefficient A was obtained based on the creep strain rate of 10^{-5} h^{-1}. The variations of maximum principal, von-Mises and hydrostatic stresses across the notch throat plane for different values of stress exponent '*n*' are shown in Fig. 6.1 and Fig. 6.2 for notch acuity ratio of 2 and 10 respectively. Similar results were also obtained for other notch acuity ratios. It was observed that except for stress exponent of 1 and 3, there exists a skeletal point at which stress variation for different stress exponent intersects. Stress exponent of 1 and 3 are not significant in this investigation since the creep deformation in the steels under investigation is controlled by dislocation creep mechanism having '*n*' value more than 4 (Fig. 3.4). Similar observations have been

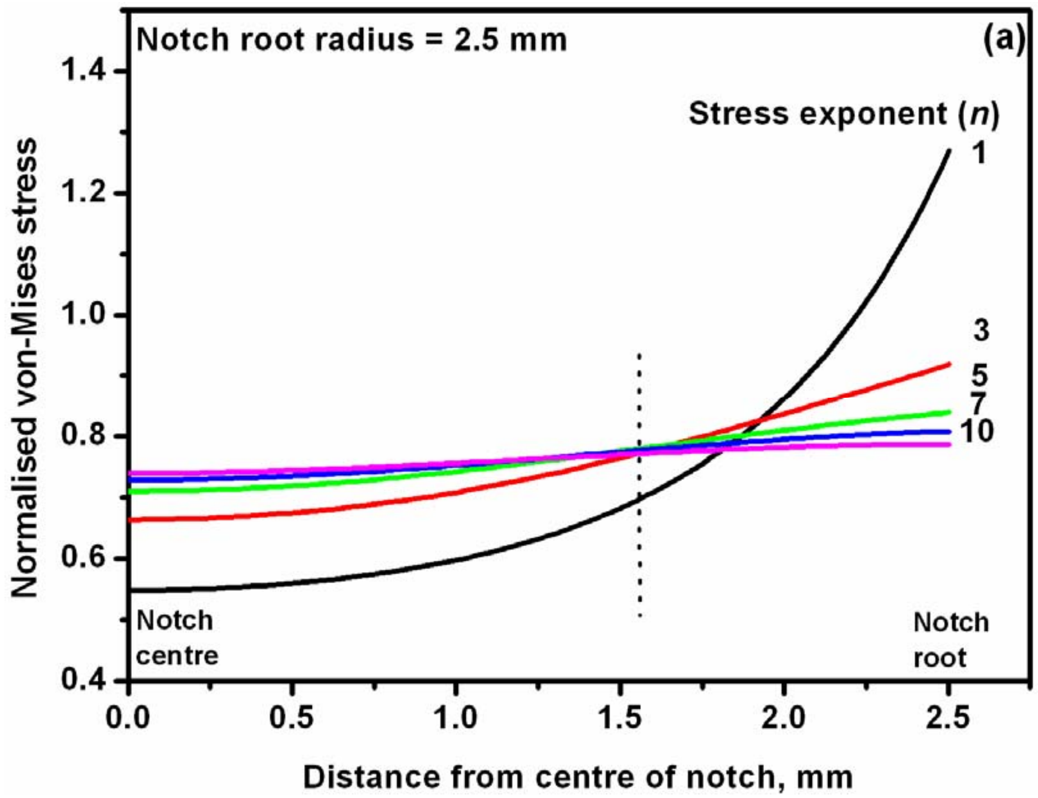
Notch root radius = 2.5 mm
(a)
Stress exponent (n)
1
3
5
7
10
Notch centre
Notch root
Normalised von-Mises stress
Distance from centre of notch, mm
0.4
0.6
0.8
1.0
1.2
1.4
0.0
0.5
1.0
1.5
2.0
2.5

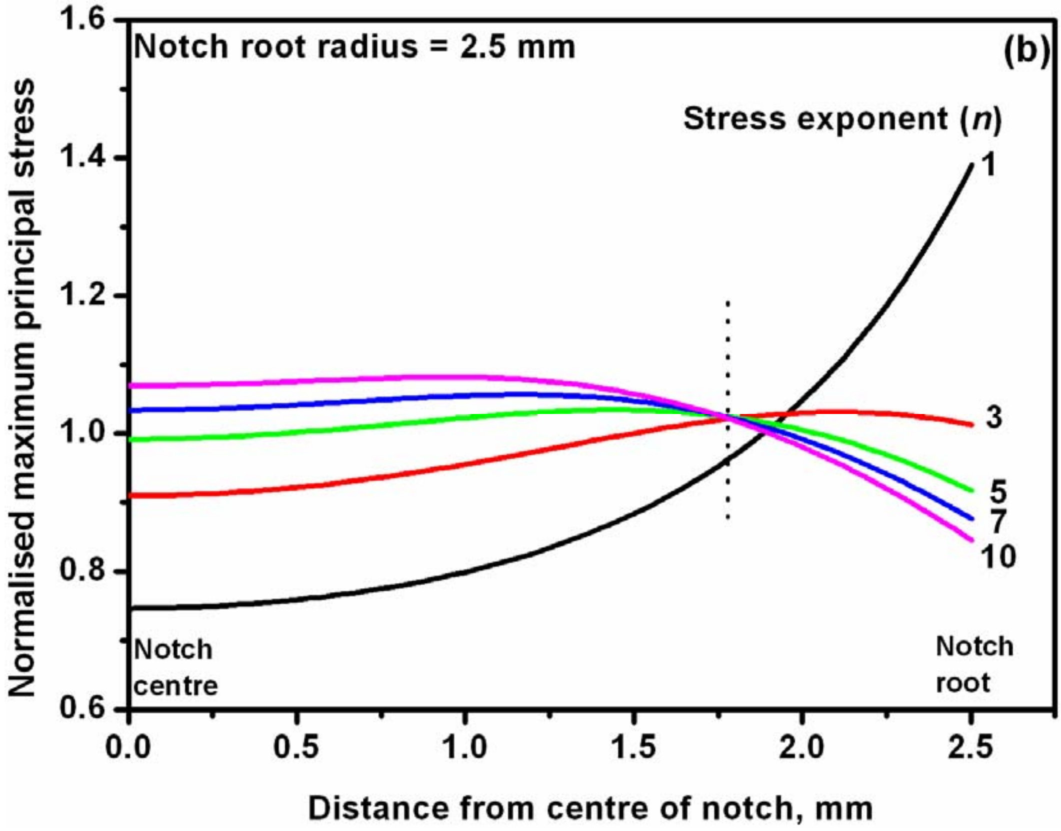
Notch root radius = 2.5 mm
(b)
Stress exponent (n)
1
3
5
7
10
Notch centre
Notch root
Normalised maximum principal stress
Distance from centre of notch, mm
0.6
0.8
1.0
1.2
1.4
1.6
0.0
0.5
1.0
1.5
2.0
2.5

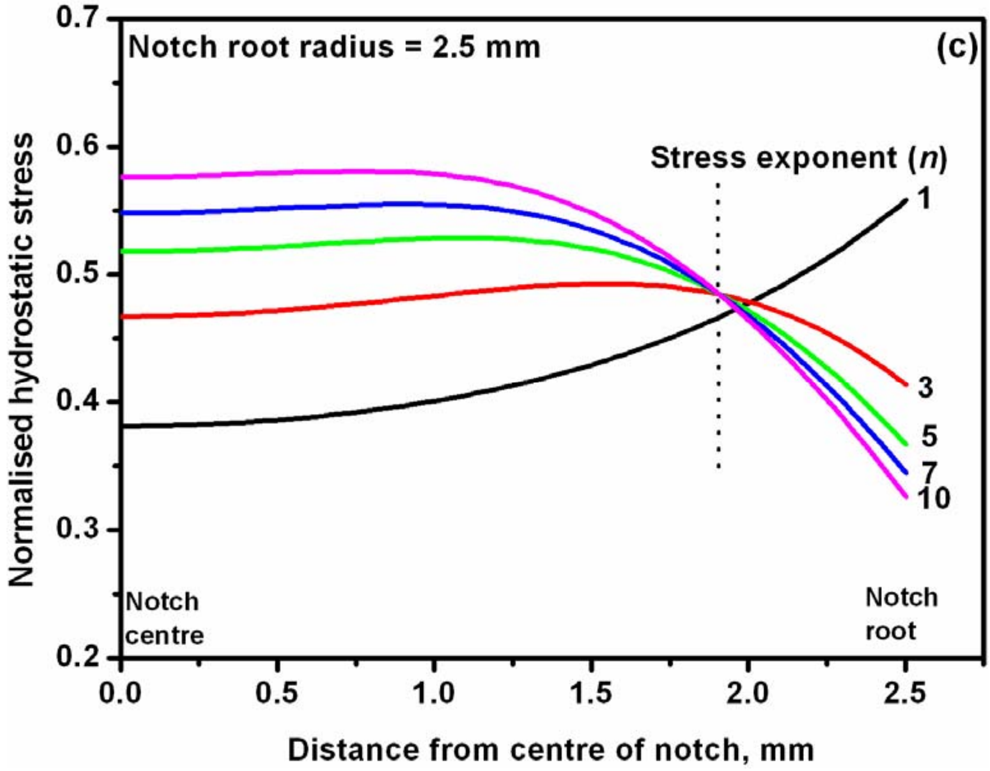

Fig. 6.1 Variation of normalized (a) von-Mises, (b) maximum principal and (c) hydrostatic stress across the notch throat plane for different values of stress exponent (Notch acuity ratio = 2).

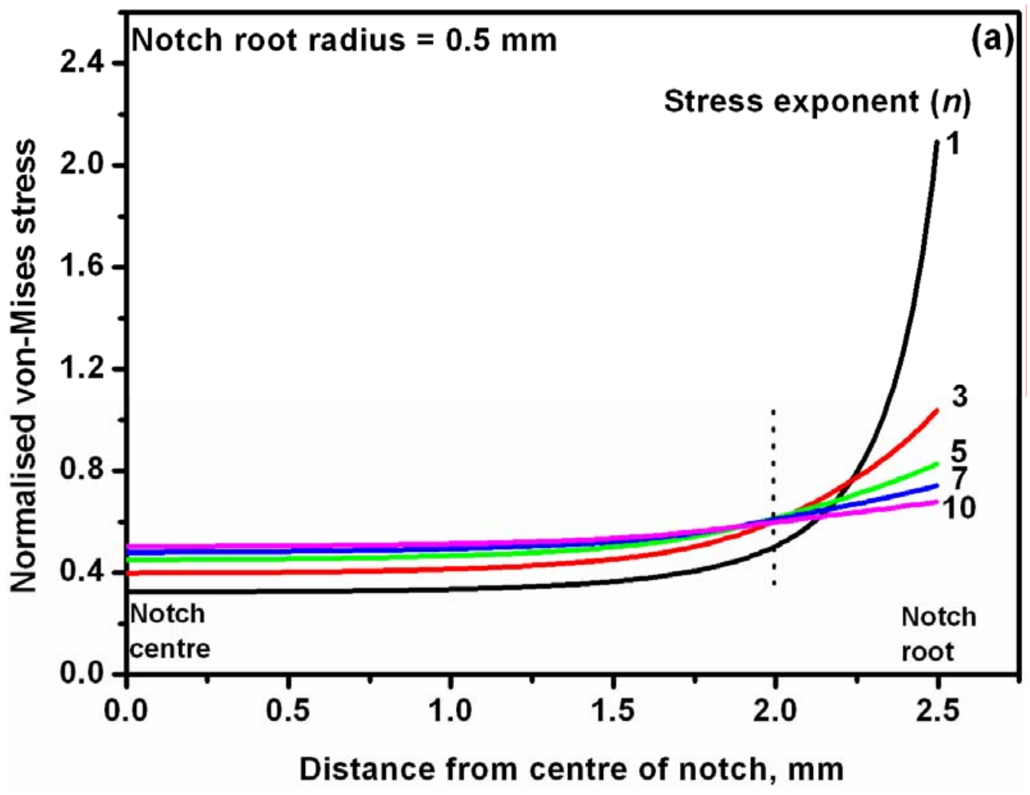

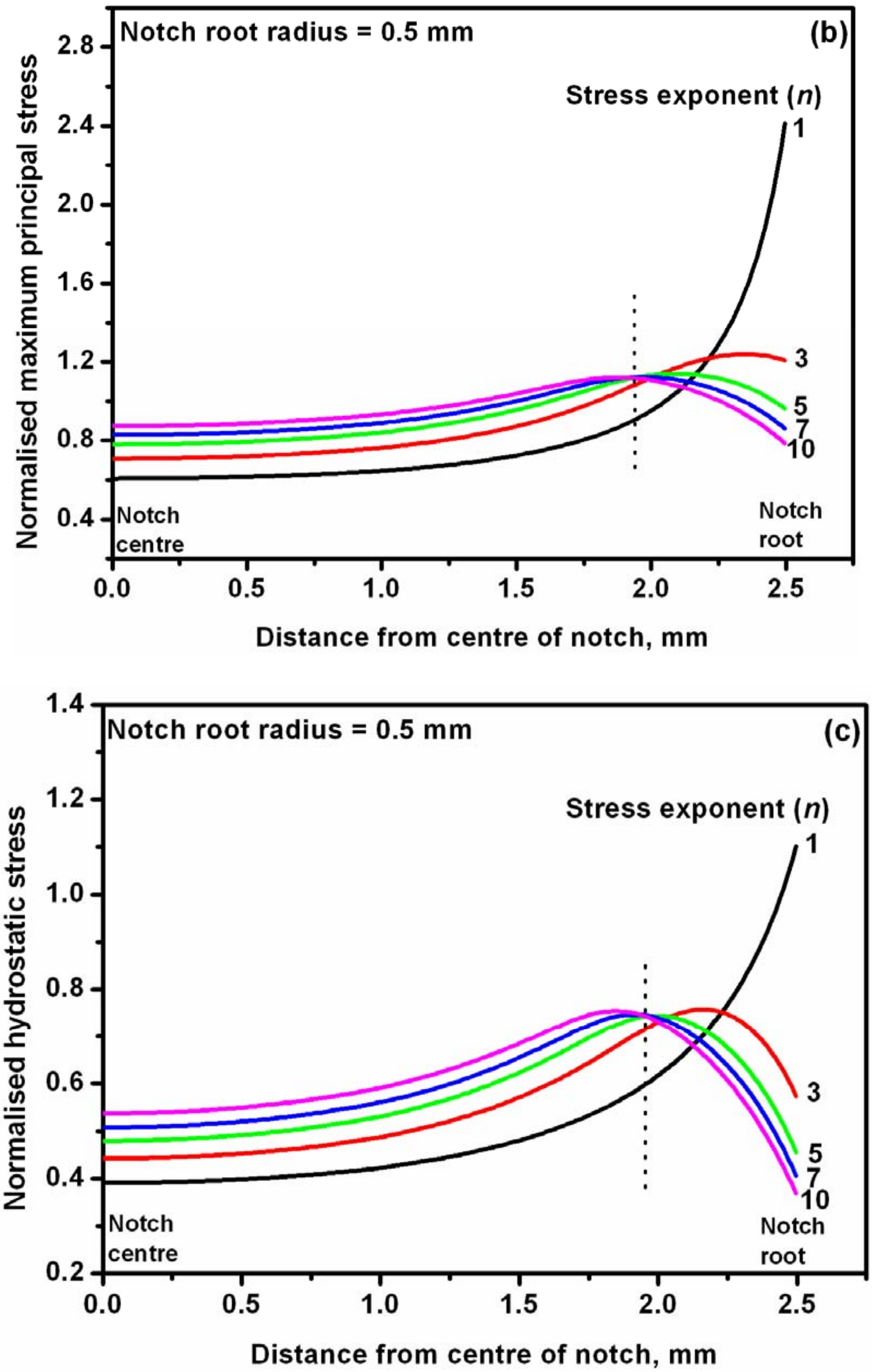

Fig. 6.2 Variation of normalized (a) von-Mises, (b) maximum principal and (c) hydrostatic stress across the notch throat plane for different values of stress exponent (Notch acuity ratio = 10).

reported by Webster et al. [48]. For a given notch geometry, the radial position of skeletal point remained in a narrow band of distance for all the stresses. The radial position of skeletal point shifted from close to centre towards the notch root and tends to saturate for higher notch acuity ratio.

Variation of skeletal point stresses with notch acuity ratio is shown in Fig. 6.3. The maximum principal and hydrostatic stresses at skeletal point increased with notch acuity ratio and tend to saturate at higher notch acuity ratio; whereas von-Mises stress decreased with increase in notch acuity ratio. The value of maximum principal stress at the skeletal point was more than the net applied stress. However, the von-Mises and hydrostatic stresses at the skeletal point were lower than the net applied stress for all notch acuity ratios. The stresses at the skeletal point for a given notch acuity ratio and net applied stress can be calculated by multiplying the normalized stresses, Fig. 6.3, with the net applied stress.

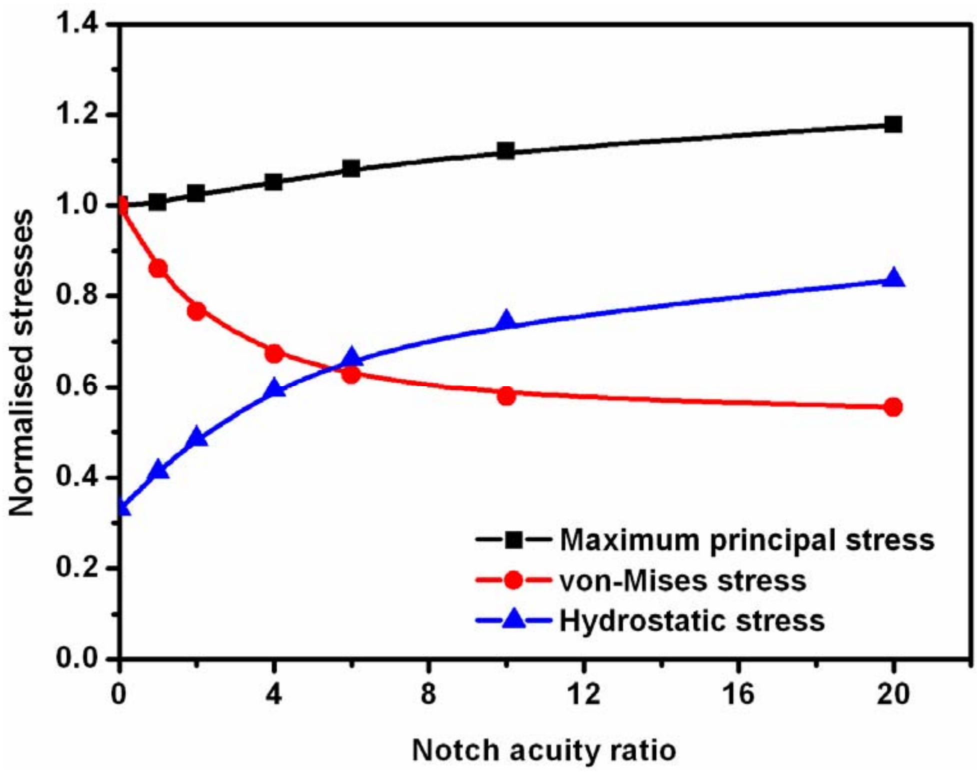

Fig. 6.3 Variation of skeletal point stresses as a function of notch acuity ratio.

6.4 Creep life prediction based on representative stress

6.4.1 Hayhurst model

The model proposed by Hayhurst [58] relates the representative stress as algebraic sum of maximum principal stress and von-Mises stress incorporating a material dependent parameter influencing the contribution of each stress on multiaxial stress rupture criteria, Eq. 6.5. In order to determine the parameter (α) for these steels under tested conditions, regression analysis was carried out for the representative stress (σ_{rep}) based on skeletal point stresses for each notch geometry. The best fit value of α was found out to be 0.12, 0.18 and 0.07 for 2.25Cr-1Mo, 9Cr-1Mo and modified 9Cr-1Mo steel, respectively, Fig. 6.4. The creep rupture life of the steels under multiaxial state of stress is considered to be governed predominantly by von-Mises stress with only 12 %, 18 % and 7 % maximum principal stress for 2.25Cr-1Mo, 9Cr-1Mo and modified 9Cr-1Mo steel, respectively. Representation of multiaxial creep data in terms of representative stress as a function of rupture life for all the steels with optimized value of α is shown in Fig. 6.5. A high value of correlation coefficient (0.96 to 0.98) clearly indicates that multiaxial creep rupture behaviour of the materials is well represented by Hayhurst model.

6.4.2 Cane Model

The model proposed by Cane [61] relates the representative stress as the multiplication of the maximum principal stress and von-Mises stress incorporating a material dependent parameter influencing the contribution of each stress on multiaxial stress rupture criteria, Eq. 6.4. In order to determine the parameter (γ) for these steels under conditions of testing, regression analysis was carried out for the representative stress (σ_{rep}) based on skeletal point stresses for each notch geometry. The optimized value of γ for 2.25Cr-1Mo, 9Cr-1Mo and modified 9Cr-1Mo steel was found to be 1.0, 1.9 and 1.1 respectively, Fig. 6.6. The variation of representative stress as a function of creep life for all the steels with optimized value of γ is shown in Fig. 6.7. A high value of correlation coefficient (0.96 to 0.98) clearly indicates that multiaxial creep rupture behaviour of the materials is well represented by Cane model.

6.4.3 Nix Model

The representative stress considered as principal facet stress determined based on Eq. 6.6 has been plotted against the rupture life in Fig. 6.8. The multiaxial creep rupture lives of the steels were not found to be represented well based on representative stress calculated base on the Nix model. The multiaxial creep data was found not to superimpose with the uniaxial creep data. Nix model is particularly applicable for creep cavity prone materials. However, the steels used in the present investigation are not very prone to intergranular creep cavitation.

Both the models proposed by Hayhurst and Cane represented the creep behaviour of the investigated steels under multiaxial state of stress well. However, the model proposed by Cane [61] would be preferable in terms of the physical processes occurring in the materials during creep exposure. Browne et al. [116] and Aplin et al. [65] commented that the creep deformation and damage incurred by different components of stresses in multiaxial state of stress under creep condition are not independent to each other and hence can not be represented as an algebraic sum of their contribution. Based on this understanding, further analysis of creep damage and rupture life prediction have been carried out adopting the model proposed by Cane [61].

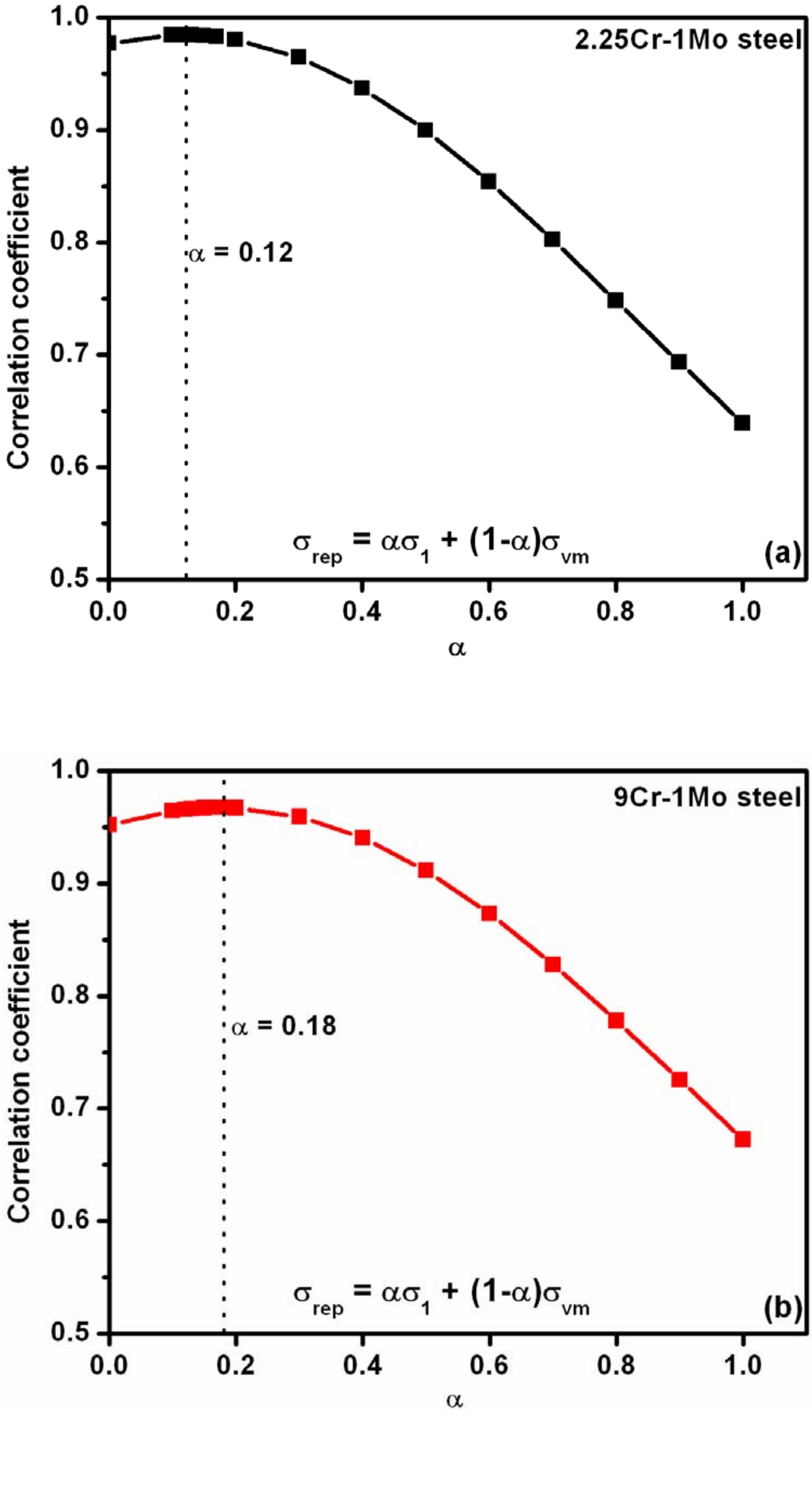

2.25Cr-1Mo steel
α = 0.12
σrep = ασ1 + (1-α)σvm
(a)
Correlation coefficient
α
1.0
0.9
0.8
0.7
0.6
0.5
0.0
0.2
0.4
0.6
0.8
1.0
9Cr-1Mo steel
α = 0.18
σrep = ασ1 + (1-α)σvm
(b)

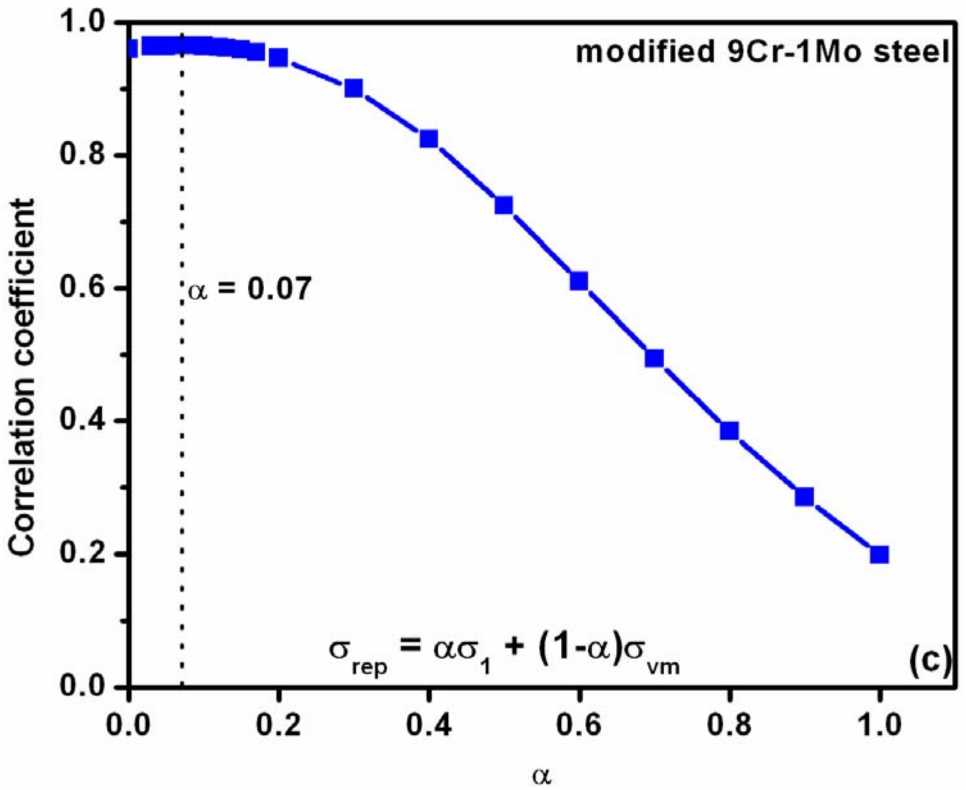

Fig. 6.4 Optimization of the value of α in the representative stress for (a) 2.25Cr-1Mo, (b) 9Cr-1Mo and (c) modified 9Cr-1Mo steels.

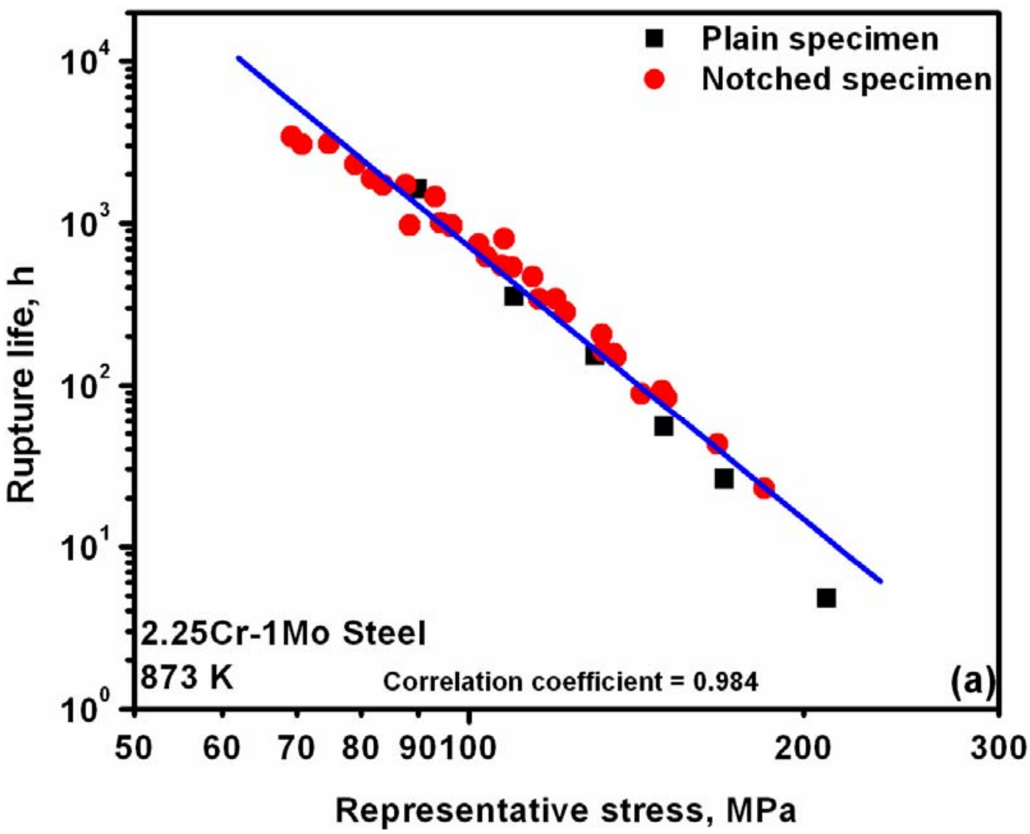

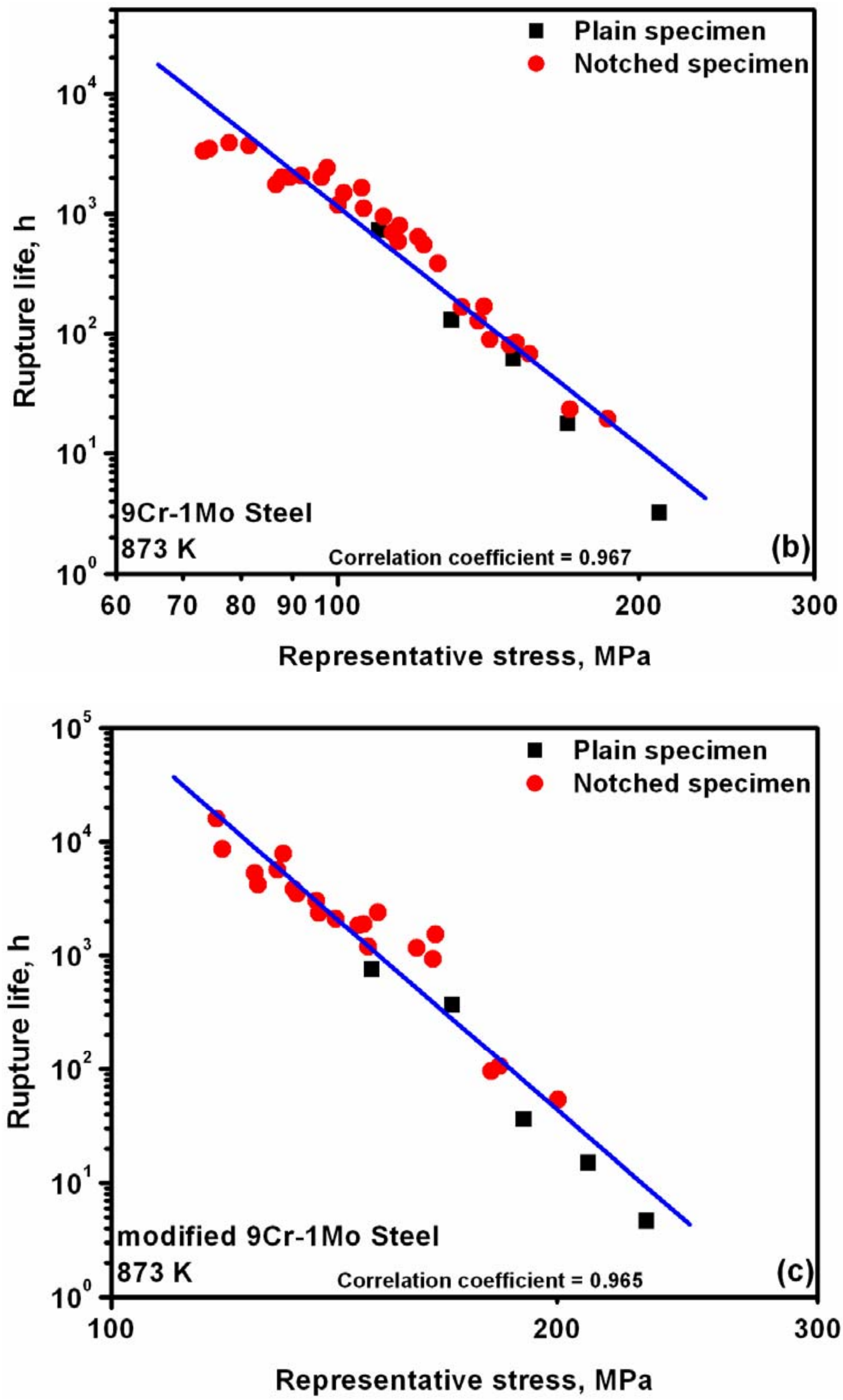

Fig. 6.5 Presentation of multiaxial creep rupture data by representative stress calculated based on Hayhurst model, for (a) 2.25Cr-1Mo, (b) 9Cr-1Mo and (c) modified 9Cr-1Mo steel.

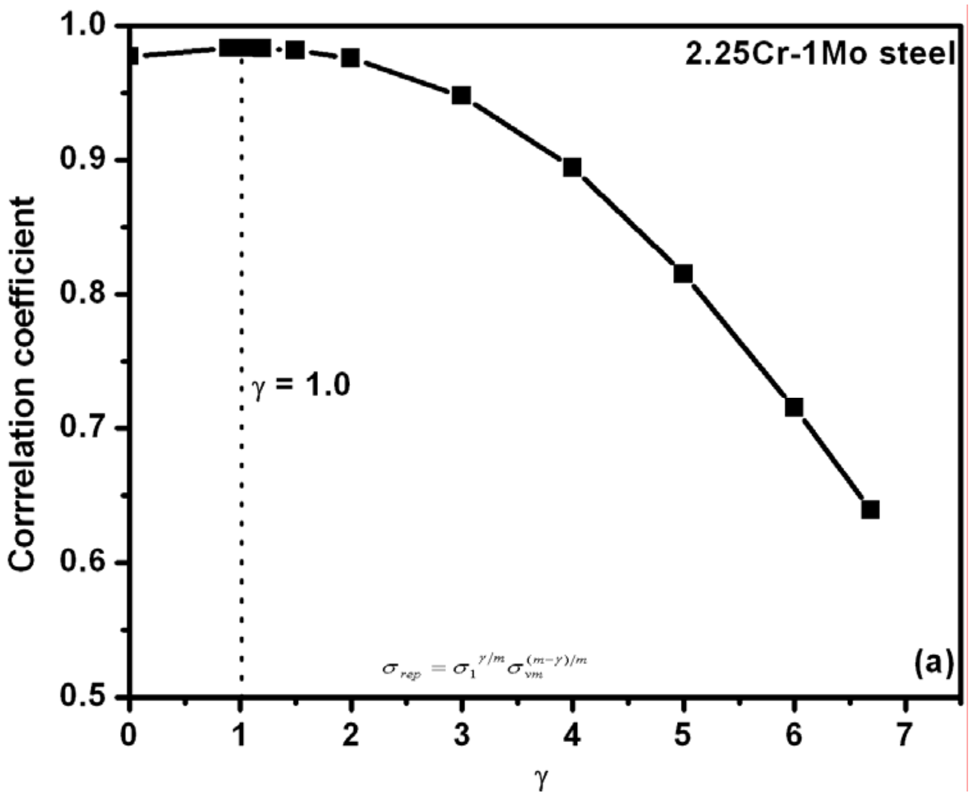

2.25Cr-1Mo steel
Correlation coefficient
γ = 1.0
$\sigma_{rep} = \sigma_1^{\gamma/m} \sigma_{vm}^{(m-\gamma)/m}$
(a)
γ

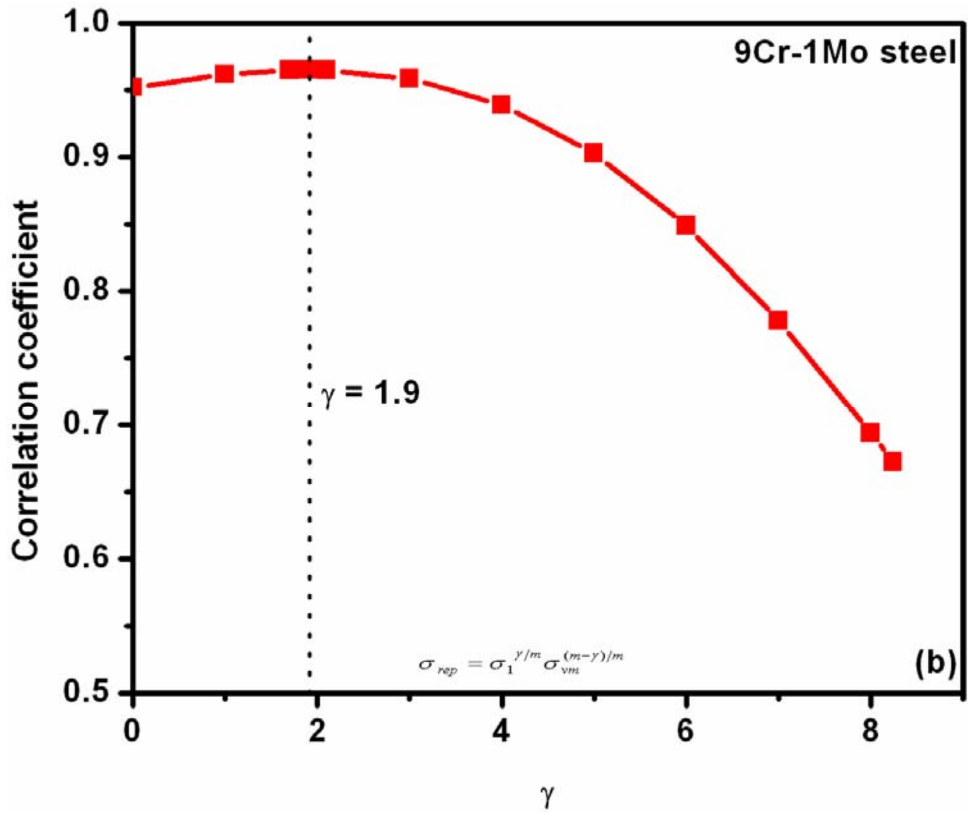

9Cr-1Mo steel
Correlation coefficient
γ = 1.9
$\sigma_{rep} = \sigma_1^{\gamma/m} \sigma_{vm}^{(m-\gamma)/m}$
(b)
γ

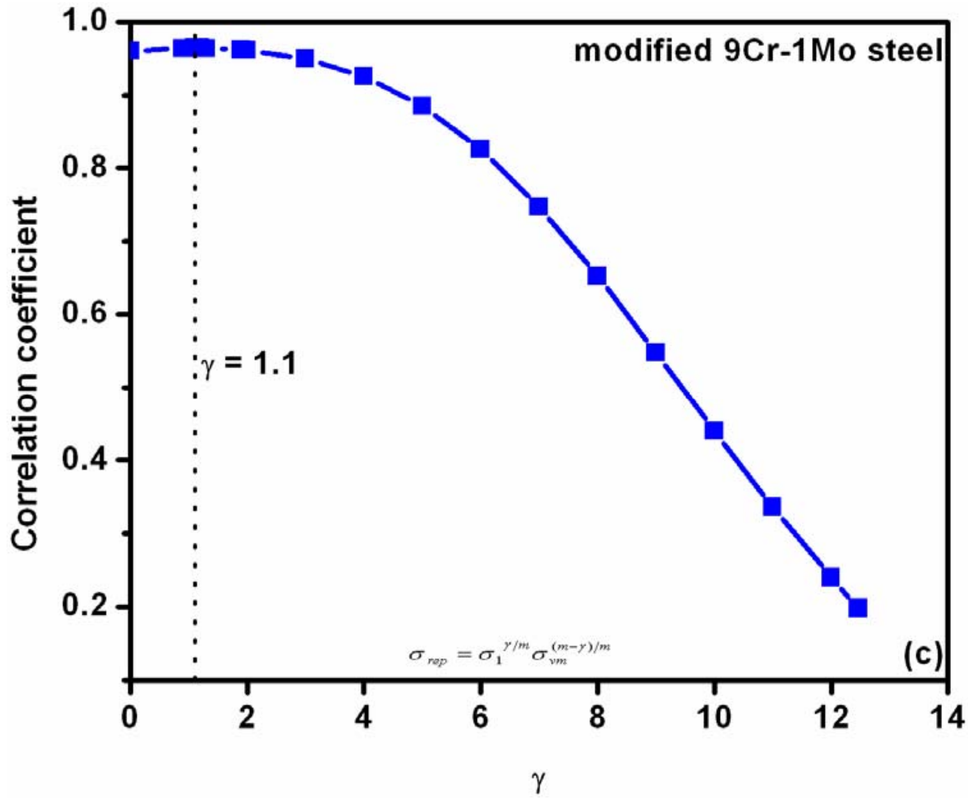

Fig. 6.6 Optimization of the value of γ in the representative stress for (a) 2.25Cr-1Mo, (b) 9Cr-1Mo and (c) modified 9Cr-1Mo steels.

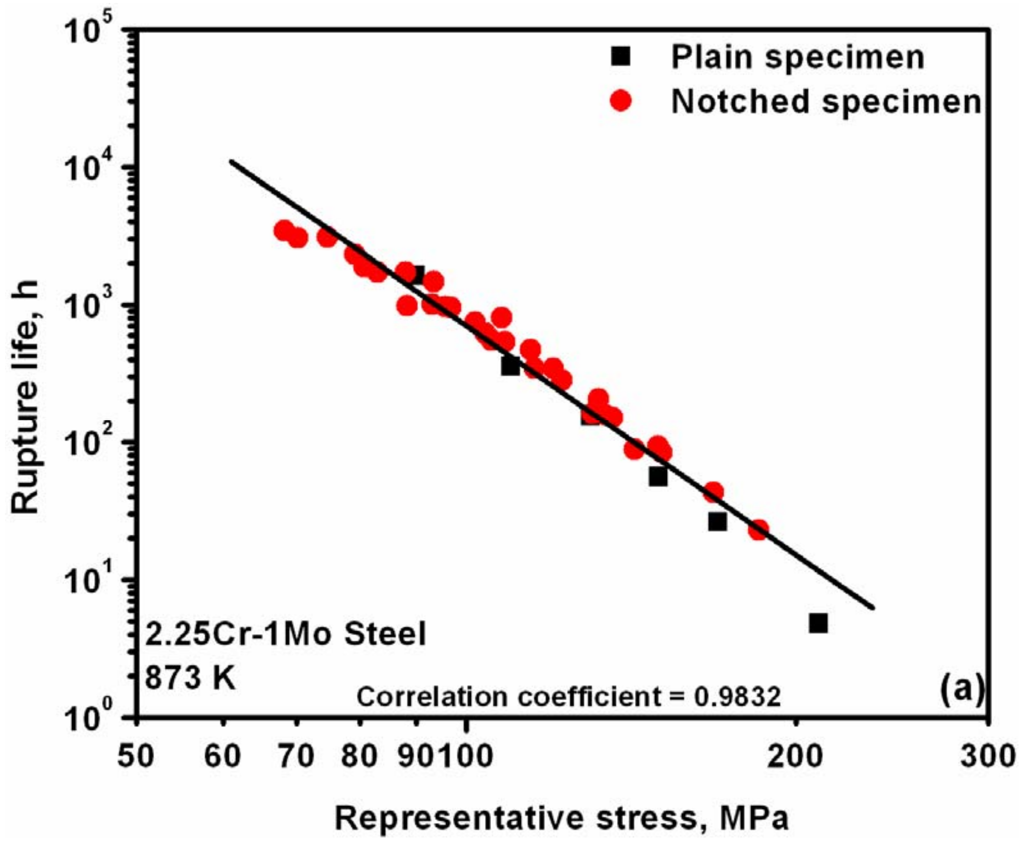

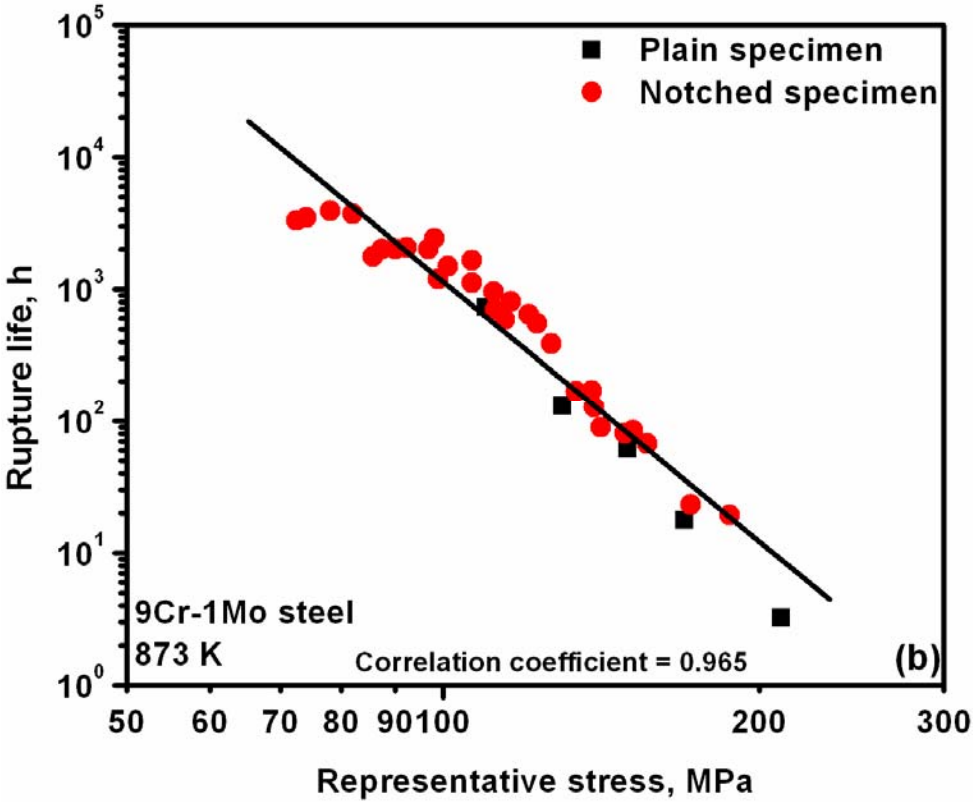

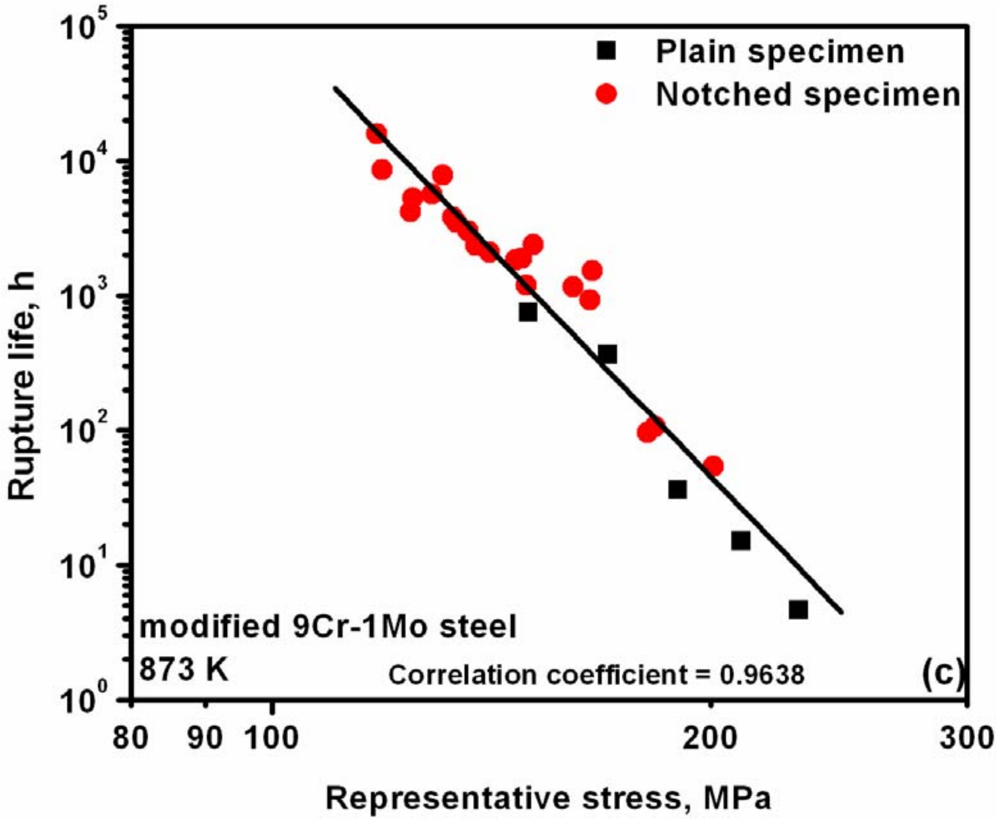

Fig. 6.7 Presentation of multiaxial creep rupture data by representative stress calculated based on Cane model, for (a) 2.25Cr-1Mo, (b) 9Cr-1Mo and (c) modified 9Cr-1Mo steel.

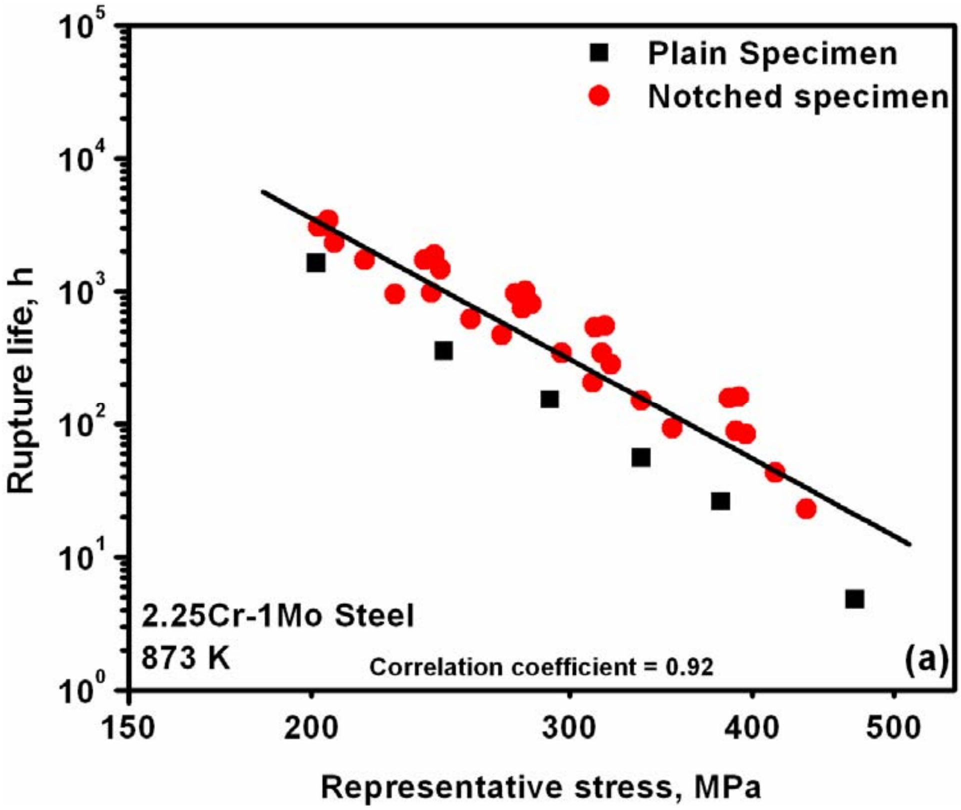

Plain Specimen
Notched specimen
Rupture life, h
2.25Cr-1Mo Steel
873 K
Correlation coefficient = 0.92
(a)
Representative stress, MPa

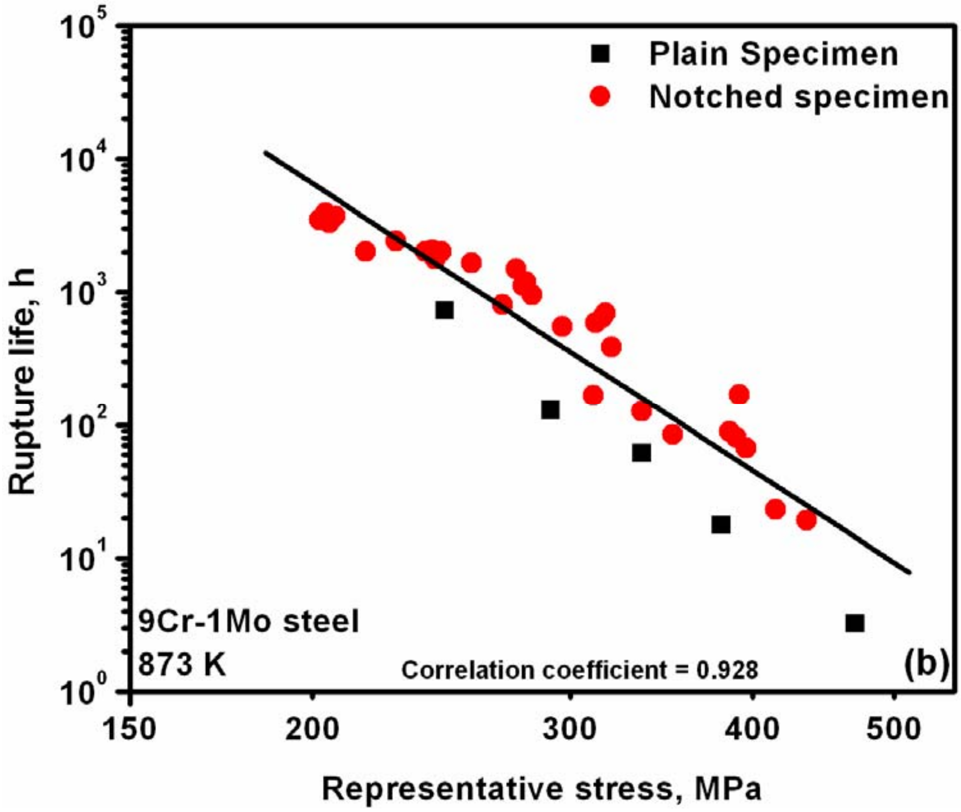

Plain Specimen
Notched specimen
Rupture life, h
9Cr-1Mo steel
873 K
Correlation coefficient = 0.928
(b)
Representative stress, MPa

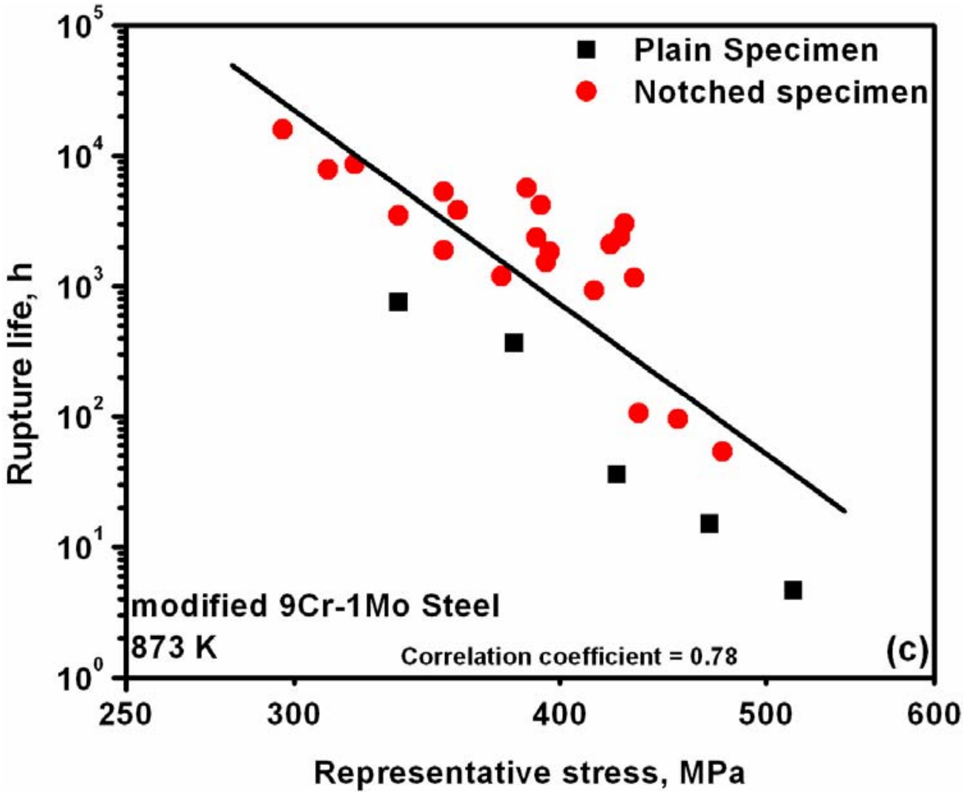

Fig. 6.8 Presentation of multiaxial creep rupture data in terms of representative stress as principal facet stress for (a) 2.25Cr-1Mo, (b) 9Cr-1Mo and (c) modified 9Cr-1Mo steels.

6.5 Creep damage and life prediction based on FE analysis coupled with CDM

FE analysis coupled with continuum damage mechanics (FE-CDM) has been extensively used for creep damage and rupture life prediction under multiaxial state of stress [71,60,75-78]. In this investigation, the prediction of creep rupture life under uniaxial and multiaxial creep condition has also been carried out based on FE analysis coupled with CDM. FE analysis of creep damage was carried out using ABAQUS finite element solver incorporating the creep damage law proposed by Kachanov [23] and creep rate equation (Eq. 2.1) in VUMAT subroutine. A user material subroutine VUMAT was written in FORTRAN and implemented in the ABAQUS Explicit for calculating the stresses, creep strains and damage in the plain and notched specimens. In order to predict the creep rupture life of plain specimen, B and ϕ coefficients of creep damage (Eq. 2.2) were obtained by trial and error method considering the good fit of estimated creep strain and rupture life using Eq. 2.6 with the experimental values. The values of material constants used in the analysis are given in Table 6.1.

VSPRINC utility subroutine was used for calculating the maximum principal stress at each integration point which was used for estimating representative stress along with von-Mises stress. The rate equations for creep strain (Eq. 2.1) and damage (Eq. 2.2) were solved and increment of variables was calculated and at the end of increment, all the variables were updated within the VUMAT subroutine and passed on to main program. The critical value of damage parameter was chosen as 0.5. As the damage parameter increased beyond this value, the accelerated creep rate led to severe distortion of the elements. The creep damage produced in the steels under uniaxial and multiaxial state of stress has been calculated to estimate the creep rupture life.

Table 6.1 Elastic, creep and damage constants of the steels at 873 K

Material	E (GPa)	υ	A	n	χ	ϕ	B
2.25Cr-1Mo steel	160	0.3	9.17×10^{-17}	6.02	6.69	4.8	0.91×10^{-17}
9Cr-1Mo steel	160	0.3	1.27×10^{-21}	8.34	8.24	10.0	2.076×10^{-21}
modified 9Cr-1Mo steel	160	0.3	3.57×10^{-33}	12.92	12.47	11.1	0.66×10^{-31}

6.5.1 Uniaxial creep

The VUMAT subroutine was first tested for prediction of creep strains and rupture lives of the steels under uniaxial state of stress before applying it to multiaxial state of stress. The comparison of estimated creep curves based on FE-CDM with the analytically derived creep curves based on CDM (Eq. 2.8) and experimental data is shown in Fig. 6.9.

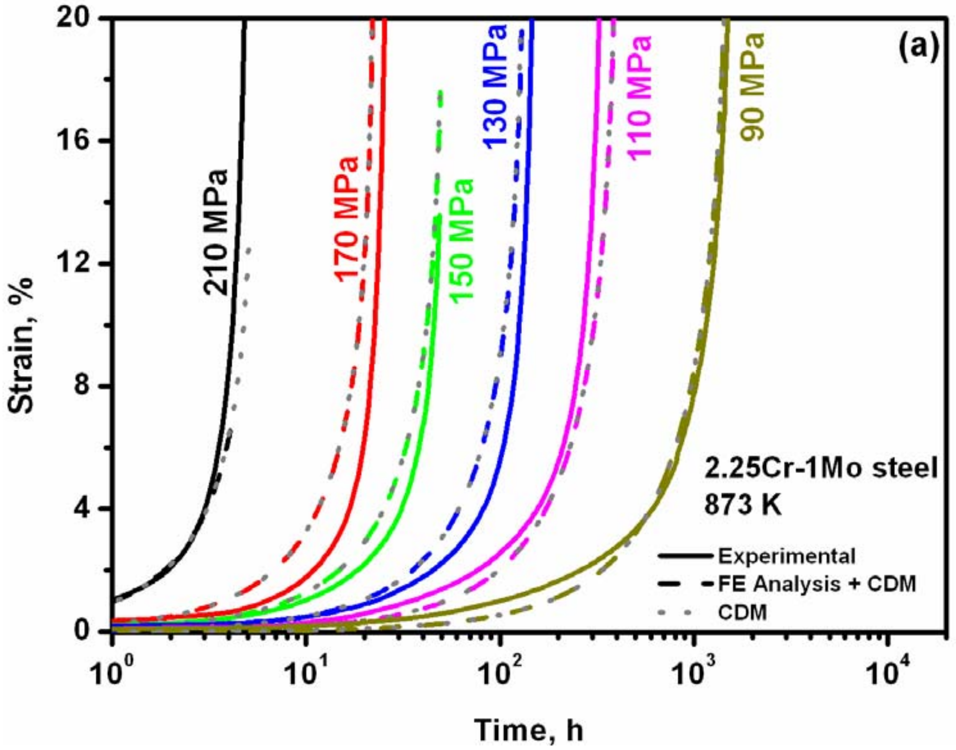
(a)
Strain, %
Time, h
210 MPa
170 MPa
150 MPa
130 MPa
110 MPa
90 MPa
2.25Cr-1Mo steel
873 K
Experimental
FE Analysis + CDM
CDM

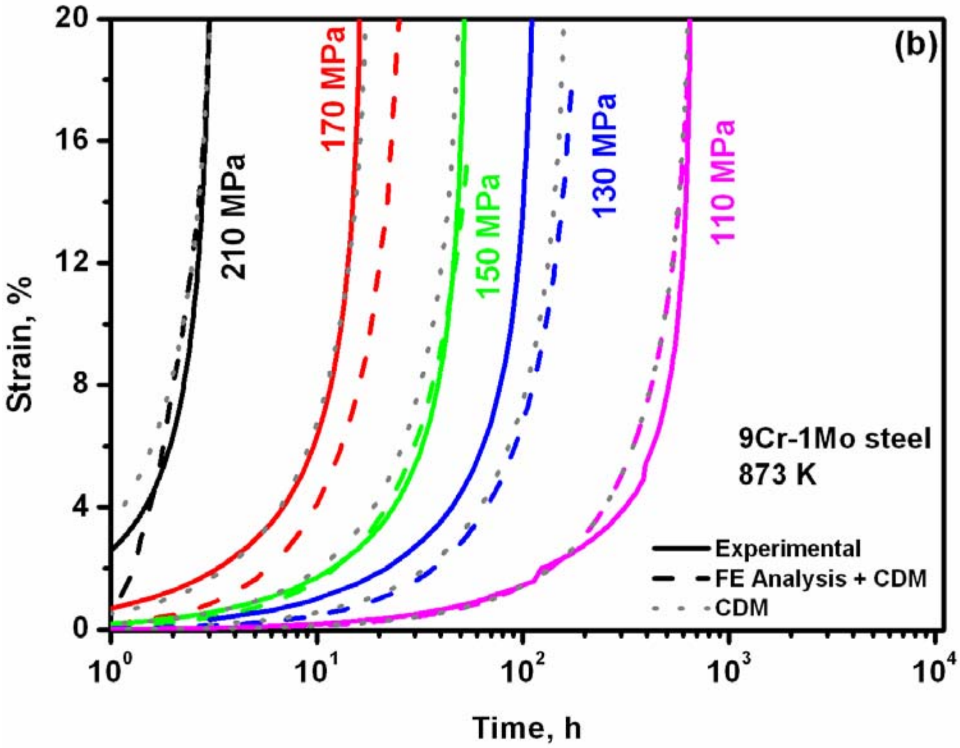
(b)
Strain, %
Time, h
210 MPa
170 MPa
150 MPa
130 MPa
110 MPa
9Cr-1Mo steel
873 K
Experimental
FE Analysis + CDM
CDM

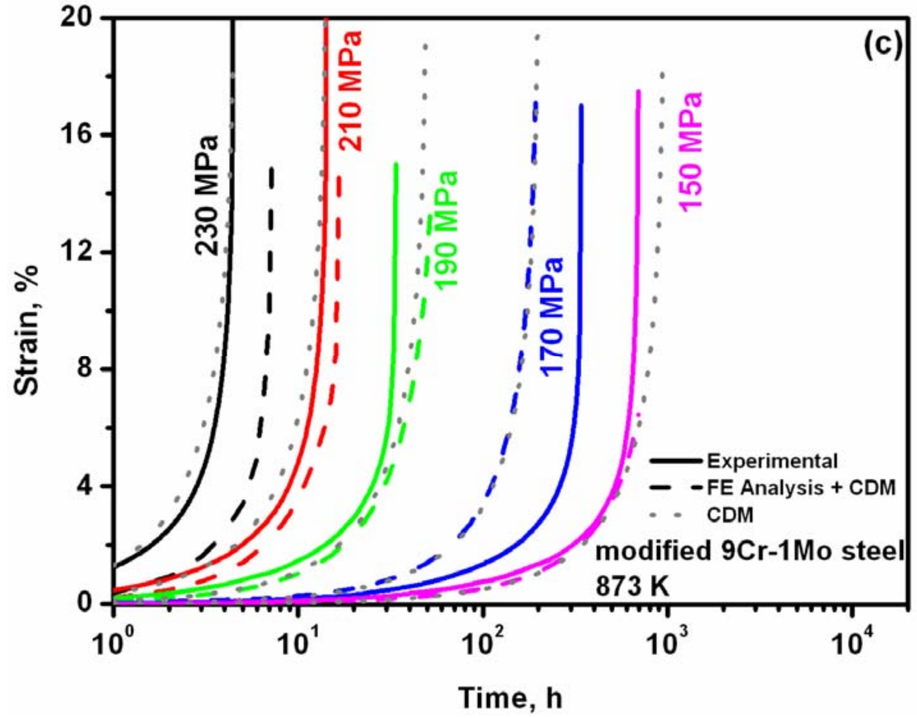

Fig. 6.9 Comparison of creep strain in experiments, FE-CDM and CDM analysis at different stress levels and 873 K for (a) 2.25Cr-1Mo, (b) 9Cr-1Mo and (c) modified 9Cr-1Mo steels.

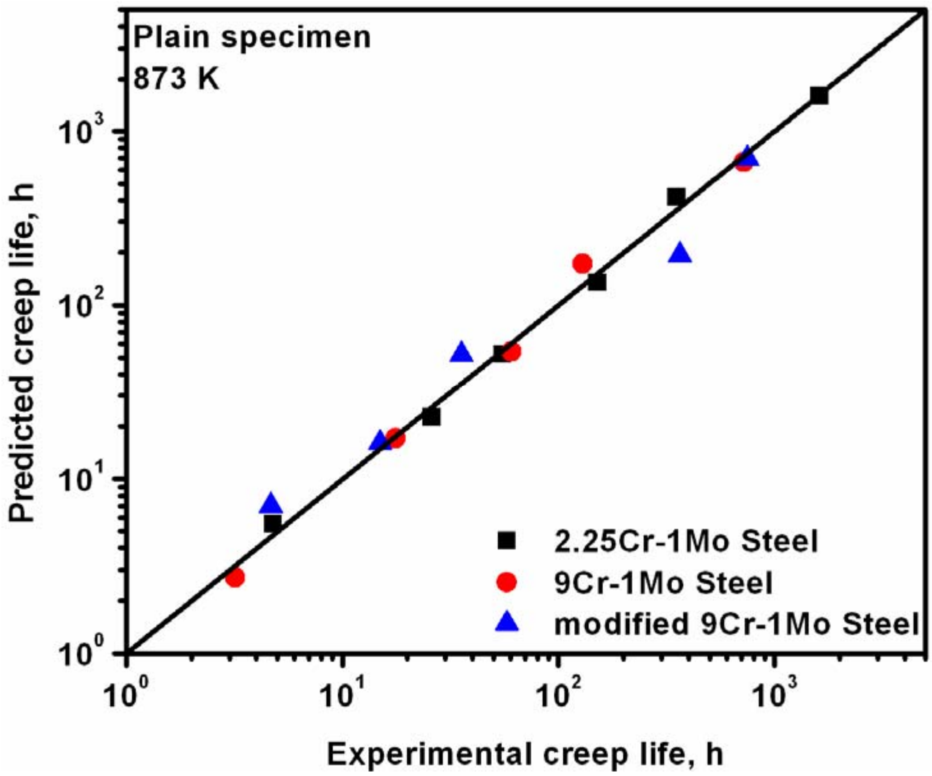

Fig. 6.10 Prediction of creep rupture life of plain specimens at various applied stresses and 873 K for all the steels.

The predicted creep curves based on FE-CDM were found to be in good agreement with the experimental creep curves for 2.25Cr-1Mo, 9Cr-1Mo and modified 9Cr-1Mo steels. The comparison between experimental and predicted creep rupture life for plain specimen is shown in Fig. 6.10. The predicted creep rupture life was found to be in good agreement with the experimentally observed creep rupture life within a factor of around 1.5. The VUMAT is further extended for prediction of damage evolution and creep rupture life under multiaxial state of stress.

6.5.2 Multiaxial creep

6.5.2.1 Damage evolution

In order to corroborate the fracture behaviour under multiaxial state of stress, analysis of damage evolution was carried out using FE analysis incorporating creep damage constitutive equations. The creep damage across the notch in relatively shallow notch (notch root radius = 2.5 mm) in 9Cr-1Mo steel for different creep exposure is shown in Fig. 6.11. The damage was found to initiate at the notch root due to the higher stresses that develop as a result of stress concentration, Fig. 6.11(a). However, the stress relaxation takes place due to difference in creep rates across the notch plane (Fig. 5.19) and results in shifting of damage towards the centre of notch, Fig. 6.11(b). At the later stage when the damage increases, further redistribution of stress takes place for maintaining the strain compatibility with the more damaged centre of the notch due to the dependency of damage rate on current damage [74]. The shedding of load takes place from centre of the specimen to the less damaged notch root. Finally, the critical damage ($\omega = 0.5$) reaches at the centre of notch resulting cup and cone type fracture as observed experimentally, Fig. 5.7. Quite different accumulation of creep damage behaviour in relatively sharper notches was observed, resulting in fracture appearance as shown in Fig. 5.9. The damage accumulation with creep exposure for relatively sharper notch (notch root radius = 0.5 mm) of 9Cr-1Mo steel is shown in Fig. 6.12. The stress redistribution across the notch throat plane led to the higher stresses at the notch root region, Fig. 5.19. Unlike in shallow notches, in sharper notches the damage continues to accumulate at the notch root region and reaches critical value, Fig. 6.12. The crack propagates (Fig. 5.11) from the notch root region towards centre resulting in fracture appearance depicted in Fig. 5.9.

Relative creep damage evolution in the different ferritic steels under multiaxial state of stress has been assessed by carrying FE analysis on incorporating the constitutive damage equations of the individual steel. The accumulations of creep damage across the notch having root radius of 2.5 mm for creep exposure of half of their respective rupture life (t_r / 2) are compared in Fig. 6.13 for the steels. The creep damage accumulation was significantly high for 2.25Cr-1Mo than those in 9Cr-steels. The extent was in the decreasing order of 2.25Cr-1Mo, 9Cr-1Mo and modified 9Cr-1Mo steel. Under uniaxial state of stress, the onset of tertiary creep stage was found to be in the increasing order of modified 9Cr-1Mo, 9Cr-1Mo and 2.25Cr-1Mo steel (Fig. 3.8), reflecting greater extent of creep damage accumulation in 2.25Cr-1Mo steel than in the 9Cr-steels for a given fraction of creep rupture life. In the estimated damage accumulation in the steels under multiaxial state of stress (Fig. 6.13), the experimentally observed behaviour of creep damage accumulation under uniaxial stress has also been replicated with higher creep damage in 2.25Cr-1Mo steel than that of other two steels. Less creep cavitation in 9Cr-1Mo steel (Fig. 5.15) than in 2.25Cr-1Mo steel (Fig. 4.8 and 5.11) support the FE analysis of creep damage accumulation in the steels.

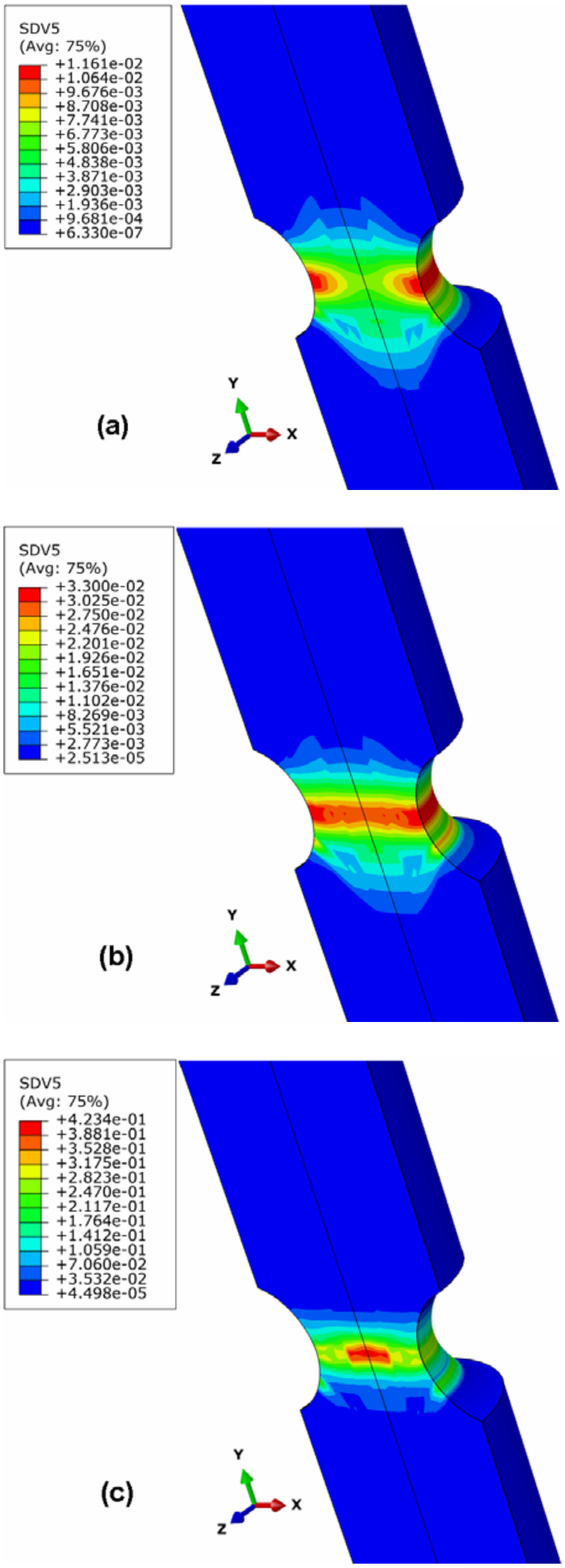

Fig. 6.11 Damage evolution in relatively shallow notch of acuity ratio 2 with creep exposure (a) 3 h, (b) 45 h and (c) 189 h in 9Cr-1Mo steel.

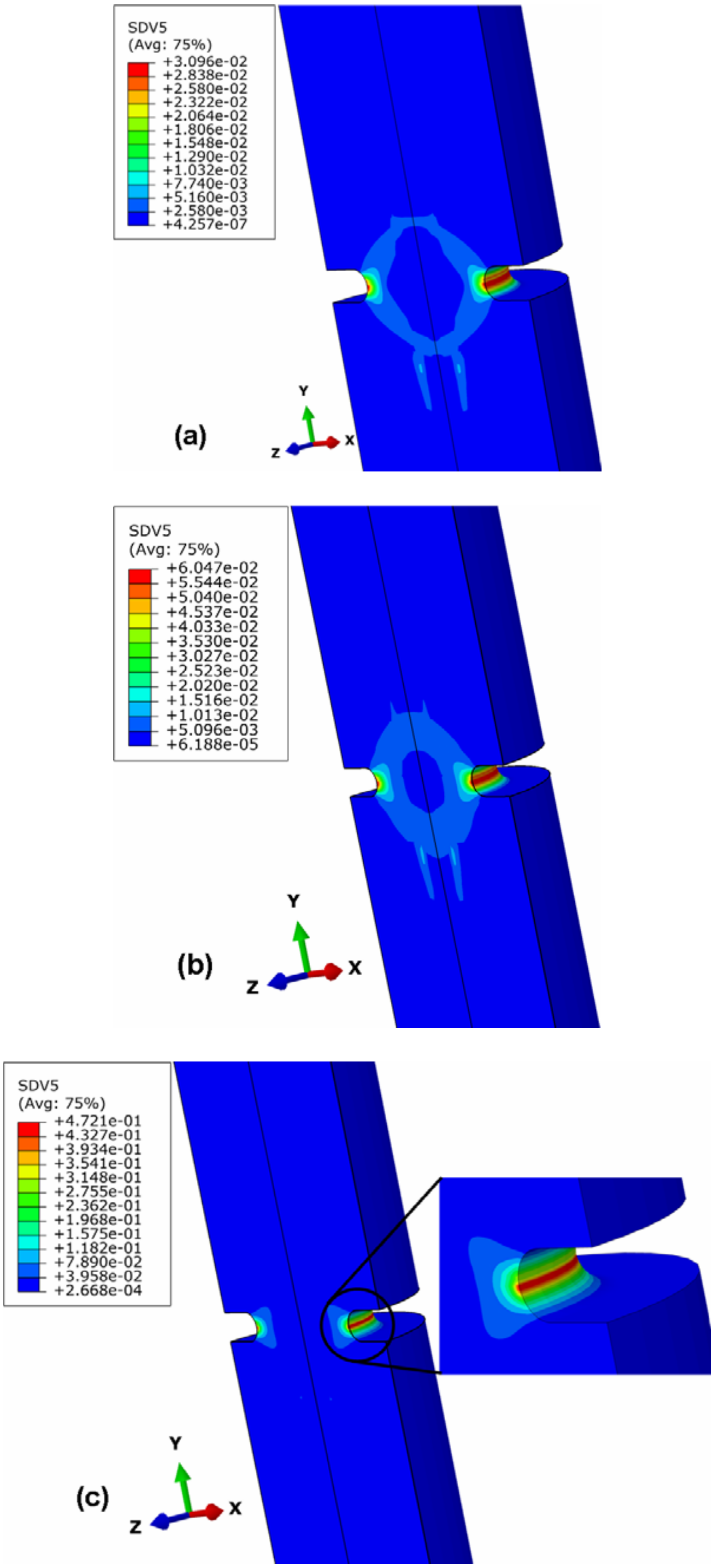

Fig. 6.12 Damage evolution in relatively sharper notch of acuity ratio 10 with creep exposure (a) 4 h, (b) 100 h and (c) 584 h in 9Cr-1Mo steel.

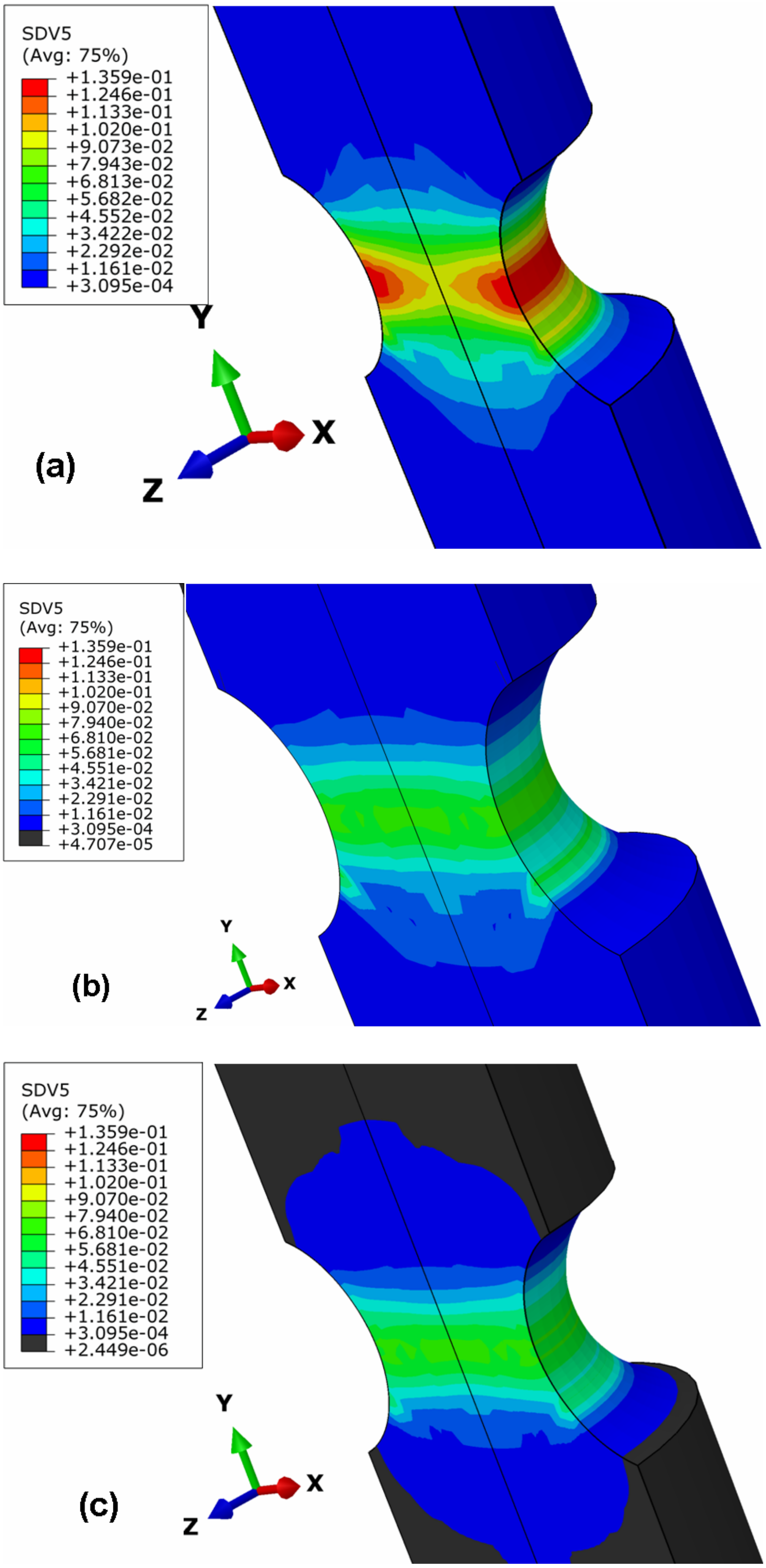

Fig. 6.13 Damage evolution at half of creep rupture life in relatively shallow notch of acuity ratio 2 at 170 MPa (a) 2.25Cr-1Mo, (b) 9Cr-1Mo and (c) modified 9Cr-1Mo steel.

6.5.2.2 Creep rupture life prediction

The creep rupture life of the steels under multiaxial state of stress has been predicted based on the representative stress associated with creep damage (Eq. 2.2) using FE analysis coupled with creep damage mechanics. The representative stress was calculated within the VUMAT subroutine at each integration point during increment by using von-Mises stress and maximum principal stress. The rupture life of the steels predicted based on the continuum damage mechanics coupled with FE analysis was found to be in good agreement with the experiments within a factor of 3 as shown in Fig. 6.14. The creep damage analysis carried out by Hayhurst et al. [117] considering the damage originated due to (i) softening due to multiplication of mobile dislocations (ii) softening due to void nucleation and growth and (iii) softening due to continuum cavity growth could estimate the creep rupture life within a factor 2.4. Yatomi et al. [66] carried out FE analysis using strain based damage mechanics approach for notched specimens considering initial plastic deformation, primary, secondary and tertiary stage of creep deformation, and elastic damage underestimated the creep rupture life. In relatively microstructurally stable nickel base and titanium base superalloys, Hyde et al. [74] could predict the creep rupture life of notched specimens within a error band of 20 %.

Ashby and Dyson [28] and Dyson [29] developed the microstructure based constitutive equations for creep damage in the ferritic steels. Microstructure of tempered bainitic / martensite ferritic steels is complex and thermodynamically unstable during creep exposure. The microstructural features which contribute to the damage in the ferritic steels under creep conditions are: (i) strain-induced coarsening of subgrains and decrease in the density of mobile dislocations and (ii) the coarsening of precipitate particles. Oruganti et al. [118] and Christopher et al. [119] successfully

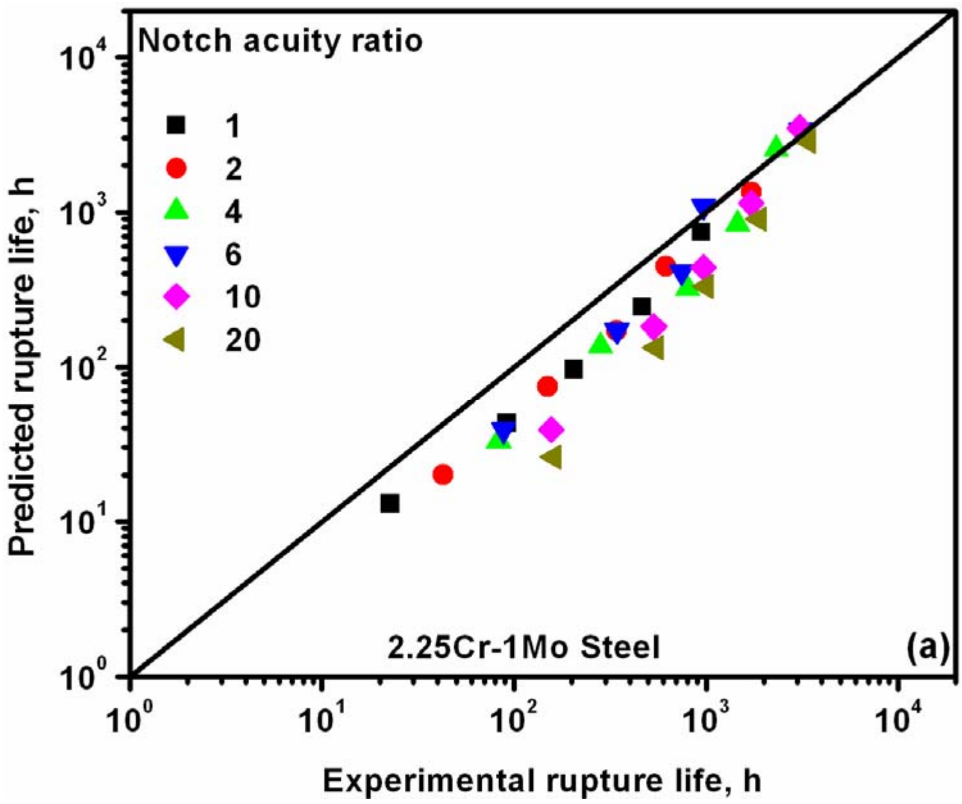
Notch acuity ratio
1
2
4
6
10
20
Predicted rupture life, h
Experimental rupture life, h
2.25Cr-1Mo Steel
(a)

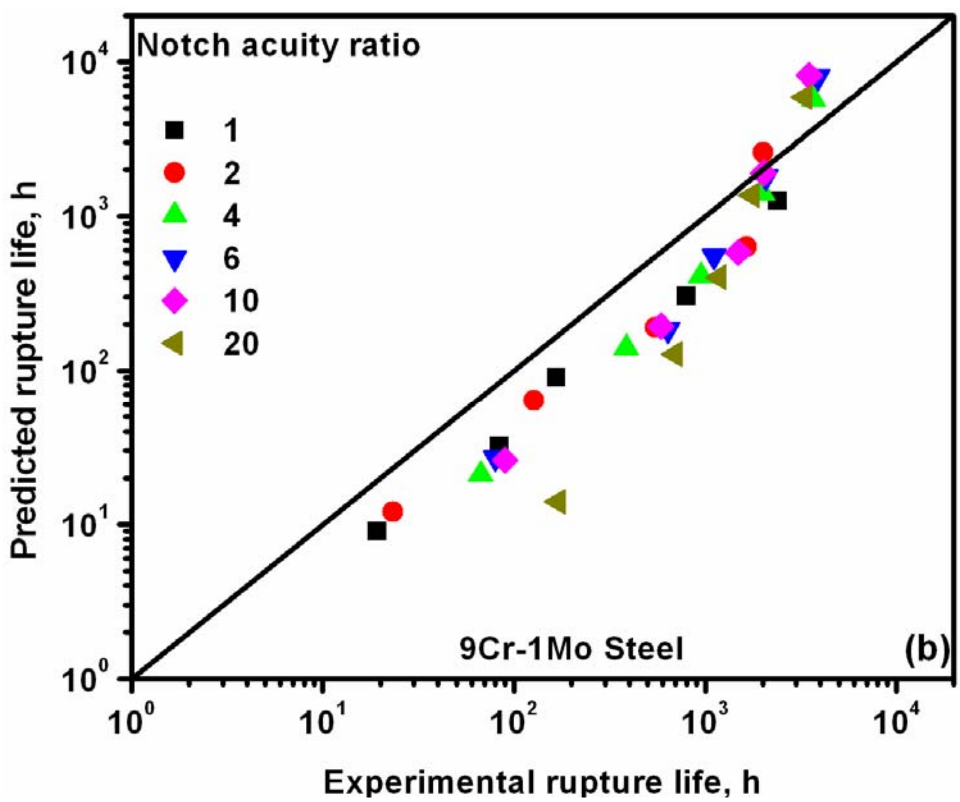
Notch acuity ratio
1
2
4
6
10
20
Predicted rupture life, h
Experimental rupture life, h
9Cr-1Mo Steel
(b)

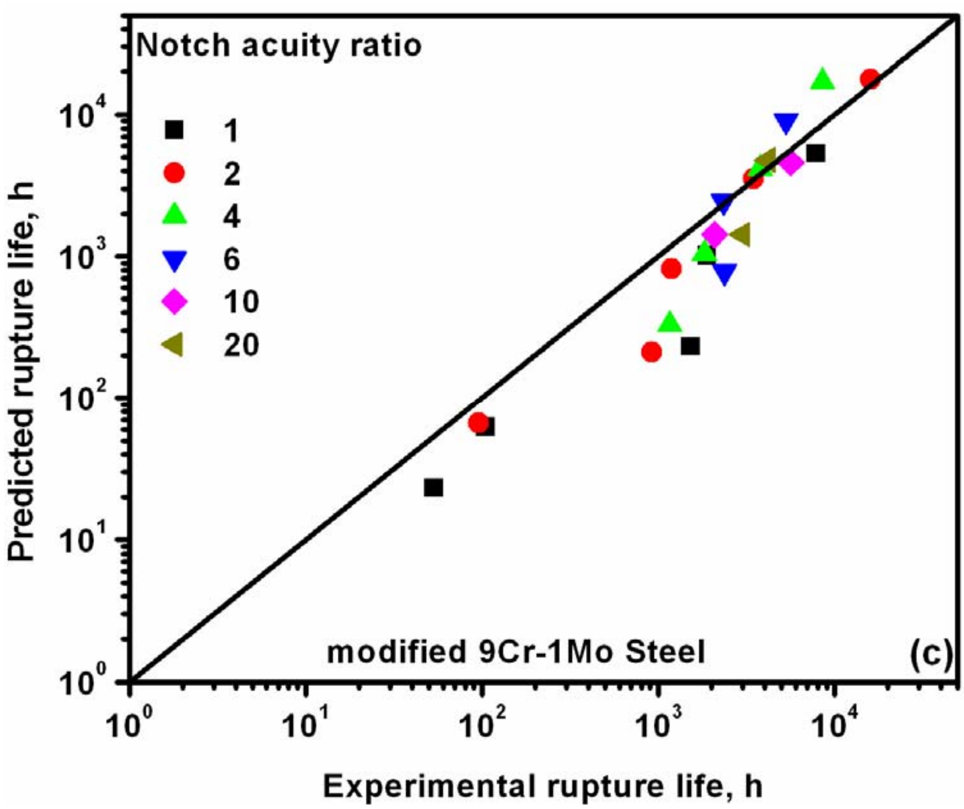

Fig. 6.14 Prediction of creep rupture life of notched specimens at various applied stresses and notch acuity ratios at 873 K for (a) 2.25Cr-1Mo (b) 9Cr-1Mo and (c) modified 9Cr-1Mo steels.

implemented the constitutive equations and estimated the creep life under uniaxial state of stress for 9Cr-steels. However, the mechanisms dependent on state of stress would be affected in presence of notch and would result in scatter in prediction under multiaxial state of stress [117]. Microstructural degradation under multiaxial state of stress is manifested in the reduction of hardness of the steel on creep exposure. The micro-hardness measurements were taken on un-failed notch of creep tested specimens. The variations of hardness across the notch throat plane for notch of root radius 1.25 mm creep tested at 210 and 110 MPa are shown in Fig. 6.15. The complex distribution of hardness which also depends on applied stress was observed, reflecting the complex nature of stress distribution across the notch throat plane Fig. 5.23. The reduction in hardness was also found to depend on the material (Fig. 6.16).

In the present investigation, the accuracy of prediction of creep rupture life under multiaxial state of stress is found to be slightly poor compared to uniaxial specimens. The predictions of creep rupture life are based on skeletal point concept. However, in reality, the stresses vary significantly across the notch throat plane. This would lead to slight inaccuracy in prediction of rupture life of steels under multiaxial state of stress. In addition to that, the damage has been considered in the form of creep cavitation. However, if the other damage mechanisms like strain induced microstructural damage, decrease in mobile dislocation density and particle coarsening associated with damage in ferritic steels are included, predictions would have been better. This can be considered for future investigations.

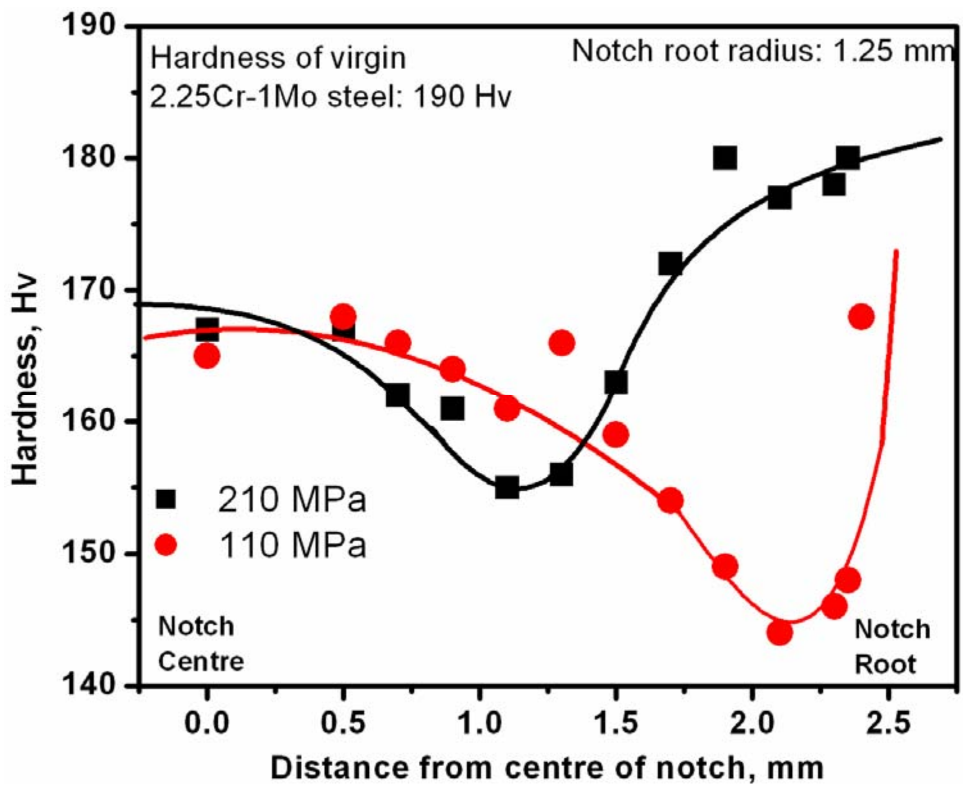

Fig. 6.15 Variation of hardness across the notch throat plane for notch root radius of 1.25 mm in un-failed notch creep tested at 210 and 110 MPa.

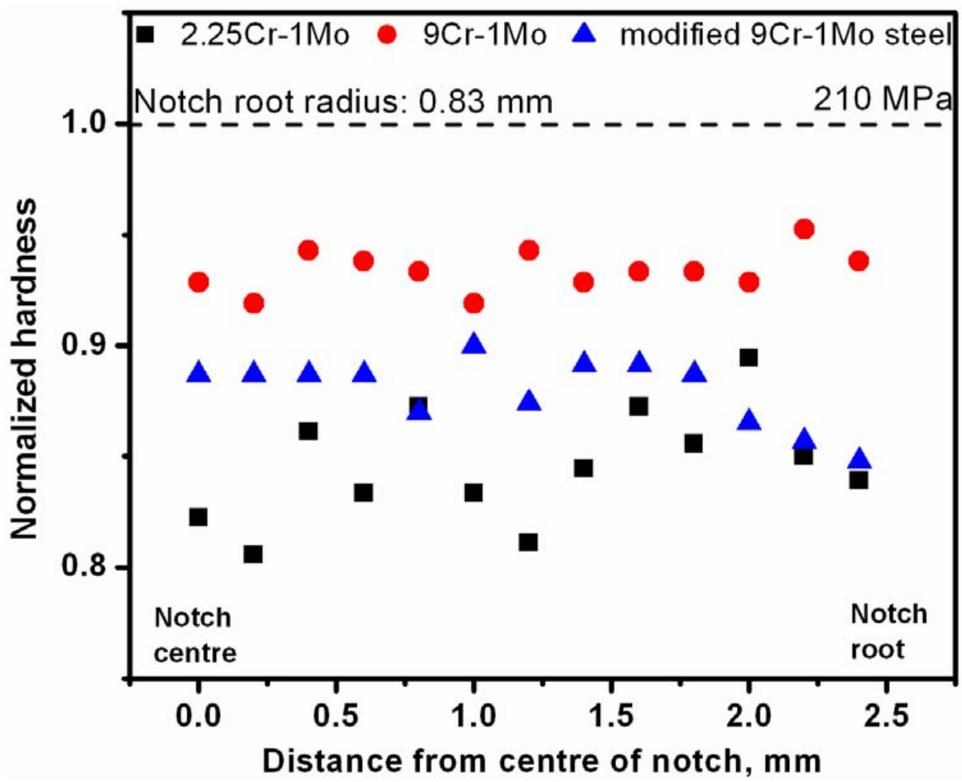

Fig. 6.16 Variation of hardness across the notch throat plane for notch root radius of 0.83 mm in un-failed notch creep tested at 210 MPa for the steels.

6.6 Conclusions

Based on the prediction of creep rupture life of 2.25Cr-1Mo, 9Cr-1Mo and modified 9Cr-1Mo steels under multiaxial state of stress from the detailed creep experiments on notched and plain specimens and finite element analysis coupled with continuum damage mechanics, the following conclusions have been drawn

1. The rupture life under multiaxial state of stress has been predicted based on representative stress considering the available models. The model proposed by Cane represented the experimental multiaxial creep data well for the steels. Skeletal point concept was adopted for estimating the representative stress in notched specimens.

2. Creep strain and rupture life of the steels under uniaxial state of stress were very well predicted using the FE analysis incorporating damage mechanics equations in the model.
3. The FE analysis coupled with continuum damage mechanics under multiaxial loading was found to predict the rupture lives of the steels within a factor of 3.
4. The damage evolution across the notch estimated based on FE-CDM correlated well with the experimental variation of fractographic observations.

CHAPTER 7

SUMMARY AND SCOPE FOR FUTURE WORK

Summary and scope for future work

The studies pertaining to the effect of multiaxial state of stress, introduced by incorporating circumferential U-notches of various notch radii on cylindrical specimens, on creep rupture behaviour of 2.25Cr-1Mo, 9Cr-1Mo and modified 9Cr-1Mo steels have been summarized:

7.1 Summary

The rupture life of all the steels in presence of notch was found to be higher than those of plain specimens, exhibiting notch strengthening behaviour. The strengthening of the steels in presence of notch was found to be in the increasing order of 2.25Cr-1Mo steel, 9Cr-1Mo steel and modified 9Cr-1Mo steel. Ductility of the steels decreased in presence of notch. Fractographic studies revealed typical cup and cone transgranular ductile fracture for all the steels at relatively higher stresses. The evidence of creep cavitation induced brittle fracture at relatively lower applied stresses was observed.

The rupture life of the steels was found to increase with notch sharpness (notch acuity ratio) and tends to saturate at relatively higher notch acuity ratio. The extent of strengthening with notch acuity ratio was found to depend on the material. It was in the increasing order of 2.25Cr-1Mo, 9C-1Mo and modified 9Cr-1Mo steel. Creep rupture ductility of the steels decreased significantly with increase in notch acuity ratio and tends to saturate at higher notch acuity ratio. The increase in notch sharpness decreased the creep rupture ductility to a greater extent in modified 9Cr-1Mo steel and least in 9Cr-1Mo steel.

Significant variation in creep fracture appearance was observed depending on the material and notch sharpness. Shear-lip type of failure of the notched specimen was observed for notches of relatively lower notch acuity ratio < 4 whereas, for notch acuity ratio ≥ 4, intergranular creep cavitation close to notch root and the ductile dimple fracture around the central region of notch throat plane were observed. Under multiaxial state of stress, 2.25Cr-1Mo was found to be more susceptible to creep cavitation and 9Cr-1Mo steel the least.

The FE analysis revealed the presence of multiaxial state of stress across the notch. With creep exposure, the stress distribution changed progressively to attain a stationary state. The von-Mises stress was found to remain below the net applied stress resulting in notch strengthening in the steels. The decrease in von-Mises stress with increase in notch sharpness led to higher strengthening. The saturating tendency of von-Mises stress with increase in notch acuity ratio resulted in saturation of notch strengthening. The faster stress relaxation of von-Mises stress for modified 9Cr-1Mo steel resulted in higher extent of notch strengthening than those in 2.25Cr-1Mo and 9Cr-1Mo steels.

The variation in maximum principal stress across the notch throat plane showed a maxima having value more than the net applied stress. The maxima in principal stress increased with notch acuity ratio and its position progressively shifted towards the notch root region. For the relatively shallow notches (notch acuity ratio $<$ 4), the presence of relatively high and uniform von-Mises stress across notch throat plane induced uniform cavity nucleation across the notch throat plane. Presence of high maximum principal and hydrostatic stresses at the central region of notch throat plane caused preferential growth of the nucleated cavities, resulting in dimple ductile appearance, as observed experimentally.

For relatively sharper notches (notch acuity ratio ≥ 4) maximum von-Mises stress at the notch root region led to nucleation of creep cavities. High principal stress along with high hydrostatic stress resulted in growth of the nucleated cavities at the near notch root region. Coalescence of the creep cavities would have led to the propagation of crack from the notch root region towards the central region of the notch throat plane, as observed experimentally.

Prediction of creep rupture behaviour of the steels under multiaxial state of stress was carried out based on representative stress concept. The relative contribution of maximum principal stress, hydrostatic stress and von-Mises stress to the representative stress in governing the creep rupture life under multiaxial state of stress was assessed. The stresses estimated at skeletal point were implemented to estimate the representative stress. The model proposed by Cane, which considers the inter-relationship between creep deformation and cavitation, represented the experimental multiaxial creep data well for the steels. The von-Mises stress was found to predominantly govern creep rupture life of the steels under multiaxial state of stress.

The multiaxial creep rupture behaviour of the steels was also predicted based on the FE analysis coupled with continuum damage mechanics (CDM). The creep deformation and damage laws were incorporated in FE analysis using VUMAT subroutine for calculating the stresses, creep strains and damage in the plain and notched specimens. The VUMAT subroutine was first implemented for prediction of creep strains and rupture lives of the steels under uniaxial state of stress before applying it to multiaxial state of stress. The predicted creep strains and rupture life was found to be in good agreement with the experimental data, which validated the procedure adopted in the subroutine for FE analysis considering CDM. The estimated creep damage evolution of the steel under multiaxial state of stress could predict the observed variations in fracture behaviour of the steels. The assessment predicted the higher rate of creep damage accumulation in 2.25Cr-1Mo steel than in 9Cr-steels. Experimentally observed higher propensity to creep cavitation in 2.25Cr-1Mo steel than in 9Cr-steels under multiaxial state of stress has been validated. The rupture life of the steels under multiaxial state of stress predicted based on the continuum damage mechanics coupled with FE analysis was found to be in good agreement with the experiments within a factor of 3.

7.2 Suggestions for future work

Based on the study of effect of multiaxial state of stress on creep behaviour of 2.25Cr-1Mo, 9Cr-1Mo and modified 9Cr-1Mo steels, following suggestions have been made for further investigation

1. Creep deformation and rupture behaviour of materials subjected to sharper notches as encountered in fabricated component may be carried out to establish the multiaxial state of behaviour of component.
2. Response of material to multiaxiality, incorporated by other means like bi-axial and torsion etc., can be assessed and compared for realistic prediction of creep deformation, damage and rupture.
3. The prediction of creep rupture life under multiaxial state of stress can be validated by performing component testing.
4. Multiaxial creep response of material can be utilized for predicting type IV cracking behaviour of ferritic steel weld joints which are subjected to multiaxial stress due to microstructural inhomogeneity.
5. Long term creep tests can be performed to assess the notch strengthening / weakening behaviour of these steels.

6. Studies can also be extended to dynamic loading condition to assess creep-fatigue interaction under multiaxial state of stress.
7. The studies can be extended to diverse materials having different deformation characteristics.

REFERENCES

[1] R. Viswanathan, Damage mechanisms and life assessment of high temperature components, ASM international, US, 1989.

[2] B. Neubauer and U. Wedel, Rest life estimation of creeping components by means of replicas, in Advances in life prediction methods, D.A, Woodford and J.R. Whitehead Eds. ASME, New York, 1983, 307- 314.

[3] H.J. Frost and M.F. Ashby, Deformation mechanism maps, Pergamon Press, 1982.

[4] M.F. Ashby, C. Gandhi and D.M.R. Taplin, Fracture mechanism maps and their construction for FCC metals and alloys, Acta Met., 27 (1979) 699- 729.

[5] S.H. Goods and L.M. Brown, The nucleation of cavities by plastic deformation, Acta Met., 27 (1979) 1- 15.

[6] W.D. Nix, Mechanisms and controlling factors in creep fracture, Mater. Sci. Engg. A, 103 (1988) 103- 110.

[7] M.E. Kassner and M.T.P. Prado, Fundamental of creep in metals and alloys, Elsevier, 2004.

[8] R. Raj and M.F. Ashby, Intergranular fracture at elevated temperature, Acta Met., 23 (1975) 653- 666.

[9] C. Gandhi and R. Raj, Intergranular fracture in bicrystals, Acta Met., 30 (1982) 505- 511.

[10] E. Smith and J. T. Barnby, Nucleation of grain boundary cavities during high temperature creep, Metal Sci., 1 (1967) 1- 4.

[11] L.M. Brown and W.M. Stobbs, The work hardening of copper-silica vs. equilibrium plastic relaxation by secondary dislocations, Phil. Mag., 34 (1976) 351- 372.

[12] J.W. Hancock, Creep cavitation without a vacancy flux, Metal Sci., 10 (1976) 319- 325.

[13] F.A. McClintock, A criterion for ductile fracture by the growth of holes, J. Appl. Mech., 35 (1968) 363- 371.

[14] P.F. Thomason, A theory of ductile fracture by internal necking of cavities, J. of Inst Metals, 96 (1968) 360- 365.

[15] P.F. Thomason, A theoretical relation between fracture toughness and basic material properties, Int. J. Frac. Mech., 7 (1971) 409- 419.

[16] L.M. Brown and J.D. Embury, The initiation and growth of voids at second phase particles. Proc 3rd Int Conf on the Strength of Metals and Alloys, Inst of Metals, London, 1973, pp. 164- 169.

[17] D. Hull and D.E. Rimmer, The growth of grain boundary voids under stress, Phil. Mag., 4 (1959) 673- 687.

[18] W. Beere and M.V. Speight, Creep cavitation by vacancy diffusion in plastically deforming solid, Met. Sci, 12 (1978) 172- 176.

[19] B.F. Dyson, Constraints on diffusional cavity growth rates, Metal Sci., 18 (1976) 349- 353.

[20] B.J. Cane, Interrelation between creep deformation and creep rupture in 2.25Cr-1Mo steel, Metal Sci., 13 (1979) 287- 294.

[21] Y. Ishida and D. McLean, The formation and growth of cavities in creep, Metal Sci., 1 (1967) 171- 172.

[22] A. Needleman and J.R. Rice, Plastic creep flow effects in the diffusive cavitation of grain boundaries, Acta metall., 28 (1980) 1315- 1332.

[23] L.M. Kachanov, The Theory of Creep (Ed. A.J. Kennedy), National Lending Library, Boston Spa, UK, 1967.

[24] Y.N. Robotnov, Creep problems in structural members, North-Holland, 1969.

[25] K. Naumenko and H. Altenbach, Modeling of creep for structural analysis, Springer, 2007.

[26] J. Lemaitre and J.L. Chaboche, Mechanics of solid materials, Cambridge University Press, Cambridge, 1990.

[27] F.C. Monkman and N.J. Grant, Empirical relation between rupture life and minimum creep rate in creep rupture tests, Proc. Amer. Soc. Testing Mater., 56 (1956) 593- 620.

[28] M.F. Ashby and B.F. Dyson, Creep damage mechanics and micromechanisms, Eds. R.S. Valluri, Advances in Fracture Research, vol. 1, Pergamon Press, Oxford, 1984, pp. 3- 30.

[29] B.F. Dyson, Use of CDM in materials modeling and component creep life prediction, Trans ASME, J. Press. Vess. Tech., 122 (2000) 281- 296.

[30] B.F. Dyson and M. McLean, Microstructural evolution and its effects on the creep performance of high temperature alloys, Microstructural stability of

creep resistant alloys for high temperature plant applications, Eds. A. Strang, J. Cawley and G.W. Greenwood, The Institute of materials, London, UK, 1998, 371- 394.

[31] S. Goyal, K. Laha, K.S. Chandravathi, P. Parameswaran and M.D. Mathew, Finite element analysis of Type IV cracking in 2.25Cr-1Mo steel weld joint based on micro-mechanistic approach, Phil. Mag., 91 (2011) 3128- 3154.

[32] J.T. Boyle and J. Spence, Stress analysis for stress, Camelot press, London, 1983.

[33] D.J. Gooch and I.M. How, Techniques for multiaxial creep testing. Elsevier Applied Science, Amsterdam, 1986.

[34] W. Trampczynski and Z. Kowalewski, A Tension-torsion testing technique, Techniques for multiaxial creep testing. Eds. D.J. Gooch and I.M. How, Elsevier Applied Science, Amsterdam, 1986, pp. 79- 92.

[35] R.C. Hurst and I.M. How, Potential for standardization of techniques for creep testing of internally pressurized tubular components, Techniques for multiaxial creep testing. Eds. D.J. Gooch and I.M. How, Elsevier Applied Science, Amsterdam, 1986, pp. 267- 293.

[36] C.J. Morrison, Biaxial testing using cruciform specimens, Techniques for multiaxial creep testing. Eds. D.J. Gooch and I.M. How, Elsevier Applied Science, Amsterdam, 1986, pp. 111- 126.

[37] D.R. Hayhurst, Creep rupture under multi-axial states of stress, J. Mech. Phy. Solids, 20 (1972) 381- 390.

[38] B.F. Dyson and M. S. Loveday, Creep fracture in Nimonic 80A under triaxial tensile stressing, Proc. Creep in Structures, TUTAM Symp. Pergamon Press, Oxford, pp. 406- 421.

[39] K.D. Al-Faddagh, G.A. Webster and B.F. Dyson, Influence of state of stress on creep failure of 2.25%Cr-1%Mo steel, Mechanical behaviour of materials IV, Eds, Carlsson J. and Ohlson N. G, Oxford, (1984), pp. 289-295.

[40] S.E. Ng, G.A. Webster and B.F. Dyson, Notch weakening and strengthening in creep of 0.5Cr-0.5Mo-0.25V steel, Advances in fracture research, ICF-5, Eds. D. Francois *et al.*, 1980, Pergamon Press, Oxford, UK, pp. 1275- 1283.

[41] G. Eggeler, W. Tato, P. Jemmely and B. deMestral, Creep rupture of circular notched P91 specimens: influence of heat treatment and notch geometry, Scripta Metall. Mater., 27 (1992) 1091- 1096.

[42] D.R. Hayhurst, F.A. Leckie and J.T. Henderson, Design of notched bars for creep-rupture testing under tri-axial stresses, Int. J. Mech. Sci., 19 (1977) 147-159.

[43] D.R. Hayhurst and G.A. Webster, An overview on studies of stress state effects during creep of circumferentially notched bars. Techniques for multiaxial creep testing. Ed. D.J. Gooch and I.M. How, Elsevier Applied Science, Amsterdam, 1986, pp. 137- 175.

[44] D. Wu, E.M. Christian and E.G. Ellison, Influence of constraint on creep stress distribution in notched bars, J. Strain Analysis, 19 (1984) 209-220.

[45] D.R. Hayhurst and J.T. Henderson, Creep stress redistribution in notched bars, Int. J. Mech. Sci., 19 (1977) 133- 146.

[46] P.W. Bridgman, Studies in large plastic flow and fracture, McGraw-Hill, New York, 1952.

[47] B.J. Cane, Creep damage accumulation and fracture under multiaxial stresses, Advances in Fracture Research. Proc. 5th Int. Conf. Fract. Cannes, 1981, Vol. 3, pp. 1285- 1293.

[48] G.A.Webster, K.M. Nikbin and F. Biglari, Finite element analysis of notched bar skeletal point stresses and dimension changes due to creep, Fat. Frac. Engg. Mater. Struct. 27 (2004) 297- 303.

[49] D. McLean, B.F. Dyson and D.M.R. Taplin, The prediction of creep fracture in engineering alloys, The Fourth International Conference on Fracture, Vol. 1, Ed. D. M. R. Taplin, University of Waterloo Press, Waterloo, Canada, 1977, pp. 325- 362.

[50] E.A. Davis and M.J. Manjoine, Effect of notch geometry on rupture strength at elevated temperatures, ASTM STP 128, pp. 67- 87.

[51] M.C. Pandey, A.K. Mukherjee and D.M.R. Taplin, Effect of triaxial stress-state on creep fracture in Inconel alloy- 750, J. Mater. Sci., 20 (1985) 1201-1206.

[52] P.S. Webster and A.C. Pickard, The prediction of stress rupture life of notched specimens in the beta-processed Titanium alloy Ti5331s, J. Strain Analysis, 22 (1987) 145- 153.

[53] O. Kwon, C.W. Thomas and D. Knowles, Multiaxial stress rupture behavior and stress-state sensitivity of creep damage distribution in Durehete 1055 and 2.25Cr-1Mo steel, Int. J. Press. Vess. Piping, 81 (2004) 535- 542.

[54] D.R. Hayhurst and F.A. Leckie, The effect of creep constitutive and damage relationships upon the rupture time of a solid circular torsion bar, J. Mech. Phy. Solids, 21 (1973) 431- 446.

[55] V.P. Sdobyrev, Long term strength of EI-437B under complex stresses, Izv. Akad. Nauk SSSR, Otd. Tekh. Nauk, 4 (1958) pp. 92- 97.

[56] A.E. Johnson, J. Henderson and V.D. Mathur, Complex stress creep fracture of an aluminum alloy: An investigation conducted at an elevated temperature, Aircraft Engg. Aerospace Tech., 32 (1960) 161- 170.

[57] A.E. Johnson, J. Henderson and V.D. Mathur, Combined stress creep fracture of commercial copper at 250° C, The Engineer, 2.2 (1956) 261- 265.

[58] D.R. Hayhurst, Creep rupture under multi-axial states of stress, J. Mech. Phy. Solids, 20 (1972) 381- 390.

[59] D.R. Hayhurst, On the role of creep continuum damage in structural mechanics, Engineering Approaches to High Temperature Design, Chapter-4, Pineridge Press, Swansea, 1983.

[60] D.R. Hayhurst, P.R. Dimmer and C.J. Morrison, Development of continuum damage in the creep rupture of notched bars, Phil. Trans. Royal Soc. London, 311 (1984) 103- 129.

[61] B.J. Cane, Creep cavitation and rupture in 2.25Cr-1Mo steel under uniaxial and multiaxial stresses. In: Proceedings of the Int. Conf. on Mechanical behavior of Materials, Eds. K.J.Miller and R.F. Smith, Pergamon Press, Oxford, 1979, 173- 182.

[62] B. Al-Abed, R. Timmins, G.A. Webster and M. S. Loveday, Validation of a code of practice for notched bar creep rupture testing: procedures and interpretation of data for design, Mater. High Temp., 16 (1999) 143- 158.

[63] W.D. Nix, J.C. Earthman, G. Eggeler and B. Ilschner, The principal facet stress as a parameter for predicting creep rupture under multiaxial stresses, Acta Metall., 37 (1989) 1067-1077.

[64] R.L. Huddleston, An improved multiaxial creep-rupture strength criterion, Trans. ASME, J. Press. Vessel Technol., 107 (1985) 412- 429.

[65] P.F. Aplin and G.F. Eggeler, Multiaxial stress rupture criteria for ferritic steels, Proceedings of the Int. Conf. on Mechanics of Creep brittle materials,

Eds. A.C.F. Cocks and A.R.S. Ponter, Elsevier Applied Science, 1988, 245-261.

[66] M. Yatomi, A.D. Bettinson, N.P.O'Dowd and K.M. Nikbin, Modeling of damage development and failure in notched bar multiaxial creep tests, Fat. Frac. Engg. Mater. Struct., 27 (2004) 283- 295.

[67] T.H. Hyde, A.A. Becker, W. Sun and J.A. Williams, Finite element creep damage analysis of P91 pipes, Int. J. Press. Vess. Piping, 83 (2006) 853- 863.

[68] E. Hosseini, S.R. Holdsworth and E. Mazza, Stress regime dependent creep constitutive model considerations in finite element continuum damage mechanics, Int. J. Damage Mech., DOI: 10.1177/1056789513479810.

[69] A.M. Othman, D.R. Hayhurst and B.F. Dyson, Skeletal point stresses in circumferentially notched tension bars undergoing tertiary creep modelled with physically based constitutive equations, Proc. Royal Soc. Lond. A, 441 (1993) 343- 358.

[70] G.A. Webster, S.R. Holdsworth, M.S. Loveday, K. Nikbin, I.J. Perrin, H. Purper, R.P. Skelton and M.W. Spindler, A code of practice for conducting notched bar creep tests and for interpreting the data, Fat. Frac. Engg. Mater. Struct., 27 (2004) 319- 342.

[71] T.H. Hyde, W. Sun and A.A. Becker, Failure prediction for multi-material creep test specimens using a steady-state creep rupture stress, Int. J. Mech. Sci., 42 (2000) 401- 423.

[72] Y.P. Jiang, W.L. Guo, Z.F. Yue and J. Wang, On the study of notch shape on creep damage development under constant loading, Mat. Sci. Engg. A, 437 (2006) 340- 347.

[73] H. Yao, Investigations on multiaxial creep theory and design criteria for high temperature structures, J. Press. Equipment Systems, 6 (2008) 115- 118.

[74] T.H. Hyde, L. Xia and A.A. Becker, Prediction of creep failure in aeroengine materials under multiaxial stress states, Int. J. mech. Sci., 38 (1996) 385- 403.

[75] A.M. Othman, J. Lin, D.R. Hayhurst and B.F. Dyson, Comparison of creep rupture lifetimes of single and double notched tensile bars, Acta Met., 41 (1993) 1215- 1222.

[76] F.R. Hall and D.R. Hayhurst, Continuum damage mechanics modeling of high temperature deformation and failure in a pipe weldment, Proc. Royal Soc. Lond. A, 433 (1991) 383- 403.

[77] I.J. Perrin and D.R. Hayhurst, Creep constitutive equations for 0.5Cr-0.5Mo-0.25V ferritic steel in the temperature range 600- 675° C, J. Strain Analysis, 31 (1996) 299- 314.

[78] Z.L. Kowalewski, D.R. Hayhurst and B.F. Dyson, Mechanism based creep constitutive equations for an aluminum alloy, J. Strain Analysis, 29 (1994) 309- 316.

[79] D.J.F. Ewing, The plastic yielding of v-notched tension bars with circular roots, J. Mech. Phy. Solids, 16 (1968) 81- 98.

[80] W. Szczepiński, L. Dietrich, E. Drescher and J. Miastkowski, Plastic flow of axially symmetric notched bars pulled in tension, Int. J. Solids Struct., 2 (1966) 543- 554.

[81] Y. Kim, C. Oh, M. Myung and J. Park, Fully plastic analyses for notched bars and plates using finite element limit analysis, Engg. Frac. Mech., 73 (2006) 1849- 1864.

[82] A.G. Miller, Review of limit loads of structures containing defects, Int. J. Pres. Ves. Pip., 32 (1988) 191- 327.

[83] H.E. Evans, Mechanisms of creep fracture, Elsevier Applied Science Publisher, 1984.

[84] F.A. McClintock, A criterion for ductile fracture by the growth of holes, J. Appl. Mech., 35 (1968) 363- 371.

[85] J.R. Rice and D.M. Tracey, On ductile-enlargement of voids in triaxial stress fields, J. Mech. Phy. Solids, 17 (1969) 201- 217.

[86] A.C.F. Cocks and M.F. Ashby (1980) Intergranular fracture during power-law creep under multiaxial stresses, Metal. Sci., 14 (1980) 395- 402.

[87] M.W. Spindler, The multiaxial creep ductility of austenitic stainless steels, Fat. Frac. Engg. Mater. Struct., 27 (2004) 273- 281.

[88] R. Hales, The role of cavity growth mechanisms in determining creep rupture under multiaxial stresses, Fat. Frac. Engg. Mater. Struct., 17 (1994) 579- 591.

[89] R.L. Klueh and D.R. Harries, High chromium ferritic and martensitic steels for nuclear applications, ASTM International, 2009.

[90] R.G. Baker and J. Nutting, The tempering of 2.25Cr-1Mo steel after quenching and normalizing, J. Iron Steel Inst., 192 (1959) 257- 268.

[91] S.C. Chetal, P. Chellapandi, P. Puthiyavinayagam, S. Raghupathy, V. Balasubramaniyan, P. Selvaraj, P. Mohankrishnan and Baldev Raj, Current status of fast reactors and future plans in India, Energy Procedia, 7 (2011) 64-73.

[92] J.M. Vitek and R.H. Klueh, Precipitation reactions during the heat treatment of ferritic steels, Met. Trans. A, 14 (1983) 1047- 1055.

[93] B.A. Senior, F.W. Noble and B.L. Eyre, The effect of ageing on the ductility of 9Cr-1Mo steel, Acta Met., 36 (1988) 1855- 1862.

[94] A. Gocmen, P.J. Uggowitzer, C. Solenthaler, M.O. Speidel and P. Ernst, in Microstructural Stability of Creep Resistant Alloys for High Temperature Plant Applications, Eds. Strang A, Cawley J and Greenwood GW, Microstructure of High Temperature Materials, No. 2, Ed. Strang A, The Institute of Materials (1998).

[95] P.J. Ennis, A. Zielifiska-Lipiec and A. Czyrska-Filemonowicz, Microstructural Stability of Creep Resistant Alloys for High Temperature Plant Applications, Eds. A. Strang, J. Cawley, and G. W. Greenwood, The Inst. of Materials, London, (1998) 135- 144.

[96] V.K. Sikka, Development of modified 9Cr-1Mo steel for elevated temperature service, Proc. Topical Conference on Ferritic Alloys for Use in Nuclear Energy Technologies, Eds. Davis JW and Michel DJ, Snowbird, Utah (1983) pp. 317- 327.

[97] ABAQUS finite element software, V6.10, Dassault Systemes, 2012.

[98] W.D. Pilkey and D.F. Pilkey, Peterson's Stress Concentraton Factors, 3rd Edition, John Wiley & sons, 2008.

[99] C.R. Calladine, Time-scales for redistribution of stress in creep of structures, Proc. Royal Soc. Lond., A 309 (1969) 363- 375.

[100] T.H. Hyde, W. Sun and A.Tang, Determination of material constants in creep continuum damage constitutive equations, Strain, 34 (1998) 83 - 90.

[101] J.H. Hollomon, Tensile deformation, Trans. AIME, 162 (1945) 268- 290.

[102] F. Abe, S. Nakazawa, H. Araki and T. Noda, The role of microstructural instability on creep Behavior of a Martensitic 9Cr-2W Steel, Metall. Trans. A, 23 (1992) 469- 477.

[103] B.K. Choudhary, S. Saroja, K. Bhanu Sankara Rao and S.L. Mannan, Creep-rupture behavior of forged, thick section 9Cr-1Mo ferritic steel, Metall. Trans. A, 30 (1999) 2825- 2834.

[104] K. Laha, K.S. Chandravathi, P. Parameswaran, S. Goyal and M.D. Mathew, A comparison of creep rupture strength of ferritic/austenitic dissimilar weld joints of different grades of Cr-Mo ferritic steels, Metall. Trans. A, 43 (2012) 1174- 1186.

[105] K. Laha, K.S. Chandravathi, K. Bhanu Sankara Rao, S.L. Mannan and D.H. Sastry, A comparison of creep rupture behaviour of 2.25Cr-1Mo and 9Cr-1Mo steels and their weld joints, High Temp. Mat. Processes, 19 (2000) 141- 150.

[106] B.W. Jones, C.R. Hills and D.H. Polonis, Microstructural evolution of modified 9Cr-1Mo steel, Metall. Trans. A, 22 (1991) 1049- 1058.

[107] J. Vanaja, K. Laha, R. Mythili, K.S. Chandravathi, S. Saroja and M.D. Mathew, Creep deformation and rupture behaviour of 9Cr-1W-0.2V-0.06Ta reduced activation ferritic-martensitic steel, Mat. Sci. Engg. A, 533 (2012) 17-25.

[108] F.A. Leckie and D.R. Hayhurst, Constitutive equations for creep rupture, Acta Metall., 25 (1977) 1059- 1070.

[109] B.F. Dyson and T.B. Gibbons, Tertiary creep in nickel-base superalloys: analysis of experimental data and theoretical synthesis, Acta Metall., 35 (1987) 2355- 2369.

[110] S. Chaudhuri and R.N. Ghosh, Some aspects of mechanisms and modeling of creep behaviour of 2.25Cr-1Mo steel, ISIJ International, 38 (1998) 881- 887.

[111] B.K. Choudhary and E. I. Samuel, Creep behaviour of modified 9Cr-1Mo ferritic steel, J. Nuclear Mat., 412 (2011) 82- 89.

[112] K. Wasmer, F. Bilgari and K.M. Nikbin, Multiaxial failure behaviour in advanced steels at elevated temperatures, European conference on fracture; ECF 14, fracture mechanics beyond 2000, (2002), pp. 553- 562.

[113] G. Eggeler and C. Wiesner, A numerical study of parameters controlling stress redistribution in circular notched specimens during creep, J. Strain Analysis, 28 (1993) 13- 22.

[114] I.J. Perrin and D.R. Hayhurst, Continuum damage mechanics analyses of type IV creep failure in ferritic steel cross-weld specimens, Int. J. Press. Vess. Piping, 76 (1999) 599- 617.

[115] Z.F. Yue, Z.Z. Lu and X.M. Wang, A numerical study of damage development and creep life in circular notched specimens during creep, Mat. High Temp., 19 (2002) 147- 152.

[116] R.J. Browne, D. Lonsdale and P.E.J. Flewitt, Multiaxial stress rupture testing and compendium of data for creep resisting steels, Trans ASME, J. Engg. Mat. Tech., 104 (1982) 291- 296.

[117] D.R. Hayhurst, J. Lin and R.J. Hayhurst, Failure in notched tension bars due to high-temperature creep: Interaction between nucleation controlled cavity growth and continuum cavity growth, Int. J. Solids Struct., 45 (2008) 2233-2250.

[118] R. Oruganti, M. Karadge and S. Swaminathan, Damage mechanics-based creep model for 9-10 % Cr ferritic steels, Acta Met., 59 (2011) 2145- 2155.

[119] J. Christopher, G. Sainath, V.S. Srinivasan, E. I. Samuel, B.K. Choudhary, M.D. Mathew and T. Jayakumar, Continuum damage mechanics approach to predict creep behaviour of modified 9Cr-1Mo ferritic steel at 873 K, Procedia Engg., 55 (2013) 798- 804.